UNIVERSITE LIBRE DE BRUXELLES
Faculté des Sciences appliquées

Année académique 2009 - 2010

Atmospheric Bromine Monoxide: multi-platform observations and model calculations

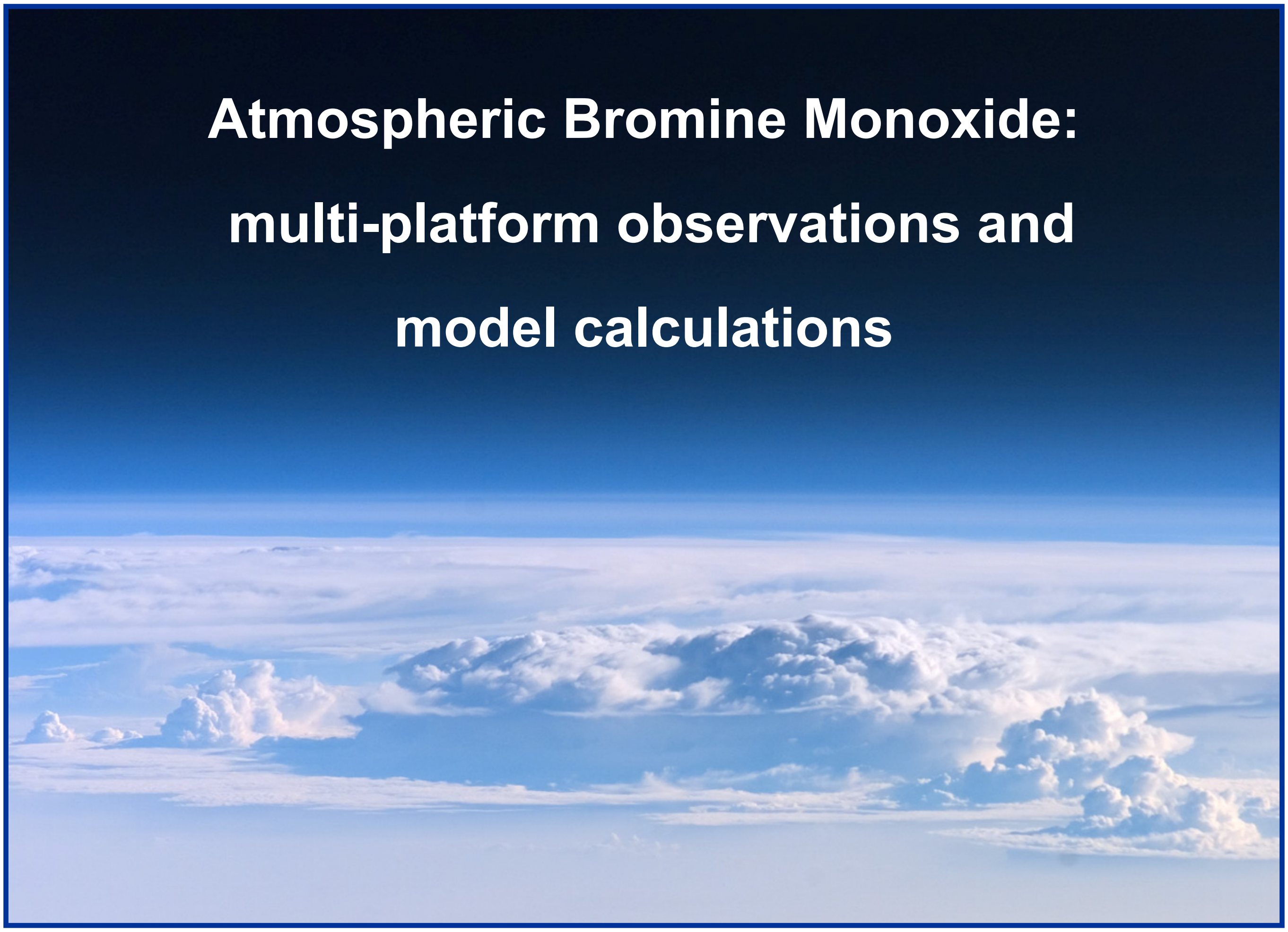

Directeur de Thèse : Michel Herman

Co-promoteur : Michel Van Roozendael

Dissertation présentée par
Nicolas THEYS en vue de
l'obtention du grade de
Docteur en Sciences de l'Ingénieur

Cover :
Looking through the Earth's atmosphere from on board the International Space Station (ISS).
Credits: European Space Agency (ESA)

ULB UNIVERSITÉ LIBRE DE BRUXELLES,
UNIVERSITÉ D'EUROPE

aeronomie.be

UNIVERSITE LIBRE DE BRUXELLES
Faculté des Sciences appliquées

Année académique 2009 - 2010

Atmospheric Bromine Monoxide: multi-platform observations and model calculations

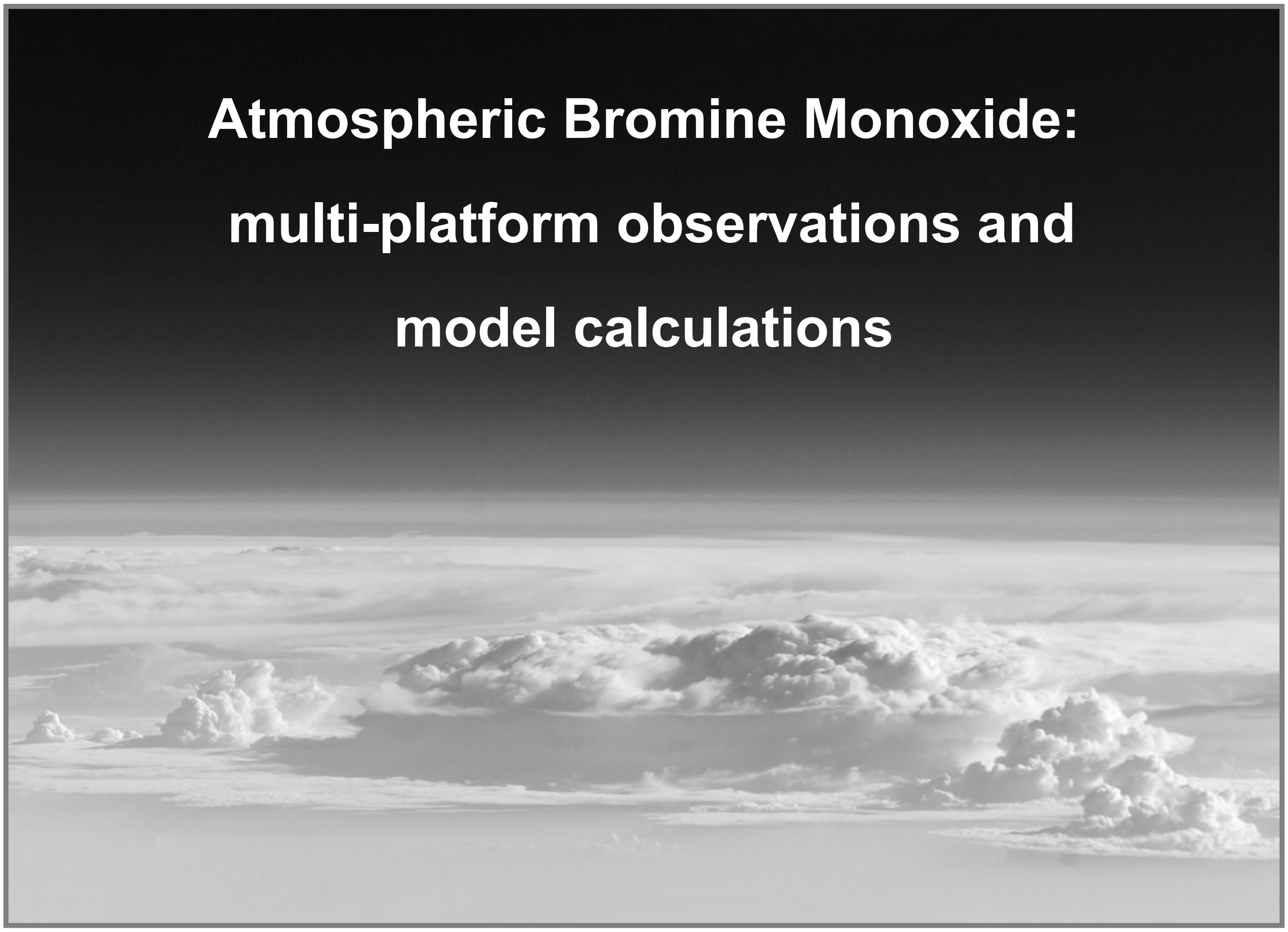

Directeur de Thèse : Michel Herman

Co-promoteur : Michel Van Roozendael

Dissertation présentée par
Nicolas THEYS en vue de
l'obtention du grade de
Docteur en Sciences de l'Ingénieur

Remerciements

Le travail présenté dans cette thèse a été réalisé à l'Institut d'Aéronomie Spatiale de Belgique (IASB) à Bruxelles.

Je tiens à remercier chaleureusement Michel Van Roozendael, mon promoteur de thèse à l'IASB, pour la confiance qu'il m'a accordée au cours de ces dernières années. La porte de son bureau a toujours été grande ouverte pour un conseil ou une discussion. Il n'a jamais compté les heures qu'il m'a consacrées, malgré la pile de tâches urgentes qui l'attendaient parfois. Son œil critique et son enthousiasme ont toujours été un moteur important pour mon travail et pour la rédaction de cette thèse. Mes remerciements vont aussi à Michel Herman, mon directeur de thèse à l'Université Libre de Bruxelles, pour sa disponibilité, ainsi qu'aux membres de mon comité d'accompagnement, Michel Carleer et Michel Godefroid.

Je voudrais aussi particulièrement remercier François Hendrick, pour sa patience et sa gentillesse. Son soutien sans faille et nos discussions ont toujours été constructives pour mon travail de recherche. Je le remercie également pour la relecture minutieuse de ce manuscrit et de mes publications.

Un grand merci à mes chers collègues de bureau Isabelle De Smedt, Gaïa Pinardi et Christophe Lerot, pour leur amitié, leur bonne humeur et aussi pour m'avoir supporté au quotidien.

Je remercie également Caroline Fayt, Christian Hermans, Martine De Mazière, Jean-Christopher Lambert, José Granville, Pierre Gerard, Quentin Errera, Simon Chabrillat, Franck Daerden, Paul Simon, Jean-François Müller, Trissevgeni Stavrakou, Corinne Vigouroux et Bart Dils qui ont tous, de près ou de loin, contribué à mon travail, par un conseil, une discussion ou un support technique.

Mes remerciements vont aussi à ma famille, mes amis et toutes les personnes de mon entourage qui m'ont soutenu lors de ces cinq années. Je tiens enfin à remercier tendrement ma fille Noémie et Laurence, les deux femmes de ma vie.

Ces recherches ont été financées par la Politique Scientifique Fédérale (BELSPO), l' Agence Spatiale Européenne (ESA) et l'Organisation Européenne pour l'Exploitation de Satellites Météorologiques (EUMETSAT) via les projets AGACC, Prodex/NOy-Bry, Prodex/SECPEA et les projets TEMIS (ESA DUE) et Ozone SAF (BrO Visiting Scientist).

Nicolas Theys
Uccle, Novembre 2009

Résumé

Les composés bromés jouent un rôle important dans la stratosphère et la troposphère en tant que catalyseurs de la destruction d'ozone. Bien que l'impact des espèces bromées sur la chimie de la stratosphère soit largement compris, il reste de nombreuses incertitudes en ce qui concerne les sources et les pertes de brome dans l'atmosphère ainsi qu'à propos de la chimie et de l'impact des espèces bromées sur la troposphère.

Le travail présenté dans ce manuscrit porte sur la télédétection du monoxyde de brome (BrO) à partir de spectres du rayonnement solaire diffusé, mesurés dans l'ultraviolet à partir d'instruments au sol de type multi-axis et satellitaires à visée nadir (GOME et GOME-2). La méthode de spectroscopie d'absorption optique différentielle est utilisée pour inverser la colonne intégrée de BrO le long du chemin optique effectif dans l'atmosphère. Nous avons développé de nouveaux algorithmes afin de dériver les colonnes verticales de BrO résolues en leurs contributions stratosphérique et troposphérique. Pour la géométrie d'observation au sol, un moyen a été trouvé pour déterminer indépendamment les colonnes de BrO stratosphérique et troposphérique, et cela à partir de la variation diurne des mesures de BrO. Pour les observations satellitaires, la contribution de la stratosphère à la colonne mesurée de BrO est estimée à partir d'une climatologie innovante de BrO stratosphérique. Cette climatologie est basée sur un modèle de pointe de la chimie et du transport de la stratosphère; par ailleurs, elle tient compte explicitement de l'impact de la dynamique atmosphérique et de la photochimie sur la distribution du BrO dans la stratosphère. La fraction troposphérique de la colonne totale mesurée de BrO est quant à elle dérivée à partir d'une technique résiduelle tenant compte des effets des nuages et de la réflectivité de la surface.

Soutenus par un vaste jeu de données corrélatives, les résultats présentés dans ce travail permettent d'étudier de manière appropriée l'évolution spatiale et temporelle du BrO atmosphérique à l'échelle globale. Ces résultats permettent également de mieux estimer l'importance du BrO dans la couche limite planétaire polaire et dans la troposphère libre ainsi que la contribution des précurseurs bromés à temps de vie court sur le budget de brome dans la stratosphère. Nous présentons également la première détection satellitaire de BrO dans un panache volcanique, à l'aide de mesures effectuées avec l'instrument GOME-2.

Abstract

Bromine compounds play an important role as catalyst of the ozone destruction in both the stratosphere and troposphere. While the impact of bromine species on the chemistry of the stratosphere is known to a large extend, a number of uncertainties remain regarding the sources and sinks of atmospheric bromine as well as the chemistry and impact of bromine species on the troposphere.

This work describes remote-sensing observations of bromine monoxide (BrO) derived from scattered sunlight spectra in the ultraviolet region measured by ground-based multi-axis and satellite nadir viewing instruments (GOME and GOME-2). The method of differential optical absorption spectroscopy is used to retrieve the columnar concentration of BrO along the effective light path through the atmosphere. New algorithms to derive vertical columns of BrO resolved into their stratospheric and tropospheric contributions are developed and described. For the ground-based geometry a way was found to determine independently the stratospheric and tropospheric BrO columns from the diurnal variation of the BrO measurements. For the satellite observations, the contribution of the stratospheric BrO to the measured column is estimated using an innovative stratospheric BrO climatology. This climatology is based on a state-of-the-art stratospheric chemical transport model, and explicitly accounts for the impact of atmospheric dynamics and photochemistry on the stratospheric BrO distribution. As for the tropospheric fraction of the measured total BrO column, it is derived using a residual technique accounting for the effects of clouds and surface reflectivity.

Supported by an extensive set of correlative data, the results presented here allow to study properly the spatial and temporal evolution of atmospheric BrO at the global scale and enable to better assess the significance of BrO in the polar planetary boundary layer and free-troposphere as well as the contribution from very short-lived brominated sources gases to the stratospheric bromine budget. We also report on the first satellite detection of BrO in a volcanic plume, using GOME-2 measurements.

Atmospheric Bromine Monoxide: multi-platform observations and model calculations

Table of contents

Chapter 4 – Instruments 61

Chapter 1

Introduction

Centered at around 20-25 km altitude, the stratospheric ozone layer plays a major role in protecting life on Earth. Owing to the strong ultraviolet (UV) absorption of ozone in the Hartley-Huggins bands, the incoming solar UV radiation is largely absorbed and converted into heat, affecting temperatures and dynamical flow patterns. Ozone has also strong infrared absorption bands and thus affects the radiation back from Earth into space. This alters the temperature structure of the troposphere and influences the climate. Ozone is also present in the lower troposphere, where it has important effects on human health (particularly on the respiratory system). In contrast to stratospheric ozone that is of natural origin, tropospheric ozone is mainly a product of pollution.

Since the 1970's and the pioneering studies of Crutzen (1970) and Molina and Rowland (1974), anthropogenic emissions of nitrogen and halogen compounds have been shown to exert a large influence on the stratospheric ozone budget. This was spectacularly confirmed in 1985 by the discovery of the ozone hole phenomenon over Antarctica (Farman et al., 1985) whereby each spring the ozone layer is almost completely destroyed between 12 and 20 km of altitude. This destruction extends over several tens of million square km. Observations in the northern hemisphere have shown that analogous ozone depletion - although less severe – also occurs in the Arctic regions. The formation of the ozone hole was soon identified to be due to the presence of inorganic chlorine and bromine (hereinafter referred to as Cl_y and Br_y)[1] in the stratosphere. A prerequisite is the formation of a strong winterly cyclone over the pole - the polar vortex. Inside the polar vortex, the temperature can drop to very low values, so that polar stratospheric clouds (PSCs) can form. Heterogeneous reactions on the surface of PSCs then convert inorganic halogen compounds such as $ClONO_2$, HCl and $BrONO_2$ into more reactive species as Cl_2, HOCl and BrCl (Solomon et al., 1986). When the sunlight returns after polar night, these species are photodissociated and destroy stratospheric ozone through catalytic cycles. In addition to the stratospheric ozone depletion over the poles, a significant although lower ozone loss also occurs at mid-latitudes. The increased levels of chlorine and bromine also contribute to mid-latitudes ozone loss through heterogeneous reactions on the surface of stratospheric background aerosols. It should be noted that bromine species are less abundant by about two orders of magnitude compared to chlorine. However, on a molecule to molecule basis the ozone depletion potential of bromine is much larger than that of chlorine. Consequently, bromine species account for about 25% of the ozone loss at mid-latitudes while in polar regions this contribution may reach 50%.

The sources of inorganic halogens in the stratosphere originate from the emissions of organic halogen compounds (mainly man-made chlorofluorocarbons (CFCs), halons, methylchloride and methylbromide) that are transported into the stratosphere before being converted into inorganic forms by photolysis or reaction with $O(^1D)$ and OH

---

[1] $X_y \equiv X+XO+HX+HOX+XONO_2+\ldots$ (X=Cl or Br) is the total number of inorganic molecules.

radicals. After the recognition of the involvement of halogen species in the depletion of stratospheric ozone, the Montreal Protocol on Substances that Deplete the Ozone Layer was agreed in 1987, leading to the progressive phase-out of many long-lived ozone depleting substances. After five successive amendments to the Montreal Protocol, the cumulative levels of chlorine and bromine from the ozone depleting substances are now decreasing in the atmosphere. Of relevance for the study of the evolution of the ozone layer is the distinction between the source gases that are regulated by the Montreal Protocol and the naturally emitted halogen-containing compounds. In that respect, bromine compounds are of particular interest because about half of the stratospheric Br_y loading is due to natural sources (compared to about 15% for chlorine). These source gases are generally released by biological processes (e.g., in the oceans) and are characterized by low atmospheric lifetimes (typically <6 months).

After the role of bromine in the destruction of stratospheric ozone was highlighted, it became soon clear that inorganic bromine compounds could also have a significant effect in the troposphere (for an overview see, e.g., von Glasow and Crutzen, 2007). In the boundary layer, it was found that large amounts of inorganic bromine are seasonally released in polar regions in both hemispheres during spring due to a phenomenon known as Polar-bromine explosion. These emissions are responsible of complete ozone depletion events in the polar boundary layer, as well as interactions with mercury chemistry. Although more localized, inorganic bromine emissions have also been identified over salt lakes, in the marine boundary layer and in volcanic plumes. Furthermore, observations from space, the ground and balloons have shown that inorganic bromine may be produced and sustained in the free troposphere at the global scale. Elaborating on these observations, modeling results have shown that free-tropospheric bromine might have a significant impact on tropospheric ozone (and on tropospheric chemistry in general), leading to a reduction in the O_3 mixing ratio of up to 40% locally.

Currently, several scientific issues regarding atmospheric bromine still remain:

- The sources and sinks of the bromine short-lived species, as well as their regional variability, are characterized by large uncertainties. Much research is devoted to assess the importance of these organic bromine short-lived species on the stratospheric chemistry. How the very short-lived substances enter the stratosphere through the tropical tropopause is also not fully characterized (World Meteorological Organization report 2007, Chapter 2 on halogenated very short-lived substances). Furthermore, many of the underlying physical and chemical processes leading to the release of inorganic bromine to the stratosphere are potentially sensitive to climate change (Salawitch, 2006).
- The exact mechanism, which leads to an initial bromine release in the polar boundary layer as well as the influence of transport and chemical processes on bromine, is still not clearly characterized (Simpson et al., 2007).
- The origin of free-tropospheric bromine is not fully understood. It has been speculated that it might be due to uplifting of surface Bry, downward transport from the stratosphere, volcanic activity or the decomposition of short-lived organic bromine compounds under the action of heterogeneous and/or gas-phase photochemical reactions.

The active form of bromine, taking part in the destruction of ozone, is bromine monoxide (BrO). During daytime, BrO is the most abundant inorganic bromine species (typically 30 to 70% of total Br_y). It is also the bromine species that can be measured with highest accuracy using absorption spectroscopy techniques[1]. Over the last two decades, many observations of BrO were performed using instruments based on ground, balloon, aircraft and satellite platforms. These measurements have contributed significantly to improve our understanding of atmospheric bromine. To a large extent, they were achieved through the exploitation of BrO electronic bands in the near ultraviolet[2] and using the technique of differential optical absorption spectroscopy (DOAS; Platt and Stutz, 2008).

The objective of this PhD thesis is to contribute to a better understanding of atmospheric bromine by studying the BrO content in both the troposphere and stratosphere and by characterizing quantitatively its spatial and seasonal variations. For this purpose, we will determine vertically integrated concentrations (vertical column amount) of BrO in both the troposphere and stratosphere by using (1) ground-based and satellite nadir DOAS instruments, and (2) stratospheric model calculations.

This thesis is organized in nine chapters. **Chapter 2** gives an overview of the role of bromine and its chemistry in the atmosphere. The observation principles and the DOAS instruments are described in **chapters 3 and 4** respectively. Ground-based and satellite instruments used in this work have in common that they all measure the solar UV radiation scattered from the atmosphere and reflected by the ground; the analysis of the measured spectra with the DOAS method then provides the BrO absorption averaged over all light paths contributing to the signal. The retrieved quantity can be regarded as the integrated BrO concentration along the mean optical light path (it is often referred to as the 'slant column density'). Since the light that reaches the instrument travels through the entire atmosphere, the measured slant column contains absorption from both stratosphere and troposphere. Evaluating the tropospheric and stratospheric BrO columns from the measurements requires essentially two additional steps which are at the heart of our study:

- the separation of the stratospheric and tropospheric contributions to the measured BrO slant columns.
- the conversion of the (tropospheric and stratospheric) slant columns into vertical columns, using adequate modeling of the transfer of the radiation in the atmosphere. Important parameters affecting the optical light path (such as the observation geometry, surface reflectivity, atmospheric gases, clouds and aerosols) need to be accounted for.

In practice, the inversion of stratospheric and tropospheric BrO columns from an individual DOAS observation is an ill-posed problem. In **chapter 5**, we present a retrieval method that enables the inversion of independent tropospheric and stratospheric BrO columns from a combination of several observations made from a ground-based

---

[1] Besides BrO, only few measurements of inorganic bromine species exist: HBr, HOBr and recently stratospheric $BrONO_2$ (Höpfner et al., 2009). Note that it is also possible to detect several organic and inorganic bromine compounds using in-situ measurements.

[2] Rotational lines in the microwave region can also be used to detect BrO (Kovalenko et al., 2007) but the estimated precision and accuracy is less good.

platform. In contrast to satellite nadir instruments that provide snapshots in time[1], ground-based instruments have the great advantage to measure the atmosphere at a given location continuously during the day. Moreover, with the ground-based system used here, the same air mass is sounded sequentially under different viewing directions, from the horizon to the zenith (Multi-axis DOAS or MAXDOAS measurements). It is therefore particularly well suited to combine the measurements acquired from noon to twilight in the different viewing directions to infer the stratospheric and tropospheric BrO columns. This stratosphere-troposphere separation is achieved by exploiting the different evolution of the measurement sensitivity in the stratosphere and the troposphere as a function of solar zenith angle and viewing directions. We have applied this retrieval algorithm to measurements performed at Reunion Island (21.06°S, 55.47°E, Indian Ocean). The location of this site is specially interesting since only few BrO measurements have been performed in tropical region so far, in spite of the importance of the tropics for the atmosphere (and besides for setting the chemical boundary conditions of the stratosphere). In particular, a remote area as Reunion-Island is ideal to investigate the delivery of Br_y from oceanic short-lived bromine species to the free-troposphere and lower stratosphere. Moreover, tropical BrO measurements are also needed to validate (and even constrain) satellite data. Indeed, the measurement conditions at low latitudes (high sun and short light path through the atmosphere) make the BrO retrieval particularly challenging for the satellite instrument.

The method developed for the ground-based observations to separate the tropospheric and stratospheric BrO columns, can not be transposed to satellite nadir observations. The strategy we adopted in this thesis is, in a first step, to build a consolidated stratospheric BrO dataset that can be used afterwards as reference to separate with good accuracy the stratospheric and tropospheric contributions to the satellite measured BrO columns. This is the subject of **chapter 6**. We have developed a new method to determine stratospheric BrO concentration profiles (and columns) using a climatological approach. The proposed climatology is able to reproduce the important spatial and temporal variations of stratospheric BrO by using dynamical and chemical indicators. The adopted parameterization is based on output data from a global 3-D model of the chemistry and transport of the stratosphere (BASCOE). The model simulations are optimized for bromine species by the implementation of an up-to-date photochemistry and a realistic total bromine budget (including a contribution from short-lived bromine source gases). We have made comparisons of modeled BrO and an extensive data set of stratospheric BrO observations from ground-based (including the reference set of Reunion Island), balloon and satellite limb-viewing instruments. There are three reasons for this validation exercise: (1) test our understanding of stratospheric bromine, (2) assess the consistency of the stratospheric BrO observational data set, and (3) extend the observations at the global scale via the model.

Chapter 7 deals with the determination of global stratospheric and tropospheric BrO columns using GOME and GOME-2 satellite nadir observations. The stratospheric BrO columns are estimated using the stratospheric BrO climatology (underlying the currently available stratospheric BrO observations). Although based on model simulations, the calculated stratospheric BrO columns are still representative of the sounded air masses as they are evaluated based on measured quantities. The tropospheric BrO columns are

---

[1] This is true for the low Earth orbit satellites used here, but obviously not for geostationary orbit platforms.

estimated from a residual technique that combines measured and calculated stratospheric columns, and that accounts for the impact of clouds, surface reflectivity and viewing geometry on the measurement sensitivity. For the first time, it was possible to properly quantify the BrO amount in the global troposphere using satellite nadir instruments. The seasonal variation and spatial distribution of the retrieved tropospheric BrO columns are interpreted in the light of our current understanding of tropospheric bromine. In particular, the existence of a free-tropospheric BrO background at the global scale is investigated. It is also shown that our method enables to separate the large-scale stratospheric BrO structures from those of tropospheric origin in the total BrO column field measured from space. It allows studying unambiguously the development and transport of BrO plumes in the polar boundary layer. The tropospheric BrO results were compared to correlative ground-based data as well as modeling calculations and a good agreement was found.

Chapter 8 presents a side study focused on the satellite detection of volcanic BrO emissions after the major eruption of the Kasatochi volcano in Alaska (52.17°N, 175.51°W) on August 2008. Using a Lagrangian trajectory model, it was possible to simulate the transport of the volcanic plume and estimate the total mass of reactive bromine emitted by the volcano. These results represent the first ever space-based observation of BrO released by volcanic activity. This study further strengthens the idea that volcanoes probably play an important role as a source of bromine in the atmosphere.

In **chapter 9**, this study ends with the conclusions and perspectives.

Chapter 2

General aspects

In this chapter some aspects concerning atmospheric dynamics and chemistry will be introduced. A strong emphasis is given on the role of the bromine species in the atmosphere, and on the physical and chemical processes influencing their distribution in the stratosphere and the troposphere.

2.1 Dynamics of the atmosphere

2.1.1 Vertical structure of the atmosphere

The atmosphere (from Greek *ατμός* - *atmos*, “vapor” + *σφαίρα* - *sphaira*, “sphere”) of the Earth is commonly described as a series of layers or “spheres” defined by their thermal characteristics (see Figure 2.1).

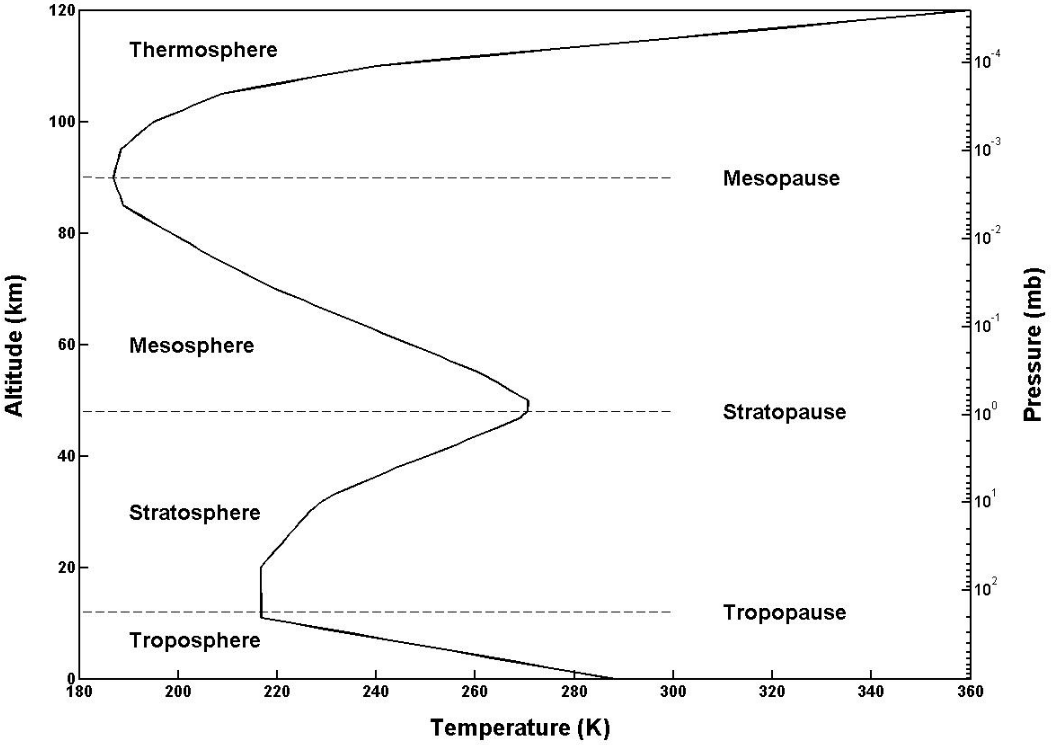

Figure 2.1 Vertical structure of the Earth’s atmosphere. The temperature profile is taken from the U. S. Standard Atmosphere (Anderson et al., 1986).

Specifically, each layer is a region where the change in temperature with respect to the altitude (lapse rate) has a constant sign. The layer above the surface is known as the troposphere, and contains approximately 75% of the atmosphere's mass. The troposphere is characterized by a decrease of the temperature with altitude (at a mean lapse rate of 6.5 K/km), due to the adiabatic expansion of rising air and the consequent cooling. The troposphere is therefore characterized by convection and strong mixing of air masses. It is the layer where most of the weather phenomena and atmospheric turbulence occur. The troposphere is usually divided in two regions: (1) the boundary layer, directly influenced by the presence of the Earth's surface, responds to surface forcing with a time scale of about an hour or less. The convective air motions generate intense turbulent mixing. The boundary layer has a thickness varying from 300 m to 2000 m, depending on the local atmospheric energy budget. (2) the free-troposphere is the layer above the boundary layer, which is not directly affected by the surface. Long-range transport and vertical motions of gases and fine particles (aerosols) are frequent features in that region. The upper boundary of the troposphere is called the tropopause and is marked by a sharp change of the lapse rate[1]. The tropopause temperature and height depends on the latitude, season and daily changes in meteorological conditions. Typical tropopause height for tropical regions is of 16 to 18 km, and the corresponding temperature is about 200K, while in the polar regions the tropopause elevation is only of about 8 km, and the temperature roughly 220 K.

Above the tropopause, temperature first remains constant and then increases in the stratosphere, due to ozone heating by absorption of ultraviolet radiation from the sun. The vertical stratification, with warmer layers above and cooler layers below, makes the stratosphere dynamically stable. In contrast to the troposphere, the stratosphere involves only weak vertical motions and is dominated by radiative processes. The stratosphere extends to about 50 km, where the temperature exhibits a maximum at the stratopause. At higher altitude, the temperature again decreases up to 90 km, where another temperature minimum is found. This layer is called the mesosphere and its upper boundary is the mesopause. The region above the mesopause is called the thermosphere and is characterized by an increase of temperature with height, due to the absorption of extreme ultraviolet radiation by molecular and atomic oxygen.

The work presented in this thesis is concerned by aspects related to the so-called middle atmosphere, i.e., the troposphere and the stratosphere only.

2.1.2 Dynamics of the atmosphere influencing trace gases distribution

The distributions of the atmospheric constituents result from the competition of atmospheric dynamics and chemistry. The relative importance of both effects can be evaluated from an analysis of the time constants related to these dynamical and chemical processes (production and destruction). While several species are only influenced by photochemistry, other atmospheric constituents are characterized by time constants related to chemical processes that are much larger than the time constants associated to the dynamics in the atmosphere. In this case, the distributions of these constituent are

---

[1] The thermal tropopause height is defined by the World Meteorological Organization (WMO) as the height of the base of a layer at least 2km thick, in which the rate of decrease of temperature with height is less than 2 K/km.

solely influenced by dynamical effects and the chemical constituent can be considered as a good indicator of the dynamic of the atmosphere[1]. This section aims presenting some basis on the large scale atmospheric circulation patterns which contribute to the spatial distribution of trace gases[2]. A general description of the transport processes in the troposphere and the stratosphere will be given. The reader is referred to the literature (e.g., M. Salby; Holton et al., 1995) for a detailed treatment of the theory of the atmospheric transport.

Tropospheric circulation

Unequal heating is the main driving mechanism responsible for the global tropospheric circulation. At the equator, warm moist air is lifted aloft in low pressure areas. The cooling of rising air causes the formation of clouds by condensation of water vapor. The temperature inversion at the tropopause then acts as a 'roof' and hinders the upward motion of air, causing it to spread and move poleward. At about 30° latitude, dry air descends in a high pressure area. Some of the air masses travel back to the equatorial region, closing the loop of the convection cell. Such large scale convection systems are observed in both hemispheres and are known as the Hadley cells (see Figure 2.2).

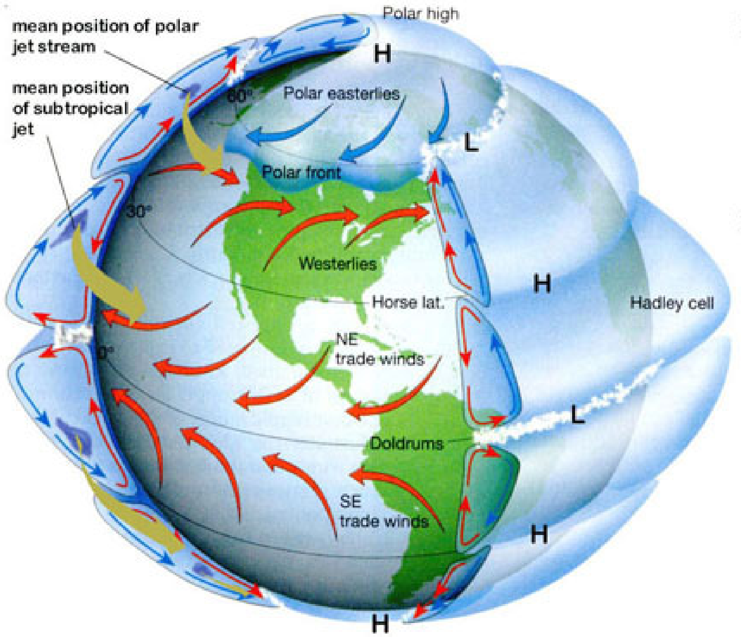

Figure 2.2 Schematic view of the global circulation in the troposphere.
© http://www.sbg.ac.at/ipk/avstudio/pierofun/atmo/el-scans/hadley.jpg

---

[1] Hereafter we will refer to the widely used term 'tracer of the atmospheric dynamics'. Note that it is possible to demonstrate using the law of conservation of mass that the volume mixing ratio of a tracer is conserved during atmospheric transport.

[2] The term 'trace gas' refers to a gas which makes up less than 1% by volume of the earth's atmosphere. It includes all gases except nitrogen (78.1%) and oxygen (20.9%).

In addition, the air flow is also deflected from west to east under the action of the Coriolis force, leading to the formation of the well-known near-surface trade winds and the subtropical jet winds (typically located between 10 and 16 km).

In the polar regions, air masses at ~60° latitude are sufficiently warm and moist to undergo convection as well and drive a thermal loop (called the polar cell). Air circulates within the troposphere, limited vertically by the tropopause at about 8 km. Warm air rises at lower latitudes and moves poleward through the upper troposphere at both the North and South poles. When the air reaches the polar areas, it has cooled considerably, and descends as a cold, dry high pressure area, moving away from the pole along the surface, but twisting westward as a result of the strong Coriolis effect to produce the Polar easterlies.

A third circulation cell, the Ferrel cell, is also present between ~ 30° and 60° latitudes (in both hemispheres) and results mainly from the entrainment of air masses by the Hadley and polar cells. The wind along the surface in the Ferrel cell is westerly in both hemispheres due to the Coriolis force. Noteworthy is the presence of fast flowing airs within the transitional zone between the tropopause and the Ferrel cell (polar jet streams).

Stratospheric circulation

The transport in the stratosphere is fundamentally different from what is occurring in the troposphere. Indeed, the temperature inversion above the tropopause effectively inhibits vertical transport in the stratosphere, and the important convection cells and subsequent mixing of air typical of the troposphere are not observed in the stratosphere.

The dominant feature of the global stratospheric wind system is the presence of strong mean zonal winds (wind in the longitudinal direction), which tend to eliminate the longitudinal gradients of the chemical constituents in the stratosphere. As a first approximation, it can be assumed that the air masses are transported adiabatically (motion along quasi-horizontal isentropic surfaces). Solving the fundamental equations of the fluid mechanics for adiabatic parcel displacements leads to the conceptual view that zonal winds are thermal winds, in the sense that the zonal wind field is proportional to the horizontal temperature gradient. As a consequence of the temperature difference between the tropical lower stratosphere and the polar stratosphere, an easterly wind forms in the summer hemisphere, whereas a westerly wind appears in the winter hemisphere.

The most striking dynamical structure observed in the stratosphere, related to the presence of zonal winds, is probably the polar vortex. During the polar winter night, the stratosphere is not exposed to sunlight and the air masses undergo a severe cooling. A large temperature gradient appears between the mid-latitudes and the pole, and hence leads to the formation of a rapid circumpolar wind. The strong jet wind at the edge of the so-called vortex acts a dynamical barrier and has the effect to isolate the air over the polar region. It should be noted that some diabatic processes have an important influence on the stability of the polar vortex, and are responsible at the end of its dislocation by mixing of air. As a matter of fact, at the beginning of spring, the sun is heating the polar stratospheric air masses again, and weakens the polar vortex. In addition, the polar vortex is further disturbed and destabilized by atmospheric waves (called planetary waves or Rossby waves), forced from beneath and propagating into the stratosphere. These waves result of the different heat capacity of land and water and are induced by the build-up of temperature and pressure gradients. Their amplitudes increase over a more variable surface topography. Whereas the Antarctic continent is centered on the pole and surrounded solely by water, the topography of the northern hemisphere is more complex. This leads to a more stable and circular vortex in the southern hemisphere than in the northern hemisphere. We will see in the next section that it has a crucial impact on the depletion of polar stratospheric ozone. The polar vortex is not the unique example of dynamical barrier in the stratosphere. Indeed, the difference in temperature between the tropical lower stratosphere and the extra-tropical stratosphere is responsible for the appearance of the subtropical jet winds located around 30°N and 30°S. These strong winds form the so-called tropical barrier which has the effect to isolate the tropics from the extra-tropical air masses.

Besides the zonal circulation described above, meridional (in the latitudinal direction) and vertical transport of air masses plays also a major role on the distribution of chemical species in the stratosphere. Note however that the mean meridional and vertical winds in the stratosphere are very small compared to those of the zonal winds. The overall feature of the mean stratospheric meridional-vertical circulation is well described by the Brewer-Dobson circulation, and is illustrated in Figure 2.3.

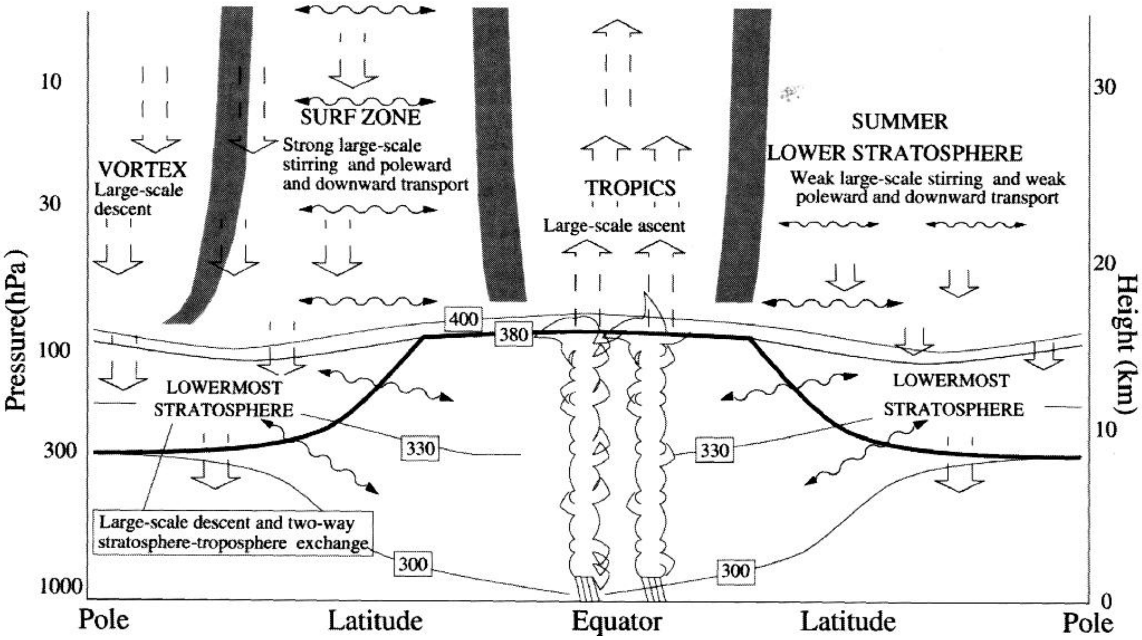

Figure 2.3 Schematic diagram showing the Brewer-Dobson stratospheric circulation. The tropopause is shown by the thick line. Thin lines are isentropic or constant potential temperature[1] surfaces labeled in Kelvins. The shaded regions represent the dynamical barriers in the stratosphere (polar vortex and tropical barriers). © NASA. Studying Earth's Environment from Space (http://www.ccpo.odu.edu/SEES/index.html).

---

[1] The potential temperature is a quantity conserved in an adiabatic air motion. It represents the temperature which an air parcel would attain if it were adiabatically compressed or expanded starting from a temperature T and pressure p to a pressure of 1000 mb, and is given by: $\theta=T(1000/p)^{\kappa}$ where $\kappa=R/c_p=0.286$.

Recognition of such stratospheric transport is historically based on observations of long-lived chemical species (water vapor and ozone) that suggested a circulation exhibiting a rising motion only in the tropics, and descending motion at extra-tropical latitudes. The Brewer-Dobson circulation brings air masses from the tropics to mid- and high-latitudes. In the winter hemisphere, a large-scale descent of air masses from the upper stratosphere is observed in the polar vortex[1]. Transport of air masses is also arising from the tropical region toward the pole through the 'extra-tropical pump', which is largely driven by the breaking of Rossby waves in the so-called 'surf zone' of mid-latitudes. It should be emphasized that the Brewer-Dobson circulation is a very slow process, so that the air will cycle through the stratosphere within ~ 5 years.

Despite the fact that the tropopause tends to isolate the stratosphere from the troposphere (because of the temperature gradient inversion), several pathways are possible for stratosphere-troposphere exchange of mass and chemical species. Clearly, the strong tropical convection is responsible for the injection of constituents in the stratosphere (often because of the fast transport of air due to the formation of tropical convective clouds). The large-scale descent of air in the polar region brings air back to the troposphere. According to Figure 2.3, stratosphere-troposphere exchange is also possible at mid-latitudes, through adiabatic transport (some isentropic surfaces cross the tropopause) or wave-induced forcing.

2.2 Stratospheric photochemistry

In this section, photochemical processes relevant to important constituents of the stratosphere will be discussed. We first focus on the photochemistry of ozone, hydrogen, nitrogen and halogen compounds. We will then describe the physical and chemical processes taking place in the stratosphere leading to the so-called stratospheric ozone hole.

2.2.1 Ozone chemistry

One of the most important stratospheric species is ozone (O_3). Although ozone is present in both stratosphere and troposphere, the bulk of ozone resides in the stratosphere (with the maximum concentration around ~22 km) and constitutes the commonly referred ozone layer. Despite the small concentration of ozone in the stratosphere, it is playing an essential role for the protection of living organisms on Earth[2] by absorbing most of the harmful ultraviolet (UV) radiation emitted from the sun. The absorption of short wavelength solar radiation by ozone leads also to the heating of the stratosphere, which in turn drives the stratospheric circulation. Furthermore, ozone interacts with long wavelength radiation (infrared radiation) and hence contributes to the greenhouse effect of the Earth's atmosphere.

A photochemical scheme for the formation and destruction of ozone in the stratosphere based on oxygen-only chemistry was first proposed by Chapman (1930):

---

[1] This phenomenon is sometimes called 'air subsidence'.

[2] The progressive formation of the ozone layer has constituted a fundamental prerequisite for the evolution of life outside the oceans, about 400 million years ago.

$O_2 + h\nu \rightarrow O + O$ $(\lambda < 242\ \text{nm})$ (R 1)
$O + O_2 + M \rightarrow O_3 + M$ (R 2)
$O_3 + h\nu \rightarrow O(^1D) + O_2$ $(\lambda < 308\ \text{nm})$ (R 3)
$O(^1D) + M \rightarrow O(^3P) + M$ (R 4)
$O_3 + h\nu \rightarrow O(^3P) + O_2$ $(\lambda < 1180\ \text{nm})$ (R 5)
$O + O + M \rightarrow O_2 + M$ (R 6)
$O(^3P) + O_3 \rightarrow 2\ O_2$ (R 7)

where M is any arbitrary molecule. The fast interchange between ozone and atomic oxygen through the Chapman cycle leads to a photochemical equilibrium explaining the persistence of a stratospheric ozone layer. According to this simple model of ozone production, the photodissociation of O_2 is maximum with overhead sun. Ozone is thus mostly produced in the equatorial region (even if the production rate is still effective at higher latitudes). Moreover, the production of ozone occurs mainly in the upper stratosphere, because of the strong attenuation of the short wavelength radiation that controls the photodissociation of O_2 (R 1).

It should be noted that the individual species of the Chapman cycle have a short lifetime (e.g., about an half hour for O_3), but if we define the O_X family as the sum of the odd-oxygen species ($O_X = O_3 + O(^1D) + O(^3P)$) then the reactions (R 1-7) only convert one species of the O_X family into another and the lifetime of O_X as a whole is much longer, about several months to a year in the lower stratosphere (at the altitude of the maximum ozone concentration). Odd-oxygen species can thus be transported from the equatorial region toward the poles[1], as a result of the Brewer-Dobson circulation. Hence, the global distribution of ozone depends on latitude and season. This is illustrated in Figure 2.4 that shows the average amount of total ozone column[2] at a given latitude band as a function of time, as recorded by the TOMS satellite instrument between 1979 and 1992. One can see that the ozone column is rather small at the equator and increases toward the poles. This is due to the peak in ozone mixing ratio occurring in the polar regions at lower altitudes, where the increased pressure corresponds to increased molecule numbers. It can also be seen that the maximum of ozone column is found at northern high-latitudes in spring. Note that this maximum is surprisingly not found at high-latitudes in austral spring, as it would have been expected from the hemispheric alternation of the Brewer-Dobson circulation. Instead, a dramatic decrease of the ozone column is observed – the stratospheric ‘ozone hole’.

Well before the discovery of the ozone hole by Farman et al. (1985), it was recognized that the mechanism of Chapman was not sufficient to explain the observations of ozone.

---

[1] In the stratosphere ozone is much more abundant than atomic oxygen so that $O_X \approx O_3$. Hence ozone can be considered to a certain point as a tracer of the dynamics of the stratosphere.

[2] The thickness of the ozone layer is determined by the amount of ozone molecules in a column overhead per surface unit, and is calculated by integrating the ozone concentration profile along the vertical axis. The ozone column is often expressed in Dobson units (DU) – one DU refers to a layer of ozone that would be 10 μm thick under standard temperature and pressure.

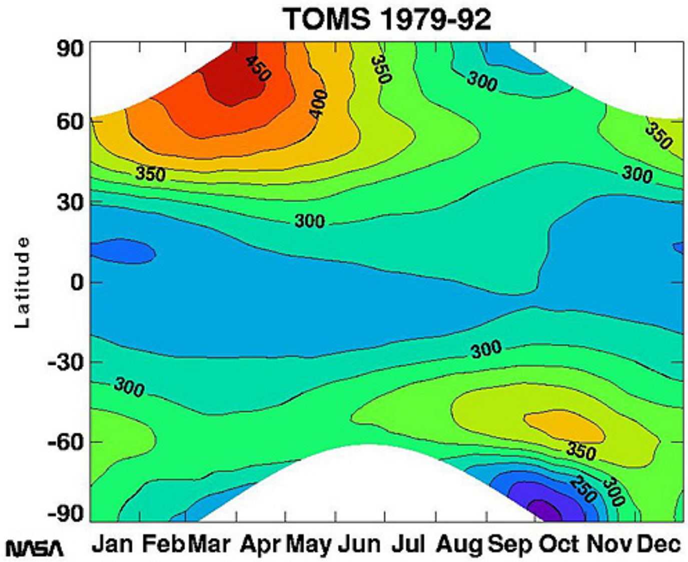

Figure 2.4 Mean annual cycle of the total ozone column (expressed in DU) as measured by the TOMS satellite instrument (1979-1992). © NASA. Studying Earth's Environment from Space (http://www.ccpo.odu.edu/SEES/index.html).

Indeed, the ozone concentrations modeled by the Chapman cycle are largely overestimating the observations of ozone. In particular, the oxygen-only chemical scheme predicts a maximum of the ozone column at the equator which is in total contradiction with the observations. It became clear that stratospheric ozone was not only chemically destroyed by photolysis or reaction by atomic oxygen but also by catalytic reactions involving hydrogen, nitrogen, chlorine and bromine species:

$$X + O_3 \rightarrow XO + O_2 \qquad \text{(R 8)}$$
$$XO + O \rightarrow X + O_2 \qquad \text{(R 9)}$$
$$\text{net:} \quad O_3 + O \rightarrow 2\,O_2 \qquad \text{(R 10)}$$

where X represents one of the radicals OH, NO, Cl or Br. The radical cycle is regenerated by reaction (R 9) and is available for another ozone destruction cycle until it is removed by a sink process. Thus a small quantity of X can have a large impact on the ozone concentration.

Another catalytic cycle involving species of different families is:

$$X + O_3 \rightarrow XO + O_2 \qquad \text{(R 11)}$$
$$Y + O_3 \rightarrow YO + O_2 \qquad \text{(R 12)}$$
$$XO + YO \rightarrow X + Y + O_2 \qquad \text{(R 13)}$$
$$\text{net:} \quad 2\,O_3 \rightarrow 3\,O_2 \qquad \text{(R 14)}$$

where X=OH and Y=Cl, X=OH and Y=Br or X=Cl and Y=Br. Since no atomic oxygen is consumed, this cycle is particularly important in the lower stratosphere where the recycling of the radicals by reaction with O (R 9) is less effective.

The relative contributions of the various cycles to the ozone depletion vary as a function of altitude, latitude, season and local photochemical conditions. Furthermore, the abundance of the ozone-depleted substances is related to the source gases that are closely linked to the biogenic and anthropogenic activities at the surface of the Earth. Most of the source gases are long-lived species, so they can be transported to the stratosphere and be converted into radicals through photolysis or oxidation (by OH or $O(^1D)$).
The following sections are dedicated to the study of the hydrogen, nitrogen and halogen compounds, with respect to the photochemistry and the source gases. The main concepts related to ozone depletion are well documented (see e.g., Solomon, 1999), and here we intend to give a brief description of the key processes.

2.2.2 Hydrogen and nitrogen chemistry

Hydrogen chemistry

The involvement of hydrogen in catalytic ozone depletion cycles was first proposed by Bates and Nicolet (1950). The reactive hydrogen species of H, OH, HO_2 and H_2O_2 are often denoted by the term HO_x. The catalytic ozone destruction cycles involving HO_x dominate the ozone loss in the lowermost stratosphere (below 20 km):

$$\begin{array}{rll} OH + O & \rightarrow & HO_2 \qquad (R\ 15) \\ HO_2 + O & \rightarrow & OH + O_2 \qquad (R\ 16) \\ OH + O_3 & \rightarrow & HO_2 + O_2 \qquad (R\ 17) \\ HO_2 + O_3 & \rightarrow & OH + 2\,O_2 \qquad (R\ 18) \\ \text{net: } 2\,O + 2\,O_3 & \rightarrow & 4\,O_2 \end{array}$$

The HO_x species are formed in the stratosphere mainly by the (slow) reaction of excited O atoms with H-containing atmospheric species like water vapor (H_2O) and methane (CH_4):

$$\begin{array}{rll} H_2O + O(^1D) & \rightarrow & 2\,OH \qquad (R\ 19) \\ CH_4 + O(^1D) & \rightarrow & CH_3 + OH \qquad (R\ 20) \\ H_2O + h\nu & \rightarrow & H + OH \qquad (R\ 21) \end{array}$$

The major sink processes for the hydroxyl radical are the reaction with HO_2, nitric (HNO_3) and hydrochloric (HCl) acids:

$$\begin{array}{rll} OH + HO_2 & \rightarrow & H_2O + O_2 \qquad (R\ 22) \\ OH + HNO_3 & \rightarrow & H_2O + NO_3 \qquad (R\ 23) \\ OH + HCl & \rightarrow & H_2O + Cl \qquad (R\ 24) \end{array}$$

Nitrogen chemistry

The stratospheric ozone loss between 25 and 40 km is predominantly caused by nitrogen catalytic cycles (Crutzen, 1970; Johnston, 1971):

$NO + O_3 \rightarrow NO_2 + O_2$ (R 25)
$NO_2 + O \rightarrow NO + O_2$ (R 26)
net: $O_3 + O \rightarrow 2\,O_2$

$NO + O_3 \rightarrow NO_2 + O_2$ (R 27)
$NO_2 + O_3 \rightarrow NO_3 + O_2$ (R 28)
$NO_3 + h\nu \rightarrow NO + O_2$ (R 29)
net: $2O_3 \rightarrow 3\,O_2$

NO and NO_2 are in a photochemical steady-state during daytime via the fast reactions (R 25-29) and the photodissociation of NO_2

$NO_2 + h\nu \rightarrow NO + O$ (R 30)

and form the so-called reactive NO_x (=NO+NO_2) family[1].

The impact of the reactive nitrogen species on the ozone destruction is however moderated by a number of three-body reactions converting NO_x species into reservoirs species:

$NO_2 + NO_3 + M \rightarrow N_2O_5 + M$ (R 31)
$NO_2 + OH + M \rightarrow HNO_3 + M$ (R 32)
$NO_2 + HO_2 + M \rightarrow HO_2NO_2 + M$ (R 33)

The reactive species can also be released from the reservoirs by:

$N_2O_5 + M \rightarrow NO_3 + NO_2 + M$ (R 34)
$N_2O_5 + h\nu \rightarrow NO_3 + NO_2$ (R 35)
$HNO_3 + h\nu \rightarrow OH + NO_2$ (R 36)
$HNO_3 + OH \rightarrow NO_3 + H_2O$ (R 37)
$HO_2NO_2 + h\nu \rightarrow HO_2 + NO_2$ (R 38)

There also exist several reactions between NO_x and reactive halogenated species that form important halogenated-nitrogen reservoirs. We have intentionally omitted to list these reactions here, as they will be treated in the next section which is dedicated to the chemistry of halogen compounds in the stratosphere.

The reactions listed above largely explain the observed diurnal variation of NO_x species: Dinitrogen pentoxide (N_2O_5) is produced (through R 31) almost entirely at night (because NO_3 is rapidly photodissociated during daytime), and thus constitutes an important nighttime nitrogen reservoir. The fast photolysis of NO_2 together with the slow photolysis

---

[1] We also define the NO_y family as the sum of all nitrogen species (reactive and reservoirs nitrogen species), i.e. $NOy= NO+NO_2+NO_3+2N_2O_5+HNO_3+HO_2NO_2+ClONO_2+BrONO_2$

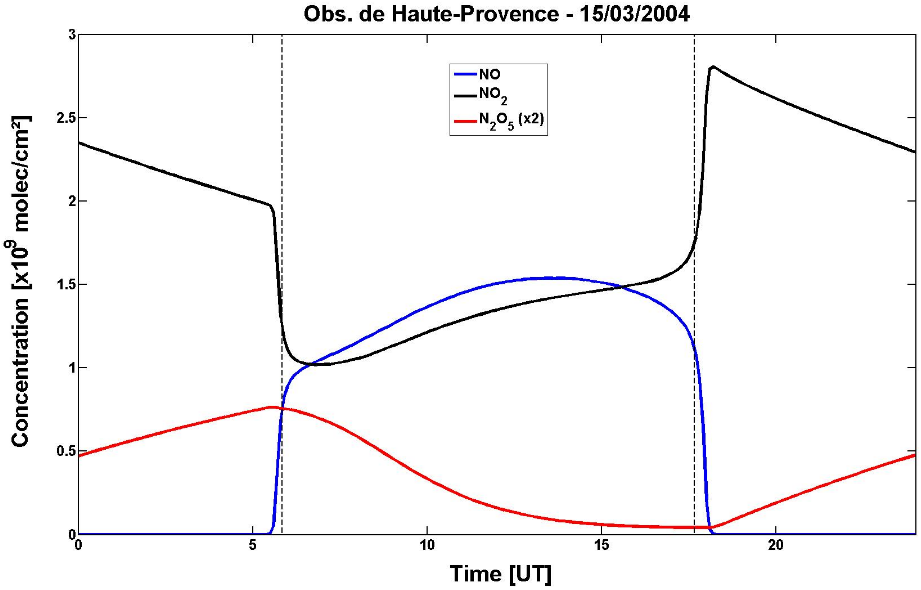

Figure 2.5 Diurnal variation of NO, NO_2, N_2O_5 (X2) concentrations at 30 km height, calculated by the PSCBOX photochemical model (courtesy of F. Hendrick). The data are shown for Observatoire de Haute-Provence (44°N, 6°E) for 15 March 2004. The dashed lines show the time of sunrise and sunset (90° of solar zenith angle).

of N_2O_5 is responsible for the typical diurnal variation of NO_2 (see Figure 2.5). As the sun begins to rise, a strong decrease of NO_2 concentration is observed, due to photolysis. During the day, the NO_2 concentration slowly increases because of N_2O_5 photolysis. At sunset, the concentration of NO_2 increases rapidly due to the absence of photodissocation.

The presence of NO_y in the stratosphere is primarily due to the decomposition of nitrous oxide (N_2O) emitted at the surface:

$$N_2O + O(^1D) \rightarrow 2\ NO \qquad \text{(R 39)}$$

Nitrous oxide is produced by denitrifying and nitrifying soil bacteria. Other sources contributing to the stratospheric NO_y budget include NO_x transported to the stratosphere and produced by solar proton events and cosmic rays (in the mesosphere and thermosphere) or by tropospheric lighting.

The major removal processes for stratospheric NO_x is via the formation of nitric acid (R 32). The atmospheric lifetime of HNO_3 is of ~1 month in the lower stratosphere, because of the relative inefficiency of reactions (R 36-37). Nitric acid has also the important property of being soluble, so that HNO_3 can be uptaken into aqueous and solid particles. Another important heterogeneous reaction that favored the conversion of NO_y into nitric acid in the liquid or solid phase (phenomenon called denoxification) is the hydrolysis of N_2O_5:

$$N_2O_5 + H_2O\ (s) \rightarrow 2\ HNO_3\ (s) \qquad \text{(R 40)}$$

Here, (s) refers to the solid or liquid phase.

The irreversible removal of stratospheric NO_y (denitrification) occurs by the progressive sedimentation in the polar regions of large particles that contain a substantial amount of HNO_3.

The heterogeneous reactions implying nitrogen and halogen species are not listed above, but will be treated in section 2.2.4.

2.2.3 Halogen chemistry and source gases

Halogen species (F, Cl, Br, I) play an important role in stratospheric ozone destruction and are responsible for the formation of the polar ozone hole (see section 2.2.4). The halogen atoms released in the stratosphere from the decomposition of halogenated organic source gases can form acids and nitrates (through reaction with NO_2). In case of fluorine, the acid HF is rapidly and irreversibly formed, hence fluorine has a negligible impact on ozone. Chlorine forms both HCl and $ClONO_2$ reservoirs. These gases can, contrary to fluorine, be reconverted to chlorine atoms by gas-phase or heterogeneous chemistry (see below). The amount of chlorine available for ozone destruction cycles depends critically on the chemical rates of destruction and formation of the chlorine reservoirs, i.e. on the partitioning of chlorine between the reactive gases and the reservoirs. Bromine is less bonded than chlorine because the reservoirs (mostly $BrONO_2$) photolyse and react rapidly with OH. Bromine is thus more effective for ozone loss than chlorine. Iodine may also participate to the stratospheric destruction, but its contribution to stratospheric ozone loss is believed to be very small because the iodine-containing gases are largely removed in the troposphere before reaching the stratosphere.

Chlorine is responsible of about 60% of the ozone destruction under ozone hole conditions. Despite its low abundance in the stratosphere, bromine contributes to ~ 30% of polar ozone loss owing to an Ozone Depletion Potential (ODP)[1] that is ~ 60 times higher than chlorine.

2.2.3.1 Chlorine and bromine source gases

The various sources of reactive halogens in the stratosphere are halocarbon gases of anthropogenic and natural origin. Once emitted at the Earth's surface, they all experience similar processes. After accumulating in the troposphere, the halogen source gases are transported to the stratosphere (mainly in the tropics) were they are progressively converted to Cl and Br by photolysis or reactions with OH or $O(^1D)$. The atomic Cl and Br then react with O_3 (chemical ozone destruction) to form halogen oxides (ClO and BrO) that are later on converted (by a number of reactions described in section 2.2.3.2) into other stratospheric inorganic halogen species[2]. Source gases with a long lifetime and low solubility in water have a great chance of reaching the stratosphere. In contrast, gases with the shortest lifetime are to a large extent converted into inorganic halogens species

---

[1] The ODP of a compound is a relative measure of its ability to destroy stratospheric ozone. It is calculated on a 'per mass' basis, as the ratio of the total amounts of ozone destroyed by the compound and by the same mass of CFC-11 (see below).

[2] We define the inorganic halogen families:
inorganic chlorine $Cl_y=Cl+ClO+2Cl_2O_2+ClOO+OClO+ClONO_2+HOCl+HCl+BrCl$
and inorganic bromine $Br_y=Br+BrO+BONO_2+HOBr+HBr+BrCl$.

already in the troposphere where they are mainly removed from the atmosphere through washout by falling ice or rain. Therefore, only a small fraction of these source gases enter into the stratosphere. The most important sources of chlorine and bromine in the stratosphere are the chlorofluorocarbons (CFCs) and halons (bromine containing species), industrially manufactured since the 1950's. These compounds have been widely used during the 20th century as refrigerants (freons), foam blowing agents, solvents, aerosol spray propellants, fire extinguishing agents and chemical reagents. The lifetime of these gases is high, varying from years to centuries and resulting in almost uniform distribution in the troposphere. Table 2.1 presents an overview of the chemical lifetime and abundance of the main halogen containing species.

CFCs, along with carbon tetrachloride (CCl_4) and methyl chloroform (CH_3CCl_3) are the most relevant chlorine source gases of anthropogenic origin. Methyl chloride (CH_3Cl) is the only important natural chlorine source species. Based on a budget of the different chlorine source gases and their chemical lifetimes, the delivery of Cl_y in the stratosphere is estimated to be about 3400 parts per trillion volume (pptv).

The major source of bromine is methyl bromide (CH_3Br) which provides more than 50% of the bromine content from long-lived source species. CH_3Br is released by natural (biomass burning, oceans) and anthropogenic (e.g., soil fumigation) processes. Additional sources of bromine are the man-made halogenated hydrocarbons gases (mainly halon-1211 and 1301) initially developed to extinguish fires.

Table 2.1 Atmospheric lifetime and mole fraction (in 2004) for the primary halogen source gases of chlorine and bromine for the stratosphere. Adapted from WMO report 2007.

Common name	Chemical formula	Lifetime (years)	Mole fraction in 2004 (pptv)
Chlorine			
CFC-12	CCl_2F_2	100	540
CFC-11	CCl_3F	45	254
CFC-113	CCl_2FCClF_2	85	79
HCFCs	$CH_xCl_yF_z$	1-20	205
Carbon tetrachloride	CCl_4	26	95
Methyl chloride	CH_3Cl	1	527
Methyl chloroform	CH_3CCl_3	0.5	22
Bromine			
Halon-1211	$CBrClF_2$	16	4.5
Halon-1301	$CBrF_3$	65	2.8
other halons		3-20	~ 1
Methyl bromide	CH_3Br	0.7	9
Short lived species		12-150 days	variable

The estimate of the stratospheric Br_y loading due to long-lived organic bromine compounds is of about 16-17 pptv (Wamsley et al., 1998). However, several recent studies based on measurements of stratospheric BrO using remote-sensing UV-visible techniques (see chapters 3 and 4) from ground-based (Sinnhuber et al., 2002; Schofield et al., 2004 and 2006; Hendrick et al., 2007; Theys et al., 2007), balloon-borne (Pundt et al., 2002; Salawitch et al., 2005; Dorf et al., 2006a,b and 2008) and space-borne limb (Sinnhuber et al., 2005; Sioris et al., 2006) instruments have inferred a total inorganic bromine loading of 18-25 pptv, suggesting that an additional contribution must be considered, possibly due to bromine release from short-lived biogenic organic compounds (such as $CHBr_3$, CH_2Br_2, CH_2BrCl, $CHBr_2Cl$, $CHBrCl_2$, CH_2BrCH_2Br) or even through direct injection of inorganic bromine from tropospheric origin into the lower stratosphere (WMO report 2007, Chapter 2 on halogenated very short-lived substances VSLS). As a result, the ozone loss due to bromine might be underestimated in current models and in ozone trend simulations (e.g. Salawitch et al., 2005; Feng et al., 2007).

In the years 1980s, continued research led to the scientific consensus that man-made CFCs and halons posed a serious threat to the ozone layer. In response, the Montreal Protocol agreement was negotiated in 1987. This agreement regulated the production of chlorofluorocarbons and halons. Some revisions of this agreement have been made latter in the light of advances in scientific understanding. Due to its widespread adoption[1] and adherence it has been hailed as an example of exceptional international cooperation and success. The main CFCs, CH_3Br and halons were not produced anymore by any of the signatories after the end of 1995. The CFCs were replaced by partly halogenated substitutes (the so-called HCFCs), which are less stable and hence have a shorter lifetime. The cumulative levels of chlorine are now decreasing in both the troposphere (Montzka et al., 1996) and the stratosphere (Anderson et al., 2000; Froidevaux et al., 2006). Long-term observations of CH_3Br at the surface have shown that this substance, after peaking in 1998, has declined by 1.3 pptv by mid-2004 (Montzka et al., 2003; see also Figure 2.6 a). In case of the halons, they are still increasing, but at a slower rate. Decadal observations of stratospheric BrO from balloon (Dorf et al., 2006) and ground-based (Hendrick et al., 2008) instruments have confirmed that the decline observed in methyl bromide is now followed in a decline in stratospheric inorganic bromine. This is illustrated in Figure 2.6 where long-term observations of stratospheric BrO from ground-based instruments at two different sites, together with measurements of CH_3Br and halons are shown. At both stations, a positive trend of BrO of about + 2.5% per year is found for the 1995-2001 period, while a negative trend of about -1% per year is obtained between 2001 and 2005. Note that there is a discrepancy between the moment the tropospheric organic bromine has peaked (~1998) and the moment the stratospheric bromine became maximum (~2001). This delay of approximately 3 to 4 years corresponds to the time for the organic bromine species emitted at the surface, to be transported into the stratosphere.

---

[1] The Montreal Protocol and amendments have been signed by 193 countries.

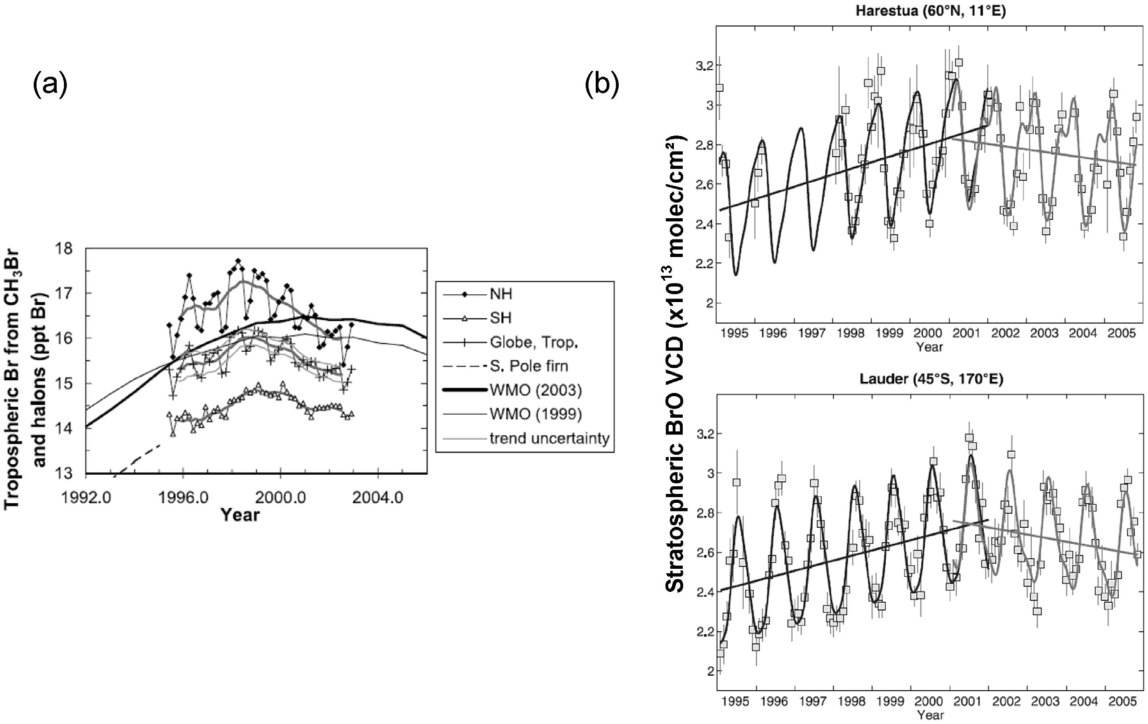

Figure 2.6 (a) Mean tropospheric organic Br from measurements of CH_3Br and the most abundant halons, and in several scenario calculations (WMO). The different curves stand for observations in the northern-hemisphere (NH), southern-hemisphere (SH) and globally average (Globe Trop). Adapted from Montzka et al.(2003). (b) Time series of monthly averaged ground-based stratospheric BrO vertical column densities at (top) Harestua (60°N) and (bottom) Lauder (45°S). The thick straight lines correspond to the linear trend for the 1995-2001 and 2001-2005 periods. Adapted from Hendrick et al. (2008).

These declining chlorine and bromine species abundances clearly reflect the success of the Montreal Protocol and its amendments in controlling the global production and consumption of ozone-depleting substances. However, the very long lifetime of inorganic chlorine and bromine species (and precursors) in the stratosphere let us anticipate a large and long effect of these species on the ozone layer in the next decades, and emphasizes the need to monitor and quantify the concentration of these active molecules in the atmosphere. Different projection scenarios have been used to predict when ozone recovery will occur. Those predictions fall within a 15-year range around the year 2050. Intense research is currently made to assess the mechanisms connecting ozone depletion with climate change. The recovery of the ozone hole might be delayed in response to changes in stratospheric temperature and circulation as a consequence of the release of greenhouse gases.

There is also an intense questioning concerning the evolution of the emissions of short-lived bromine species, in a perspective of a global climate warming (Salawitch, 2006). Indeed, the relevant short-lived bromocarbons are of oceanic origin. Their productions are thus sensitive to ocean temperature and nutrient supply. If in the future the atmosphere becomes warmer and more strongly convective, increased bromine production might result in additional stratospheric ozone destruction.

2.2.3.2 Chlorine and bromine chemistry

An overview of the chlorine and bromine gas-phase chemistry is given in this section, whereas the heterogeneous chemistry of halogens will be presented in the next section. As this thesis is concerned by atmospheric bromine, a strong emphasis will be given in the foregoing discussion on the bromine photochemistry (Lary, 1996; Lary et al., 1996).
The importance of ClO_x[1] and BrO_x[2] catalytic cycles on the destruction of stratospheric ozone was first highlighted respectively by the studies of Molina and Rowland (1974) and Wofsy et al. (1975). Once chlorine and bromine are released from their source gases, they undergo a variety of reactions:

$Cl + O_3 \rightarrow ClO + O_2$ (R 41a) $Br + O_3 \rightarrow BrO + O_2$ (R 41b)
$ClO + O \rightarrow Cl + O_2$ (R 42a) $BrO + O \rightarrow Br + O_2$ (R 42b)
$ClO + NO \rightarrow Cl + NO_2$ (R 43a) $BrO + NO \rightarrow Br + NO_2$ (R 43b)
$ClO + OH \rightarrow Cl + HO_2$ (R 44)

including photolysis:

$ClO + h\nu \rightarrow Cl + O$ (R 45a) $BrO + h\nu \rightarrow Br + O$ (R 45b)

The reactive halogens are also converted into their reservoirs through the reactions:

$ClO + NO_2 + M \rightarrow ClONO_2 + M$ (R 46a) $BrO + NO_2 + M \rightarrow BrONO_2 + M$ (R 46b)
$ClO + HO_2 \rightarrow HOCl + O_2$ (R 47a) $BrO + HO_2 \rightarrow HOBr + O_2$ (R 47b)
$Cl + HO_2 \rightarrow HCl + O_2$ (R 48a) $Br + HO_2 \rightarrow HBr + O_2$ (R 48b)
$Cl + CH_4 \rightarrow HCl + CH_3$ (R49) $Br + HCHO \rightarrow HBr + CHO$ (R50)

Note that the formation of HBr and HCl plays a substantial role as these acids are soluble in water, and can therefore be removed from the atmosphere by washout. It constitutes an important sink of halogens in the stratosphere, in spite of the long time constant associated to these loss processes.
The conversion of the reservoirs into the active forms is achieved through the reactions:

$ClONO_2 + h\nu \rightarrow ClO + NO_2$ (R 51a) $BrONO_2 + h\nu \rightarrow BrO + NO_2$ (R 51b)
$ClONO_2 + h\nu \rightarrow Cl + NO_3$ (R 52a) $BrONO_2 + h\nu \rightarrow Br + NO_3$ (R 52b)
$HOCl + h\nu \rightarrow Cl + OH$ (R 53a) $HOBr + h\nu$ or $O \rightarrow Br + OH$ (R 53b)
$HCl + OH \rightarrow Cl + H_2O$ (R 54a) $HBr + OH \rightarrow Br + H_2O$ (R 54b)

During high chlorine activation (see next section), the following reactions are important

$BrO + ClO \rightarrow Br + OClO$ 59% (R55a) $OClO + h\nu \rightarrow ClO + O$ (R 56a)

---

[1] $ClO_x = Cl + ClO + 2Cl_2O_2$.
[2] $BrO_x = Br + BrO$

$BrO + ClO \rightarrow Br + ClOO$ 34% (R55b) $ClOO + h\nu \rightarrow ClO + O$ (R 56b)
$BrO + ClO \rightarrow BrCl + O_2$ 7% (R55c) $BrCl + h\nu \rightarrow Br + Cl$ (R 56c)

and link the BrO_x and ClO_x catalytic cycles enhancing the efficiency of both cycles.

The most important gas-phase photochemical reactions in the stratosphere involving chlorine and bromine species are synthetically presented in Figure 2.7. The chemistry of chlorine is quite similar to that of bromine. Therefore, for the sake of simplicity, the element X represents either Cl or Br, while Y stands for Br or Cl, respectively.

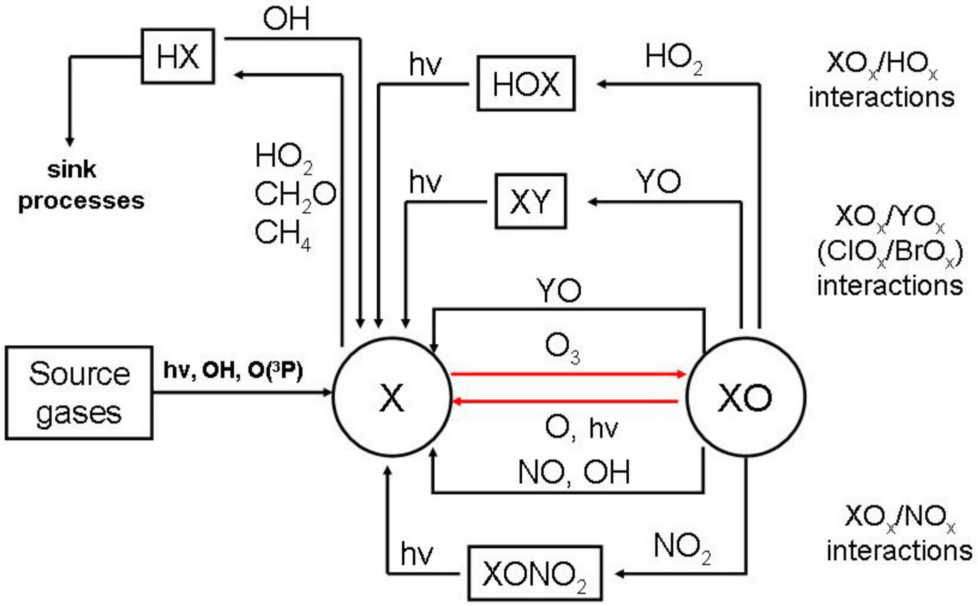

Figure 2.7 Overview of the relevant chlorine and bromine gas-phase photochemical reactions in the stratosphere. The element X represents Cl or Br, whereas Y is Br or Cl respectively.

Although the photochemical scheme is the same for chlorine and bromine species, it is important to notice that the actual atmospheric partitioning between the active radical and the reservoirs largely differs from chlorine to bromine species. This is due to differences in reaction rate and photodissociation coefficients of the above presented reactions for chlorine and bromine species. For chlorine, the photolysis of the reservoirs is quite inefficient and as already mentioned, most of the chlorine species is present as HCl and $ClONO_2$. The impact of chlorine on stratospheric ozone is thus restricted to altitude between 30 and 40 km (i.e. in the upper stratosphere) in usual conditions. For perturbed conditions, heterogeneous reactions lead to efficient recycling of active chlorine (the so-called chlorine activation – see next section) and an efficient stratospheric ozone destruction. In contrast, the photodissociation of the bromine reservoirs is very efficient so that the partitioning between the active and reservoirs species is shifted towards the active forms compared to chlorine. Thus, one can say that bromine species are always ‘activated’ and that bromine is more efficient in destroying ozone than chlorine. These findings are somehow illustrated in Figure 2.8, where the relative contributions to O_x loss by the catalytic cycles involving ClO_x, BrO_x but also NO_x and HO_x are depicted as a function of altitude, for March 1995, 32°N. Note that for this example, a contribution of 4 pptv from VSLS has been added to stratospheric Br_y derived only from the breakdown of methyl bromide and halons.

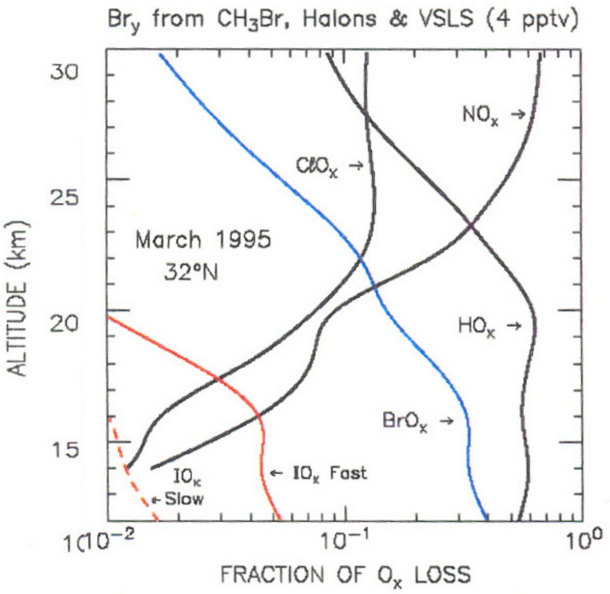

Figure 2.8 Example of calculated fractional contribution O_x loss by catalytic cycles: NO_x, HO_x, ClO_x, BrO_x and IO_x (negligible). Adapted from WMO report (2007).

It can be seen that the ozone loss is dominated by HO_x and BrO_x catalytic cycles in the lower stratosphere, whereas the NO_x cycle is the most important one above ~ 25 km. Chlorine species play a marginal role on the ozone destruction for this particular example. Nevertheless, the picture of Figure 2.8 dramatically changes under chlorine activation conditions.

Now we would like to describe more specifically the stratospheric partitioning generally exhibited by the inorganic bromine species, as a result of the photochemical scheme presented above. The photochemical reactions experienced by the inorganic bromine species are all fast. The species have short chemical lifetime (ranging from ~ 1 s to several minutes) in the sunlit stratosphere, except HBr which has a lifetime close to a day in the lower stratosphere. Hence the inorganic bromine species are subject to strong diurnal variations. As an example, Figure 2.9 shows the modeled diurnal cycle of bromine partitioning at two altitudes (18 and 40 km) and at two locations, calculated using a photochemical box model (1D model accounting for the relevant stratospheric photochemical reactions; see Hendrick et al., 2004, 2007).

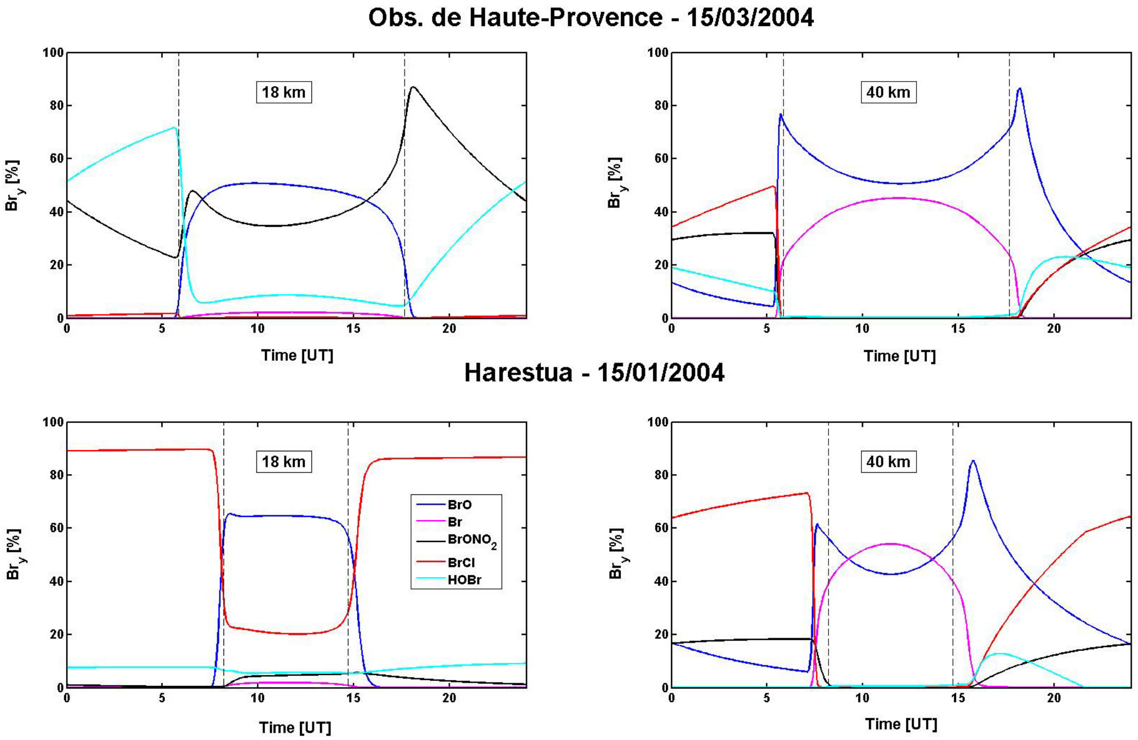

Figure 2.9 Diurnal cycle of the relative contribution of the most important inorganic bromine species in the stratosphere at the altitudes of 18 and 40 km, calculated by the PSCBOX photochemical model (courtesy of F. Hendrick). The examples are given for (top) Observatoire de Haute-Provence (44°N, 6°E) for 15 March 2004 and (bottom) Harestua (60°N, 11°E) for 15 January 2004. The dashed lines show the time of sunrise and sunset (90° of solar zenith angle).

The top plots present an example for Observatoire de Haute-Provence for 15 March 2004 and show the typical behavior at mid-latitude. In the lower stratosphere, bromine monoxide is about half of the available inorganic bromine during daytime[1], and bromine nitrate is the most important bromine reservoir. HOBr has a lower photolytic stability and forms only about 10% of total Br_y during daytime. A photochemical steady-state appears between BrO and $BrONO_2$ through the fast reactions of formation (R 46b) and destruction by photolysis (R 51b) of $BrONO_2$. During sunset, the atmosphere is less exposed to radiation and the BrO concentration decreases very rapidly, as the reservoir species become more and more abundant. It should be noted that the model used here includes also heterogeneous reactions (not yet detailed), and in particular the reaction of conversion of $BrONO_2$ into HOBr by hydrolysis on stratospheric sulfate aerosols:

$$BrONO_2 + H_2O\ (s) \rightarrow HOBr + HNO_3\ (s) \qquad \text{(R 57)}$$

As a consequence of the hydrolysis of bromine nitrate, HOBr forms progressively during the night and constitutes the major bromine reservoir before sunrise in the lower stratosphere. The hydrolysis of $BrONO_2$ is of importance, as it influences the HO_x and

---

[1] Atomic bromine (Br) is present in a small amount since it reacts very quickly with O_3.

NO_x abundances, which has significant effects on the lower stratospheric ozone depletion. Note that higher stratospheric BrO is found at sunrise than at sunset. The rapid increase of BrO at sunrise is due to the fast photolysis of HOBr. The decrease of BrO during the day is related to the increase of NO_2. It can be stated that the partitioning of the bromine species in the stratosphere depends strongly on the profiles of the reservoir precursors and on the incoming radiation flux as a function of altitude. Hence seasonal and latitudinal variations of stratospheric BrO have to be expected from the variations of these parameters. Higher in the stratosphere, the ultraviolet flux is higher and the production of oxygen atom becomes significant. This leads to a progressive conversion of the bromine reservoirs into reactive bromine (Br and BrO). In the upper stratosphere (around 40 km), a photochemical equilibrium between Br and BrO is reached during daytime (see Figure 2.9), through the two reactions R 41b and R 42b.

The bottom plots of Figure 2.9 present the situation for high chlorine activation at a high-latitude site (Harestua) for 15 January 2004. For this particular day, the site of Harestua was in the polar vortex. The photochemical conditions in the lower stratosphere are completely different from that at Observatoire de Haute-Provence, with a small concentration of NO_2 (due to denoxification processes) and a large amount of reactive chlorine. As a result, the concentrations of $BrONO_2$ and HOBr are very low and inorganic bromine is almost exclusively partitioned between BrO and BrCl. The reservoir BrCl is photolysed very efficiently, leading to a partitioning where more than 60% of the inorganic bromine species is in the form of BrO. The rapid photolysis of BrCl explains also the sharp transition of BrO between day and night.

2.2.4 Heterogeneous chemistry – the stratospheric ozone hole

After the discovery of the Antarctic ozone hole in 1985 (Farman et al., 1985), it was soon recognized that heterogeneous reactions play a crucial role on the build up of active ClO_x and BrO_x that ultimately lead to the polar ozone destruction. The mechanisms responsible for the formation of the ozone hole are complex and involve diverse non-linear processes that are competing, sometimes with typical timescales varying by several orders of magnitude. Here we intend only to give a brief introduction of the key processes for this study. We focus here on the Antarctic region, where the phenomenon is by far more important than for the Arctic region, due to weaker dynamic disturbances. For further details, the reader is referred to the literature (e.g., Solomon, 1999).

The stratospheric particles providing the surface for heterogeneous reactions are formed for temperature below 196 K and are called Polar Stratospheric Clouds (PSCs). They are formed in the winter polar vortex at altitudes between ~ 12 and 25 km. The persistence, strength and temperature of the polar vortex largely determine the formation of PSCs. The mechanisms of formation and the precise constitution of PSCs is still a subject of active research, but a classification of the PSCs is usually made based on their composition and formation temperature as presented in Table 2.2.

Table 2.2 PSC classification, composition and formation temperature.

Type	Composition	Temperature
PSC Ia	nitric acid trihydrate (NAT), $HNO_3 . 3\ H_2O$	< 196 K
PSC Ib	supercooled ternary solution (STS) of $H_2SO_4/H_2O/HNO_3$	< 196 K
PSC II	pure ice	< 188 K

There are essentially two types of PSCs:

- PSC type I: As the stratosphere cools in the polar region, the stratospheric sulfate aerosols absorb gaseous water and nitric acid, forming supercooled ternary solutions (STS) of $H_2SO_4 – H_2O – HNO_3$. Continued water and nitric acid uptake from additional cooling can dilute the H_2SO_4 concentration to the extent that the solution is essentially a $HNO_3 – H_2O$ mixture. By freezing, it forms nitric acid trihydrate (NAT). Type Ia refers to the PSCs containing solid hydrates of nitric acid, while in type Ib nitric acid is in solution with water and sulfuric acid.
- PSC type II: These PSCs are mainly composed of ice, and are formed when the temperature falls below the ice frost point (~188 K). They are mainly associated with the colder, more stable vortex of Antarctic winters.

Once the PSCs are formed, a number of heterogeneous reactions convert nitrogen and halogen reservoir species[1] to more reactive species:

$$N_2O_5 + HCl\ (s) \rightarrow ClONO + HNO_3\ (s) \qquad (R\ 58)$$
$$N_2O_5 + H_2O\ (s) \rightarrow 2\ HNO_3\ (s) \qquad (R\ 59)$$

$$ClONO_2 + HCl\ (s) \rightarrow Cl_2 + HNO_3\ (s) \qquad (R\ 60)$$
$$ClONO_2 + H_2O\ (s) \rightarrow HOCl + HNO_3\ (s) \qquad (R\ 61)$$
$$HOCl + HCl\ (s) \rightarrow Cl_2 + H_2O\ (s) \qquad (R\ 62)$$

$$BrONO_2 + HCl\ (s) \rightarrow BrCl + HNO_3\ (s) \qquad (R\ 63)$$
$$BrONO_2 + H_2O\ (s) \rightarrow HOBr + HNO_3\ (s) \qquad (R\ 64)$$
$$HOBr + HCl\ (s) \rightarrow BrCl + H_2O\ (s) \qquad (R\ 65)$$

The reactions R 58 and R 59 are particularly important in the polar vortex. Indeed, during winter polar night, the stratosphere is not exposed to sunlight. A consequence of the absence of light is that no photochemistry takes place in the stratosphere. Thus, the NO_x species are progressively converted in N_2O_5 through the reaction R 31. The heterogeneous conversion of N_2O_5 into nitric acid, sequestered within the PSCs, leads to the complete denoxification of the lower stratosphere. Note that the sedimentation of large PSC particles can even lead to an irreversible removal of HNO_3 (denitrification) and H_2O (dehydration) from the polar stratosphere.

---

[1] Note that HCl and HBr are effectively absorbed on ice (PSC type II) and NAT (PSC type Ia) solid phase surfaces.

In early polar spring (beginning of August), the unstable chlorine compounds produced during polar night by the heterogeneous reactions R 60-62, photodissociate rapidly and release Cl atoms (chorine activation):

$Cl_2 + h\nu \rightarrow 2\,Cl$ (R 66)
$HOCl + h\nu \rightarrow Cl + OH$ (R 67)

Several effective catalytic mechanism involving ClO dimer cycle (Molina and Molina 1987) and ClO/BrO cycle (McElroy et al., 1986) then occur:

$ClO + ClO + M \rightarrow Cl_2O_2 + M$ (R 68)
$Cl_2O_2 + h\nu \rightarrow Cl + ClOO$ (R 69)
$ClOO + M \rightarrow Cl + O_2$ (R 70)
$2\,(Cl + O_3 \rightarrow ClO + O_2)$ (R 71)
net: $2\,O_3 \rightarrow 3\,O_2$

$ClO + BrO \rightarrow Cl + Br + O_2$ (R 72)
$\rightarrow BrCl + O_2$ (R 73)
$BrCl + h\nu \rightarrow Br + Cl$ (R 74)
$Cl + O_3 \rightarrow ClO + O_2$ (R 75)
$Br + O_3 \rightarrow BrO + O_2$ (R 76)
net: $2\,O_3 \rightarrow 3\,O_2$

Note that BrO plays an important role during the active photochemistry period since the ClO/BrO cycle leads to an additional provisioning of reactive Cl and Br atoms.

The key concept to explain a strong and long lasting ozone depletion is that no NO_x is available (due to denoxification and the isolation of air in the polar vortex) to moderate the Cl catalysis. Furthermore, only a small supply of NO_x and O_3 by upper stratospheric layers is expected since the vertical transport is very slow (the vertical wind speed is of about 1 km/month in the polar vortex). In the meantime, the stratosphere becomes warmer at the beginning of polar spring, and the PSCs progressively evaporate starting with PSCs type II. This releases HO_x radicals in the stratosphere and conducts to the partial conversion of Cl into HCl (R 48a). However, this mechanism occurs after significant ozone loss. In late spring, PSCs of type I evaporate, releasing NO_x in the stratosphere. Chlorine nitrate is then formed by the reaction between ClO and NO_2 (R 46a). Progressively, the chlorine reservoirs (HCl and $ClONO_2$) return to their pre-ozone hole levels.

In late spring, the polar vortex also begins to weaken and ozone-rich mid-latitudinal air starts to mix with the low ozone air from the polar vortex. Later on, the polar vortex becomes very unstable and breaks. By summer (December), the ozone layer has recovered by dynamical mixing of air.

The chemical scheme presented here is particular as it leads to the complete destruction of ozone between ~ 12 and 24 km of altitude in few weeks time. This is illustrated in Figure 2.10 (left plot) showing a comparison between ozone profiles before and after the activation of chlorine species. The ozone concentrations at altitudes where usually the maximum of the ozone layer resides are nearly equal to zero.

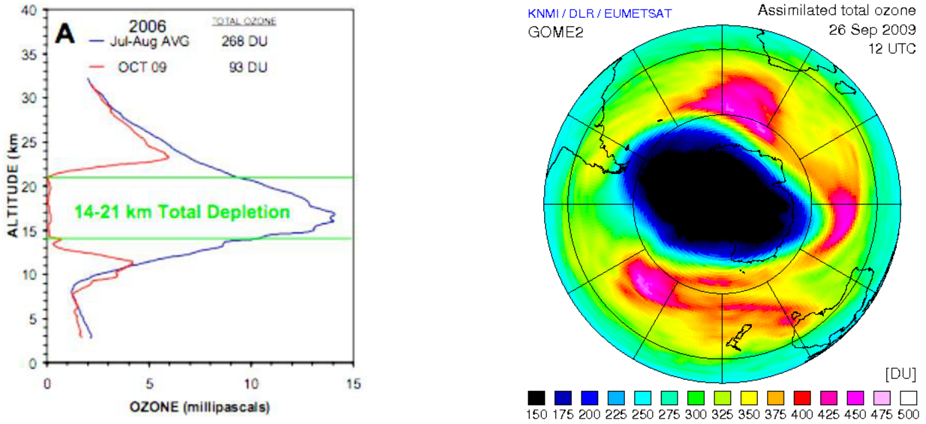

Figure 2.10 (left) South Pole ozone sonde data in 2006 showing ozone profiles before and after the polar spring ozone destruction event (adapted from the SPARC report 2008). (right) Total ozone column over the Antarctic continent showing the extent of the ozone hole for the 26th of September 2009. This map is based on observations made using the GOME-2 satellite instrument (http://www.temis.nl).

The right plot of Figure 2.10 shows the extent of the ozone hole for a day in September 2009 where it is maximum in size (~ 25 million km²) and depth.

It should be noted that there are large interannual differences of the duration and strength of the ozone hole. This is linked to the year-to-year variations for the persistence and strength of the polar vortex (dynamical aspects), temperature of the stratosphere, halogen loading, PSCs formation and sedimentation rates. The same processes that lead to ozone loss in Antarctica certainly occur in the Arctic, but are weaker and more variable, with large interannual differences in the strength of the polar vortex and the duration of low temperatures.

In addition to the processes leading to the polar ozone hole, heterogeneous chemistry can also play a role at mid-latitude. The heterogeneous reactions are not occurring on PSCs anymore, but on liquid stratospheric sulfuric acid aerosols. The existence of sulfur in the stratosphere is mostly due to emissions of carbonyl sulfide (COS) and SO_2 emitted from large volcanic eruptions[1]. Sulfate forms a layer in the stratosphere (known as the Junge Layer) distributed globally and consisting mainly of H_2SO_4/H_2O droplets. The presence of background aerosols alters substantially the partitioning of several nitrogen (R 58-59) and halogens (R 60-65) reservoirs. As the maximum sulfate density coincides with the maximum ozone density, significant ozone loss although weaker than in the polar region occur at mid-latitudes.

---

[1] Noteworthy is the eruption of Mount Pinatubo (Philippines) in June 1991 that injected a large amount of aerosols and SO_2 (~ 2 Tg) into the stratosphere.

2.3 Tropospheric bromine chemistry

Halogens are known to affect also the chemistry of the troposphere. They are of special interest because they are involved in many reaction cycles that can influence the oxidation power of the troposphere by influencing the main oxidants O_3, OH and NO_x. While the sources of reactive halogens in the stratosphere are mostly of anthropogenic origin, the presence of inorganic halogens in the troposphere is mainly due to natural sources and processes. Although the chlorine and iodine compounds are important for the chemical composition of the troposphere, these halogens will not be treated in this study. Only the role of bromine on tropospheric chemistry will be discussed here. The aim of this section is to give a brief overview of the mechanisms driving the release of reactive bromine in the troposphere and the measurements of BrO associated to these events. Brominated compounds are responsible for sporadic, rapid ozone depletion in the troposphere. High levels of BrO have been observed in the polar boundary layer, leading to efficient ozone destruction. Evidences are accumulating that reactive bromine is also present in the marine boundary layer, in the vicinity of salt lakes and volcanoes. Other observations suggest the existence of inorganic bromine in the free-troposphere, possibly at the global scale. In contrast to the stratosphere, our understanding of the role of bromine in the global troposphere is still evolving rapidly. A number of important, unresolved questions relate to the source of bromine and the underlying processes leading to the release of bromine in the troposphere. These points will be addressed in section 2.4. For further discussion about tropospheric bromine, the reader is referred to thorough review articles (von Glasow and Crutzen, 2007; Simpson et al., 2007).

2.3.1 Tropospheric ozone

Ozone is a toxic gas that is known to have severe health effects (particularly on the respiratory system) with prolonged exposure. At the beginning of the 20th century, it was thought that ozone in the troposphere was of stratospheric origin, since the ozone production via the reactions (R 1-2) is negligible in the troposphere; the UV solar radiation required ($\lambda<242$ nm) being already absorbed in the stratosphere. As the ozone concentrations continuously increased in the urban areas, it became obvious that other mechanisms of ozone production were involved in the troposphere. It is now widely accepted that increases in NO_x and non-methane hydrocarbons (NMHC) emissions due to fossil fuel combustion are the major causes of this enhancement in tropospheric ozone. Due to the large number of different hydrocarbons, the photochemistry involved is very complex. However, the following key reactions are responsible for the production of ozone in the polluted regions (RH refers to NMHC):

$OH + RH \rightarrow R + H_2O$ (R 77)
$R + O_2 + M \rightarrow RO_2 + M$ (R 78)
$RO_2 + NO \rightarrow RO + NO_2$ (R 79)
$RO + O_2 \rightarrow R'CHO + HO_2$ (R 80)
$HO_2 + NO \rightarrow OH + NO_2$ (R 81)
$2\,(NO_2 + h\nu \rightarrow NO + O)$ (R 82)
$2\,(O + O_2 + M \rightarrow O_3 + M)$ (R 83)
net: $RH + 4O_2 + h\nu \rightarrow R'CHO + H_2O + 2\,O_3$

NMHC and NO_x are called ozone precursors. In the above scheme, NMHC is consumed, while NO_x acts as a catalyst.
In the remote oceanic boundary layer and the free troposphere, the ozone production is dominated by the oxidation of CH_4 and CO:

$OH + CH_4 \rightarrow CH_3 + H_2O$ (R 84)
$CH_3 + O_2 + M \rightarrow CH_3O_2 + M$ (R 85)
$CH_3O_2 + NO \rightarrow CH_3O + NO_2$ (R 86)
$CH_3O + O_2 \rightarrow HCHO + HO_2$ (R 87)
$HCHO + 2O_2 + h\nu \rightarrow CO + 2HO_2$ (R 88)
$3 (HO_2 + NO \rightarrow OH + NO_2)$ (R 89)
$4 (NO_2 + h\nu \rightarrow NO + O)$ (R 90)
$4 (O + O_2 + M \rightarrow O_3 + M)$ (R 91)
net: $CH_4 + 8O_2 + 5h\nu \rightarrow CO + H_2O + 2OH + 4 O_3$

Carbon monoxide produced by the methane oxidation or emitted directly from combustion can react with the hydroxyl radical:

$OH + CO \rightarrow CO_2 + H$ (R 92)
$H + O_2 + M \rightarrow HO_2 + M$ (R 93)

For high NO_x concentrations, ozone production occurs:

$HO_2 + NO \rightarrow OH + NO_2$ (R 94)
$NO_2 + h\nu \rightarrow NO + O$ (R 95)
$O + O_2 + M \rightarrow O_3 + M$ (R 96)
net: $CO + 2O_2 + h\nu \rightarrow CO_2 + O_3$

For low NO_x concentrations, ozone is destroyed via:

$HO_2 + O_3 \rightarrow OH + 2 O_2$ (R 97)
net: $CO + O_3 \rightarrow CO_2 + O_2$ (R 98)

Note that the presence of ozone in the troposphere has an important consequence because it leads to the photochemical production of OH by:

$O_3 + h\nu \rightarrow O_2 + O(^1D)$ (R 99)
$O(^1D) + H_2O \rightarrow 2 OH$ (R 100)

This aspect is crucial because OH is known to react very efficiently with a large number of molecules. The hydroxyl radical can convert non-soluble compounds into soluble ones which are then removed from the atmosphere. Thus ozone is largely influencing the oxidation capacity of the atmosphere.

2.3.2 Polar boundary layer bromine

In the 1980s, several field campaigns were conducted in the Arctic, initially to study the impact of pollutants emitted by industrialized countries on the Arctic troposphere. In addition to high ozone concentrations associated to air pollution, remarkably low surface ozone concentrations have also been measured in late winter/early spring, with ozone levels on occasion dropping below the detection limit. It was soon discovered by Barrie et al. (1988) that these ozone depletion events (ODEs) were found to coincide with high levels of bromine. The involvement of bromine in the depletion of surface O_3 have then been further confirmed by direct BrO radical measurements using DOAS (see chapter 3) instruments at Alert (Hausmann and Platt, 1994, 82.3°N, 62.2°W) and at Spitsbergen (Tuckermann et al., 1997, 78.9°N, 11.8°E). Since then many more ground-based observations of elevated BrO concentrations have been reported in the Arctic (e.g., Martinez et al., 1999; Hönninger et al., 2004a), as well as in the Antarctic (Kreher et al., 1997; Frieβ et al., 2004; Saiz-Lopez et al., 2007). In situ-measurements of BrO using the atomic fluorescence method were also made (Avallone et al., 2003).

An example of the strong anti-correlation between ozone and BrO, measured at Spitsbergen, is depicted in Figure 2.11. It can be seen that the observed bromine monoxide mixing ratios of up to 17 pptv are sufficient to destroy within few hours the 30-40 ppb of ozone typically present in the boundary layer.

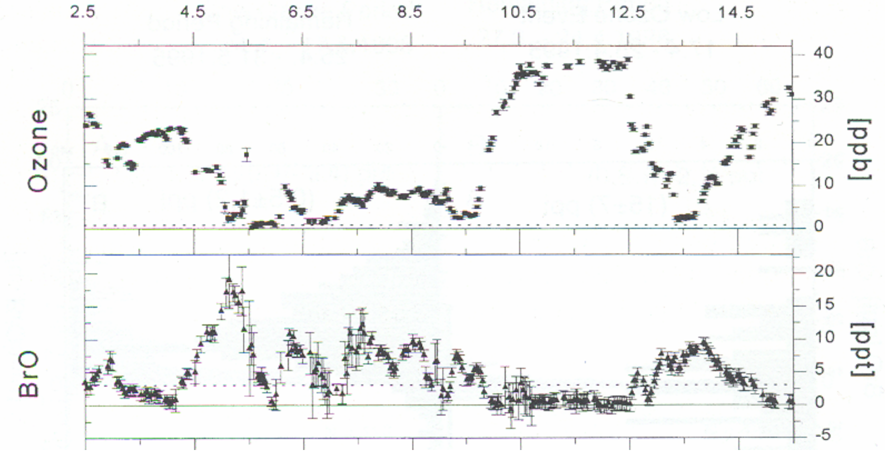

Figure 2.11 Time series of ozone and BrO mixing ratios measured at Spitsbergen, during the period 2-17 May 2006. Adapted from Tuckermann et al. (1997).

Following the early ground-based measurements of BrO during ODEs, satellite observations have shown that plumes of enhanced BrO are frequent phenomena in both hemispheres in polar spring, covering large areas mainly over sea ice and along the coasts (Wagner and Platt, 1998; Richter et al., 1998, 2002; Chance, 1998). A strong correlation with the occurrence of first-year sea-ice was found, indicating that the source is related to the enrichment of sea salt on the surface of freezing sea ice.

The understanding of the physical and chemical processes underlying the release/recycling of polar boundary layer BrO (leading to ODEs) became a major topic of research. Since the 1980s, research on ODEs has made great advances and it is now understood from intensive field campaigns as well as laboratory and modeling studies, that reactive bromine is released and sustained in the boundary layer by heterogeneous autocatalytic reactions on the surfaces of young sea-ice and sea salt aerosols. A special sequence of chemical reactions, often known as the “bromine explosion” reaction sequence, is responsible for the activation of reactive bromine in the polar boundary layer (PBL). It involves reactions in the gas phase as well as uptake of bromine species to aerosols particles or ice, reactions in the condensed phase and release of photolysable bromine to the gas phase:

$$\begin{array}{llcll}
 & \mathrm{HOBr} & \rightarrow & \mathrm{HOBr_{aq}} & \text{(R 101)} \\
 & \mathrm{HOBr_{aq} + Br^- + H^+} & \rightarrow & \mathrm{Br_{2,aq} + H_2O} & \text{(R 102)} \\
 & \mathrm{Br_{2,aq}} & \rightarrow & \mathrm{Br_2} & \text{(R 103)} \\
 & \mathrm{Br_2 + h\nu} & \rightarrow & \mathrm{2\,Br} & \text{(R 104)} \\
 & \mathrm{Br + O_3} & \rightarrow & \mathrm{BrO + O_2} & \text{(R 105)} \\
 & \mathrm{BrO + HO_2} & \rightarrow & \mathrm{HOBr + O_2} & \text{(R 106)} \\
\text{net:} & \mathrm{H^+ + Br^- + HO_2 + O_3 + h\nu} & \rightarrow & \mathrm{Br + H_2O + 2\,O_2} &
\end{array}$$

This sequence is graphically depicted in Figure 2.12.

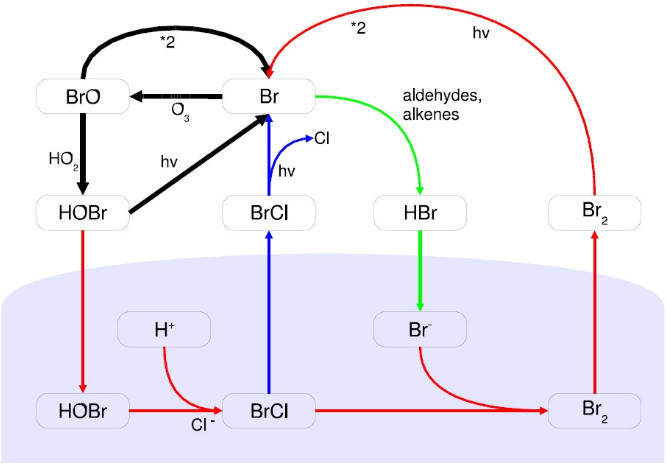

Figure 2.12 Schematic diagram of bromine explosion reactions. The blue area represents the condensed phase, whereas the white area shows the gas phase. Adapted from Simpson et al. (2007).

This sequence leads to an exponential increase of the number of bromine compounds in the gas phase[1]. Indeed, the reaction cycle consumes one bromine species (HOBr) but produces Br_2, the precursor of two reactive bromine species that then act as catalyst of the ozone destruction. It should be noted that in addition to the scheme presented in Figure 2.12, reactive bromine can also destroy PBL ozone through the BrO/BrO self reaction cycle which becomes important for high BrO concentrations:

---

[1] This is why this cycle has been termed “bromine explosion”.

$$2\,(Br + O_3 \rightarrow BrO + O_2) \quad (R\ 107)$$
$$BrO + BrO \rightarrow Br_2 + O_2 \quad (R\ 108)$$
$$Br_2 + h\nu \rightarrow 2\,Br \quad (R\ 109)$$
$$\text{net: } 2\,O_3 \rightarrow 3\,O_2$$

Several others chemical cycles implying ClO/BrO and IO/BrO cross-reactions are also playing a role but will not be addressed in this study.
From Figure 2.12, it can also be seen that the reaction (R 102) competes with:

$$HOBr_{aq} + Cl^- + H^+ \rightarrow BrCl_{aq} + H_2O \quad (R\ 110)$$

where BrCl is also photolyzed once it is released. Obviously this reaction can not lead to an increase in reactive gaseous bromine. In most cases the yield of Br_2 is strongly enhanced compared to BrCl, so that the bromine explosion can take place leading to ODEs.
It is important to stress that what actually triggers the bromine explosion cycle is the sunlight that photolyses Br_2 into two Br atoms. This is the reason why enhanced BrO concentrations are only observed in the PBL in late winter/early spring, once the polar troposphere is illuminated again, after the polar night. Another prerequisite for bromine explosion is a condensed phase highly concentrated in halogen ions (Br^- and Cl^-). Therefore the bromine release in the gas phase only occurs for $pH < 6.5$.

Sources of bromine

Early studies of Arctic ODEs identified marine influences on ozone depleted air masses. It was soon clear that sea salt is likely the major source of bromine. Later on, strong indications were found for the relevance of young sea ice in bromine activation. For example, it was shown using trajectory analysis, that enhanced levels of BrO are observed when the probed air masses have been in contact with first-year sea ice (e.g., Frieβ et al., 2004). It has still not unambiguously been shown exactly how bromine is released from the ocean to provide enough mass for bromine explosions, but it is likely that the following processes are involved: as sea water cools, ice begins to form and rejection of salts from the freezing water creates highly saline brine. The precipitation process leads to an enrichment of bromine ions.
Recently, frost flowers have raised a lot of interest as they might play a major role in the release of bromine in polar region. Frost flowers are delicate crystals that grow out of the vapor phase and transport concentrated brines of young sea ice (see Figure 2.13).

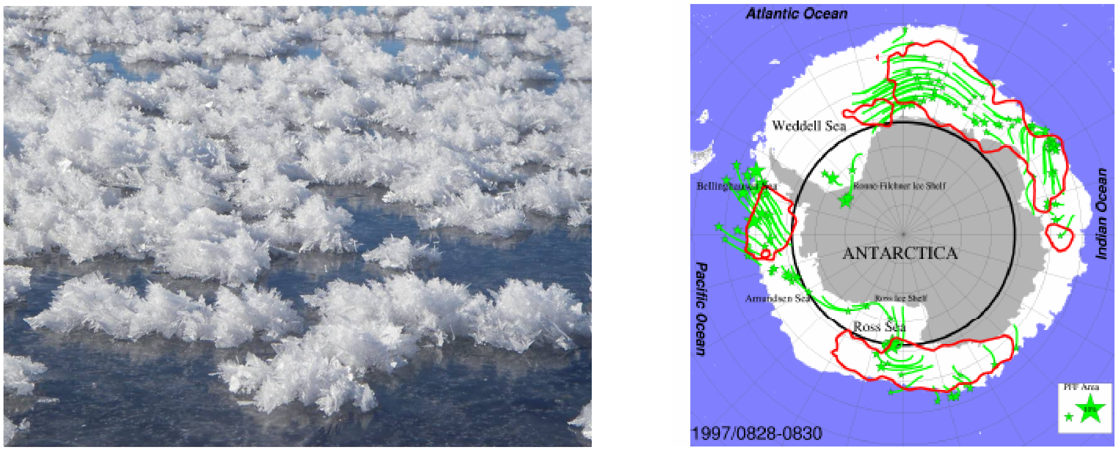

Figure 2.13 (left) A photograph of frost flowers growing on newly forming sea-ice. (right) The spatial match between potential frost flowers (PFF) shown by stars and regions of enhanced BrO (red isocontours). Adapted from Kaleschke et al. (2004).

They can persist for several days and have very large surface areas for heterogeneous reactions. Kaleschke et al. (2004) combined satellite derived maps of young sea ice with a model to estimate a potential frost flowers (PFF) coverage and compared these PFF areas with satellite observations of BrO. They showed that the PFF areas coincide with areas of high BrO levels (Figure 2.13), indicating the probable role of frost flowers in the formation of bromine explosion events. Recent research focuses on assessing the importance of some processes believed to be relevant in the starting and formation of bromine explosion events:

- Direct release of gaseous bromine from frost flowers to the gas phase.
- Production of very salty aerosols from frost flowers or sea spray, capable of sustaining bromine activation.
- Wind-blown snow soaking up brine, for example in frost flower fields, followed by a bromine explosion within the snow and release of gaseous bromine to the atmosphere.

Meteorological influences

The meteorological conditions affect dramatically the episodes of ozone depletion. Indeed, the efficiency of the bromine explosion sequence to destroy ozone is strongly dependent on the stability of the boundary layer. A stable boundary layer keeps high the concentrations of the bromine reactants close to the surface by preventing mixing of air with the free troposphere (it provides a somewhat “closed reaction chamber”). In late winter and spring, strong inversion layers are formed below 1000m of the polar atmosphere leading to strong and long lasting ozone depletion. It is likely that the termination of ODEs is associated with extensive vertical mixing. The wind speed and direction are also determinant meteorological parameters for ozone depletion events, as wind brings air masses that have been in contact with sea-ice to places with better (or not) conditions for bromine explosions (stable boundary layer and high illumination).

Another effect related to the influence of wind, can occur in polar region when cold air mass moves over a warmer surface. This results in vertical transport of air above the boundary layer, followed by long-range transport. For example, McElroy et al. (1999) have observed BrO in the Arctic free troposphere using aircraft-based instrument and argue that this is due to strong convection caused by large temperature differences of open sea water and the surrounding air. Transport of BrO plumes to lower latitudes has also been observed using satellite BrO observations (Hollwedel et al., 2004).

Bromine – Mercury interactions

The presence of highly concentrated reactive bromine in the polar boundary layer has many consequences on polar chemistry beyond the ozone-related chemical mechanisms. A remarkable example is the unique chemistry of the Arctic region that links reactive bromine species and mercury. Mercury is a global pollutant emitted from both natural and anthropogenic sources. It is a toxic compound that is usually present in the atmosphere as elemental mercury (Hg^0), a rather unreactive compound that can be transported over long ranges. Schroeder et al. (1998) were the first to report surprisingly rapid depletion of mercury (mercury depletion events, MDEs) in the polar boundary layer during ODEs. Since then, intensive research has demonstrated the key role played by reactive bromine in oxidizing mercury in the Arctic through the following reactions.

$Br + Hg^0 \rightarrow HgBr$ (R 111)
$BrO + Hg^0 \rightarrow HgO + Br$ (R 112)
$BrO + Hg^0 \rightarrow HgBrO$ (R 113)
$BrO + Hg^0 \rightarrow HgBr + O$ (R 114)

These oxidized inorganic Hg species are more reactive than elemental mercury and may directly deposit to snow/ice. The deposited mercury can ultimately reach sediments and bioaccumulate into wildlife. This may have serious consequences for the health of the aboriginal population and the Arctic ecosystems during spring ice melting.

2.3.3 Extra-polar boundary layer bromine

Reactive bromine has been found to be of importance in many other places outside the polar regions.

Salt lakes

Large BrO mixing ratios of 100-200 pptv have been measured at mid-latitudes from salt pans at the Dead-sea, Israel (Hebestreit et al., 1999; Matveev et al., 2001) and smaller values at the Great Salt Lake in Utah (Stutz et al., 2002). Measurements of BrO have shown strong anti-correlations with measurements of in-situ ozone. The likely explanation for the high bromine levels over salt lakes is related to similar release mechanisms as the ones in polar regions (bromine explosion) and is due to the presence of large salt deposits on the surface of salt lakes. These observations show that low temperatures are not a prerequisite for the chemical cycles to be efficient in bromine release.

Marine boundary layer

Approximately 70% of the Earth's surface is covered by oceans, making the processes in the marine boundary layer (MBL) potentially significant for the whole atmosphere. In the MBL, bromine is very abundant in the form of sea salt aerosols. The release of reactive bromine from sea salt aerosols could thus affect significantly the chemistry of the MBL. Short-lived brominated halocarbons can also play an important role in the MBL. Bromoform ($CHBr_3$) is a major natural ocean contributor of bromine, with tropical macroalgae constituting an important source. Open ocean source, related to phytoplankton has also been identified (Butler et al., 2007). Other important biogenic compounds of marine origin include dibromomethane (CH_2Br_2) and dibromochloromethane ($CHBr_2Cl$).

In the marine boundary layer, BrO has been detected at several mid-latitude coastal locations, Canary Islands (Leser et al., 2003), Mace Head (Saiz-Lopez et al., 2004) and Roscoff (Mahajan et al., 2009), and also at the equatorial mid-ocean site of Cape Verde (Read et al., 2008), with mixing ratios up to 10 pptv. Model calculations have indicated that the presence of few pptvs of BrO can significantly impact the O_3 budget, the NO_x and HO_x partitioning in the MBL (von Glasow et al., 2002a). Furthermore, bromine has also a potential impact on sulfur chemistry in the MBL (von Glasow et al., 2002b), as BrO is efficient to oxidize dimethyl sulphate (DMS: $(CH_3O)_2SO_2$). This is of particular interest in the remote MBL since DMS is the most important precursor of SO_2 and sulfate aerosols that are important for cloud processes and climate because they act as cloud condensation nuclei.

Volcanoes

Bobrowski et al. (2003) measured the highest atmospheric BrO mixing ratios (~1000 pptv) detected so far in the plumes of the degassing volcano of Souffrière Hills on Montserrat. Since then, BrO has been measured at several volcanoes (e.g., Oppenheimer et al., 2006; Bobrowski et al., 2007). Measurements of the BrO:SO_2 ratio and comparison of this data with model calculations have shown that the bromine explosion mechanism is sufficient to explain the amount of observed BrO. The detection of BrO in the vicinity of volcanoes attracted the attention of the scientific community to the possible contribution of active volcanoes as a source of inorganic bromine in the troposphere and, possibly, also in the stratosphere. Based on the observations mentioned above, extrapolated global source strength of 3-40 kT (Br) yr^{-1} has been derived which makes the volcanoes very important potential source of atmospheric bromine. Despite attempts to identify such volcanic emissions through correlations with SO_2 plumes observed by satellite instruments (Afe et al., 2004) no sizeable enhancement of the BrO column could be observed in any of the sounded eruptions. There is one noticeable exception with the massive eruption in 2008 of the Kasatochi volcano (Alaska), and we will present in chapter 7 the first clear evidence for the release of a large plume of volcanic BrO visible from space (Theys et al., 2009).

2.3.4 Free-tropospheric BrO

Inorganic bromine compounds can also be present in the free-troposphere. This is supported by BrO observations from space (Wagner and Platt, 1998; Richter et al., 2002; Van Roozendael et al., 2002), high-altitude aircraft (McElroy et al., 1999), ground (Hendrick et al., 2007; Theys et al., 2007) and balloon (Harder et al., 1998; Fitzenberger et al., 2000), all suggesting although with larges uncertainties the widespread presence of BrO in the free-troposphere, with background vertical columns of about 1-3 x 10^{13} molec/cm², corresponding to BrO mixing ratios in the range from 0.5 to 2 pptv if uniformly mixed. On the other hand, observations from ground (Schofield et al., 2004) and balloon (Dorf et al., 2008) contradict these findings by measuring almost no BrO in the free-troposphere. Elaborating on the above-cited free-tropoheric BrO observations, recent modeling results (von Glasow et al., 2004; Lary, 2005; Yang et al., 2005) have highlighted the possible role of free-tropospheric bromine as an additional sink for ozone, a process so far largely ignored. These studies suggest that bromine might be responsible for a reduction in the zonal mean O_3 mixing ratio of up to 18% and locally even up to 40%.

2.4 Open questions related to atmospheric bromine

While a lot of progress in our understanding of the role of bromine in the atmosphere has been made since the discovery of the stratospheric and tropospheric ozone depletion events, many open questions remain.

Stratosphere

Today it is believed that all fundamental chemical processes linked to stratospheric bromine are understood. Nevertheless, several aspects related to the total inorganic bromine loading in the stratosphere still remain unclear, at least to a certain degree.

In addition to the long-lived bromine anthropogenic compounds, additional short-lived bromine species, mainly of natural origin, are needed to explain the bromine budget in the lower stratosphere. Evaluating the contribution of VSLS to stratospheric Br_y is the subject of recent research. The understanding of the VSLS source processes, their magnitudes, temporal and spatial distributions and variability is crucial in that respect. Furthermore, the dominant pathway of VSLS from the boundary layer to the stratosphere is via convective uplift in the tropics, delivering VSLS to the tropical tropopause layer. A thorough understanding of the transport in the tropics together with an improved characterization of the atmospheric lifetimes and sinks of VSLS is thus highly relevant to assess the impact of VSLS on stratospheric Br_y budget. Other scientific questions are associated to long-term changes of stratospheric Br_y in response to the Montreal Protocol restrictions on long-lived brominated substances and to climate change feedbacks on the emissions of natural bromine species and processes (e.g. transport) controlling their impact on stratospheric Br_y.

Free-troposphere

As the stratospheric bromine source gases are first emitted in the troposphere, it is clear that the pending questions related to the impact of VSLS on stratospheric Br_y are also of great interest for the free-troposphere. Their short lifetimes of typically days and weeks mean that it is not straightforward to resolve their global budgets, especially if they might be emitted in highly variable amounts globally.

In fact, the actual sources for the free-tropospheric inorganic bromine are still poorly constrained. In addition to the decomposition of organic bromine compounds (in particular very-short lived species), they include also the release from sea salt aerosols and upward transport from the MBL, downward transport from the stratosphere, uplifting of surface BrO in the polar regions, volcanoes, salt lakes or other so far unidentified sources. Furthermore, the physical and chemical processes influencing the chemical lifetime of BrO in the free-troposphere are currently not well characterized, in particular those involving particle surfaces.

Polar boundary layer

While the autocatalytic reaction cycle for bromine explosion is relatively well characterized, the details of the initial release of bromine are not well understood. Current research also focus on the propagation and termination reactions for bromine explosion: under what conditions is the production of new BrO_x fast enough to compensate for termination processes? The maintenance of the autocatalytic bromine cycle will depend on the availability of bromine in the condensed phase, acidity, temperature and other factors. Another important question is related to the processes which bring salt from sea water to the atmosphere leading to the bromine activation.

Finally, there is a lot of interest on the influence of anthropogenic pollution and climate change on polar ODEs. For example, the extent of sea ice in summer in the Arctic has been dramatically decreasing in the last few decades. As the bromine release seems to be closely related to first-year sea ice, the extend and intensity of the bromine clouds can be expected to increase in the future as the ocean will continue to freeze during the winter, thereby producing an increasingly large area of first-year sea ice.

Chapter 3

Observation principles

This chapter gives an introduction to the technique used in this thesis to measure the abundance of atmospheric species by UV-visible absorption spectroscopy using the solar radiation as a source. General principles applicable to several atmospheric species are given along with more details on the method used to measure atmospheric bromine monoxide. First, basics on the solar radiation and the different processes experienced by a photon entering the Earth's atmosphere are given. Then the principle of Differential Optical Absorption Spectroscopy is presented. Finally, some words are given on the propagation of the radiation in the atmosphere, and the important concept of air mass factor is introduced.

3.1 Solar spectrum

Solar radiation ranges from X-rays through ultraviolet to far radiowaves. The nature of the radiation emitted by the sun is determined by the physical and chemical processes occurring inside it and within its atmosphere. Most of the solar radiation traveling through the solar system originates from the so-called photosphere of the Sun, a relatively thin layer (~1000 km) at the Sun's surface with an effective temperature of about 5900 K. The total irradiance of the sun (total radiative energy flux – also called *solar constant S*) at a mean distance from the Earth to the sun is S=1.37 kWm^{-2}. It is spectrally distributed according to Figure 3.1, with a continuum matching the black body spectrum of about 5900 K (left plot) and with a large number of absorption lines (right plot), the Fraunhofer lines, which originates from higher layers of the sun's atmosphere.

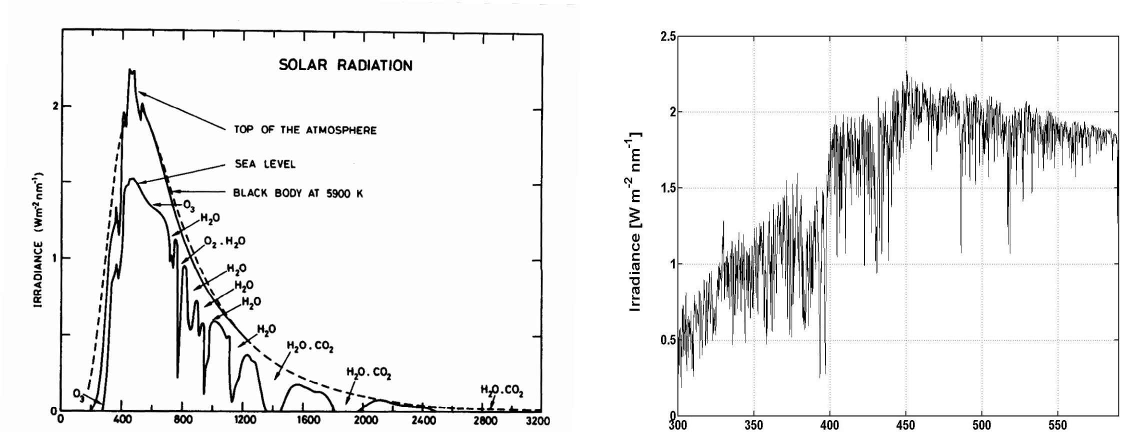

Figure 3.1 (left) The spectrum of solar radiation outside the Earth's atmosphere and at sea level compared with black body radiation at 5900 K. Adapted from Coulson (1975). (right) The solar spectrum at a spectral resolution of 0.2 nm in the wavelength interval from 300 to 600 nm. Adapted from Kurucz et al. (1984).

The analysis of the Fraunhofer lines reveals the presence of at least 60 elements in the solar photosphere, hydrogen and helium being the most abundant.

The solar irradiance is subject to fluctuations such as those associated to the Sun's rotation (28 days variation) and to the variation of the occurrence of sunspots (11 year solar cycle). The variability of the solar irradiance depends strongly on the wavelength region, with the largest value (up to 100%) in the far ultraviolet (<300 nm). Beyond 300 nm it becomes less than 1%.

3.2 Interaction processes of radiation in the atmosphere

Once a photon is emitted by the sun, it eventually reaches the Earth's atmosphere where it undergoes a variety of processes, as illustrated in Figure 3.2. The photon can be scattered by air molecules, aerosols, cloud droplets or ice particles. It can also be absorbed by the atmospheric constituents. Finally, a photon penetrating the entire atmosphere can either be absorbed or reflected by the Earth's surface. This section describes the different processes in more detail. Only the interactions in the UV-visible wavelength range (~ 300 - 700 nm) will be addressed[1].

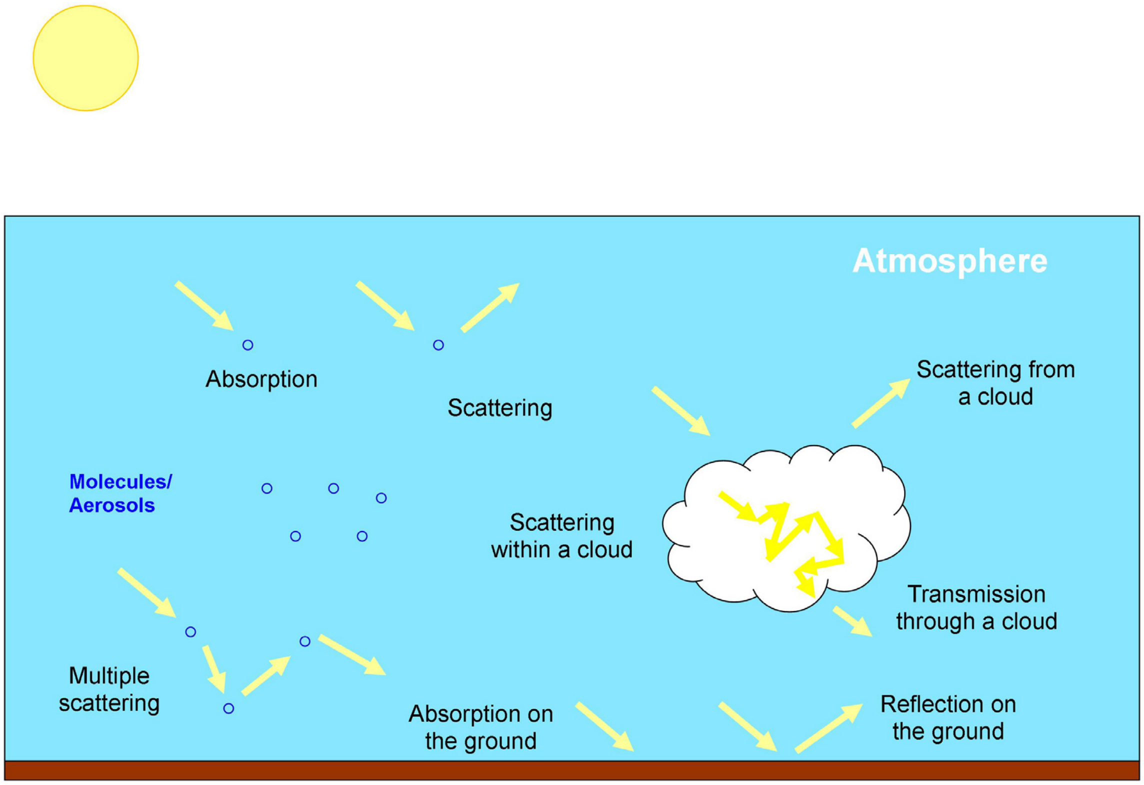

Figure 3.2 Schematic view of the interaction processes of UV-visible radiation in the atmosphere.

---

[1] The phenomenon of thermal emission will not be discussed here. Indeed, the black-body Planck function for typical temperatures of the atmosphere, clouds or the earth's surface has a maximum in the infrared region (around 15 µm) and is negligible for UV-visible wavelengths.

In section 3.4, the propagation of radiation in an absorbing and scattering atmosphere will be studied in a more rigorous way using the 'radiative transfer equation'. This formulation links the radiance[1] to the elementary processes described here.

3.2.1 Absorption

An atom or molecule can be excited from its current energy state to a higher energy state by absorption of a photon, if the energy difference of the two states equals the energy of the absorbed photon. While only electronic transitions are possible for atoms, the atmospheric molecules are characterized by discrete rotational and vibrational energy states, as well as by their electronic configurations. Photons of the UV-visible wavelength region have energies in the range of about several electron volts. This radiation is energetic enough to cause electronic transitions between ground and excited states when it is absorbed. These electronic transitions are usually accompanied by changes in the vibrational and rotational states of the molecule[2]. Hence molecular absorption spectra in the UV-visible wavelength range consist of rotational-vibrational spectra of different electronic transitions. While in the microwave and infrared regions it is often possible to resolve the individual lines, in the UV-visible region the usual situation is that the rotational structures can not be separated and form a quasi-continuous absorption within a vibrational 'band'. This is either due to the broadening of the spectral lines under atmospheric conditions (Doppler and pressure broadening, which are caused by thermal motion and collisions between the molecules, respectively) so that the width of the lines are larger than their spacing or because the typical spectral resolution of the instruments used does not allow to resolve the individual lines.

The absorption characteristics of an atom or molecule are usually expressed in terms of an absorption cross-section, which is a measure of the probability of photon absorption at a certain wavelength. The unit of absorption cross-section is that of a surface, commonly [cm²] or [cm² molec^{-1}].

3.2.2 Elastic scattering

In the dense layers of the atmosphere, solar radiation undergoes elastic scattering (i.e. scattering without change of the photon energy) due to the presence of large concentrations of air molecules and aerosol particles. Depending on the ratio of the size of the scattering particle to the wavelength of the light, different regimes of atmospheric scattering can be distinguished:

- Rayleigh scattering occurs if the dimension of the constituent is small compared to the wavelength of the incident radiation (e.g., air molecules). The scattered light can be considered as emitted by an oscillating dipole, excited by the field of the incident

---

[1] The radiance $I(\bar{r},\bar{\Omega})$ at wavelength λ is defined as the incident radiant energy per time dW at the location $\bar{r}$ traversing an area element dS perpendicular to the propagation direction $\bar{\Omega}$ and in a solid angle dω: $I(\bar{r},\bar{\Omega})$=dW/dSdω.

[2] Vibrational and pure rotational transitions correspond to lower spectral energies in the infrared and microwave regions, respectively.

electromagnetic wave. The intensity of Rayleigh scattering is described by the Rayleigh scattering cross-section σ_R (expressed in [cm² molec^{-1}]) and the angular distribution of the scattered light by the dimensionless Rayleigh scattering phase function p_R.

The Rayleigh scattering cross-section (Rayleigh, 1899) is given by:

$$\sigma_R(\lambda) = \frac{8\pi^3}{3\lambda^4 N_{air}^2}(\mu^2 - 1)^2 D \tag{3.1}$$

where λ is the wavelength in cm, N_{air} is the air number density at standard conditions, μ is the refractive index of air and D is the depolarization factor which expresses the influence of molecular anisotropy ($D \approx 1.061$).

The Rayleigh scattering phase function is given by:

$$p_R(\Theta) = \frac{3}{4}(1 + \cos^2\Theta) \tag{3.2}$$

where Θ is the angle between incident and scattered radiation. According to this expression, the scattered light is distributed preferentially (and equally) into the forward and backward directions.

- Mie scattering occurs when the dimension of the particle is equal or greater than the wavelength of the incident light (e.g., aerosols and cloud droplets). In this case, the emission of a large number of excited dipoles and the resulting interference of the emitted radiation has to be considered. The determination of the Mie scattering cross-section and phase function can be very complicated. These parameters are calculated using numerical models that solve the Maxwell equations for given wavelength, refractive index, aerosol type, particle size and shape. The most noticeable difference compared to Rayleigh scattering is the much weaker wavelength dependence of the Mie scattering cross-section (typically proportional to $\lambda^{-1} \ldots \lambda^{-1.5}$) and a strong dominance of the forward direction in the scattered light. A widely used parameterization of the Mie scattering phase function p_M is the Henyey-Greenstein phase function:

$$p_M(\Theta) = \frac{1 - g^2}{(1 + g^2 - 2g\cos\Theta)^{3/2}} \tag{3.3}$$

where Θ is the angle between incident and scattered radiation and g is the asymmetry factor usually assumed to be in the range of 0.6 to 0.7.

3.2.3 Raman scattering

In addition to elastic Rayleigh and Mie scattering, inelastic Raman scattering on air molecules is also important in the atmosphere. Raman scattering occurs if the scattering particle changes its state of excitation during the scattering process. The term rotational

Raman scattering is used if only the rotational state is affected. Although less frequent, the vibrational state can also change. In this case, the term vibrational Raman scattering is used. Raman scattering moves the energy of the incoming photon to neighbouring energies and thus affects the spectral distribution of the scattered light.

Although Raman scattering constitutes only about 4% of all Rayleigh scattering, it is of importance for measurements of scattered sunlight as it is responsible for the “filling-in” of solar Fraunhofer lines. This effect is referred to as the Ring effect (Grainger and Ring, 1962; see section 3.3.2).

3.2.4 Interaction on the surface

At the lower boundary of the atmosphere, the Earth’s surface partially absorbs the down-welling radiation. The remaining radiation is reflected back into the atmosphere. Since many processes which depend on the surface type (water, vegetation, snow,..) and the physical conditions are involved, it is very difficult to model the reflection in details. Instead, the average properties are parameterized.

Generally speaking, the reflection is described for every direction $\overline{\Omega}$ by a bidirectional reflection distribution function (BRDF) $\rho(\overline{r},\overline{\Omega},\overline{\Omega}')$ depending on the location $\overline{r}$ on the surface and the direction of the incoming radiation $\overline{\Omega}'$. The BRDF also depends on the wavelength of the radiation.

In practice, a widely used approximation is to assume that the reflected light is redistributed isotropically (the so-called Lambertian surface reflection). It is possible to demonstrate that in this case, the reflection on a homogeneous surface is given by the simple formula:

$$\rho(\overline{r},\overline{\Omega},\overline{\Omega}') = A\frac{\cos\theta(\overline{\Omega}')}{\pi} \tag{3.4}$$

where $\theta(\overline{\Omega}')$ is the zenith angle of the incoming radiation and A is the surface albedo, i.e. the ratio of the fluxes[1] of reflected (up-welling) and incident (down-welling) radiation:

$$A = \frac{F^{\uparrow}}{F^{\downarrow}} \quad A \in [0,\ 1] \tag{3.5}$$

The albedo is generally dependent on the wavelength of the radiation. In the UV-visible wavelength range, the albedo of the Earth’s surface varies strongly with the surface type with the lowest values over oceans (A~0.05) and albedo up to 0.95 above fresh snow surfaces.

---

[1] The flux is defined as the surface integral over the half sphere: $F = \int_{2\pi} \overline{I}\overline{dS}$ where I is the radiance.

3.3 Differential Optical Absorption Spectroscopy

The Differential Optical Absorption Spectroscopy (DOAS) is a method developed in the 1970's (e.g., Noxon, 1975) to determine the chemical composition of gases from measurements of light in the UV, visible and near-infrared spectral ranges. The basic principle of the DOAS technique is to use multi-wavelengths light intensity measurement to retrieve the amount of atmospheric trace gases. Indeed, as many molecules are susceptible of absorbing light at a given wavelength (see Figure 3.3), it is generally impossible to discriminate the absorption of the different species from a monochromatic light intensity measurement.

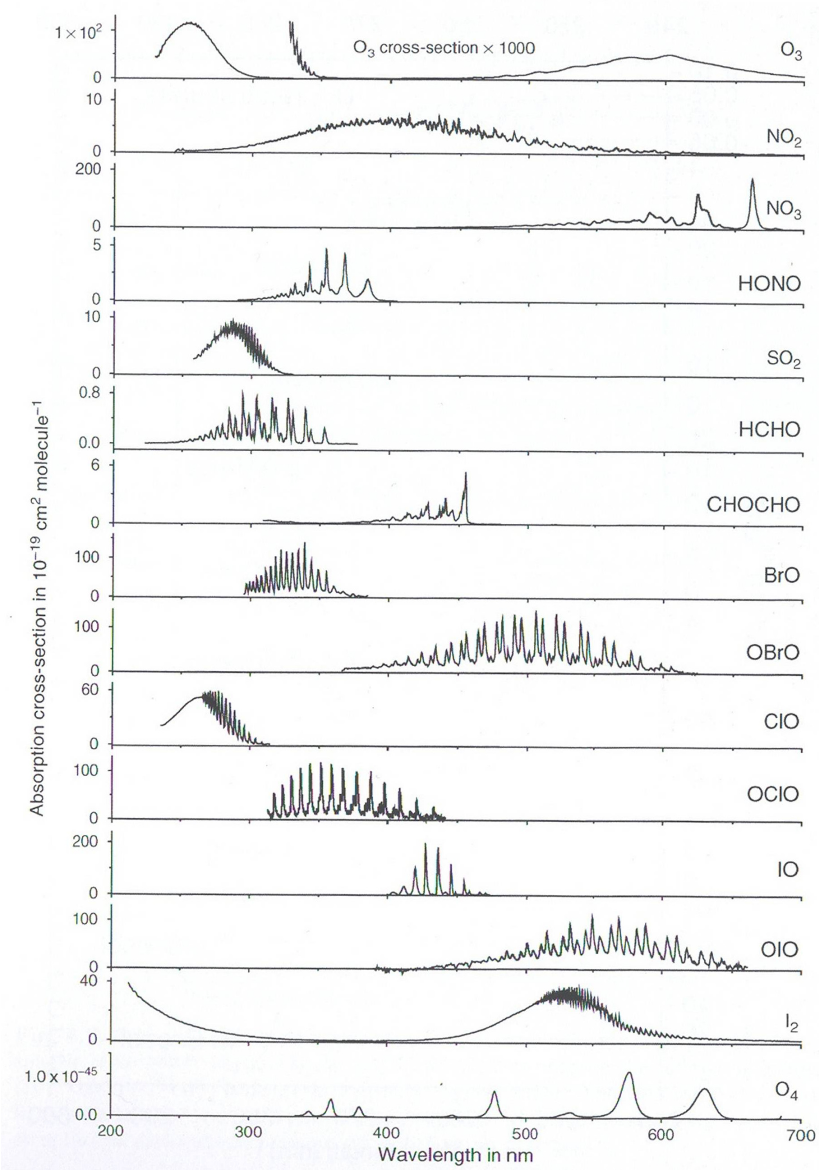

Figure 3.3 Absorption cross-sections of a number of species of atmospheric interest as a function of wavelength. Adapted from Platt and Stutz (2006).

However, it can be seen from Figure 3.3 that the absorption spectrum of each species exhibits a unique spectral structure that is a combination of electronic, vibrational and rotational transitions proper to the molecule. Hence if a continuous spectrum is measured in a selected interval, a separation of the absorptions is theoretically possible by using the characteristic structures of the absorption cross-sections. The reader is referred to the thorough work of Platt and Stutz (2006) for extensive details on the DOAS method.

3.3.1 DOAS principle

The basis of the DOAS method is the Beer-Lambert law that describes the reduction of the light intensity (or radiance) I by the amount dI, after traversing an atmospheric layer of thickness ds:

$$dI(\lambda) = -I(\lambda)k_e(\lambda)ds \tag{3.6}$$

where k_e is the extinction coefficient. In an absorbing and scattering atmosphere, the extinction has contributions from the loss by absorption (k_a) and scattering (k_s):

$$k_e(\lambda) = k_a(\lambda) + k_s(\lambda) \tag{3.7}$$

The absorption coefficient k_a is the sum of all absorbers i with absorption cross-section $\sigma_{a,i}$ and density n_i:

$$k_a(\lambda) = \sum_i \sigma_{a,i}(\lambda)\, n_i \tag{3.8}$$

Neglecting inelastic Raman scattering, the coefficient k_s includes Rayleigh scattering by molecules and Mie scattering by aerosols and cloud droplets:

$$k_s(\lambda) = \sigma_R(\lambda)n_R + k_M(\lambda) \tag{3.9}$$

σ_R being the Rayleigh scattering cross-section, n_R the air density and k_M the Mie extinction coefficient[1]. Integration of equation 3.6 for a finite light path L leads to the relationship between the incident light intensity I_o and the transmitted light intensity I:

$$I(\lambda) = I_o(\lambda)\exp(-\int_0^L [\sum_i \sigma_{a,i}(\lambda)\, n_i + \sigma_R(\lambda)n_R + k_M(\lambda)]ds) \tag{3.10}$$

It should be noted that the Beer-Lambert law as formulated in equation 3.10 is only an approximation of the propagation of radiation in the atmosphere. This is mainly due to the fact that scattered light can propagate along a large number of light paths in the

---

[1] As a mixture of different size aerosols is found in the atmosphere, the extinction coefficient is used instead of the scattering cross section. This extinction coefficient is defined as the integral over the particle size distribution times the Mie scattering cross section and the particle surface.

atmosphere, rather than a unique path as assumed here. We will see in section 3.4 that the radiative transfer equation leads to a more proper and comprehensive way of handling the transport of the radiation in the atmosphere.
An alternative of equation 3.10 is obtained by introducing the optical depth τ:

$$\tau(\lambda) = -\ln\left[\frac{I(\lambda)}{I_0(\lambda)}\right] = \sum_i \left(\int_0^L \sigma_{a,i}(\lambda)\ n_i ds\right) + \int_0^L \sigma_R(\lambda) n_R ds + \int_0^L k_M(\lambda) ds \tag{3.11}$$

This expression becomes:

$$\tau(\lambda) = \sum_i \left(\int_0^L \sigma_{a,i}(\lambda)\ n_i ds\right) + \tau_R(\lambda) + \tau_M(\lambda) \tag{3.12}$$

τ_R and τ_M being the Rayleigh and Mie scattering optical depths, respectively.

The DOAS technique applies the Beer-Lambert law to atmospheric measurements, where I_0 is the initial intensity of the light source and I the radiance measured by a telescope. The method considers a certain wavelength interval and relies on the assumption that one effective photon path can be defined, which represents on average over the wavelength interval the complex path of scattered photons in the atmosphere. This hypothesis is largely verified for optically thin absorbers. Assuming absorption cross-sections weakly dependent on the temperature and pressure along the effective light path, the optical depth τ can be expressed as:

$$\tau(\lambda) = \sum_i \sigma_{a,i}(\lambda) SCD_i + \tau_R(\lambda) + \tau_M(\lambda) \qquad SCD_i = \int_0^L n_i ds \tag{3.13}$$

where SCD_i is the so-called slant column density of the absorber i. The slant column density is the quantity obtained when performing a DOAS retrieval and represents the concentration of the absorber integrated along the effective light path. One of the shortcomings of the DOAS technique is the assumption that the absorption cross-sections are independent of temperature and pressure, which is usually not fulfilled. This aspect will be discussed in section 3.3.2.
The key principle of DOAS is that Rayleigh and Mie scattering vary weakly with wavelength (the scattering cross-sections have a λ^{-n} dependency, with n ranging between 1 and 4), while molecular absorption cross-sections usually consist of narrow absorption bands. Accordingly, each absorption cross-section can be split into a portion $\sigma_{a,i}^s$ which vary slowly with the wavelength and a portion $\sigma_{a,i}'$ which has narrow structures:

$$\sigma_{a,i}(\lambda) = \sigma_{a,i}^s(\lambda) + \sigma_{a,i}^{'}(\lambda) \tag{3.14}$$

Thus the optical depth can be rewritten:

$$\tau(\lambda) = \underbrace{\sum_i \sigma_{a,i}^{'}(\lambda) SCD_i}_{\tau^{'}(\lambda)} + \underbrace{\sum_i \sigma_{a,i}^{s}(\lambda) SCD_i + \tau_R(\lambda) + \tau_M(\lambda)}_{\tau^{s}(\lambda)} \tag{3.15}$$

where the first term describes the effect of the structured ‘differential’ absorption of trace gases, while the second term constitutes the slowly varying absorptions as well as the influence of scattering. This is illustrated in Figure 3.4.

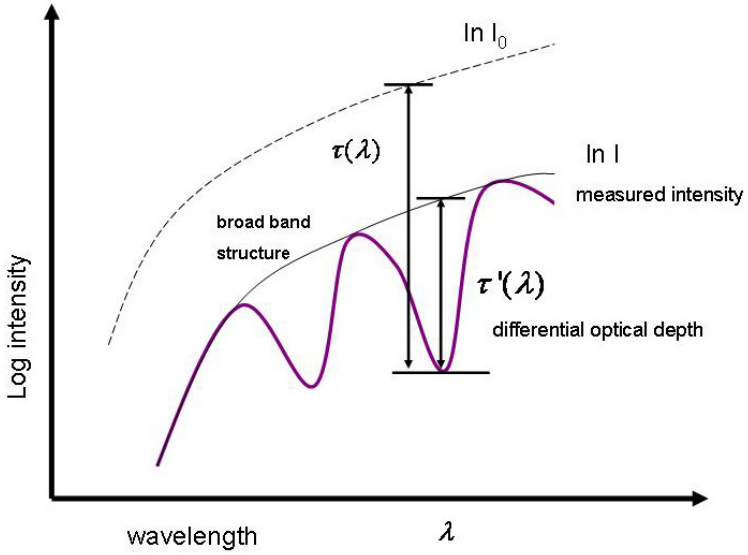

Figure 3.4 Sketch of the DOAS technique. Adapted from the thesis of J. Hollwedel.

The slant column densities SCD_i can be retrieved by adjusting the differential absorption cross-sections (determined from laboratory measurements) to the measured optical depth where the broadband features have been removed using a low-pass filtering method.

3.3.2 Particular aspects of the DOAS technique

The recording of a spectrum I_{meas} with a spectrograph consists in reality of a convolution of the incoming radiance with the instrument slit function S of the instrument:

$$I_{meas}(\lambda) = \int I(\lambda - \lambda')S(\lambda')d\lambda' \tag{3.16}$$

Moreover, the detector generally consists of a diode array. The covered wavelength range is thus mapped to n discrete pixels, each integrating the light in a wavelength interval

$$I_{meas}^{j} = \int_{\lambda_j}^{\lambda_{j+1}} I_{meas}(\lambda')d\lambda' \qquad j = 1,..,n \tag{3.17}$$

Similarly to equation 3.13 we can write:

$$\tau_{meas}^{j} = \sum_i \sigma_{a,i}^{j} SCD_i + \tau_R^j + \tau_M^j \qquad j = 1,..,n \tag{3.18}$$

The DOAS evaluation consists in practice, of the minimisation of a cost function:

$$\chi^2 = \sum_{j \in W_{\mathrm{int}}} (\tau_{meas}^{j} - \sum_{i} \sigma_{a,i}^{j} SCD_i - \sum_{k} a_k \lambda_j^k)^2 \tag{3.19}$$

where the summation is made for all wavelengths included in a chosen fitting wavelength interval W_{int}. The derived fitted parameters are the slant column densities of the absorbing species and the coefficients of a polynomial that is usually used to account for broad band features[1]. The minimization is usually achieved using a non-linear Levenberg-Marquardt fitting procedure (Levenberg, 1944; Marquardt, 1963).

Although simple and powerful in principle, the retrieval of SCDs by the DOAS method is complicated for various reasons. Above all, the absorptions to be measured are generally very small. Achieving good accuracy therefore requires great care in controlling the following aspects of the analysis and spectral data characterization:

Wavelength interval

In principle, each trace gas has an optimal wavelength interval. It is clear that spectral regions with higher differential absorption cross-sections show the largest optical depths and are thus preferred for DOAS measurements since the sensitivity improves in these wavelength regions. However, it should be noticed that, given the spectral resolution of the instrument used, several absorbers may exhibit similar absorbing structures. Under some circumstances, these correlations can lead to systematic biases in the retrieved SCDs. In general, the cross-sections correlations decrease with increasing fit range, but using a wavelength interval as large as possible does not insure to maximize the sensitivity to the target absorber. Moreover, the presence of strong ozone absorption bands constitutes an additional difficulty in an extended wavelength interval. In some conditions, the ozone absorption becomes so large that the assumption that one effective photon path can be defined over the entire wavelength interval may not be fully satisfied, leading to systematic misfit effects that may also introduce biases in the retrieved SCDs.

In summary, finding the optimal wavelength interval is usually determined empirically in an attempt to maximize the sensitivity to the trace gas and at the same time minimize interferences with other absorbers and undesired instrumental spectral effects.

Instrumentation

The idealized DOAS instrument would have (1) an excellent signal-to-noise ratio in order to measure with a low detection limit the weak absorption features usually displayed by atmospheric absorbers, (2) a wide spectral range to measure a large number of species, (3) a good spectral resolution and sampling to resolve the spectral structures to be observed and (4) a good stability. In practice, having all these qualities is generally not possible because the improvement of one of these instrumental characteristics comes usually at the expenses of another. The instrument is thus designed in a way that a

---

[1] As any broad band structure is accounted for by this polynomial, the absolute or differential quantities (optical depths and absorption cross-sections) can be used indifferently in a DOAS evaluation.

compromise between the different instrumental performances is obtained, that still meets the requirements of the specific application for which the instrument is dedicated.

Reference spectrum

The intensity spectrum Io (also called reference spectrum) is the intensity of the light source used in DOAS. It can be the spectrum of an artificial light source (active DOAS applications) or the spectrum from the sun[1] (passive DOAS) as it is the case here. In the case of satellite measurements, there exists the possibility to record an extraterrestrial spectrum of the solar radiation, which can then be used as reference spectrum. For ground-based observations, this is not possible and it is a common method to use a measured spectrum with small atmospheric absorptions as reference spectrum (self-calibration technique). The absorber amount in the reference spectrum is then determined by an extrapolation method (e.g., the Langley-plot analysis) and added to the results.

Absorption cross-sections

The fingerprint of the atmospheric absorbers is the fundamental information used to retrieve slant columns of trace gases. For this reason, high quality measurements of absorption cross-sections are needed. As the absorption cross-sections of the atmospheric species have to be convolved to the spectral resolution of the instrument, they have to be determined from laboratory measurements at a spectral resolution at least as good as the DOAS instrument resolution.

Furthermore, most absorption cross-sections in the UV-visible wavelength region show a pressure and temperature dependence. Indeed, the absorption lines broadened as pressure increases. With changing temperature, state populations change according to Boltzmann statistics and thereby the probability for some transitions change, which in turn has an impact on the observed absorption cross-sections. Because of these pressure and temperature dependencies, the assumption of constant cross-sections along the effective light path (section 3.3.1) is difficult to sustain for some DOAS applications. This can affect the retrieval of the slant columns and result in large residual structures, due to the change of the absolute value, and the variation of the shape of the absorption cross-sections. To overcome this problem, an approximate solution that gives satisfactory results in a large number of cases, is to use a small number of different cross sections for individual pressure and temperature conditions. Note that, from the two effects, the temperature dependence of the cross-sections generally has a larger impact on the results (in the UV-visible region). Therefore, an absorption cross-section is approached by a linear combination of cross-sections corresponding to different temperatures usually encountered in the atmosphere. In practice, this procedure is generally applied to strong absorbers (e.g., ozone) as it significantly decreases the residual of the DOAS fitting. For weak absorbers (e.g., BrO) the use of more than one absorption cross-section does not lead necessarily to better results[2]. Therefore, one cross-section is usually selected, at a temperature representative of atmospheric conditions. Note that it constitutes an error

---

[1] Some applications also use the moon or stars as a light source.

[2] Note that for some atmospheric species, the absorption cross-section varies only slightly with temperature.

source in the DOAS retrieval and limits the accuracy of the results (for example to ~10% for BrO).

Ring effect

The filling-in of solar Fraunhofer lines due to Raman scattering has an effect on observations using scattered sun-light that is the Fraunhofer lines do not cancel out when the radiance and the reference spectra are divided, leading to large spectral structures. To correct for the Ring effect, a pseudo absorption cross-section is generally included in the DOAS fit. This Ring cross-section is usually generated using radiative transfer model calculations.

Shift and Stretch

As part of the DOAS minimization procedure, several additional spectral parameters are adjusted to account for possible differences in the wavelength-pixel mapping of the reference spectrum and the absorption cross-sections compared to the measured spectrum. In practice, the reference spectrum and cross-sections can be wavelength shifted or stretched. In general, these corrections are required to compensate the misalignment of spectra as a result of different measurement conditions (e.g., temperature, pressure) and optical effects.

Other effects

A number of effects can affect the results of the DOAS analysis if they are not taken into account. They include the instrumental wavelength calibration, spectral stray light caused by reflections inside the spectrograph and other subtle instrumental-related effects (e.g., the 'undersampling effect', coming from the poor spectral sampling ratio of some instruments, and the 'solar I_0 effect', arising from the fact that the laboratory absorption cross-sections are generally measured using spectrally flat light source rather than the highly-structured solar spectrum). Note that there are also several instrumental effects that can result in spectral structures that can not be removed easily (e.g., spectral changes due to thermal instability or variation in the polarization response of the instrument).

3.3.3 Application: BrO retrieval

The bromine monoxide molecule shows a pronounced spectral structure in the UV region between 310 and 360 nm. This wavelength range contains the vibrational band structure assigned to the A $^2\Pi_{3/2} \leftarrow$ X $^2\Pi_{3/2}$ electronic transition. Due to the weakness of the atmospheric BrO absorption (typically of the order of 0.1% or less) and the presence of strong absorption bands from ozone below ~ 335 nm, not all BrO absorption bands are exploited to retrieve BrO slant columns. Usually, the DOAS technique takes benefit of four vibrational bands (4-0 at 354.9 nm, 5-0 at 348.9 nm, 6-0 at 344.0 nm and 7-0 at 338.6 nm). This is illustrated in Figure 3.5 that shows the absorption cross-section as a function of wavelength, at a resolution of 0.2 nm typical for the GOME satellite instrument (see chapter 4).

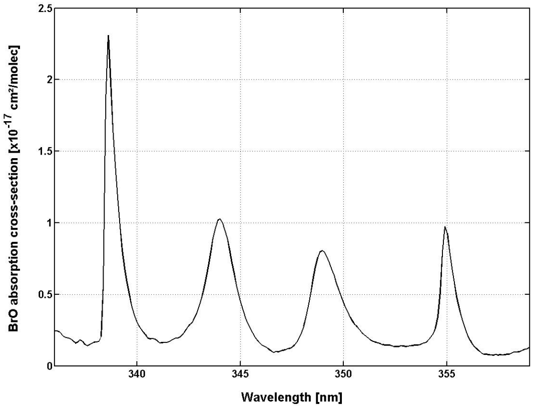

Figure 3.5 BrO absorption cross-section from Fleischmann et al. (2004) as a function of wavelength in the UV-visible region commonly used for DOAS BrO retrieval. The cross-section is measured at 223 K and is convolved at the resolution of the GOME satellite instrument.

In addition to the BrO absorption, several other atmospheric species have overlapping absorption spectral features in the spectral range shown in Figure 3.5. The DOAS fitting analysis usually includes cross-sections of O_3 (at two temperatures), NO_2, HCHO, O_4 (the collision induced oxygen dimer O_2-O_2), OClO and a calculated Ring spectrum.

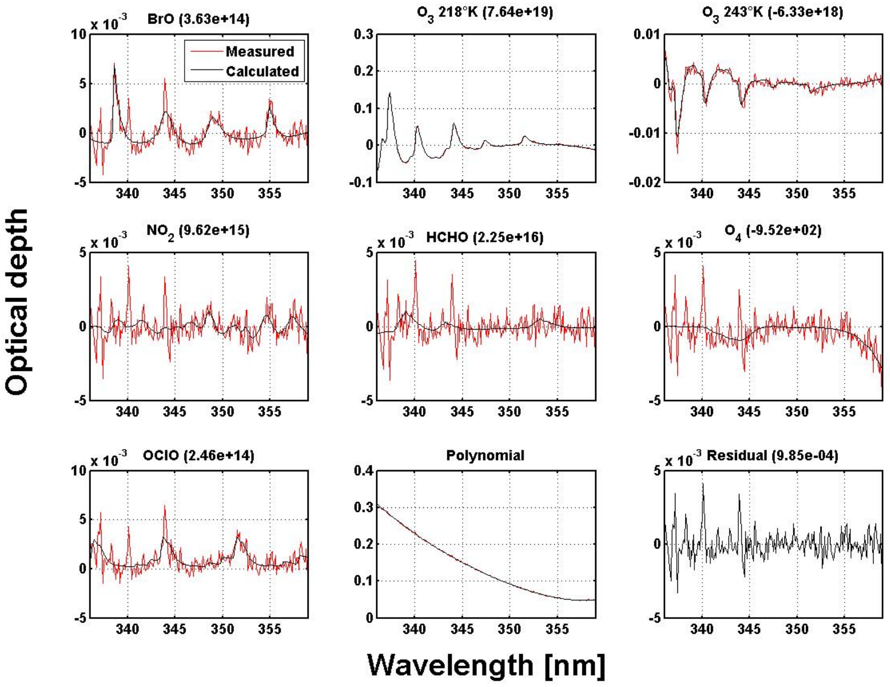

Figure 3.6 Example for the BrO DOAS evaluation of a GOME spectrum. Black lines are laboratory references and red lines are the fit results. The numbers correspond to the retrieved slant column densities.

Figure 3.6 shows an example of the BrO spectral fitting for a spectrum measured by the GOME instrument (orbit: 25560 – 10 March 2000, pixel number: 234, latitude: 79.82°N, longitude: 102.14°E). Here the wavelength interval (336-359 nm) includes four BrO absorption bands, and it can be seen that BrO could be detected unambiguously for this particular measurement.
The number of absorption bands selected to retrieve BrO slant columns depends on what instrument is used. In chapters 5 and 7, the BrO DOAS settings for the ground-based and satellite instruments used in this work will be given. As the author of this PhD thesis was not personally involved in establishing the optimal BrO DOAS settings for these instruments, no details will be provided on how they have been established.

3.4 Atmospheric radiative transfer

The basic quantity provided by the DOAS analysis is the slant column density, which is the concentration integrated along the mean optical light path. For scattered sunlight measurements, the interpretation of the DOAS results can be difficult, because the propagation of radiation (radiative transfer) in absorbing and scattering media, such as the atmosphere, is complex. This is due to the fact that scattered light can propagate in any direction and can undergo further scattering and absorption processes. In this section, we introduce the radiative transfer equation (RTE) that describes the radiation propagation and accounts for these aspects. We will also introduce the concept of air mass factor that is necessary to quantitatively analyze DOAS observations.

3.4.1 Radiative transfer equation

Before entering into the details, let us consider the atmosphere as a plane-parallel medium, with composition and optical properties homogeneous in the horizontal direction. We can define $I(z,\mu,\varphi)$ as the radiance at the altitude z in the direction ($\mu=\cos\theta$, φ), where θ is the zenith angle away from the vertical and φ the azimuth angle (see Figure 3.7).

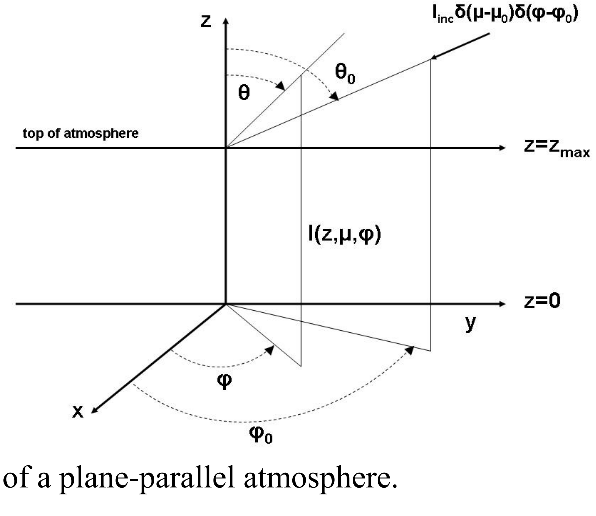

Figure 3.7 Geometry of a plane-parallel atmosphere.

We also introduce I_{inc} as the solar radiation incident at the top of the atmosphere with a solar zenith angle θ_0 ($\mu_0=\cos\theta_0$) and solar azimuth angle φ_0. The radiance and solar irradiance I_{inc} also depend on the wavelength λ of the radiation, but the wavelength index is skipped for better readability.

It is possible to show that the propagation of the radiation in a plane-parallel atmosphere is described by the following equation of radiative transfer (Chandrasekhar, 1950), which is an expression of the energy balance including absorption and scattering[1]:

$$\mu \frac{d}{dz} I(z,\mu,\varphi) = -(k_a(z)+k_s(z))I(z,\mu,\varphi) \tag{3.20a}$$

$$+\frac{k_s(z)}{4\pi} p(z,\mu,\varphi,\mu_0,\varphi_0) F_{sol} e^{-\tau(z)/\mu_0} \tag{3.20b}$$

$$+\frac{k_s(z)}{4\pi} \int_0^{2\pi} d\varphi' \int_{-1}^{1} d\mu' \, p(z,\mu,\varphi,\mu',\varphi') I(z,\mu',\varphi') \tag{3.20c}$$

$$+\frac{k_s(z)}{4\pi} F_{sol} e^{-\tau_0/\mu_0} \int_0^{2\pi} d\varphi' \int_{-1}^{1} d\mu' \, p(z,\mu,\varphi,\mu',\varphi') A e^{-(\tau_0-\tau(z))/\mu'} \tag{3.20d}$$

where k_a and k_s are the absorption and scattering extinction coefficients (eq. 3.8 and 3.9)

p is the scattering phase function[2]

F_{sol} is the incoming solar flux, $F_{sol}=\pi . I_{inc}$

A is the surface albedo

τ is the vertical optical depth: $\tau(z)=\int_z^{z_{\max}} k_e(z')dz'$, k_e being the extinction coefficient ($k_e = k_a + k_s$).

The radiative transfer equation (3.20) can be divided in four parts:

a) The loss by absorption and scattering of radiation crossing an atmospheric layer of the thickness $ds=dz/\mu$. This term is similar to equation 3.6.

b) The gain of radiation by single scattering of sunlight: the amount of solar radiation is first multiplied by a factor $e^{-\tau(z)/\mu 0}$ to account for its attenuation from the top of the atmosphere to the altitude z, then by the probability of scattering $k_s(z)p(z,\mu,\varphi,\mu_0,\varphi_0)/4\pi$ from the direction (μ_0,φ_0) to the direction (μ,φ).

c) The gain of radiation by multiple scattering: it is given by the amount of light coming from a given direction $I(z,\mu',\varphi')$ (already scattered at least once) multiplied by the scattering probability into the direction of interest $ks(z)p(z,\mu,\varphi,\mu',\varphi')/4\pi$ integrated over all possible directions.

d) The gain of radiation by scattering of direct sunlight reflected from the surface: the solar radiation propagates from the top of the atmosphere to the surface (attenuation by a factor $e^{-\tau 0/\mu 0}$, τo being the total vertical optical depth of the atmosphere), where a part of the light is reflected (multiplication by the surface

---

[1] In this expression, we have neglected any contribution from emission and Raman scattering.

[2] The scattering angle Θ and the zenith and azimuthal angles are related through the expression:
$\cos\Theta = \cos\theta\cos\theta_0 + \sin\theta\sin\theta_0\cos(\varphi-\varphi_0)$

albedo A) and redistributed isotropically. The amount of radiation gained is obtained by integrating over all directions (μ',φ') the radiation that propagates from the surface to the altitude z (attenuation by $e^{-(\tau 0-\tau(z))/\mu'}$ and that is scattered in the direction (μ,φ) (multiplication by $k_s(z)p(z,\mu,\varphi,\mu',\varphi')/4\pi$).

It should be noted that the assumption made here of a plane-parallel atmosphere looses its validity for solar zenith angles (SZA) greater than ~75° because it does not account for the curvature of the atmosphere. This is a severe limitation to the usefulness of plane-parallel radiative transfer models, particularly in applications using observations by satellite and ground-based instruments. Nevertheless, there are ways to treat the effects of the curved atmosphere. One possibility is to reformulate the RTE in spherical coordinates (Dahlback and Stamnes, 1991). However, solving the full-spherical radiative transfer equation (e.g., SCIATRAN model (Rozanov et al., 2005a)) is generally difficult and is computationally intensive. An alternate method is provided by the pseudo-spherical approximation (Anderson, 1983) which treats the direct light attenuation in a curved atmosphere, but leaves all scattering processes in the plane-parallel approximation. The RTE in the pseudo-spherical approximation is thus identical to the formulation of equation 3.20, except for the attenuation factors ($\exp[-\tau/\mu]$) that are replaced by the curvilign integral ($\exp[-\int_{s}^{s_{\max}} k_e(s')ds']$). The advantage of this approach is that it utilizes the speed and flexibility of the plane-parallel formalism and provides sufficiently accurate solution for solar zenith angles up to 90°.

The radiative transfer as formulated in equation 3.20 or in the pseudo-spherical approximation is a multi-dimensional integro-differential equation which depends on several atmospheric and optical variables. In general, solutions have to be calculated by numerical methods. They can be divided into two groups. First, numerical solutions for the resulting radiation field can be calculated using discretization methods. Second, the radiation field can be derived from Monte Carlo methods (e.g., TRACY model (von Friedeburg, 2003)), that simulate a large number of trajectories of photons through the atmosphere using probabilistic methods.

In this work, the model package used to solve the RTE is the UVspec/DISORT tool (Mayer and Kylling, 2005). UVspec is a user-friendly and flexible interface that enables to work for a variety of atmospheric conditions. It is constituted of a bunch of routines that uses a description of the atmosphere provided by the model user as follows:

- absorption cross-sections and concentration profiles of the atmospheric absorbers.
- air density, temperature and pressure profiles.
- wavelength.
- zenith angles (θ,θ0) and azimuth angles (φ,φ0).
- altitude z.
- solar spectrum and surface albedo.
- aerosol properties (extinction profile and scattering phase function).

UVspec converts these atmospheric parameters into optical properties required as input of the radiative transfer equation solver, and handles post-processing of the solver output. The RTE solver is DISORT (Stamnes et al., 1988), which is an advanced multiple scattering radiative transfer model that uses the pseudo-spherical approximation. A RT equation similar to the formulation given here is solved using the ‘Discrete Ordinate Method’. The azimuth dependence of the radiation field is expressed as a Fourier cosine series in azimuth. The solution of the Fourier components is obtained using a numerical quadrature scheme, allowing replacing the integrals by sums and thus reducing the RTE to the solution of a set of coupled linear first-order differential equations.

3.4.2 Air Mass Factor calculation

The determination of the abundance of an atmospheric species commonly involves a two-step procedure. First, the slant column density is retrieved by analyzing the observed spectrum with the DOAS technique, as presented in section 3.3. Second, the slant column density is converted into a more physical variable, namely the vertical column density (VCD) that is the vertically integrated trace gas concentration. This conversion is usually performed using the so-called air mass factor (AMF):

$$AMF = \frac{SCD}{VCD} \tag{3.21}$$

The use of the air mass factor concept for atmospheric observations implies that the AMF contains all information about the viewing geometry of a specific measurement and the actual atmospheric conditions. Hence the determination of an air mass factor requires accounting for any atmospheric parameter influencing the photons path: solar zenith angle, instrument viewing angles, surface altitude, surface albedo, atmospheric absorption, scattering on molecules, aerosols and clouds. The basic idea is that if the parameters influencing the sensitivity of the measurement are known, the measured slant column and the vertical column are proportional. However, it should be noted that an important limitation of the AMF approach lies in the fact that for most applications, some of these parameters are to a large extend unknown or known at inappropriate spatial and temporal resolution. Moreover, the AMF depends on the vertical distribution of the atmospheric absorbers. These concentration profiles have thus, to be known a priori.

Once all the parameters influencing the measurement are set the air mass factor is calculated using a radiative transfer model. Usually, this is done by performing two simulations, one with and one without the absorber of interest. The AMF is thus given by:

$$AMF = -\frac{\ln[I^{w} / I^{wo}]}{\sigma_a \ . VCD} \tag{3.22}$$

where I^w denotes the simulated radiance with the absorber and I^{wo} without the absorber, σ_a and VCD are the absorption cross-section and vertical column of the trace gas.

This way of calculating air mass factors is easy and fast, but its use for DOAS applications requires carefulness. In general, the air mass factor depends on the wavelength as scattering and absorption processes vary with wavelength. Thus, for certain situations, the change in AMF within the DOAS wavelength interval can be important, so that applying equation 3.22 might not be straightforward.

An illustration of the AMF wavelength dependence for BrO is shown in Figure 3.8 in the UV-visible region useful for the BrO DOAS retrieval. One can observe the presence of peaks that are due to ozone absorption bands below 345 nm. However, it can be seen that, for this particular measurement condition, the AMF varies only slightly over the wavelength interval given here (differences smaller than 1%).

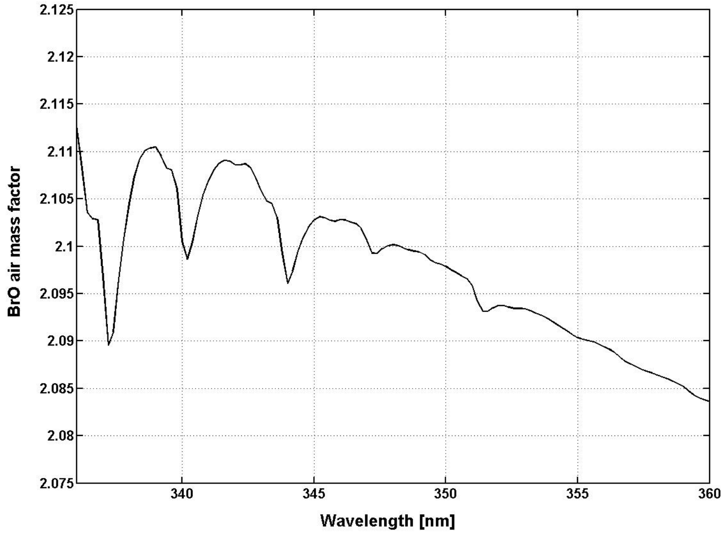

Figure 3.8 BrO air mass factor as a function of wavelength in the region commonly used for DOAS BrO retrieval. The calculations are made with the UVspec model for an instrument at the ground measuring in zenith-sky geometry (θ=0) for a SZA of 60°. The BrO and O_3 profiles used are typical mid-latitude stratospheric profiles (O_3 column: 450 DU).

Accordingly, a single air mass factor can be defined that is representative for the entire wavelength interval. In practice, it is customary to choose the midpoint wavelength of the DOAS fitting window used. It should be noted that as the solar zenith angles increases, the AMF wavelength dependence becomes more important because of the strong ozone absorption. For example, the error on the BrO AMFs over the wavelength interval of Figure 3.8 is of about 2% and up to 10%, for SZA of 80° and 90°, respectively. Another important issue for high sun condition is related to the wavelength dependence of the ozone AMFs. Indeed, at large SZA, the ozone absorption becomes so large that the fundamental DOAS hypothesis of a unique effective photon path representative for the entire fitting interval (optically thin approximation) is not fully satisfied. This can lead to systematic structures in the measured spectra that are affecting dramatically the retrieval of weak absorbers (e.g., BrO).

In summary, for optically thin absorbers, a single air mass factor can be applied to the measured SCD and is calculated using equation 3.22. For these conditions, it is possible to prove that the AMF can also be written as follows (Palmer et al., 2001):

$$AMF = \frac{\int w(z) n(z) dz}{\int n(z) dz} \tag{3.23}$$

In this expression, n(z) is the concentration profile of the atmospheric species of interest and w(z) is the so-called weighting function that contains all the dependences to all the parameters influencing the AMF, except the atmospheric profile n(z). The weighting function represents the sensitivity of the measurement at a certain altitude and can be interpreted as a height-resolved air mass factor. One can notice that the AMF calculated by equation 3.23 does not depend on any normalization factor applied to the profile n(z). The AMF only depends on the shape of the profile. A major advantage of the expression 3.23 is to decouple the contributions from the radiative transfer model and from the profile, thus allowing flexibility in the AMF calculation. Values of w(z) can be readily tabulated and then used in combination with a vertical shape profile, that usually comes from an atmospheric chemistry model, for fast calculation of the AMF.

Examples of BrO weighting functions are given in Figure 3.9 for a ground-based zenith sky viewing instrument, at different solar zenith angles.

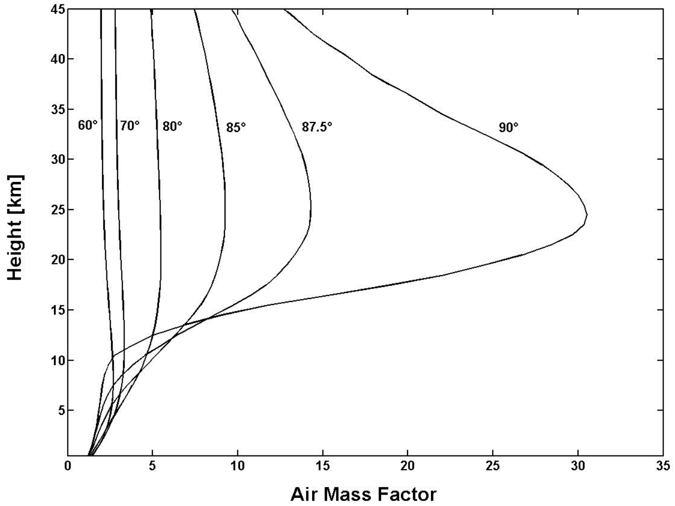

Figure 3.9 BrO air mass factors as a function of altitude (weighting functions) for different solar zenith angles. The calculation is made at 352 nm, for a ground-based instrument in the zenith-sky viewing geometry.

It can be seen that the weighting functions strongly increase in the stratosphere with the solar zenith angle. This is due to the enhancement of the light path in the stratosphere as the SZA becomes larger. In contrast, the weighting functions in the troposphere are only weakly dependent on the solar zenith angle. This is because at large SZA most of the scattering takes place in the stratosphere and the underlying tropospheric levels are traversed almost vertically (w~1).

We will present in chapters 5 and 7 more details on the weighting functions for ground-based and satellite BrO observations, particularly regarding their dependences with solar zenith angles, viewing angles, clouds, surface altitude, surface albedo and the resulting implications for the interpretation of the DOAS results.

Chapter 4

Instruments

This chapter presents the remote-sensing techniques employed in this work to retrieve atmospheric BrO. The ground-based and satellite instruments used are described together with their viewing geometries. All these instruments have in common that they measure UV-visible light scattered by the Earth's atmosphere or reflected by the surface, which is then analyzed by means of the DOAS method.

4.1 Ground-based measurements

The UV-visible DOAS group of the Belgian Institute of Spatial Aeronomy (BIRA-IASB) has an important part of its activities dedicated to ground-based atmospheric research and therefore operates an ensemble of instruments deployed throughout the world (details can be found at http://uv-vis.aeronomie.be/groundbased/). The aim of this research is threefold: (1) the long-term monitoring of stratospheric ozone and minor components involved in the ozone destruction (NO_2, BrO, OClO), (2) the study of anthropogenic pollution by measurements of aerosols, tropospheric pollutants and ozone precursors (like NO_2, SO_2, HCHO and CHOCHO), (3) the use of ground-based data for satellite validation.

The ground-based BrO observations used in this work have been conducted by BIRA-IASB at three stations part of the Network for the Detection of Atmospheric Composition Change (NDACC, http://www.ndacc.org): Harestua – Norway (60.22°N, 10.75°E), Observatoire de Haute-Provence - France (OHP, 43.94°N, 5.71°E) and Reunion Island – France (21.06°S, 55.47°E). The location of the stations is displayed in Figure 4.1.

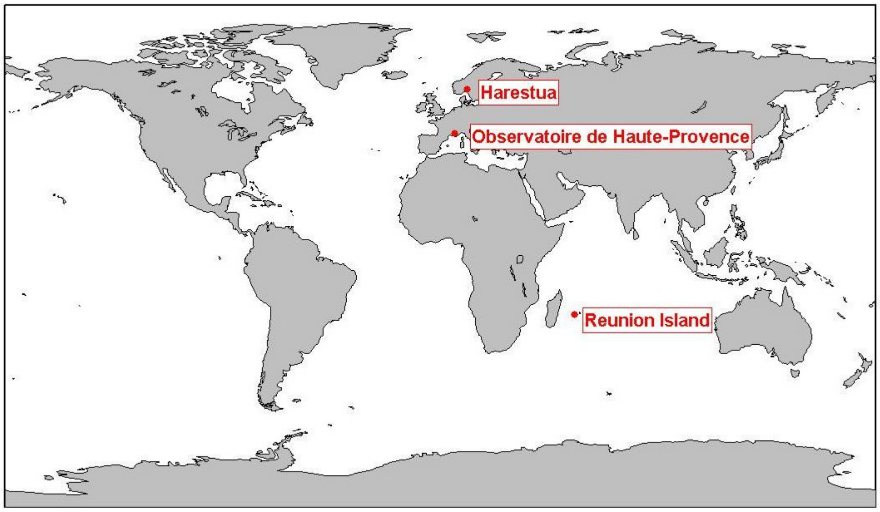

Figure 4.1 Geographical location of the stations of Harestua, Obsevatoire de Haute-Provence and Reunion Island.

The distribution of the stations samples latitudes from polar to tropical regions. This is particularly useful (e.g. for validation purposes) as a broad range of atmospheric situations and measurement conditions are covered.

4.1.1 Instruments

The instruments (see Figure 4.2) have been designed and assembled at BIRA-IASB. They all consist of at least one grating spectrometer installed in a temperature regulated box and connected through a fiber optic bundle to an entrance telescope.

Figure 4.2 Photographs of the instruments at Harestua, Obsevatoire de Haute-Provence and Reunion Island.

The telescope is itself connected to a rotating mirror allowing measurements for different viewing elevation angles (see section 4.1.2). The control of the acquisition cycle including the positioning of the pointing mirror, the optimization of the exposure time to ensure adequate photon filling of the CCD (charge-couple device) detector and the spectral acquisition is fully automated.
Table 4.1 summarizes some of the technical characteristics of the instruments used.

Table 4.1 Overview of the main instrumental characteristics.

	Harestua	**OHP**	**Reunion Island**
Spectrometer	Oriel Multispec 77400 (UV[a]) focal length: 120 mm	Jobin-Yvon Triax 180 focal length: 190 nm	ARC SpectraPro 275 focal length: 275 nm
Detector	diode array (1024 pixels) Hamamatsu from Princeton Instruments, cooled at -40 C	diode array (1024 pixels) Hamamatsu from Princeton Instruments, cooled at -40 C	1300x400 CCD detector from Princeton Instruments, cooled at -40 C
Grating	2400 grooves/mm	1800 grooves/mm	600 grooves/mm
Resolution[b]	0.6 nm FWHM, sampling of about 9 pixels/FWHM	0.7 nm FWHM, sampling of about 10 pixels/FWHM	0.75 nm FWHM, sampling of about 7 pixels/FWHM
Wavelength Range	323-390 nm	330-390 nm	300-450 nm
Observation period	Continuously since 1998	Continuously since 2005	August 2004 -June 2005
Azimuth direction	-	follows the solar azimuth every 4 days, otherwise the instruments points at -22° (SSE)	North (sea direction)
Viewing geometry	Zenith-sky	Zenith-sky+3,6,10,18° elevations angles: from 2005 to June 2007[c]	Zenith-sky+3,6,10,18° elevations angles
Twilight viewing mode (SZA>85°)	-	The instruments switch to a dedicated stratospheric mode where only zenith-sky measurements are taken.	
Sequence time	Continuously	~ 15 minutes: from 2005 to June 2007[c]	~ 15 minutes

[a] Another spectrometer records radiances in the visible region as well, but is not used in this work.

[b] FWHM: full width at half maximum

[c] Since June 2007, the measurements are made in zenith-sky+3,4,5,6,8,10,12,14,16,20,25,30° elevations angles in about 30 minutes. However, these data will not be exploited in this work.

4.1.2 Viewing geometries

At Harestua, the spectroscopic observations are made in the zenith-sky viewing geometry (see Figure 4.3). The intensity measured by the instrument consists of light that has traversed a number of atmospheric layers before being scattered in the zenith direction and recorded by the detector. The scattering altitude is determined by the SZA, the density of air, aerosols and the wavelength. Above this altitude (mostly in the stratosphere), the absorption path follows basically the geometrical light path. Below this altitude the light traverses a vertical path into the detector[1].

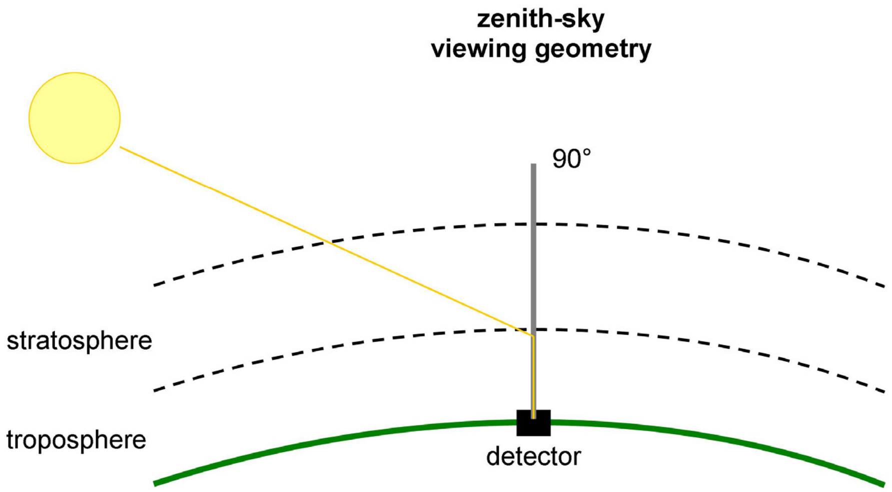

Figure 4.3 Sketch of a zenith-sky viewing measurement (only the mean effective light path has been drawn).

At twilight, the measurement sensitivity in the stratosphere is high as a result of the long light path. Therefore zenith-sky observations are adequate to measure stratospheric constituents. However, for all conditions, there exists a significant although weaker sensitivity of the zenith-sky measurements to the troposphere. Thus, it is in principle also possible to measure tropospheric constituents.

An interesting aspect of the ground-based zenith-sky measurements is their ability to provide information on the vertical distribution of atmospheric species by making use of the diurnal variation of the measured slant columns (e.g. Hendrick et al., 2007). Basically, the mean scattering altitude increases with increasing SZA, and scans the atmosphere (mostly the upper troposphere and the stratosphere), yielding height-resolved information on the absorption by the trace gases of interest. Thus, combining the slant columns measured from noon to twilight and the corresponding measurement vertical sensitivity functions (weighting functions; see e.g. Figure 3.9), it is possible to derive concentration profiles (though with low vertical resolution). It should be noted that many atmospheric species (such as BrO) exhibit a strong diurnal variation, making interpretation difficult. Therefore profiling techniques are usually combined with photochemical model results to account for these diurnal changes.

At OHP and Reunion-Island, the measurements are performed in the multi-axis viewing geometry (see Figure 4.4). For this viewing mode, the classical zenith-sky observation is complemented by 'off-axis' measurements, i.e. the telescope is pointing to the horizon instead of the zenith. The off-axis viewing elevation angles for both instruments are of 3°, 6°, 10° and 18°.

---

[1] However, an enhancement of the light path is often observed, due to multiple scattering in the zenith direction.

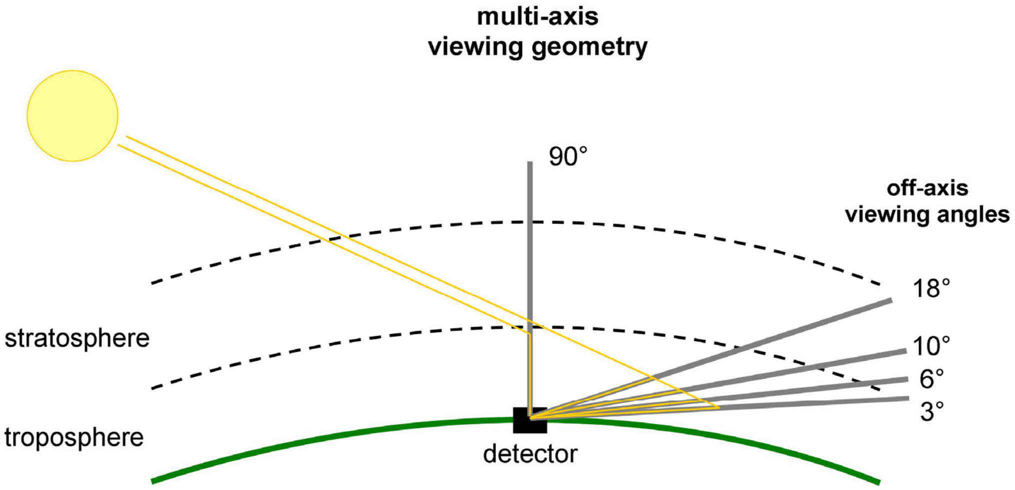

Figure 4.4 Sketch of a multi-axis viewing measurement cycle (only the mean effective light paths have been drawn).

As the light path through the troposphere increases with low elevation angles, off-axis measurements are very sensitive to tropospheric trace gas absorption. On the other hand, the light path through the stratosphere is in good approximation independent of the instrument pointing. Thus, combining in a retrieval scheme measurements acquired in different viewing elevations (from the horizon to the zenith), enables to determine independent amount of trace gas in both the stratosphere and troposphere, making the multi-axis DOAS technique (MAX-DOAS; see e.g. Hönninger et al., 2004) particularly powerful. Nevertheless, an important limitation resides in the fact that the length of the light path of the off-axis observations is very sensitive to aerosols, clouds or any item that alters the measured light intensity. Hence the retrieval of vertical profiles or columns generally requires accurate and extensive radiative transfer model calculations.

4.2 Satellite measurements

The space-based sensors used in this work are onboard three platforms (see Figure 4.5) part of the space missions for the observation of the Earth of the European Space Agency (ESA, http://www.esa.int): ERS-2 (Second European Remote Sensing satellite), ENVISAT (Environmental Satellite) and MetOp-A (Meteorological Operational satellite -A[1]).

Figure 4.5 Artistic view of the European satellites ERS-2, ENVISAT and MetOp-A. Courtesy of ESA and EUMETSAT.

Each satellite flies at about 800 km height in a near-polar sun-synchronous orbit. It means that it crosses the equator line always at the same local time, and each orbit takes approximately 100 minutes (~ 14 orbits/day).

4.2.1 Instruments

GOME

The Global Ozone Monitoring Experiment (GOME) instrument was launched on board the ERS-2 satellite in April 1995. The main objective of GOME is the global measurement of vertical columns of O_3. However, ozone profiles and vertical columns of

---

[1] MetOp-A is the first in a series of three operational satellites meant to monitor the Earth's atmosphere. MetOp-B and -C are scheduled to be launched in 2010 and 2015, respectively.

other trace gases such as NO_2, SO_2, H_2O, HCHO, OClO and BrO can be retrieved from the spectra as well. Other products include cloud parameter information and absorbing aerosol index.

GOME is observing the atmosphere with four spectral channels that comprise the wavelength intervals 240-295 nm, 290-405 nm, 400-605 nm and 590-790 nm, with a moderate spectral resolution of 0.2 to 0.4 nm. The GOME instrument is a double monochromator which combines a predisperser prism, a channel-separator prism and in each of the four optical channels a holographic grating as dispersing elements. A schematic diagram of the GOME optical layout is shown in Figure 4.6. The spectra are sampled with four linear Reticon silicon-diode arrays with 1024 spectral pixels each. In order to reduce the dark current, the detectors are cooled to about -40 C using Peltier elements.

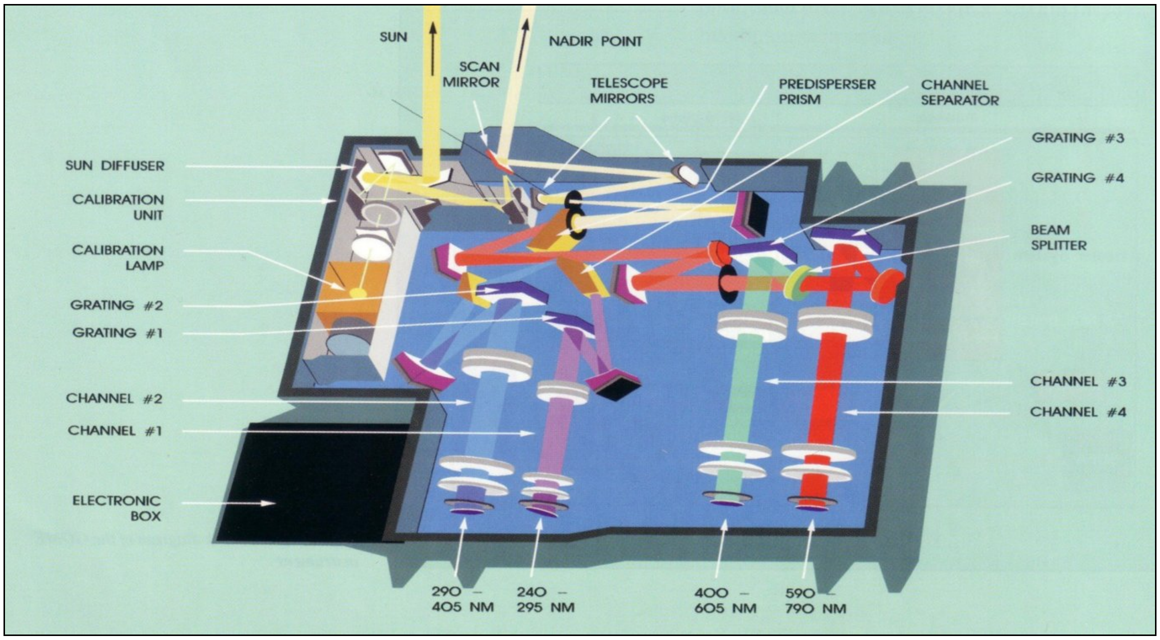

Figure 4.6 Instrumental set-up of GOME. Courtesy of ESA.

Except for the scan mirror, all parts of the instrumental set-up are fixed. The light which reaches the predisperser prism is split into two branches. The first one (not shown in Figure 4.6) is recorded with three broadband Polarization Measurement Devices (PMDs). PMDs are measuring light in a direction parallel to the slit. The PMDs main purpose is to generate a polarization correction for the measured spectra, but they are also used for cloud detection. The second, moderately wavelength dispersed beam is focused by a parabolic mirror into the channel separation prism. GOME has also a Pt-Ne-Cr lamp for in-flight wavelength calibration and a diffuser plate in order to perform a direct solar irradiance measurement (once per day). More details on the GOME instrument are given by Burrows et al. (1999).

SCIAMACHY

The SCanning Imaging Absorption spectroMeter for Atmospheric CartograpHY (SCIAMACHY) instrument is in operation on the ENVISAT platform since July 2002 (Bovensmann et al., 1999). The measurements of light are performed in eight spectral channels covering the 240-2400 nm wavelength range with a spectral resolution of 0.2 to 1.5 nm. In addition to the trace gases already measured by GOME, the SCIAMACHY instrument is also able to monitor the abundances of other species such as CH_4, CO, CO_2 and N_2O, owing to its infrared spectral channels.

The optical layout of the SCIAMACHY instrument is similar in concept to the GOME instrumental set-up, involving a separation of the light into the wavelength intervals of the height different channels (instead of four for GOME) by a series of prisms, beam splitters, gratings and lenses. The main difference between both instruments lies in the fact that SCIAMACHY has been equipped with two scan mirrors in the light path: one at the front of the elevation scanner module (ESM) and one at the front of the azimuth scanner module (ASM). This is justified by the more sophisticated viewing geometries (see section 4.2.2) of SCIAMACHY, that alternates measurements in a nadir mode (using the ESM mirror only) and in limb mode (using both ESM and ASM mirrors).

GOME-2

The GOME-2 instrument was launched on board the MetOp-A satellite in October 2006. It performs spectral measurements in the 240-790 nm wavelength interval with a spectral resolution of 0.25 to 0.5 nm. Beyond various technical improvements, the optical design of the GOME-2 instrument is very similar to its predecessor GOME. More details on the GOME-2 instrument can be found in Munro et al. (2006).

4.2.2 Viewing geometries, spatial resolution and coverage

Nadir viewing geometry

The GOME, SCIAMACHY and GOME-2 instruments perform measurements in nadir geometry (see Figure 4.7). In nadir mode, the sounder observes the light reflected by the ground and scattered from the air masses beneath the spacecraft. To this aim, the instrument scans the atmosphere back and forth across the satellite track, thanks to its rotating scan mirror. The edge of the swath width has a line-of-sight (LOS) varying from 0° to a maximum of about 31° for GOME and SCIAMACHY and 57° for GOME-2. It corresponds to a across track full swath width on the ground of 960 km for GOME and SCIAMACHY and of 1920 km for GOME-2.

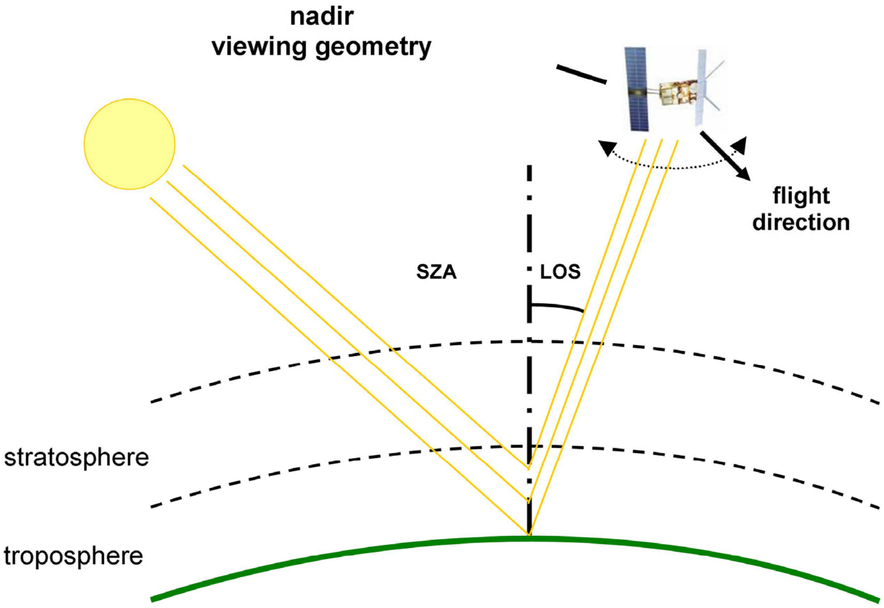

Figure 4.7 Sketch of a nadir-viewing satellite measurement (the optical paths have been drawn with an offset for clarity only).

One complete nadir scan cycle consists of a series of forward scans from east to west, followed by one or more back scans. In the nominal mode of observation in the BrO retrieval wavelength region, the full swath width is divided into 3, 16 and 24 forward ground pixels for GOME, SCIAMACHY and GOME-2, respectively. The individual spatial resolution in the direction across track is determined by the scan speed and the integration time, and is of about 320 km, 60 km and 80 km for the three respective instruments. The ground pixel dimension parallel to the flight direction is of 30 km (SCIAMACHY) to 40 km (GOME and GOME-2), depending on the instrumental field of view along track. The area sounded on ground is thus equal to 320 x 40 km², 60 x 30 km² and 80 x 40 km² respectively for the GOME, SCIAMACHY and GOME-2 instruments[1]. It should be noted that integration times are longer in the polar region close to the terminator (beyond 85° of SZA), to compensate for lower light intensities. This results in larger ground pixels for these conditions.

For each satellite instrument, the nadir observations are made during the illuminated part of the orbit, which starts close to the North Pole and ends nearby the South Pole. The mean local equator crossing time is in the morning (GOME: 10:30, SCIAMACHY: 10:00 and GOME-2: 09:30). Figure 4.8 shows the orbit tracks for one day of measurements with the GOME, SCIAMACHY and GOME-2 instruments.

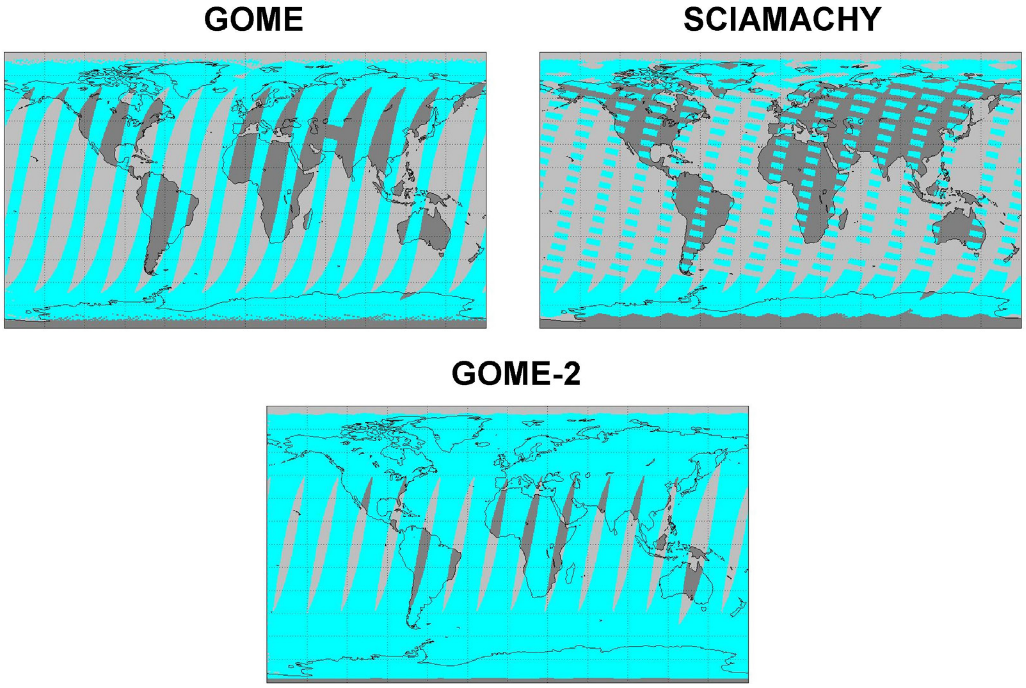

Figure 4.8 Illustration of the spatial coverage achieved in one day with the GOME, SCIAMACHY and GOME-2 satellite instruments (in nadir viewing mode). The gaps in the SCIAMACHY orbits are due to the alternance of nadir and limb viewing measurements.

Using the maximum scan width, GOME, SCIAMACHY and GOME-2 achieve global coverage at the equator[2] within 3 days, 6 days and 1.5 days respectively. The relatively long time required by SCIAMACHY to obtain global coverage is a result of the alternate nadir limb viewing (see below).

A summary of the observational features of the GOME, SCIAMACHY and GOME-2 satellite instruments in nadir viewing mode, is given in Table 4.2.

---

[1] The ground spatial resolution of SCIAMACHY and GOME-2 is higher than in the case of GOME but with an equivalently lower signal to noise ratio due to the shorter integration time.

[2] Global coverage is even achieved in one day at higher latitudes (poleward of ± 67.5°, 45° for GOME and GOME-2 respectively).

Table 4.2 Main viewing properties of the GOME, SCIAMACHY and GOME-2 satellite instruments in nadir viewing mode.

	GOME	**SCIAMACHY**	**GOME-2**
Nominal scan angle	±31°	±31°	±57°
Across track swath width	960 km	960 km	1920 km
Instantaneous field of view (across track x along track)	0.14° x 2.9°	0.045° x 1.8°	0.286° x 2.75°
Integration time	1.5 s	0.5 s	0.1875 s
Spatial resolution (outside the polar region)	320 km x 40 km	60 km x 30 km	80 km x 40 km
Global coverage at the equator	3 days[a]	6 days	1.5 days
Equator crossing local time	10:30	10:00	09:30

[a] GOME has been operational since July 1995, but spatial coverage has been limited to parts of the Northern hemisphere and Antarctica since July 2003 due to problems with tape storage on ERS-2.

Limb viewing geometry

In addition to the nadir measurements, SCIAMACHY has the capability to scan the atmosphere in limb viewing geometry[1]. In the limb mode, the spectrometer slit is projected parallel to the horizon in flight direction (see Figure 4.9). The ASM mirror scans the atmosphere through different tangent heights from 0 to 100 km in horizontal direction; whereas, appropriate movement of the ESM mirror results in a vertical (elevation) scan direction. A typical limb scan cycle comprises 34 horizontal scans at different tangent heights, starting 3 km below the horizon. The individual spatial resolution is typically 240 km within a 960 km swath width in the horizontal direction across track.

The limb observations are particularly interesting scientifically speaking, as they provide vertical profiles of trace gases concentration. In contrast, only integrated column amounts can be retrieved from nadir measurements. However, one of the main issues for these limb observations is the accuracy with which the tangent heights can be reconstructed. The knowledge of orientation and position of the spacecraft is particularly strict for limb-viewing instruments, because of the large distance between the satellite and the sampled air mass.

---

[1] SCIAMACHY also performs solar and lunar occultation measurements. This type of observation will not be presented and developed here, since these measurements are not used in this work.

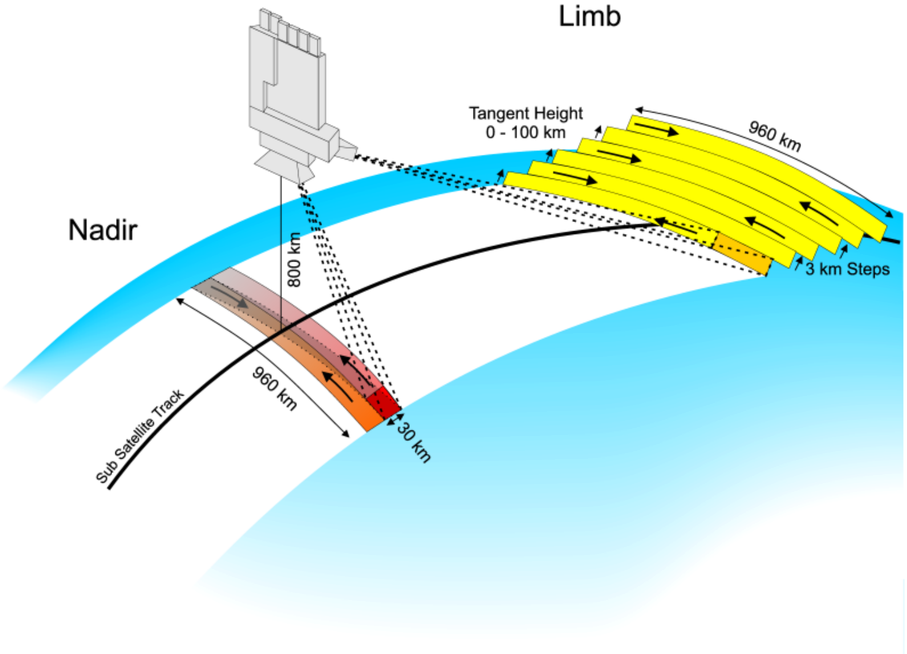

Figure 4.9 Illustration of the alternance of nadir and limb viewing measurements for the SCIAMACHY instrument. Courtesy of ESA.

Limb viewing observations are mostly exploited for the stratosphere. Low tangent height measurements are indeed very difficult to use, as they are generally contaminated by the presence of clouds.

An interesting feature in the design of the SCIAMACHY instrument is the so-called limb-nadir-matching: about 7 minutes after a measurement in the limb mode has been carried out, the same atmospheric air mass is measured in the nadir mode. In principle, it permits to separate the tropospheric trace gas amount from the total column for a given atmospheric trace gas.

Chapter 5

Ground-based multi-axis DOAS BrO observations at Reunion-Island[1]

Abstract

Spectral measurements of BrO using zenith-sky and off-axis viewing geometries are combined in a linear multiple regression retrieval algorithm to provide stratospheric and tropospheric BrO vertical columns. One year of measurement data are investigated over Reunion-Island, from August 2004 to June 2005. A comparison between the stratospheric columns retrieved at 45°, 80°, 85°, 87.5° and 92.5° solar zenith angles and photochemical simulations initialized by chemical fields from the 3D-CTM SLIMCAT and further constrained by observed NO_2 profiles shows a good agreement only by considering a contribution from the very short-lived organic bromine substances to the stratospheric inorganic bromine budget, of 6 to 8 pptv. Furthermore, stratospheric BrO profiles retrieved from late twilight zenith-sky observations are consistent with a total inorganic bromine loading of approximately 23 pptv. This represents 6 to 7 pptv more than can be supplied by long-lived organic bromine sources, and therefore supports an added contribution from very short-lived organic bromine substances as recently suggested in several other studies. Moreover strong evidences are presented for the existence of a substantial amount of BrO in the tropical free-troposphere, around 6 km altitude, possibly supplied by the decomposition of short-lived biogenic bromine organic compounds. Tropospheric BrO vertical columns of $1.1 \pm 0.45 \times 10^{13}$ molec/cm^2 are derived for the entire observation period. Comparisons between ground-based BrO vertical columns and total BrO columns derived from SCIAMACHY (onboard the ENVISAT satellite) nadir observations in a latitudinal band centered around 21°S present a good level of consistency, which further strengthens the conclusions of our study.

5.1 Introduction

In this chapter, we present an original retrieval method enabling the simultaneous determination of both tropospheric and stratospheric BrO vertical columns, based on multi-axis UV-visible DOAS observations. By combining in a retrieval scheme measurements of the scattered sky light acquired from noon to twilight in different

---

[1] This chapter is based on : Theys, N., Van Roozendael, M., Hendrick, F., Fayt, C., Hermans, C., Baray, J.-L., Goutail, F., Pommereau, J.-P., and De Mazière, M., *Retrieval of stratospheric and tropospheric BrO columns from multi-axis DOAS measurements at Reunion Island (21°S, 56°E)*, Atmos. Chem. Phys., 7, 4733-4749, 2007.

viewing elevations (from the horizon to the zenith) and making use of the change in sensitivities associated to the different observations geometries, the vertical distribution of the BrO concentration can be inferred. The analysis explicitly takes into account the effect of the BrO photochemical variations, in particular for the simulation of the radiative transfer at twilight when photochemical gradients along the slant stratospheric photon path are important. The retrieval algorithm has been applied to observations performed from August 2004 to June 2005 at Saint-Denis, La Reunion (21.06°S, 55.47°E, Indian Ocean), a latitude where currently available BrO observations are very sparse. It has been recently argued that biogenic short-lived organic compounds (e.g. $CHBr_3$) that are mainly released by oceans could be rapidly transported in the upper troposphere/lower stratosphere region under the action of the strong tropical convection. This highlights the importance of tropics in determining the atmospheric bromine budget as pointed out by several authors (Salawitch 2006; Carpenter et al., 2000; Yang et al., 2005; Sinnhüber et al., 2005).

This chapter is organized in three parts. The methodology applied to retrieve stratospheric and tropospheric BrO vertical columns is detailed in section 5.2. This section also includes a quantitative discussion of the information content of the retrieval according to Rodgers (2000) as well as a comprehensive error budget. This is followed in section 5.3 by a presentation of the results and their discussion in the light of our current understanding of bromine photochemistry in the atmosphere. Conclusions are given in section 5.4.

5.2 Data analysis

The data analysis involves two main steps. First, the total slant column amount of BrO is determined for each viewing direction according to the DOAS technique. Second, model simulations of the BrO slant column obtained from coupled radiative transfer and photochemical model calculations are adjusted to the observations until a consistent stratospheric and tropospheric BrO vertical column solution is obtained that matches all viewing directions.

5.2.1 DOAS slant column retrieval

The spectral interval chosen to retrieve BrO slant columns is in the range from 345 to 359 nm (two absorption bands). Further details on the optimization of this fitting interval are given below. The spectral evaluation consists in a least-squares fit procedure where cross-sections of BrO (228 K) (Wilmouth et al., 1999), ozone (223 K and 243 K) (Bogumil et al., 2003), NO_2 (220 K) (Vandaele et al., 1997), HCHO (293 K) (Meller and Moortgat, 2000), and the collision pair of oxygen molecules O_4 (Greenblatt et al., 1990) are adjusted to the log-ratio of a measured and a reference spectrum taken at noon in zenith-sky geometry. The quantity retrieved with this method is a so-called differential slant column density (DSCD), which is the difference of the column amount of the absorber along the light path and the absorber amount in the reference spectrum. The residual broadband features due to Rayleigh and Mie scattering are removed using a third order closure polynomial. To match the spectral resolution of the instrument, the laboratory absorption cross-sections are convolved using the measured slit function at 346.6 nm. In the case of the strongest absorbers ozone and NO_2, a correction for the so-called solar I_0 effect (Aliwell et al., 2002; P.V. Johnston, unpublished results) is further applied. The wavelength calibration of the measured spectra is accurately determined by reference to the high-resolution solar atlas of Kurucz et al. (1984), according to the procedure described in Van Roozendael et al. (1999). To correct for the Ring effect (Grainger and Ring, 1962) a pseudo absorption cross-section generated after Vountas et al. (1998) using the SCIATRAN radiative transfer model (Rozanov et al., 2005a) is included in the fit. Similar settings are used for the retrieval of O_4 DSCDs except for the fitting interval, which is slightly shifted towards longer wavelengths (338.5 – 364.5 nm) in order to capture the strong O_4 absorption band centered at 360 nm.

Due to the faintness of the BrO differential absorption features (typically smaller than 0.1 % of absorbance) and the presence of much stronger interfering absorption bands from ozone in the same wavelength region, the retrieval of BrO DSCDs is difficult and requires careful treatment. Main sources of uncertainties including those related to instrumental parameters (wavelength calibration, spectral stray light, slit function, etc), the temperature dependence of the ozone absorption cross-sections or the impact of the solar I_0 effect have been addressed in the literature leading to a set of recommended BrO retrieval settings (see e.g. Arpag et al., 1994; Richter et al., 1999; Aliwell et al., 2002). In the present work, the problem of the optimization of the wavelength interval used for BrO retrieval has been revisited. As already mentioned the fitting interval is usually determined empirically in an attempt to maximize the sensitivity to the target gas and at the same time minimize interferences with other absorbers. In the case of BrO, the main difficulty comes from the unavoidable presence of strong interfering ozone absorption bands. At twilight, the ozone absorption becomes so large that the optically thin approximation used in the DOAS technique may not be fully satisfied, leading to systematic misfit effects that may introduce biases in the retrieved BrO DSCDs.

In order to assess the importance of such effects, simulations of the zenith-sky radiance have been performed using the SCIATRAN model (Rozanov et al., 2005a) and used to test different choices of fitting intervals. Radiative transfer calculations were performed in the 340 – 360 nm interval for a range of solar zenith angle values (50 – 92 degrees) and considering absorption by all relevant trace gases. Rotational Raman scattering by molecular oxygen and nitrogen (i.e. the main source of the Ring effect) was also explicitly included (Vountas et al., 1998). In order to simulate the impact of the solar I_0 effect, calculations were realized at the resolution of 0.1 nm, further convolved to the instrumental bandpass (0.7 nm FWHM) and finally resampled on the wavelength grid of the field instrument. Based on this set of synthetic spectra, test retrievals were conducted in various wavelength intervals and the resulting BrO DSCDs were compared to the reference DSCDs calculated from the radiative transfer model at the wavelength of 352 nm (reference wavelength used for BrO air mass factor calculations, see section 5.2.2).

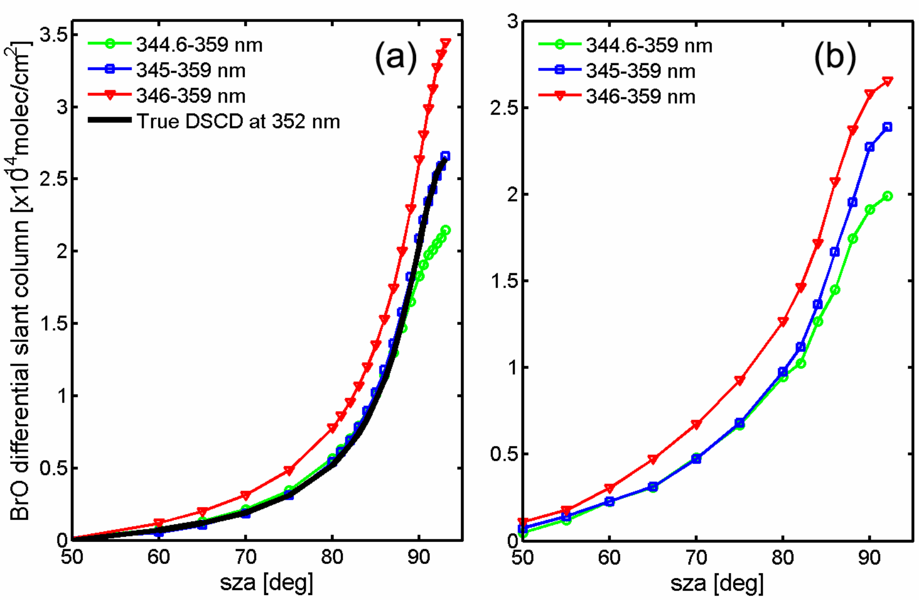

Figure 5.1 BrO differential slant columns (DSCDs) retrieved in different wavelength intervals from (a) simulated radiances generated using the SCIATRAN model, and (b) actual zenith-sky observations performed at Reunion Island. Reference DSCDs calculated at 352 nm from the model are plotted with a thick black line.

Results from these sensitivity tests are displayed in Figure 5.1(a) for three typical intervals recommended in the literature. As can be seen, differences as small as a few tenths of a nm in the selection of the shorter wavelength of the interval (where ozone absorption is strongest) can have a very significant impact on the BrO DSCD. Our simulations strongly suggest that the 345-359 nm interval efficiently minimizes the bias on the retrieved BrO columns in the full range of solar zenith angles. This interval has therefore been selected as a baseline for the present study. As an additional verification, the test fitting windows have also been applied to actual BrO measurements (see Figure 5.1b). Although the shape of the observed BrO DSCD variation cannot be precisely captured by the simulations due to the non-inclusion of BrO photochemical effects in the SCIATRAN version used here (version 1.2), one can see that both synthetic and actual retrievals display similar dependences on the fitting interval, which reinforces our confidence in the reliability of the simulations.

5.2.2 Inversion of stratospheric and tropospheric columns

As already mentioned, the quantity retrieved by the DOAS technique is the differential slant column density, which corresponds to the trace gas concentration integrated along the effective light path of scattered photons. Since the light that reaches the instrument travels through the entire atmosphere from top to bottom, the measured BrO DSCD will contain absorption originating from both stratospheric and tropospheric altitudes (provided of course that sizeable amounts of BrO do exist in both regions). In order to separate the stratospheric and tropospheric contributions, it is necessary to combine observations displaying different sensitivities to the various atmospheric layers. In this work, we first exploit the geometrical path enhancement characteristic of scattered light measurements at twilight to get information on the stratospheric part of the BrO profile in a way similar to that used in vertical profiling studies (e.g. Preston et al., 1997; Schofield et al., 2004a,b; Hendrick et al., 2004). Second MAX-DOAS observations performed at 3°, 6°, 10° and 18° of elevation above the horizon are combined with zenith-sky measurements to infer additional information on the tropospheric part of the BrO profile. The geometrical light path enhancement at low viewing angle elevation is such that the sensitivity to trace gas absorptions occurring in the atmospheric boundary layer can be increased by an order of magnitude (see e.g., Wagner et al., 2004; Wittrock et al., 2004).

The inversion method applied here is based on an analysis of the diurnal evolution of the measured BrO differential slant column, which is assumed to be well represented by the following equation:

$$\begin{aligned} DSCD(\theta(t),\varphi(t),\phi)+RSCD &= VCD_{strato}(\theta(t)).AMF_{strato}(\theta(t),\varphi(t)) \\ &+VCD_{tropo}(\theta(t)).AMF_{tropo}(\theta(t),\varphi(t),\phi) \qquad (5.\ 1) \end{aligned}$$

Where VCD is the vertical column, AMF the air mass factor, $\boldsymbol{\theta}$ the solar zenith angle (SZA), $\boldsymbol{\varphi}$ the relative azimuth angle between the sun and the viewing direction and $\boldsymbol{\phi}$ the viewing elevation angle. ***RSCD*** represents the residual slant column density in the reference spectrum, derived as explained in section. 5.3.2. As a result of the photochemically induced diurnal variation of BrO, the stratospheric and tropospheric VCDs depend on the SZA, while the AMFs depend on both viewing and solar zenith angles. Note that the stratospheric AMF can be considered with a good level of approximation as independent of the viewing angle. Photochemical effects, mostly important at twilight, are explicitly treated in the inversion process, as further explained below.

The air mass factors $\boldsymbol{AMF_{tropo}}$ and $\boldsymbol{AMF_{strato}}$ represent the enhancement of the absorption along the light path with respect to the vertical path, in the troposphere and the stratosphere respectively. In the present analysis, a tropopause height of 16 km characteristic of tropical regions has been considered, in agreement with temperature profiles from the European Centre for Medium-Range Weather Forecasts (ECMWF). The AMFs can be determined through appropriate calculation of the transfer of the solar radiation in a multiple scattering atmosphere. In addition photochemical effects that introduce spatial and temporal gradients in the BrO concentration field must be taken into account, especially for twilight conditions. In this work, forward model calculations of the BrO absolute slant columns and corresponding AMFs have been obtained using the pseudo-spherical radiative transfer model UVSpec/DISORT coupled to the stacked photochemical box model PSCBOX (Errera and Fonteyn, 2001; Hendrick et al., 2004). The PSCBOX model includes 48 variable species, 141 gas-phase photochemical reactions and is initialized at 20 independent altitude levels with 00:00 UT pressure, temperature and chemical species profiles from the 3-D chemical transport model (CTM) SLIMCAT (Chipperfield, 1999 and 2006; see also Sect. 5.3.3). A stratospheric inorganic bromine total loading of 21.2 pptv, accounting for long-lived sources (CH_3Br and halons, WMO 2003) and an additional contribution of 6 pptv from short-lived bromine compounds, has been assumed within the SLIMCAT model. Updated kinetic and photochemical data are taken from the Jet Propulsion Laboratory (JPL) 2006 compilation (Sander et al., 2006). As investigated in Fietkau et al. (2007), the reaction $BrONO_2+O(^3P)$ can play an important role in the tropical stratosphere and has thus, been included in the model simulations. The results of the photochemical model are given at chemical time steps of 6 minutes.

Model BrO profiles are supplied to the RTM code, and used to compute the AMFs. The UVSpec/DISORT model has the capability to ingest two-dimensional arrays (altitude and SZA) of BrO concentration fields so that the impact of photochemical changes along the incident light path can be accounted for in the calculations (see e.g. Fish et al., 1995). This particular feature of the model has been recently validated as part of a dedicated RTM intercomparison (Hendrick et al., 2006). As already mentioned, BrO AMFs have been calculated at the wavelength of 352 nm (center wavelength of the applied DOAS fitting interval), for a fixed albedo of 6% which has been found to be typical for sea-surface conditions (Koelemeijer et al., 2003).

Following Schofield et al. (2004a,b) and in order to limit the number of retrieval parameters, we have assumed that six profiles given respectively at 45°, 80°, 85°, 87.5° and 92.5° of SZA describe adequately the diurnal variation of BrO in the stratosphere. The stratospheric VCDs can be determined at other SZAs using simple linear interpolations. The vertical distribution of BrO being largely unknown in the troposphere, our baseline for the retrieval has been to assume a free-tropospheric profile consistent with the observed profile of Fitzenberger et al. (2000). This assumption will be further tested in section 5.3.4, where attempts to derive the vertical distribution of BrO in the troposphere from multi-axis DOAS observations are presented. Since no measurements of the diurnal variation of BrO in the troposphere are currently available, we have adopted the approach introduced in Schofield et al. (2004a,b). This consists in assuming a tropospheric BrO diurnal variation similar to the one modeled in the lowest levels of the stratosphere. It will be shown later that inversion results are weakly dependent on this assumption.

The inversion for the stratospheric and tropospheric BrO VCDs is obtained by fitting equation 5.1 to a set of measurements recorded from noon to twilight at various elevation viewing angles and solar zenith angles. Morning and afternoon measurements are treated separately. For the stratosphere-troposphere separation, the technique takes benefit of the different evolution of the stratospheric and tropospheric AMFs as a function of SZA. This is illustrated in Figure 5.2 for typical conditions in the zenith-sky geometry.

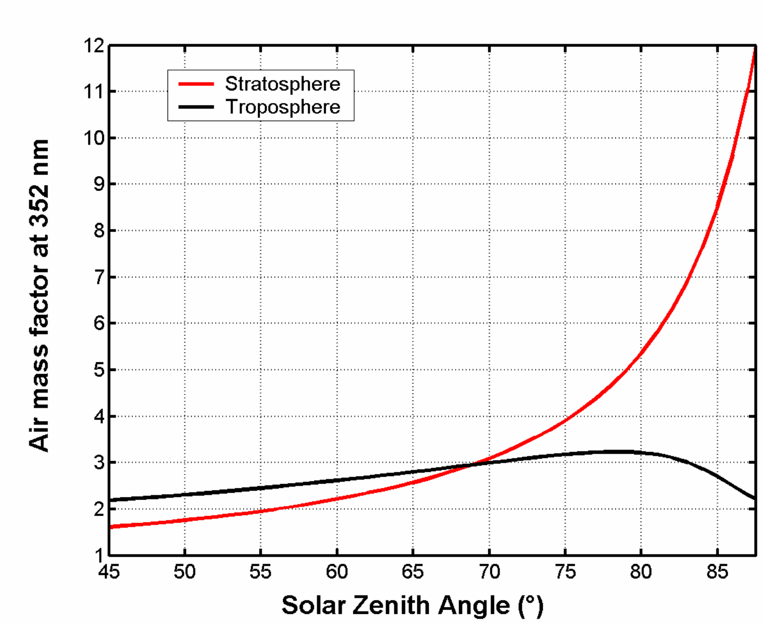

Figure 5.2 Stratospheric and tropospheric BrO air mass factors calculated at 352 nm in the zenith-sky viewing geometry. The enhancement of the sensitivity to stratospheric BrO at twilight is obvious.

In the inversion process, the stratospheric BrO VCDs are simultaneously (and independently) retrieved at five values of the SZA (45°, 80°, 85°, 87.5° and 92.5°) meaning that the diurnal variation of the stratospheric BrO column is actually retrieved from the observations and not forced a priori from photochemical model calculations. Note that photochemical calculations are in fact only used to ensure proper calculation of the late twilight AMFs when two-dimensional gradients of the BrO concentration are important.

Since the introduction of an extra retrieval parameter for the slant column in the reference spectrum (***RSCD*** in equation 5.1) can lead to unwanted uncertainties and retrieval instabilities, ***RSCD*** has been determined prior to the inversion as described in more details in Sect. 5.3.2.

5.2.3 Averaging kernels

In this section the capacity of the inversion method to separate adequately the stratospheric and tropospheric signals from the observations is addressed, based on the concept of the averaging kernels as developed in (Rodgers, 2000). The reader is referred to Appendix A for an introduction to the theory of Optimal Estimation. Basics on the error analysis and characterization of a retrieval method are presented.

The averaging kernel represents the sensitivity of the retrieval to the true state:

$$\boldsymbol{A} = \frac{\partial \hat{\boldsymbol{x}}}{\partial \boldsymbol{x}} \tag{5. 2}$$

where $\hat{\boldsymbol{x}}$ is the retrieved state vector (i.e. here the tropospheric and stratospheric VCDs) and $\boldsymbol{x}$ represents the true BrO vertical profiles. Equation 5.2 can also be written:

$$\boldsymbol{A} = \frac{\partial \hat{\boldsymbol{x}}}{\partial \boldsymbol{y}} \frac{\partial \boldsymbol{y}}{\partial \boldsymbol{x}} = \boldsymbol{G} \frac{\partial \boldsymbol{y}}{\partial \boldsymbol{x}} \tag{5. 3}$$

where $\boldsymbol{y}$ is the measurement vector, and $\boldsymbol{G}$ is the contribution matrix expressing the sensitivity of the retrieval to the measurement. The derivative of the measurement vector (the slant column densities) with respect to the BrO vertical profiles have been determined by a perturbation method using the radiative transfer model.
Figure 5.3 shows the tropospheric and stratospheric VCDs averaging kernels (AK) calculated according to equation 5.3 for three representative values of the SZA (80°, 85° and 87.5°).

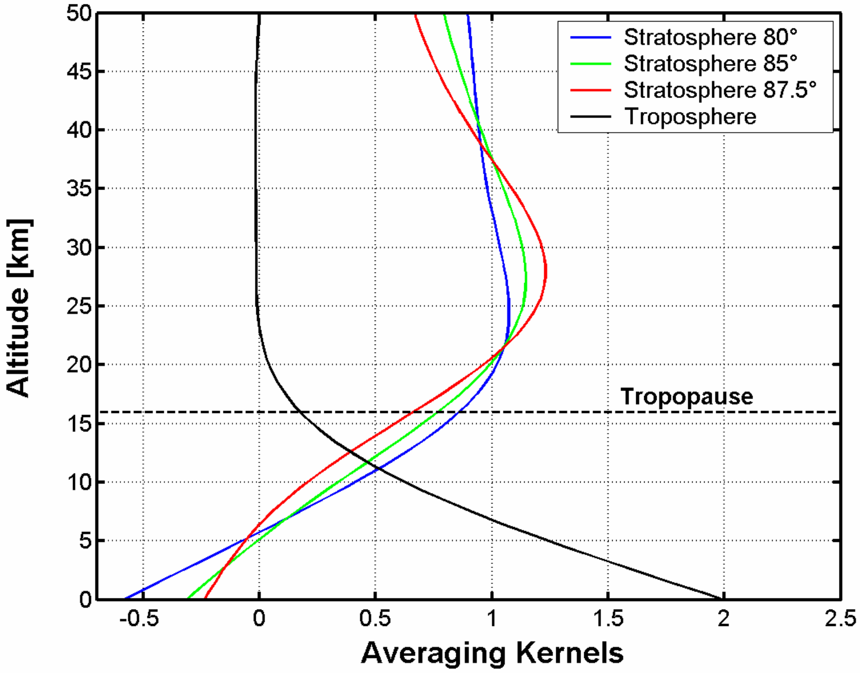

Figure 5.3 Typical examples of ground-based averaging kernels for stratospheric BrO columns (at 80°, 85° and 87.5° SZA) and for tropospheric BrO columns (see text).

The AK values represent the way the retrieval smooths the respective partial column profiles (for a 1 km layer around the altitude given in the y-axis). It can be deduced from Figure 5.3 that the inverted tropospheric columns are largely independent from the simultaneously inverted stratospheric columns. The high value of the tropospheric AK nearby the surface is related to the enhanced sensitivity of the off-axis observations in this altitude region. On the contrary, the stratospheric averaging kernels peak in the stratosphere around the maximum of BrO concentration profiles.

5.2.4 Error analysis

The contributions to the total retrieval uncertainty are divided into three categories: (1) random errors caused by measurement noise and BrO variability (2) errors affecting the slant column density in a systematic way, and (3) errors due to remaining uncertainties in the modeling and representation of the atmosphere, affecting the air mass factors.

We investigate the errors affecting the SCDs and the AMFs. A careful estimate of the uncertainties is especially crucial at high SZA. Indeed, a large part of the information used to separate the stratospheric and tropospheric BrO columns comes from measurements at high SZA. The uncertainties affecting the SCDs (random and systematic errors) as well as the AMFs are largest at low sun.

Measurement and modeling uncertainties have been estimated by means of sensitivity studies. As an example, the results for zenith-sky observations are displayed in Table 5.1 for typical low, medium and high solar zenith angles (respectively 70°, 85° and 90° SZA). The scatter of the measured DSCDs has been found to be relatively constant from month to month. Hence average values of 1.2, 1.9 and 3.4 x 10^{13} molec/cm^2 have been attributed to random error sources, respectively for the three representative SZAs. These values are also consistent with the one-sigma uncertainties derived from the DOAS fitting procedure. DSCDs systematic errors are mainly introduced by uncertainties on the absorption cross-sections of the molecules included in the analysis, leading to mutually correlated DOAS results.

In order to estimate the errors due to absorption cross-sections and their cross-correlations, one approach is to consider the cross-sections as forward model parameters of the DOAS retrieval. Following the formalism introduced by Rodgers (2000), the forward model parameter error of the retrieval can be derived from the quoted uncertainties on the cross-sections used in the DOAS analysis (more details on this part of the error calculation are provided in Appendix B). Based on literature data and sensitivity tests using various data sources, the following uncertainty figures have been adopted for BrO: 8%, NO_2: 3%, O_3: 3%, O_4: 5%, HCHO: 5% and Ring effect interferences: 5%. In addition to cross-sections, other sources of systematic errors can be identified, like the errors linked to calibration or other additional instrumental uncertainties. As already pointed out in section 5.2.1, the use of the DOAS approximation by which slant columns are assumed to be constant within the spectral fitting window, can also be a significant source of systematic uncertainty. Using the optimal fitting window derived in section 5.2.1, sensitivity studies suggest that these sources of uncertainties do not contribute more than 5% to the total SCD error. Considering absolute slant columns (i.e. corrected for the BrO residual amount in the reference spectrum), a constant additional error of $\pm$ 0.5 10^{13} molec/cm^2 has been introduced, following estimates described in section 5.3.2. From Table 5.1, it must be emphasized that SCDs errors are largely dominated at twilight by systematic biases mainly introduced by uncertainties on the absorption cross-sections.

Table 5.1 Summary error budget for BrO slant column densities (random, systematic and RSCD error sources) and air mass factors in zenith-sky geometry, for three representative solar zenith angles.

	Solar zenith angle		
Slant column density error (x 10^{13} molec/cm^2)	**70°**	**85°**	**90°**
Random	1.2	1.9	3.4
Systematic bias	0.7	4	6.8
Residual slant column density (RSCD)	0.5	0.5	0.5
Total (x 10^{13} molec/cm^2)	1.5	4.5	7.6
Total (%)	13	23	24
	Solar zenith angle		
Air mass factor error (%)	**70°**	**85°**	**90°**
Stratosphere: AM	1.5	1.5	3.5
Stratosphere: PM	1.5	1.5	2.5
Troposphere	5	15	5

In addition to the error analysis described above, an alternative study has been performed to estimate systematic errors due to absorption cross-sections uncertainties. It consisted in running test retrievals using different sources of cross-sections available from the literature and investigating the resulting variability of the retrieved BrO slant columns. Uncertainties empirically estimated in this way were found to be in good agreement with the values (see Table 5.1) deduced from the approach based on the Rodgers (2000) formalism.

Once the total uncertainties on the measurements have been estimated for each elevation angle and for all solar zenith angles, the resulting uncertainties on the retrieved stratospheric and tropospheric BrO vertical columns are given by simple error propagation (see Table 5.2). The next step is to evaluate the errors on the AMFs. For small SZA (<85°), the stratospheric AMF can be satisfactorily approached by a geometrical calculation. The error on the stratospheric AMF is therefore negligible. In contrast at high SZA, the stratospheric AMF is highly dependent on the BrO concentration at the bulk altitude for Rayleigh scattering, the latter increasing with the SZA (see e.g. Sinnhuber et al., 2002). Hence accurate modeling of the photochemistry is needed to evaluate correctly the stratospheric AMFs. To a large extent, the stratospheric BrO concentration is controlled by NO_2 through the termolecular reaction $BrO+NO_2+M$. In order to minimize errors due to the interplay between BrO and NO_2, the photochemical simulations have been constrained using NO_2 profiles derived from simultaneous zenith-sky observations in the visible region (Hendrick et al., 2004). Nevertheless remaining uncertainties in other aspects of the photochemical model calculations may have a substantial impact on the results. Hence sensitivity studies have been carried out in order

Table 5.2 Summary error budget for morning stratospheric BrO and tropospheric BrO columns.

	Stratospheric VCD error ($\times 10^{13}$ molec/cm^2)					**Tropospheric VCD error**
	Solar zenith angle (°)					
Error source	**45**	**80**	**85**	**87.5**	**92.5**	
Slant column densities	0.5	0.3	0.3	0.3	0.1	0.3
Stratospheric AMFs	<0.1	<0.1	<0.1	<0.1	<0.1	<0.1
Tropospheric AMFs	0.6	0.4	0.3	0.2	0.1	0.4
Total VCD error ($\times 10^{13}$ molec/cm^2)	0.8	0.5	0.4	0.4	0.1	0.5
Total VCD error (%)	**30**	**21**	**17**	**17**	**33**	**46**

to estimate the impact of the uncertainties on main reaction rate constants, following the work presented in Sinnhuber et al. (2002). The stratospheric AMF errors have been estimated by the standard deviation of the ensemble of AMFs generated by varying independently the reaction rate constants. Results from this analysis are summarized in Table 5.1.

The estimation of the errors on the tropospheric AMFs is difficult, mainly due to the following two reasons: (1) the treatment of the radiative transfer down to the surface strongly depends on the aerosol loading as well as the (unknown) BrO vertical distribution, and (2) the diurnal variation of the tropospheric BrO content might have to be taken into account. Since substantial uncertainties accompany these parameters, several hypotheses have been made here. Some of these will be justified later on in the discussion (see section 5.3). As a baseline for our retrievals, we have assumed that the aerosol content was small (justified in section 5.3.1) and that the bulk of the tropospheric BrO concentration was mainly located in the free-troposphere (justified in section 5.3.4).

A rough estimate of the tropospheric AMF error has been obtained by varying input BrO profiles in the RTM calculations. Gaussian profiles of various heights [5-8 km] and widths [1-4 km] have been used to this purpose. Corresponding tropospheric BrO AMFs show a root mean square deviation of less than 15% as indicated in Table 5.1. For the diurnal variation, we assume that the known photochemistry of BrO in the lower stratosphere constitutes a reasonable proxy for the free troposphere (Schofield et al., 2004a,b). In reality, one may expect the tropospheric BrO amount to vary in response to e.g. emissions from the oceans, meteorological conditions, changes in photolysis rates (e.g. due to clouds), and other physical and chemical processes. It is however difficult to comprehensively account for all these effects in a realistic way, however in order to roughly estimate the order of magnitude of errors related to diurnal variation effects, we have considered two extreme cases: (1) the baseline tropospheric BrO diurnal variation, where basically the BrO concentration drops to zero from noon to late twilight and (2) the case where tropospheric BrO has no diurnal variation at all (which is very unlikely). We assume that in reality the tropospheric BrO diurnal variation lies somewhere in between

these two cases. Test retrievals considering these two scenarios resulted in minor differences on the inverted BrO columns (approximately 1 x 10^{12} molec/cm^2).
The main sources of uncertainties on the inverted BrO VCDs (obtained by propagation of the error discussed above) are summarized in Table 5.2 for morning conditions. Although not reported here, similar results have been derived for afternoon observations. As can be seen, stratospheric VCDs have largest uncertainties (>30 %) at low sun and at very high sun, while errors are kept in the range of 20 % for intermediate values of the SZA. The absolute error on the tropospheric BrO VCD, mainly dominated by uncertainties on the tropospheric AMFs and on the measured SCDs, is estimated to be about 45 %.

5.3 Results and discussion

To simplify the discussion, we first restrict the analysis to clear-sky measurement days when the transfer of the scattered radiation can be simulated with best accuracy. We focus on the determination of three key parameters that control the accuracy of the target BrO VCD products; namely the aerosol extinction, the residual BrO slant column density in the reference spectrum and the shape of the tropospheric BrO profile. Results are then discussed with regard to our current understanding of the bromine chemistry in both the stratosphere and the troposphere. In a second step, a simplified version of the inversion algorithm is applied to the whole series of measurements from July 2004 until July 2005, and the consistency of the retrieved BrO columns is investigated in comparison with coincident satellite observations from SCIAMACHY.

5.3.1 Determination of the aerosol settings

The light path of photons scattered in the lower atmosphere is strongly dependent on the aerosol loading, especially nearby the surface. A good estimate of the aerosol extinction profile is thus needed for the calculation of the tropospheric BrO AMFs. This is especially true for small elevation angles, which in principle have the longest light paths. As suggested by Wagner et al. (2004) and Frieβ et al. (2006), multi-axis observations of the oxygen dimmer O_4 can be used to deduce the aerosol extinction profile[1]. The analysis of aerosol properties has to be limited to measurements without significant cloud influence, since O_4 absorptions are greatly affected by clouds. Out of the complete 2004 data set (i.e. approximately six months of measurements), seven days could be selected as fully clear sky days (day numbers 242, 246, 253, 271, 272, 326, 346), based on an analysis of the diurnal variation of the measured O_4 absorptions at all elevation angles. For all these days, O_4 absorptions were found to follow the same smooth diurnal evolution, indicating similar aerosols scenarios. In Figure 5.4., the O_4 DSCDs averaged on the selected days (and on a 2.5° SZA bin grid) are represented as a function of SZA for morning and afternoon observations. In order to reproduce the O_4 observations, a set

---

[1] As the volume mixing ratio profile of the oxygen dimmer varies with the square of the O_2 profile, the profile of O_4 is well known and mainly depends on the pressure and temperature profiles. Thus, deviation of the measured O_4 slant column from the clear-sky O_4 slant column (that can be simulated accurately using a RTM, for a pure Rayleigh scattering atmosphere) can be exploited to quantify Mie scattering and aerosols.

of O_4 AMFs were computed for each elevation angle and for different aerosol extinction profiles. Radiative transfer calculations were initialized using vertical profiles of O_4, pressure, temperature and O_3 characteristic of tropical regions, according to the AFGL atmospheric constituent profiles data base (Anderson et al., 1986). The aerosol extinction profile was then varied until good agreement was found for the O_4 verticals columns derived from all viewing elevations. This procedure is similar to the one proposed and applied in Heckel et al., 2005. As demonstrated in Figure 5.5, the optimal aerosol extinction profile corresponds to an aerosol visibility (Middleton, 1952) of 80 km with an enhanced maritime aerosol load (extinction ~0.2 km^{-1}) introduced into a 100 m thick layer above the surface. O_4 VCDs retrieved assuming an aerosol visibility of 40 km are also shown for comparison purpose.

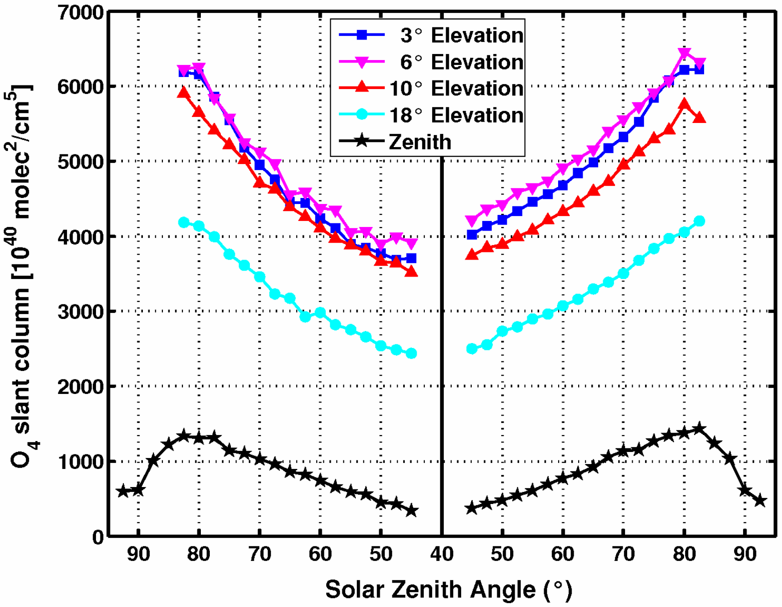

Figure 5.4 Differential slant columns of O_4 measured for different elevation angles as a function of the SZA. Morning and afternoon measurements are displayed together. The O_4 DSCDs have been averaged from a selection of 7 clear-sky days and binned on a grid of 2.5° SZA.

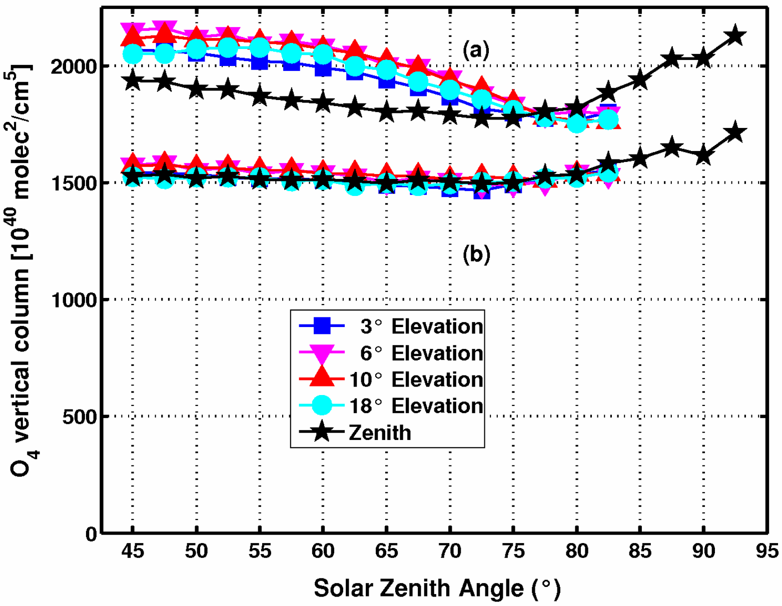

Figure 5.5 Vertical columns of O_4 calculated for all viewing directions based on AMFs for two aerosols scenarios, as a function of SZA: aerosol extinction profiles corresponding to (a) a visibility of 40 km and (b) a visibility of 80 km with a higher aerosol load (extinction:~0.2 km^{-1}) added in a thin layer close to the surface (0-100m).

5.3.2 Determination of the residual slant column density

In this work, the zenith-sky and off-axis measurements have been processed using a fixed zenith reference spectrum selected at minimum solar zenith angle (28.7° SZA) on September 2, 2004. As mentioned earlier, the introduction of an extra fitting parameter for the residual slant column (*RSCD* in equation 5.1) can be a source of uncertainty for the retrieved stratospheric and tropospheric BrO VCDs. In order to minimize this error and stabilize the retrieval process, the residual slant column density is therefore determined prior to the inversion process so that absolute slant columns (rather than differential SCDs) can be fitted.

The residual slant column density has been estimated from an average of clear days measurements (selected in section 5.3.1), assuming that the BrO field is stable enough to allow meaningful interpretation of the resulting averaged SCDs. This assumption will be further verified in section 5.3.5. Based on equation 5.1, the RSCD is treated as an additional parameter in the BrO VCDs retrieval. In order to minimize the impact of uncertainties related to the diurnal variation, systematic measurement errors or AMFs modeling errors (all becoming important at twilight), only the measurements corresponding to solar zenith angles lower than 85° are considered. This also reduces the number of fitted parameters and therefore stabilizes the inversion for the RSCD. Using this approach, residual slant column densities of 6.42 x10^{13} and 6.37 x10^{13} molec/cm² are retrieved, respectively from morning and afternoon measurements. The (small) differences in the retrieved RSCDs can be attributed to a large extend to the propagation of the measurement errors into the BrO VCDs retrieval. An error analysis according to section 5.2.4., leads to a best estimate of 6.4 ± 0.5 x 10^{13} molec/cm². Furthermore, this value is found to be consistent with the re-calculated RSCD based on the retrieved VCDs evaluated at the time of the reference spectrum.

5.3.3 Clear-sky results

The inversion technique described in section 5.2.2 has been applied to the restricted data set of clear sky measurements, also used for the aerosol and residual BrO column determination. The resulting retrieval fit results are displayed in Figure 5.6. For the sake of clarity, only afternoon results are represented for a limited number of viewing directions.

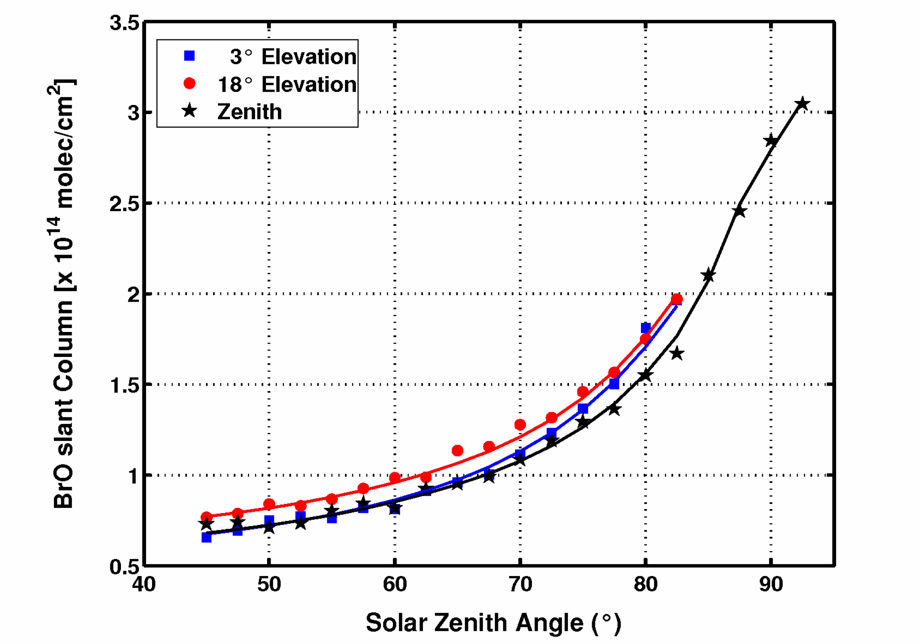

Figure 5.6 Measured and modeled afternoon BrO slant column densities, as a function of the SZA for 3 elevation viewing angles (3°, 18° and zenith).

As can be seen, the modeled SCDs are consistent with the observations, for all SZA and viewing angles. In Figure 5.7, the differences between the measured and the modeled slant column densities are shown as a function of the SZA, for the various elevation angles. A comparison with the results of the algorithm assuming that BrO would only be present in the stratosphere clearly demonstrates the need to include both a stratospheric and a tropospheric BrO contribution in the inversion process. The level of agreement between the elevation directions observations strongly depends on the hypothesis made for the tropospheric BrO profile as part of the tropospheric AMFs calculations. This will be addressed in the next section, where the relevance of using a free-tropospheric profile as derived in (Fitzenberger et al., 2000) is tested and discussed.

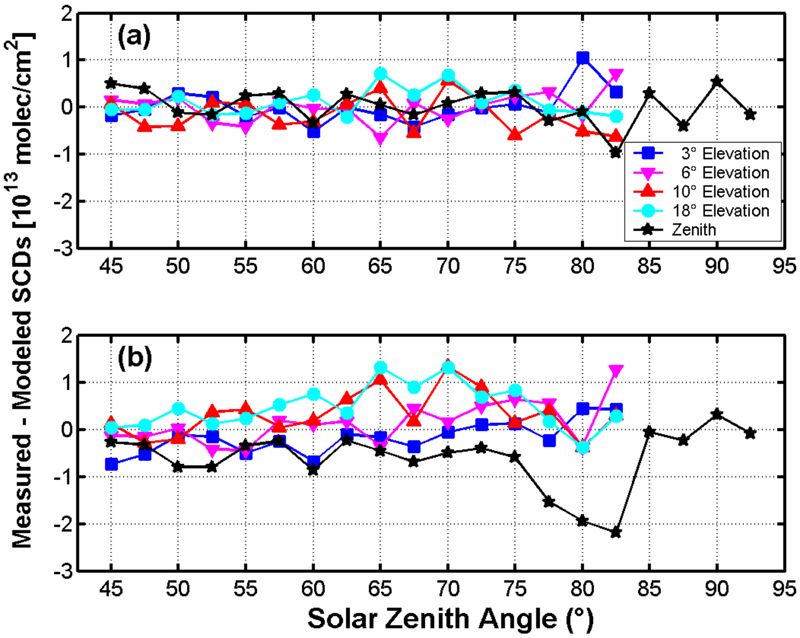

Figure 5.7 Retrieval residuals for averaged clear-sky data (see text), as a function of the SZA. The modeled SCDs are subtracted from the measured SCDs, for all viewing directions. Two different assumptions are made for the BrO vertical repartition: (a) BrO is present in both stratosphere and troposphere, (b) BrO is entirely located in the stratosphere.

The retrieved BrO vertical columns and their respective retrieval uncertainties (based on the error analysis developed in section 5.2.4) are displayed in Figure 5.8, for both morning and afternoon conditions.

5.3.3.1 Tropospheric BrO

Tropospheric BrO vertical columns (at 80° of SZA) of about 1.1 and 1.2 x 10^{13} molec/cm^2 are retrieved independently from morning and afternoon measurements separately, with a mean uncertainty of about 0.5 x 10^{13} molec/cm^2. This represents approximately one third of the total BrO column retrieved at the same SZA and therefore supports the existence of significant sources of inorganic bromine in the tropical troposphere.

Such results are roughly consistent with mid-latitude tropospheric BrO background values of 1-3 x 10^{13} molec/cm^2 obtained from GOME, ground-based and balloon measurements (e.g. Van Roozendael et al., 2002). Similarly GOME measurements over the equatorial pacific using a technique contrasting cloudy and clear-sky scenes conclude to a background tropospheric BrO column of 1-4 x 10^{13} molec/cm^2 (Richter et al., 2002). The combined use of SCIAMACHY nadir and limb observations also suggests an average global tropospheric BrO column below 15 km of about 2-4 x 10^{13} molec/cm^2 (Sinnhuber et al., 2005). On the other hand, significantly smaller tropospheric BrO columns in the range of 0.2 ± 0.4 x 10^{13} molec/cm^2 are derived

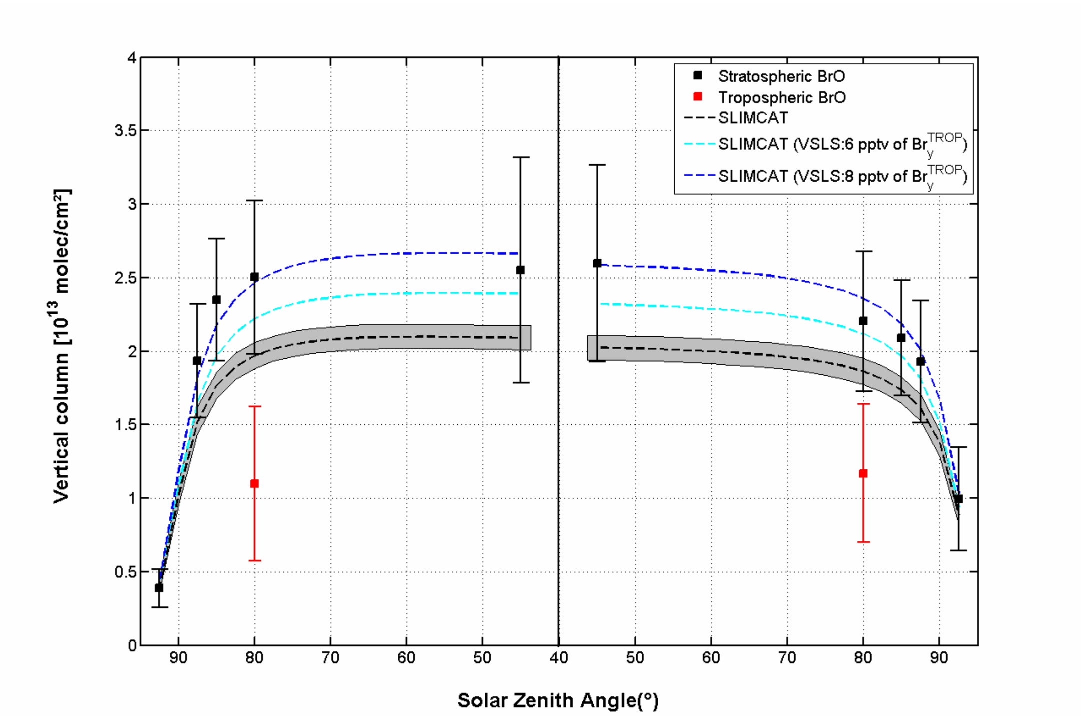

Figure 5.8 Morning and afternoon stratospheric and tropospheric BrO vertical columns retrieved from averaged clear-sky data. The dashed lines correspond to stratospheric columns obtained from photochemical model simulations initialized with SLIMCAT fields having different contributions from the very short-lived bromine species (VSLS): (black) 6 pptv, (cyan) 6 pptv and (blue) 8 pptv directly injected at the tropopause. The shaded area corresponds to the range of uncertainties associated to reaction rate constants.

from the combined use of direct sun and zenith sky measurements at the Southern mid-latitude site of Lauder (Schofield et al., 2004a).

More specifically, BrO measurements in the tropical troposphere have been very sparse and in fact limited to few studies. More recently at Nairobi, measurements similar to those reported here (Fietkau et al., 2007) conclude to tropospheric BrO columns in the range from 4 to 7.5 x10^{12} molecules/cm^2 in closer agreement with Reunion Island results although still slightly smaller. The difference could possibly be explained by the fact that the profile inversion used at Nairobi loses sensitivity above 6 km of altitude, while the different stratosphere-troposphere approach used in our study maintain better sensitivity higher up in the troposphere (see averaging kernels in Figure 5.3). Beyond retrieval issues, the possibility of an added tropospheric BrO content at Reunion Island due to influx from sea salt aerosol might also be considered (Fietkau et al., 2007).

5.3.3.2 Stratospheric BrO

The retrieved stratospheric BrO vertical columns and their respective error estimates (at the chosen SZAs of 45°, 80°, 85°, 87.5° and 92.5°) are displayed in Figure 5.8. A strong diurnal variation is observed as a result of the photochemically evolving interplay between BrO and its nighttime reservoirs (HOBr, $BrONO_2$) (e.g. Lary, 1996; Lary et al., 1996). From Figure 5.8, higher stratospheric BrO columns are found at sunrise than at sunset, for the reference SZAs of 80° and 85°. The rapid increase of BrO at sunrise is due to the fast photolysis of HOBr, which is produced during the night due to heterogeneous conversion of bromine nitrate by hydrolysis on sulfate aerosols (see section 2.2.3.2). The decrease of BrO during the day is related to the increase of stratospheric NO_2, which in turn influences the bromine partitioning through the termolecular reaction $BrO+NO_2+M$. The stratospheric column results of the photochemical model (initialized with the chemical fields from the SLIMCAT model) are also shown in Figure 5.8 (black dashed line). The diurnal evolution of the measured columns is properly captured by the model, providing strong evidence that the stratospheric bromine photochemistry is well understood and represented. It can also be seen however that modeled vertical columns are substantially smaller than the retrieved stratospheric columns. The shaded region around the modeled vertical columns indicates the impact (at the 1σ level) of the uncertainties of the rate constants for the most important reactions. One possible explanation for the underestimation of the BrO columns by the model run can be found in the way bromine sources (including the short-lived species) have been treated in the relatively old SLIMCAT version used for the present work (run D in Feng et al., 2007). These are represented using a single effective source of CH_3Br (with a mixing ratio of 21.2 pptv at the surface). Since in reality the short-lived source gases are decomposed faster than methyl bromide, the Br_y mixing ratio could be substantially underestimated by the model, especially in the lower stratosphere, which might have an important impact on the integrated BrO vertical column. In order to investigate this effect, we considered the extreme case where the short-lived species are totally converted in Br_y at the tropopause. This was achieved by applying a simple offset to the SLIMCAT Br_y mixing ratio profile (scaled for the contribution of the long-lived bromine sources only). The stratospheric BrO columns resulting from this test scenario are displayed in Figure 5.8 for contributions of 6 pptv (cyan dashed line) and 8 pptv (blue dashed line) from the decomposition of the short-lived bromine species. The value of 8 pptv can be considered as a plausible upper limit for the contribution of the bromine short-lived species, in agreement with recent studies (Pfeilsticker et al., 2000; Salawitch et al., 2005; Schofield et al., 2006; Dorf et al. 2006a,b; Sioris et al., 2006). This also confirms the findings of Feng et al. (2007), who have tested different methods of implementing the bromine source gases in the SLIMCAT model and found that the agreement between model and balloon data is significantly improved when having explicitly the short-lived source gases.

In order to gain better insight into the consistency between our retrieved stratospheric BrO content and data from the literature, the stratospheric BrO profiling algorithm of Hendrick et al. (2004, 2007) based on the Optimal Estimation Method (Rodgers, 2000), has been applied to the zenith-sky clear-sky observations performed at Reunion Island. Figure 5.9a displays a comparison of the resulting BrO profile with those obtained from the balloon-borne SAOZ instrument during the late afternoon ascent of the balloon at 75°-80° SZA at the same latitude (22.4°S, 49°W) in Brazil in November 1997 (Pundt et al., 2002), and January-February 2004 during the Hibiscus campaign (Goutail et al., personal communication). Since SAOZ balloon measurements are performed during evening twilight in ascent mode (typically around 86-87° SZA) the ground-based BrO profile was retrieved from afternoon observations at the appropriate SZA. Although

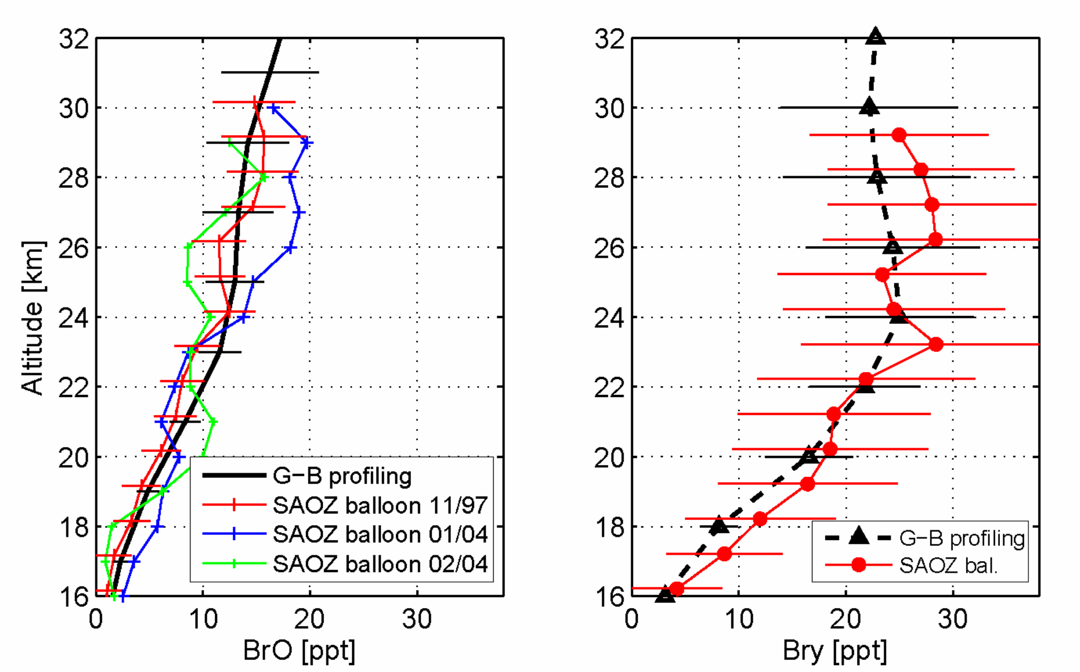

Figure 5.9 Retrieved stratospheric BrO profile compared to tropical SAOZ balloon BrO profiles (left plot). Profile of Br_y inferred from ground-based BrO profile compared to the SAOZ balloon Br_y profile at 22°S, November 1997 (right plot).

significant changes can be observed in the stratosphere from one flight to another a reasonable agreement is found between ground-based and balloon profiles at the same latitude. This is especially true for the flight in November 1997.

From the stratospheric BrO profile, it is also possible to derive a stratospheric inorganic bromine profile based on estimates of the BrO/Br_y ratio given by the photochemical model. Figure 5.9b shows the Br_y profile deduced from our retrieved tropical BrO profile. A good agreement is found with the Br_y vertical distribution derived by Salawitch et al. (2005) based on SAOZ observations.

From these results, one concludes to a total inorganic bromine content of about 23 pptv, which suggests a contribution from several short-lived organic bromine sources to the stratospheric inorganic bromine budget, in agreement with studies from Pfeilsticker et al. (2000) and Salawitch et al. (2005).

5.3.4 Determination of the tropospheric BrO vertical distribution

Since the light path through the troposphere strongly depends on both SZA and viewing elevation angle, only an appropriate tropospheric BrO vertical profile in the AMFs calculation will lead to a good agreement between the modeled SCDs and the measured SCDs, for all viewing angles. An illustration of the sensitivity of the multi-axis DOAS observations for an absorber located at different altitudes is given in Figure 5.10, in the form of air mass factor curves (weighting functions) represented for two different values of the SZA (60° and 80°). By comparing Figure 5.6 and Figure 5.10, it can be easily deduced that our observations do not show evidence for large amounts of BrO in the

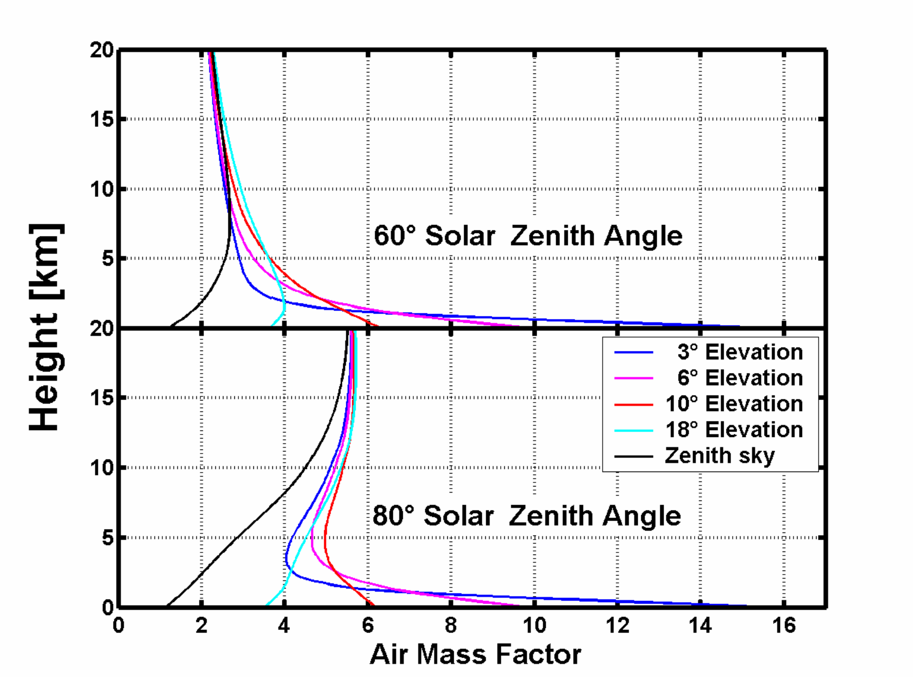

Figure 5.10 Height dependence of the sensitivity to BrO for the different viewing directions at 60° SZA (upper plot) and at 80° SZA (lower plot). The value on the x-axis is the air mass factor for a 1 km layer positioned around the height given on the y-axis.

boundary layer. Indeed this would require a systematic and pronounced increase of the measured BrO SCDs towards low elevation angles, which is definitely not observed. Based on the error budget of the retrieved BrO slant column densities (summarized in Table 5.1), one cannot exclude a possible enhancement in the range of approximately 1 x 10^{13} molec/cm², which translate to an upper limit of 0.5 pptv for BrO being possibly present in the oceanic boundary layer at Reunion Island.

If one assumes a BrO profile peaking higher up in the troposphere around 6-7 km, Fig. 5.10 indicates that at low SZA (60°) the AMF is almost the same at 3° elevation and at zenith, a sizeable enhancement of the sensitivity being only obtained at 18° of elevation. On the contrary at larger SZA (80°), larger AMF values are found at both 3° and 18° elevation. This characteristic behavior of the elevation angles sensitivities for a free-tropospheric profile is consistently observed in the measured slant columns in Fig. 5.6. In order to gain information on the vertical distribution of BrO in the troposphere, sensitivity tests have been made on the average of the 7 clear days of measurements (selected in section 5.3.3) and have consisted in varying bulk altitudes and full widths at half maximum (FWHM) of Gaussian tropospheric profiles used to calculate tropospheric AMFs. The best residuals were obtained for a concentration profile peaking at 6 km altitude with a FWHM of 2 km, for both morning and afternoon observations. A maximum of 2 to 5 pptv in the free troposphere is deduced from our estimate of the tropospheric BrO column (1.1± 0.5 x 10^{13} molec/cm²). These results are roughly in agreement with the tropospheric BrO profile measurements reported in Fitzenberger et al. (2000), based on balloon borne DOAS observations performed at Kiruna, Sweden. In contrast MAX-DOAS profile inversion results recently obtained above Nairobi, Kenya

(Fietkau et al., 2007) suggest a bulk tropospheric BrO layer located between 2 and 3 km altitude, hence slightly lower than found at Reunion Island.

This apparent discrepancy might be related to the fact that the inversion technique used in the Fietkau et al. (2007) study was essentially limited to the lowest 6.5 km. In addition, Nairobi is a continental station located at relatively high altitude (1600 m) likely not influenced by bromine emission from oceanic origin.

5.3.5 Seasonal variation

Since clear-sky observations do not show evidence for sizeable amounts of BrO being present in the lowest troposphere, one can safely expect that slant column measurements will generally be weakly affected by the presence of low altitude clouds and/or particles. Hence we decided to apply our inversion technique on a daily basis in order to derive information of the seasonal cycle of the retrieved stratospheric and tropospheric BrO vertical columns.

In order to somehow stabilize the inversion and allow its application to day-to-day observations inherently noisier than averages considered so far, the algorithm has been slightly simplified with respect to the scheme presented in section 5.2.2. Instead of retrieving the diurnal variation of the stratospheric VCD for each day, it was decided to fix this variation based on the clear-sky analysis obtained in section 5.3.3. Accordingly a single stratospheric BrO vertical column is derived from the inversion process, for a given reference SZA (80° was selected here), together with the tropospheric BrO column. This approach applied separately to morning and evening observations was found to represent the best compromise between information content and retrieval noise on a daily basis.

The resulting time-series of stratospheric and tropospheric BrO columns (hence retrieved at 80° SZA at both sunrise and sunset) are displayed in Figure 5.11, for the entire observation period. Only vertical columns corresponding to retrieval residuals lower than 2×10^{13} molec/cm^2 were considered in this analysis. This threshold has been chosen in order to reject unrealistic measurements, contaminated by thick clouds or affected by spectral artifact due e.g. to anomalously large O_4 absorption. The retrieved stratospheric and tropospheric BrO columns are on average in excellent agreement with the values derived from the averaged clear-sky observations (section 5.3.3) and show no noticeable seasonal variation. This result is somewhat in contradiction with expectations based on photochemical considerations valid for tropical latitudes. Model simulations of the noon or near twilight (SZA<80°) stratospheric BrO column at Reunion-Island indeed show a small seasonality, with an amplitude smaller than 10%. Such an effect however lies within the uncertainties of our retrieved stratospheric BrO columns, which moreover do not cover a complete annual cycle. Longer observational time series would certainly help characterizing better the seasonal variations.

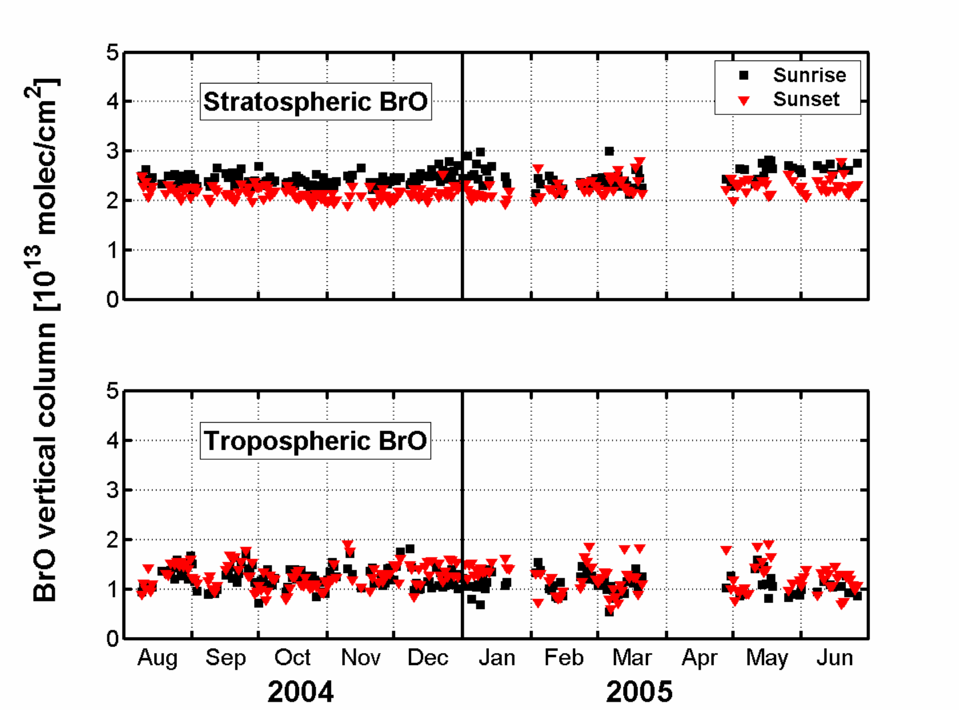

Figure 5.11 Time-series of stratospheric (top) and tropospheric (bottom) BrO columns retrieved for 80° SZA, displayed separately for sunrise (squares) and sunset (triangles).

The seasonal photochemical response of stratospheric BrO to changes in NO_2 concentration can in fact be studied with larger sensitivity when considering twilight observations above 80° SZA. To this aim, comparisons of modeled and measured BrO 90-80° differential slant columns were performed. Under these conditions, results show that both simulations and measurements present a significant seasonal cycle which follows the expected anti-correlation with NO_2, i.e. a minimum in summer and a maximum in winter. The observations also reproduces the diurnal cycle well, with PM values larger than AM ones, as reported in other studies (Sinnhuber et al., 2002; Fietkau et al., 2007).

5.3.6 Comparison with SCIAMACHY total column BrO observations

Among other geophysical data products, the vertical column of BrO can be derived from SCIAMACHY nadir measurements, using DOAS algorithms similar to those applied to ground-based measurements reported here. SCIAMACHY BrO columns used in this work were analyzed using daily sun irradiance from the ASM diffuser plate, according to retrieval settings described in Van Roozendael et al. (2004). To optimize the consistency with ground-based retrieval, SCIAMACHY BrO vertical columns were evaluated using AMFs calculated according to the BrO vertical distribution retrieved at Reunion Island.

Figure 5.12 presents the comparison between SCIAMACHY BrO vertical columns extracted from daily fields in a latitude zone of +/- 5 degrees around Reunion Island and the ground-based BrO total vertical columns, photochemically adjusted at the time of the satellite overpass using the BrO diurnal variation determined in section 5.3.3.

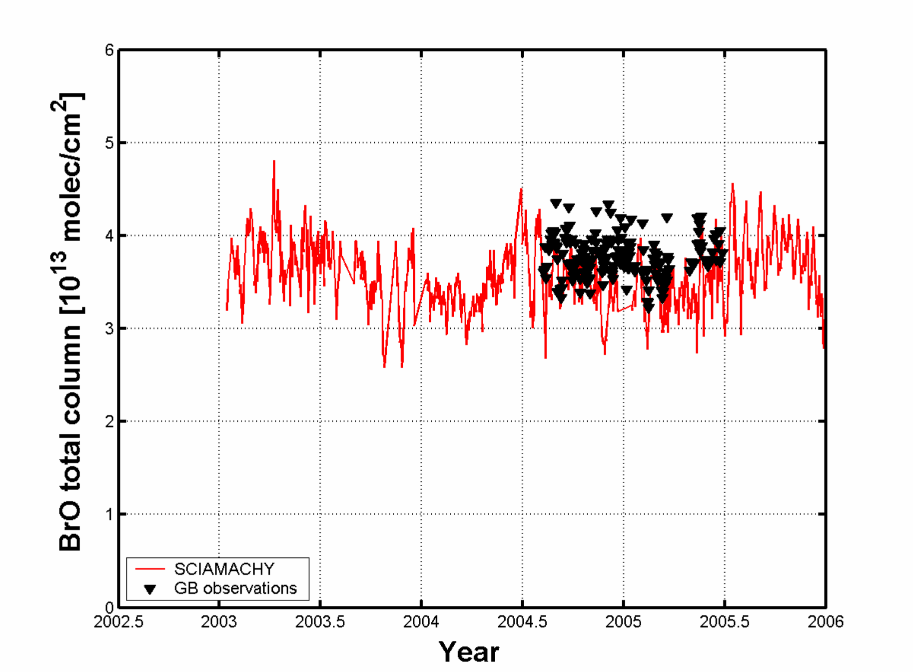

Figure 5.12 Total BrO columns retrieved from ground-based DOAS observations at Reunion-Island and from SCIAMACHY nadir observations averaged in a zonal band of 10 degrees centered at the latitude of the ground-based station.

Considering the uncertainties on both satellite and ground-based BrO measurements, the agreement obtained is highly satisfying. Since the ground-based and satellite total column analysis are essentially independent from each other (the dependency of the satellite nadir AMF on the shape of the BrO profile being in practice very small), these results consolidate our confidence in both ground-based and satellite estimates of the tropical BrO column. They also indirectly consolidate our estimate of the tropospheric BrO column, which as already stated represents a significant part (one third) of the total BrO column.

5.4 Conclusions

Tropospheric and stratospheric BrO columns were derived using a new double-column inversion method, accounting for the transfer of the radiation in the atmosphere and the BrO diurnal variation. This was applied to combined zenith-sky and off-axis ground-based UV-visible spectroscopic measurements at Reunion Island. Tropospheric BrO columns of 1.1±0.5 x10^{13} molec/cm^2 were retrieved, generally in agreement with estimations sparsely available from the literature. Sensitivity tests demonstrate a substantial contribution from the free-troposphere (around 6 km altitude) to the tropospheric BrO vertical column, however our observations do not support the existence of significant amounts of BrO in the tropical boundary layer. These results are in agreement with recent studies suggesting that tropical biogenic sources of short-lived organic bromine species might be converted into active bromine in the free-troposphere by mechanisms involving heterogeneous reactions possibly on ice crystals and water droplets (Fitzenberger et al., 2000).

The retrieved stratospheric columns show a diurnal variation coherent with photochemical model calculations based on recently updated rates. From a comparison between the retrieved stratospheric BrO columns and results from the 3D chemical-transport model SLIMCAT, one concludes that a satisfactory agreement can only be achieved by assuming an important delivery of Br_y (of about 6-8 pptv) in the stratosphere possibly produced by short-lived bromine organic compounds, rapidly converted into inorganic forms at the tropical tropopause. Based on the inversion of the stratospheric BrO profile according to Hendrick et al. (2007), a total stratospheric inorganic bromine content of about 23 pptv is inferred, which further strengthens the likely importance of short-lived bromine species as an important contribution to the Br_y budget. Total BrO columns are found to be in agreement with SCIAMACHY observations in a latitudinal band centered around Reunion Island. These results consolidate our confidence in both ground-based and satellite estimates of the tropical BrO columns.

Chapter 6

A global stratospheric BrO climatology based on the BASCOE chemical transport model[1]

Abstract

A new climatology of stratospheric BrO profiles based on a parameterization using dynamical and chemical indicators has been developed, with the aim to apply it to the retrieval of tropospheric BrO columns from space nadir measurements. The adopted parameterization is based on three years of output data from the 3D chemistry transport model BASCOE. The impact of the atmospheric dynamics on the stratospheric BrO distribution is treated by means of Br_y/ozone correlations built from 3D-CTM model results, while photochemical effects are taken into account using stratospheric NO_2 columns as an indicator of the BrO/Br_y ratio. The model simulations have been optimized for bromine chemistry and budget, and validated through comparisons using an extensive data set of ground-based, balloon-borne and satellite limb (SCIAMACHY) stratospheric BrO observations.

6.1 Motivation

One of the major objectives of this thesis is to quantitatively investigate and characterize the spatial and seasonal variations of tropospheric BrO at the global scale using satellite UV-visible nadir instruments. To achieve this goal, we have developed a technique, which will be presented in details in chapter 7, to retrieve tropospheric BrO VCDs from space-borne nadir observations. This algorithm is based on a residual method. The tropospheric contribution of the measured signal is obtained by subtracting a stratospheric slant column from the total (measured) BrO slant column. The stratospheric BrO correction is derived from estimates of the stratospheric VCD multiplied by an air mass factor reflecting the enhancement of the optical path in the stratosphere. The conversion of the tropospheric residual to a tropospheric vertical column is achieved by applying an appropriate tropospheric air mass factor that accounts for changes in measurement vertical sensitivity due to the viewing geometry, clouds and surface reflectivity.

---

[1] This chapter is based on: Theys, N., Van Roozendael, M., Errera, Q., Hendrick, F., Daerden, F., Chabrillat, S., Dorf, M., Pfeilsticker, K., Rozanov, A., Lotz, W., Burrows, J.P., Lambert, J.-C., Goutail, F., Roscoe, H.K., and De Mazière, M., *A global stratospheric bromine monoxide climatology based on the BASCOE chemical transport model*, Atmos. Chem. Phys., 9, 831-848, 2009.

A key component of this retrieval algorithm is the estimation of the stratospheric BrO contribution. This is the subject of the present chapter. The proposed approach relies on a climatology based on the output of the global 3-dimensional chemical transport model BASCOE. A new method for the estimation of the stratospheric BrO content is proposed, which is able to reproduce the important spatial and temporal variations of stratospheric BrO by using dynamical and chemical indicators. In practice, the climatology uses measured proxies to evaluate stratospheric BrO, which makes the approach simple, fast and well suited for satellite nadir retrieval since it guarantees that the sounded air masses and geophysical conditions are optimally represented. As the retrieval of tropospheric BrO from satellite observations and the present climatology requires great care to achieve good accuracy, the model simulations have been optimized for bromine chemistry and budget, and validated through comparisons using an extensive data set of stratospheric BrO observations.

In section 6.2, we briefly review the 3-D chemical transport model (CTM) which is at the heart of our study. We describe the set-up of bromine species implemented in the model, in the light of our current understanding of stratospheric bromine photochemistry and budget. The treatment of sulphate aerosols in the model is also presented, since it can have a substantial impact on the stratospheric chemistry. Comparisons between modeled results and correlative observations of O_3, NO_2 and BrO are shown in section 6.3. The stratospheric BrO profile (and corresponding column) climatology is developed and presented in section 6.4, together with an error analysis. Conclusions are given in section 6.5. The consequences to infer tropospheric BrO columns from satellite nadir measured total BrO columns and the present BASCOE stratospheric BrO climatology will be investigated in chapter 7, where the proposed method will be tested and validated.

6.2 Model

The model used is the stratospheric 3-dimensional chemical transport model which forms the core of BASCOE, a 4-dimensional variational (4D-Var) chemical data assimilation system designed for the analysis and forecast of stratospheric ozone and chemical species (see http://bascoe.oma.be). The CTM is described in Errera and Fonteyn (2001), Daerden et al. (2007) and Errera et al. (2008). It includes a full description of stratospheric chemistry based on 57 chemical species and a parameterization of the microphysics of polar stratospheric clouds (PSCs). All chemical species are advected and interact through 144 gas-phase reactions, 48 photolysis reactions and 9 heterogeneous reactions, all listed in the JPL compilation evaluation 14 (Sander et al., 2003). The CTM is driven by the European Centre for Medium-Range Weather Forecasts (ECMWF) operational analysis of temperatures and winds. The model is defined on 37 pressure levels from the surface to 0.1 hPa, on a 3.75° latitude and 5° longitude grid, with a model time step of 30 minutes. While the model extends down to the surface, it does not include any tropospheric process and is not expect to produce a realistic chemical composition below the tropopause.

The data used in this study result from a CTM run (no assimilation) initialized with analysis of MIPAS assimilation (details can be found in Errera et al., 2008). The simulations start on 1st April 2003 and end on 31st March 2006, covering three years of data.

6.2.1 Bromine species

The BASCOE 3-D CTM includes a detailed bromine chemistry scheme involving the photochemical reactions listed in Table 6.1. Inorganic bromine species interact through 30 gas-phase and heterogeneous photochemical reactions.

Table 6.1 Bromine reactions included in the BASCOE model (RB: reactions in BASCOE).

No	Reaction	No	Reaction
(RB1)	$BrO+NO_2+M \rightarrow BrONO_2+M$	(RB21)	$BrONO_2+O \rightarrow BrO+NO_3$
(RB2)	$BrO+HO_2 \rightarrow HOBr+O_2$	(RB22)	$BrONO_2+HCl \xrightarrow{Het} BrCl+HNO_3$
(RB3)	$BrONO_2+H_2O \xrightarrow{Het} HOBr+HNO_3$	(RB23)	$HOBr+HCl \xrightarrow{Het} BrCl+H_2O$
(RB4)	$BrO+NO \rightarrow Br + NO_2$	(RB24)	$HOBr+HBr \xrightarrow{Het} Br_2+H_2O$
(RB5)	$BrO+O \rightarrow Br+O_2$	(RB25)	$BrONO_2+h\nu \rightarrow BrO+NO_2$
(RB6)	$BrO+OH \rightarrow HO_2+Br$	(RB26)	$BrONO_2+h\nu \rightarrow Br+NO_3$
(RB7)	$BrO+ClO \rightarrow Br+OClO$	(RB27)	$HOBr+h\nu \rightarrow Br+OH$
(RB8)	$BrO+ClO \rightarrow Br+ClOO$	(RB28)	$BrCl+h\nu \rightarrow Br+Cl$
(RB9)	$BrO+ClO \rightarrow BrCl+O_2$	(RB29)	$BrO+h\nu \rightarrow Br+O$
(RB10)	$BrO+BrO \rightarrow 2Br+O_2$	(RB30)	$Br_2+h\nu \rightarrow 2Br$
(RB11)	$BrO+BrO \rightarrow Br_2+O_2$	(RB31)	$CH_3Br+h\nu \rightarrow Br+CH_3$
(RB12)	$Br+OClO \rightarrow BrO+ClO$	(RB32)	$CH_3Br+O(^1D) \rightarrow Br+products$
(RB13)	$Br+HO_2 \rightarrow HBr+O_2$	(RB33)	$CH_3Br+OH \rightarrow Br+H_2O+products$
(RB14)	$Br+CH_2O \rightarrow HBr+HCO$	(RB34)	$CBrClF_2+h\nu \rightarrow Br+Cl+products$
(RB15)	$Br+O_3 \rightarrow BrO+O_2$	(RB35)	$CBrClF_2+O(^1D) \rightarrow Br+Cl+products$
(RB16)	$Br_2+OH \rightarrow HOBr+Br$	(RB36)	$CBrF_3+h\nu \rightarrow Br+products$
(RB17)	$HOBr+O \rightarrow BrO+OH$	(RB37)	$CBrF_3+O(^1D) \rightarrow Br+products$
(RB18)	$HBr+O \rightarrow Br+OH$	(RB38)	$CH_2Br_2+ h\nu \rightarrow 2Br+products$
(RB19)	$HBr+OH \rightarrow Br+H_2O$	(RB39)	$CH_2Br_2+OH \rightarrow 2Br+products$
(RB20)	$HBr+O(^1D) \rightarrow Br+OH$		

Simulations include the reaction of $BrONO_2+O(^3P) \rightarrow BrO+NO_3$, since several studies (Soller et al., 2001; Sinnhüber et al., 2002) found that this reaction can lead to increasing daytime BrO amount above 25 km, especially at low latitudes. Updated kinetic and photochemical data for bromine species are taken from the JPL compilation evaluation 15 (Sander et al., 2006). Sensitivity tests have been made to estimate the impact on the simulated BrO fields of the incomplete (i.e. limited to bromine reactions) porting of the BASCOE chemical scheme to JPL evaluation 15 chemical kinetics and photochemical data. Differences in the BrO concentrations were found to be lower than 7%, with respect to a complete update of the full chemistry. This source of error is considered as being rather small compared to the BrO observational error (see section 6.3.2).

Our calculations assume a total inorganic bromine loading in the stratosphere of 23 pptv, in accordance with published results (Pfeilsticker et al., 2000; Salawitch et al., 2006; Hendrick et al., 2007 and 2008; Theys et al., 2007). The model includes the main tropospheric long-lived (LL) organic bromine sources: methyl bromide (CH_3Br), Halon-

1211 ($CBrClF_2$) and Halon-1301 ($CBrF_3$). The volume mixing ratios have been scaled and made consistent with surface values measured in 1999 by Montzka et al. (2003); i.e. CH_3Br: 9.5 pptv, Halon-1211: 4.0 pptv and Halon-1301: 3.5 pptv (a constant 1 pptv of Br from Halon-2402 has been added to the measured 2.5 pptv of Halon-1301). The full conversion of LL organic bromine compounds into inorganic forms (occurring above ~ 25 km) leads to a stratospheric Br_y loading of 17 pptv, for air of 4-5 years mean age. To account for the bromine release from very short-lived species, an additional contribution of 6 pptv has been considered, consisting of 5 pptv of Br_y from dibromomethane (CH_2Br_2) and 1 pptv of tropospheric inorganic product gas directly injected at the tropopause. This method of implementing the short-lived bromine species is similar to what has been used in Feng et al. (2007).

A loss process of Br_y in the troposphere through washout due to the high solubility of HBr, has been implemented and is described by a washout time τ. This washout time is assumed to be constant throughout the troposphere and is fixed at 15 days. Model calculations often use a mean washout time τ of about 10 to 30 days (e.g. von Glasow et al., 2004; Sinnhüber and Folkins, 2006).

6.2.2 Stratospheric aerosol settings

Particular attention has been paid to the treatment of the stratospheric sulphate aerosols and their impact on stratospheric bromine chemistry. The heterogeneous reactions on the surface of stratospheric aerosols can significantly influence the BrO/Br_y partitioning through its impact on the NO_x/NO_y ratio or directly through the heterogeneous reactions involving inorganic bromine species (Lary et al., 1996).

In the present work, an improved set-up of stratospheric aerosols has been implemented, derived from that used in Daerden et al. (2007). The aerosol surface area density is calculated based on the aerosol size distribution, which is assumed to follow a log-normal shape defined by the so-called RNS parameters (R: mean radius, N: total number density, S: standard deviation). The BASCOE aerosol configuration relies on a composite profile climatology of RNS parameter estimates for each month of the year and for 19 zonal bands. The RNS parameters have been estimated such that the corresponding 1 μm aerosol extinction is consistent with SAGE-II extinction from Bingen et al. (2004) for latitudes between ± 60° and with POAM III extinction from Fromm et al. (2003) for regions poleward of ± 60°. Adopting this approach for the treatment of stratospheric aerosols substantially improves the results. This is further verified in section 6.3.1 where BASCOE NO_2 stratospheric columns are compared with observations from ground-based UV-visible instruments of the Network for the Detection of Atmospheric Composition Change.

6.3 Verification of model results

Several studies have been conducted recently (Geer et al., 2006; Vigouroux et al., 2007; Daerden et al., 2007; Errera et al., 2008), where the BASCOE CTM has been extensively evaluated based on O_3, NO_2, H_2O, HNO_3, N_2O and CH_4 observations. These results showed that BASCOE is able to reproduce important aspects of the stratospheric composition. Here, the reliability of the BASCOE results is further assessed for ozone, nitrogen dioxide (section 6.3.1) and bromine monoxide (section 6.3.2), by means of validation using ground-based, balloon and satellite limb observations.

6.3.1 Comparison of modeled and measured stratospheric O_3 and NO_2 columns

The measurement data were obtained from zenith sky UV-visible observations, performed at four stations which are part of the NDACC. The observations are made during twilight periods for solar zenith angles ranging from 86° to 91°. At all stations, the column densities of O_3 and NO_2 along the optical path have been retrieved using the DOAS technique. The analysis is made for O_3 in the 435-555 nm wavelength interval and for NO_2 in the 420-470 nm range. Slant columns are converted into vertical columns using an air mass factor. Since ground-based measurements are made for high SZA, the retrieved O_3 and NO_2 columns are predominantly of stratospheric origin. For our comparison exercise, simulated ozone and nitrogen dioxide concentration profiles have been interpolated at the location corresponding to each station and for solar zenith angles of 90° (representative of the ground-based retrieved columns at sunrise and sunset), and then integrated between the tropopause and the highest model level.
Figure 6.1 presents the modeled and measured stratospheric O_3 columns for the period from 04/2003 to 03/2006 for Harestua (60.2°N, 10.7°E), Jungfraujoch (46.5°N, 7.9°E), Kerguelen (49.4°S, 70.3°E) and Rothera (67.6°S, 68.1°W).

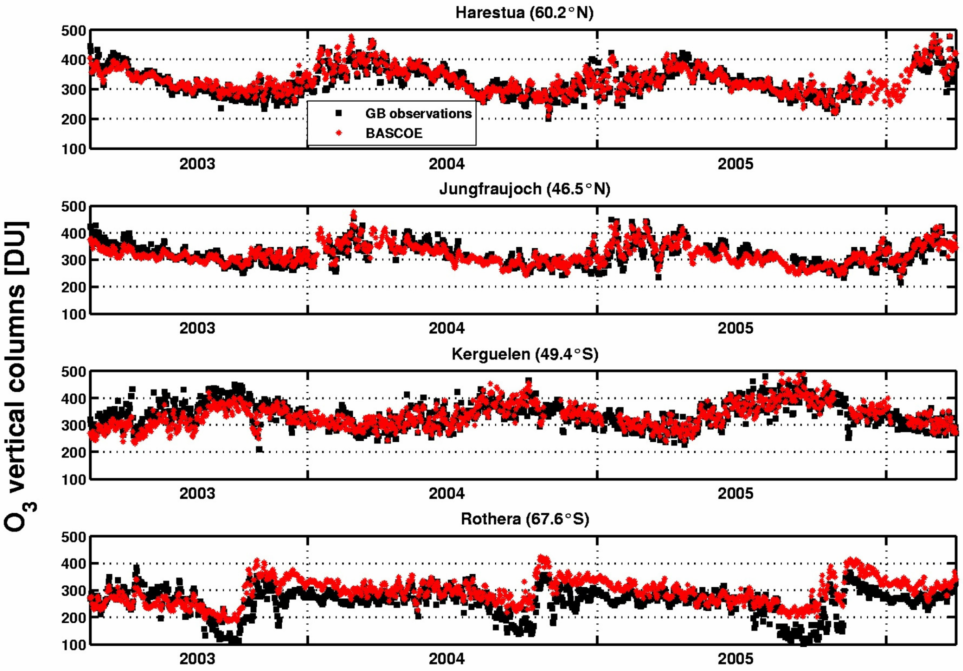

Figure 6.1 Time-series of sunset stratospheric O_3 vertical columns from BASCOE analysis and ground-based UV-visible observations at 4 NDACC stations (top to bottom): Harestua, Jungfraujoch, Kerguelen and Rothera.

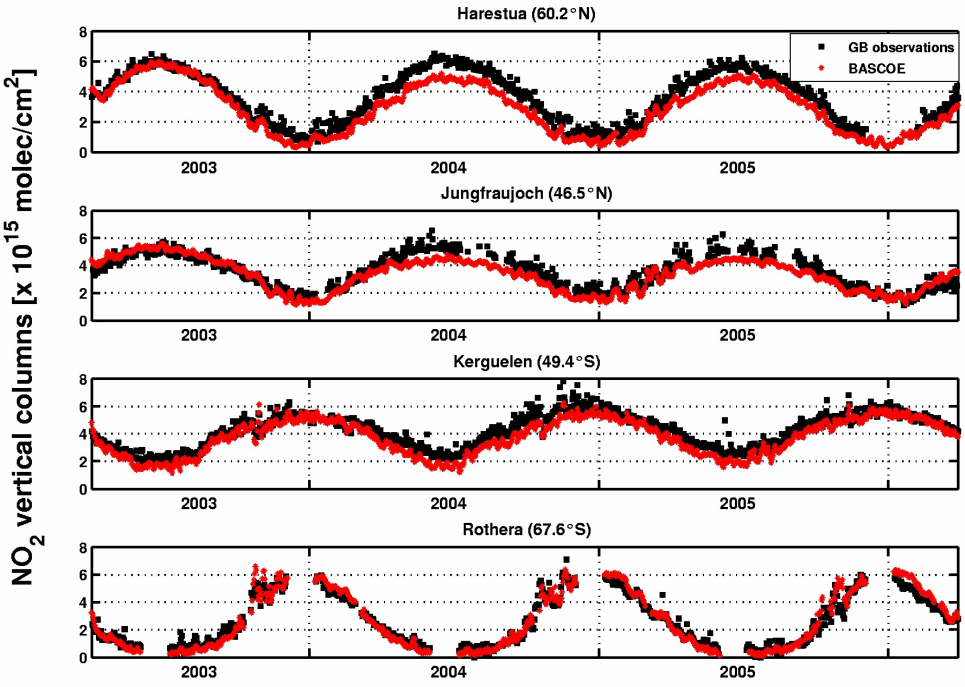

Figure 6.2 Time-series of sunset stratospheric NO_2 vertical columns from BASCOE analysis and ground-based UV-visible observations at 4 NDACC stations (top to bottom): Harestua, Jungfraujoch, Kerguelen and Rothera.

A good agreement is found for the entire period for Harestua, Jungfraujoch and Kerguelen with relative differences smaller than 15%. The observed seasonal and short-term dynamical changes are well captured by the simulations. At Rothera, the agreement is reasonable except during ozone-hole and summer conditions, where BASCOE overestimates the stratospheric O_3 columns by 50 to 100 DU. This confirms the findings of Errera et al. (2008). Note however that the measurements at Rothera have the tendency to underestimate the ozone columns by 10 to 15 DU for ozone hole conditions (Roscoe et al., 2001).

To a large extent, the lower stratospheric BrO concentration is controlled by NO_2 through the termolecular reaction $BrO+NO_2+M \rightarrow BrONO_2+M$. Accurate modeling of nitrogen dioxide is thus a prerequisite to evaluate the stratospheric BrO amount.

Figure 6.2 shows the simulated and measured stratospheric NO_2 columns for Harestua, Jungfraujoch, Kerguelen and Rothera. The results are shown for sunset, but similar agreement is obtained for sunrise conditions.

Most significant features of the observed seasonal and short-term NO_2 variabilities (related to photochemical and/or dynamical effects) are consistently reproduced by the simulations. However, the model shows a small tendency to underestimate the retrieved NO_2 columns. This might be related to the limited time/horizontal resolution and to the fact that the modeled columns are estimated at twilight, conditions where stratospheric NO_2 undergoes a rapid variation with time. Sensitivity tests show that the estimation of the modeled stratospheric NO_2 columns can be affected by this effect, up to 0.7×10^{15} molec/cm², with the largest discrepancies in summer. The absolute accuracy of the retrieved stratospheric NO_2 columns at NDACC stations can also be limited by (1) uncertainties related to the NO_2 absorption cross-sections and their temperature dependence (Koike et al., 1997; Roscoe et al., 1999; Vandaele et al., 2005), (2) AMF uncertainties associated with seasonal, meridian and diurnal variations of the NO_2 profile shape (Lambert et al., 1999). The overall uncertainty on the retrieved stratospheric NO_2 columns is of about 10%. Note that the possibility of a significant contribution to the measured column by tropospheric NO_2 from pollution is unlikely since the selected stations are located in clean areas. Nonetheless, the BASCOE model results agree in a satisfactory way with the observations (differences smaller than 1.2×10^{15} molec/cm²), knowing the uncertainties on both modelled and measured stratospheric NO_2 columns.

6.3.2 Comparison of modeled and measured stratospheric BrO

The consistency between the stratospheric BrO profiles, as simulated by the BASCOE model, and correlative data has been verified. For this purpose, the modeled BrO profiles have been interpolated at the location and at the solar zenith angle of each observation. The measurements reported in this study performed from ground-based, balloon and satellite platforms, are listed in Table 6.2. These correlative data set sample latitudes extending from polar to tropical regions, with the advantage that the resulting comparisons can be made under a large variety of photochemical regimes.

Table 6.2 Summary of the BrO observation data sets used for the comparisons with model results.

Observation type	Location	Period	Reference
Ground-based DOAS (BIRA - IASB)			
Harestua, Norway	60.22°N 10.75°E	04/2003-03/2006	*Hendrick et al. [2007]*
Observatoire de Haute-Provence, France	43.94°N 5.71°E	02/2005-03/2006	*Hendrick et al. [2009]*
Reunion Island, France	21.06°S 55.47°E	07/2004-07/2005	*Theys et al. [2007]*
Balloon LPMA/DOAS (U. Heidelberg)			
Kiruna, Sweden	67.84°N 21.06°E	24 March 2004	*Dorf et al. [2006a]*
Aire sur l'Adour, France	43.70°N 0.25°W	09 October 2003	*Dorf et al. [2006a]*
Teresina, Brazil	5.1°S 42.9°W	17 June 2005	*Dorf et al. [2008]*
SCIAMACHY limb (U. Bremen)			
	Global	04/2003-02/2004	*Rozanov et al. [2005b]*

The stratospheric BrO vertical profiles obtained by the Microwave Limb Sounder (MLS) on the Aura satellite (Kovalenko et al., 2008) has not been used for our comparisons, since these measurements are sensitive to the BrO profile over a pressure range from 10 to 3.2 hPa, where only a small fraction of the total amount of stratospheric BrO is present. Furthermore, the estimated precision and accuracy of the data make them unsuitable for our comparison study.

6.3.2.1 Comparison to ground-based stratospheric BrO data

The ground-based observations have been conducted at Harestua, Observatoire de Haute-Provence and Reunion Island. The period covered by the simulations and the observations is April 2003-March 2006 at Harestua, February 2005-March 2006 at OHP and July 2004-July 2005 at Reunion Island. The instrumental set-ups are described in chapter 4. BrO differential slant columns densities are retrieved in the 345-359 nm wavelength range according to the DOAS settings presented in chapter 5.

At Harestua and OHP, stratospheric BrO profiles are retrieved by applying a profiling technique to the measured DSCDs. The retrieval algorithm is based on the Optimal Estimation Method (Rodgers, 2000) and has been extensively described in Hendrick et al. (2007). It is based on a forward model that includes a stacked box photochemical model allowing to reproduce the strong diurnal variation of BrO at twilight. The stratospheric BrO profiles are retrieved for a solar zenith angle of 80°, separately for sunrise and sunset measurements. The characterization of the information content of the retrieval shows that high sensitivity to the stratospheric BrO profile is obtained between 12 and 28 km altitude, with a vertical resolution of approximately 8 km.

Ground-based BrO partial columns are calculated between 12-20 km and 20-28 km, in order to take benefit from the vertical resolution offered by the profiling technique, and are compared to BASCOE data. Figures 6.3 and 6.4 present the comparisons between modeled and ground-based BrO partial columns, at Harestua and OHP respectively. The error bars associated with the ground-based partial columns are estimates of the random and systematic uncertainties of the retrieval. The model and ground-based data are given at 80° SZA for sunset. At both stations, the modeled partial columns agree within 20-

25% with the values derived from the ground-based observations. In particular, the seasonality of BrO, directly linked to the NO_2 seasonal cycle, is consistently captured by both model and ground-based data. Short-term variations linked to dynamical changes are also shown by both datasets in the lower stratosphere. Although not reproduced here, similar results are found with morning data.

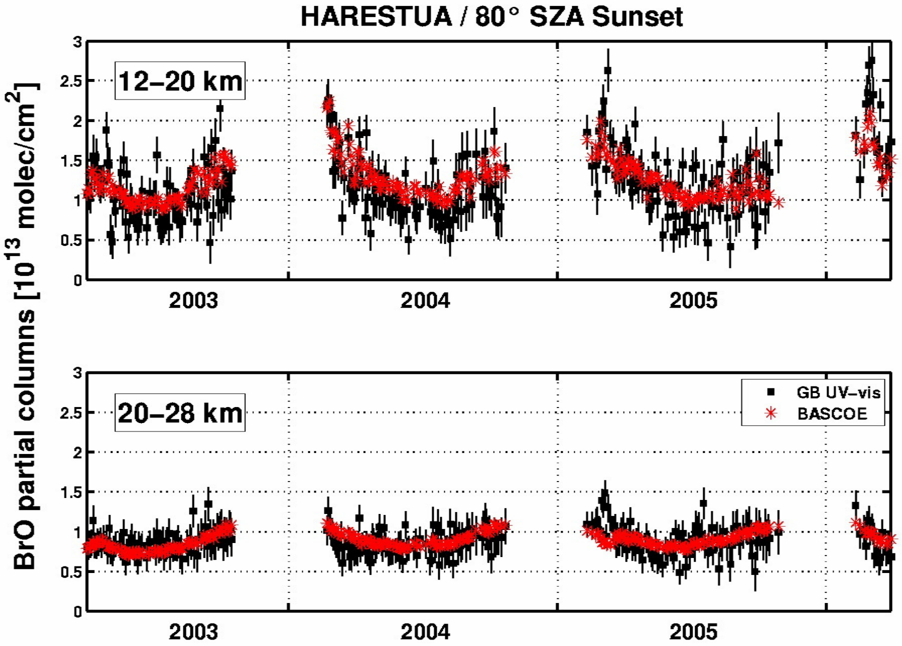

Figure 6.3 Comparison between modeled and ground-based stratospheric BrO partial columns, at Harestua for 80° SZA sunset. The BrO profiles are integrated between 12-20 km (top) and 20-28 km (bottom).

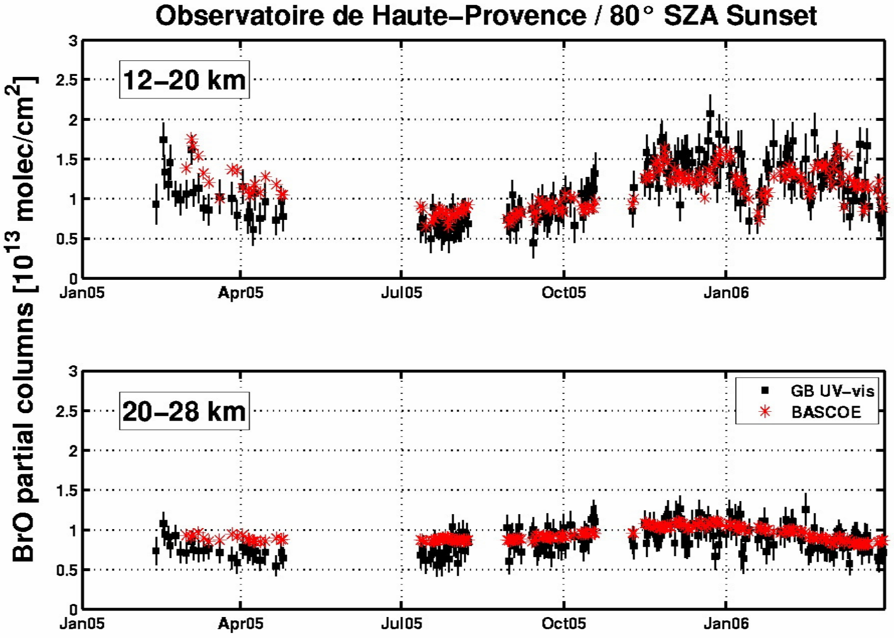

Figure 6.4 same as Figure 6.3, at Observatoire de Haute-Provence.

At Reunion Island, the inversion of stratospheric BrO profiles by applying the profiling technique has been found to be difficult for two reasons: (1) the poorer performance of the instrument in terms of the signal to noise ratio, and (2) the smaller BrO absorption at tropical latitudes. Consequently, only stratospheric BrO columns have been retrieved (chapter 5). The error estimate associated to the retrieved stratospheric columns is slightly larger for Reunion-Island than for Harestua and OHP data. For this study, we compare the retrieved and modeled stratospheric BrO columns only at a single reference SZA (fixed at 80° for sunset). The comparison between modeled and ground-based stratospheric BrO columns is displayed in Figure 6.5.

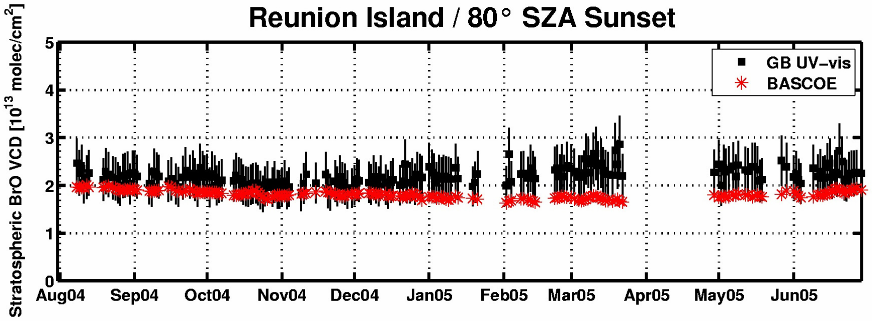

Figure 6.5 Comparison between modelled and ground-based stratospheric BrO columns, at Reunion Island for 80° SZA sunset.

The modeled BrO columns are calculated by integrating the stratospheric BrO profiles from the tropopause height, based on temperature profiles from ECMWF data, to the upper model level. Figure 6.5 shows that the modeled BrO columns are slightly smaller than the columns retrieved from ground-based measurements, but are within the error bars.

6.3.2.2 Comparison with LPMA/DOAS balloon profiles

A detailed description of the LPMA/DOAS (Limb Profile Monitor of the Atmosphere/Differential Optical Absorption Spectroscopy) BrO measurements used here can be found in Harder et al. (1998, 2000), Pfeilsticker et al. (2000) and Dorf et al. (2006a, 2006b, 2008). The LPMA/DOAS measurements use the solar occultation technique. The BrO profiles are retrieved using an Optimal Estimation Method applied to the BrO slant column densities measured during the ascent of the balloon. The accuracy of the technique is generally very good (better than ±12%, Harder et al., 1998) and the vertical resolution of the inverted stratospheric BrO profile is about 2 km.

For the present comparisons, three balloon flights originated from Kiruna, Aire sur l'Adour and Teresina are taken into account (see Table 6.2 for details). The BASCOE BrO profiles have been interpolated to the location of the balloon and at the SZA corresponding to the observation (varying during the ascent of the balloon) in order to have identical photochemical conditions between the balloon and the model profiles. Figure 6.6 shows the measured BrO balloon profiles together with the model calculation for the three flights.

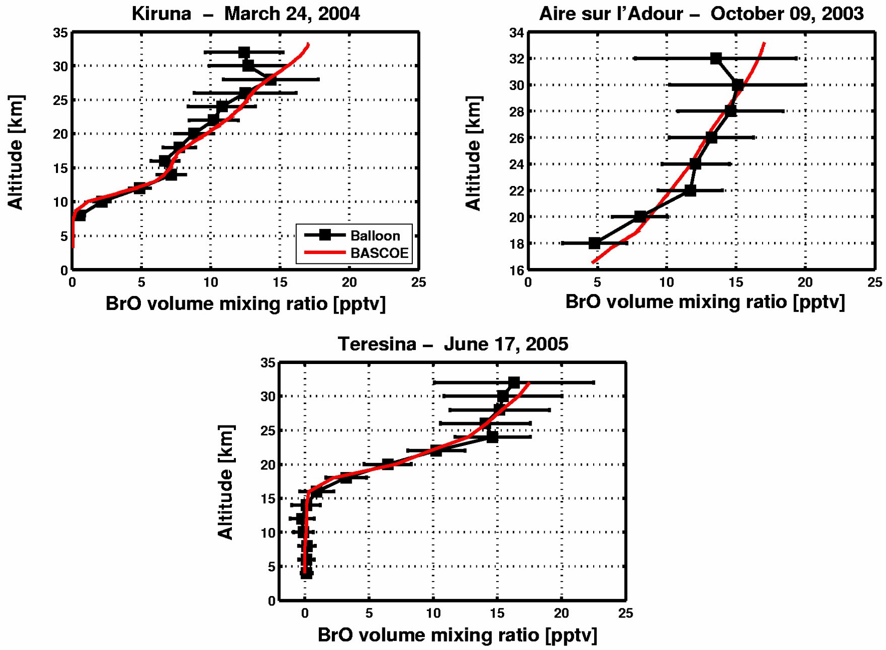

Figure 6.6 Comparison between modeled and LPMA/DOAS ascent balloon BrO profiles at Kiruna, Aire sur l'Adour and Teresina.

In general, we find a good agreement between the LPMA/DOAS and modeled BrO profiles. The observed differences are within the error bars of the balloon-borne profiles. These comparison results are similar to the ones presented in Feng et al. (2007) and Dorf et al. (2006a,b and 2008).

6.3.2.3 Comparison to SCIAMACHY limb profiles

Among other geophysical data products, stratospheric BrO profiles can be retrieved from the SCIAMACHY limb spectral measurements (Rozanov et al., 2005b; Sinnhüber et al., 2005; Sheode et al., 2006; Sioris et al. 2006) on the global scale (since ENVISAT is in polar sun-synchronous orbit). In this study, we use the BrO profiles derived at the Institute of Environmental Physics (IUP) at the University of Bremen (scientific product: version 3.2). A detailed description of the retrieval algorithm as well as the results of the error analysis and sensitivity studies can be found in (Rozanov et al., 2005b) where, however, a precursor version of the retrieval processor (version 1.x) is discussed. The most recent retrieval version 3.2, used in this study, employs the same inversion algorithm as earlier versions (e.g., version 1.x described in the above cited paper) differing, however, quite strongly in the retrieval parameter settings. For example, a slightly different spectral range (338.0 – 356.2 nm) and a higher reference tangent height (about 35 km) were used, Levenberg-Marquardt iterative scheme was replaced by more common Newton-type iterations, and the regularization parameters were optimized. Furthermore, additional information on pressure and temperature provided by the ECMWF were used. A more extensive description of the retrieval processor of version 3.2 is presented in (Hendrick et al., 2009), where also the accuracy of the retrieved BrO profiles has been assessed. A detailed list of the retrieval parameter settings for the current and previous versions of the retrieval software can be found at the data archive web page of the IUP-Bremen (http://www.iup.physik.uni-bremen.de/scia-arc). SCIAMACHY limb BrO profiles are retrieved with the highest sensitivity in the 15-27 km altitude region and the vertical resolution is between 3 and 5 km (Rozanov et al., 2005b; Hendrick et al., 2009).

For our comparison exercise, we have selected 11 complete days of data (the 15th of each month from April 2003 to February 2004). For each day, modeled and measured BrO partial columns have been calculated and compared for three altitude regions (15 to 19 km, 19 to 23 km and 23 to 27 km). Figure 6.7 shows the comparison results (zonal means, for SZA smaller than 85°), for the 15ths of April, July, October of 2003 and January 2004.

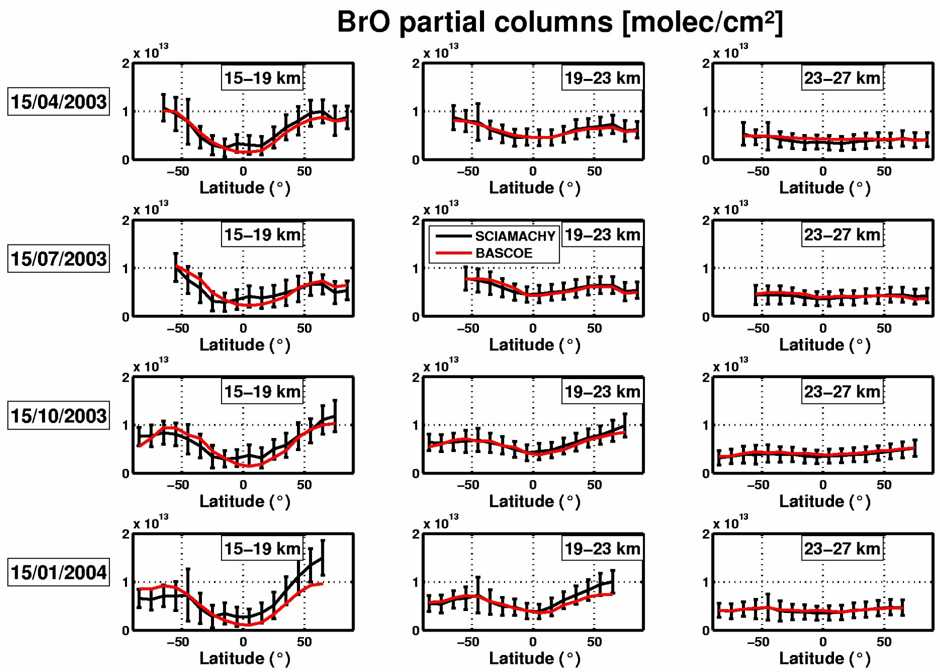

Figure 6.7 Zonal means of BrO partial columns (SZA lower than 85°), for three altitude ranges (left plots: 15 to 19 km, centre plots: 19 to 23 km, right plots: 23 to 27 km) calculated from SCIAMACHY limb profiles and BASCOE modeled profiles for the 15ths of April, July, October (2003) and January (2004).

The error bars represent the standard deviation of the SCIAMACHY partial columns within each latitudinal bin plus an estimated systematic error of 10% (added in quadrature). The minimum error is determined by the detection limit of the SCIAMACHY limb measurements which is estimated to be about 10^{12} molec/cm². Considering the uncertainties on satellite measurements, the agreement obtained is satisfying at all latitudes, for all altitude layers.

Comparison results for the 15-27 km BrO partial columns for different latitude bands (60°S-50°S, 40°S-30°S, 30°N-40°N and 50°N-60°N) are depicted in Figure 6.8, for the 11 days of data (designated by their respective months on the x-axis).

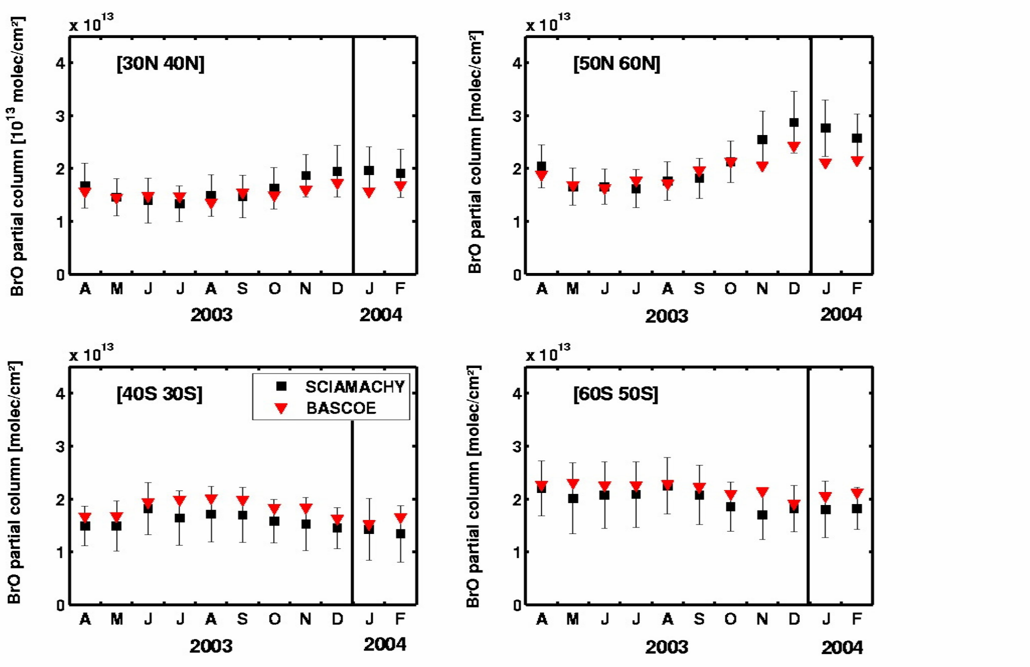

Figure 6.8 Comparison of the 15-27 km BrO partial columns (zonal means) calculated from the SCIAMACHY limb and BASCOE profiles for 11 days of data sampling the period from April 2003 to February 2004 and for different latitude bands.

It shows that the agreement between BASCOE and SCIAMACHY partial columns is reasonably good; BASCOE data are most of the time within the error bars associated to the SCIAMACHY partial columns. The seasonality of BrO is also consistently captured at all latitudes by both SCIAMACHY and BASCOE data.

6.3.2.4 Discussion

As shown in previous sections, the model calculation reproduces the observed BrO generally very well, taking into account the overall errors of the measurements (about 20-25%), for the three different types of observations (ground-based, balloon, space-borne limb measurements) used in this study. The seasonal and latitudinal variations are well captured by the model.

Model and measured data agree well assuming a total inorganic bromine loading of 23 pptv. The uncertainty on the contribution of VSLS to stratospheric Br_y has recently received a lot of attention, and is a topic stressed in the WMO report (2007). Furthermore, the quantification of the inorganic bromine amount at the lower stratospheric entry levels is difficult, because it is controlled by processes with rather large uncertainties (surface emissions, transport and chemical lifetime of brominated short-lived species). A simple way to implement the bromine short-lived species in the model has been considered by assuming that the total Br_y is coming from a single effective source of CH_3Br (with a mixing ratio of 23 pptv at the surface). The stratospheric BrO results, from this test scenario, are displayed with green lines in Figure 6.9, presenting the lower stratospheric BrO partial columns (12-20 km altitude range) at Harestua and OHP together with the measured data, for the period from January 2005 to

March 2006. It can be seen that, in general, the stratospheric BrO modeled in this way is substantially smaller than the measured stratospheric BrO.

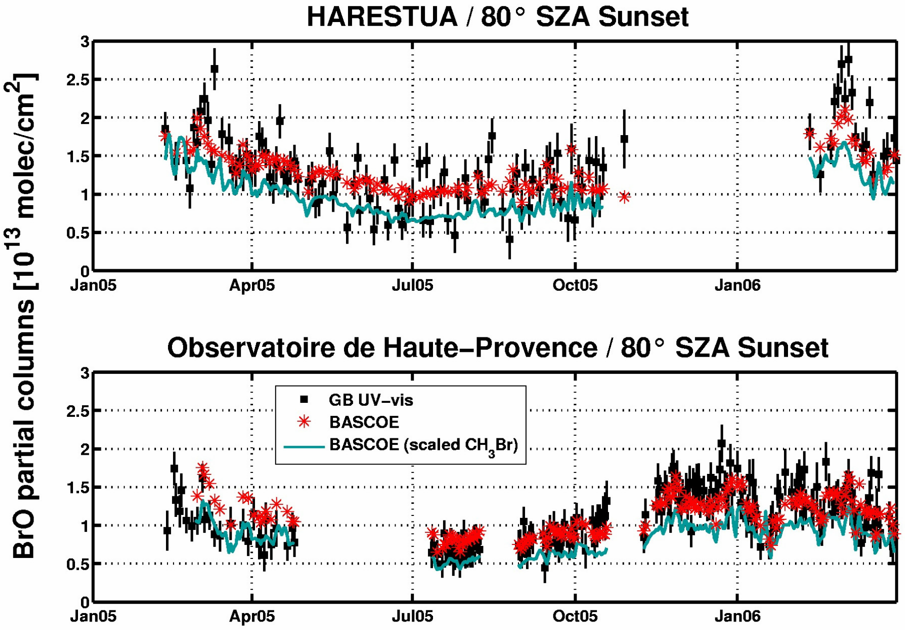

Figure 6.9 Comparison between modeled and ground-based stratospheric BrO partial columns (12-20 km altitude range), at Harestua (top) and Observatoire de Haute-Provence (bottom) for the period from January 2005 to March 2006. BASCOE assumes $[Br_y]$=23 pptv for two different scenarios: (red) stratospheric inorganic bromine has contributions from CH_3Br, halons, VSLS and product gases as described in section 6.2.1, (green) stratospheric Br_y is supplied only by the decomposition of methyl bromide (scaled). Black squares: ground-based observations.

Taking into account that the short-lived source gases are decomposed faster than methyl bromide, the set-up of short-lived species in the model as proposed in section 6.2.1 leads to a better consistency between simulated and measured stratospheric BrO. This confirms, on a larger dataset, the findings of other studies (Feng et al., 2007; Dorf et al., 2006b; Dorf et al., 2008), who found that the agreement between model and balloon data is significantly improved when having explicitly the short-lived source gases.

Sensitivity tests have been carried out in order to estimate the impact on the model results of the uncertainties on the main reaction rate constants (given in the JPL 2006 compilation), following the work presented in Sinnhüber et al. (2002) and Hendrick et al. (2008). This gives a total error on the daytime BrO concentration smaller than 15%. Further photochemical uncertainties are kept small by considering in our comparisons, only data for SZA lower than 85°.

Moreover, stratospheric BrO is strongly dependent on NO_2 and the reasonable agreement between modeled and measured NO_2 columns at the NDACC stations (see section 6.3.1), reinforce our confidence in the BrO simulations and in the fact that discrepancies due to non-appropriate simulation of NO_2 are rather small. Additional comparisons of BASCOE and SCIAMACHY limb profiles were performed for O_3 and NO_2 (details on SCIAMACHY limb retrieval can be found in Bracher et al., 2007 and Butz et al., 2006).

A satisfactory agreement has been found for both species, in accordance with the conclusions of section 6.3.1. These results further consolidate our modeled BrO results.

6.4 Stratospheric BrO climatology

6.4.1 General approach

The primary motivation behind the development of a new BrO climatology, is the retrieval of tropospheric BrO columns from satellite nadir observations, using a residual approach. To achieve this goal, the stratospheric BrO climatology has to meet specific requirements:

- Global coverage.
- The diurnal variation of BrO has to be taken into account, since the instruments are sounding the atmosphere under a large range of possible solar zenith angles. However, we restrict ourselves to SZA lower than 80°, because the retrieval of tropospheric BrO columns from space nadir observations at high solar zenith angles, is largely complicated due to two main reasons: (1) the measured signal is dominated by the absorption in the stratosphere, due to the very large photon paths in the stratosphere and the reduced sensitivity to the troposphere, and (2) stratospheric BrO has a sharp photochemical variation at twilight, that can lead to photochemical gradients along the slant stratospheric photon path, and even horizontal inhomogeneity of the BrO field within the measured pixel.
- Stratospheric BrO is highly variable in time and space, and depends on several parameters and atmospheric conditions. The BrO climatology must be able to reproduce with enough precision the BrO profiles for the large variety of possible scenarios. Misrepresentation of important patterns of stratospheric BrO (e.g. due to the effect of atmospheric dynamics) will lead to artifacts in the retrieved troposheric BrO columns.
- The stratospheric BrO climatology must provide an effective profile representative of the sounded atmosphere (averaged profile over the measured pixel).

The stratospheric BrO climatology proposed here is based on a parameterization which reflects the main dynamical and photochemical processes controlling the distribution of BrO in the stratosphere.
The stratospheric bromine monoxide profile can be written:

$$\mathrm{BrO} = \mathrm{Br_y} \ \mathrm{x} \ \frac{\mathrm{BrO}}{\mathrm{Br_y}} \tag{6.1}$$

Where Br_y is the inorganic bromine profile accounting for all inorganic bromine species (active bromine and bromine reservoirs). Since inorganic bromine can be considered as a good chemical tracer due to its long chemical lifetime, equation 6.1 effectively separates the effects on the BrO vertical distribution due to the dynamics of the atmosphere and the photochemistry. For a given stratospheric air parcel (with a constant Br_y volume mixing ratio), rapid photochemical reactions between the various inorganic bromine species are taking place and affect the partitioning of BrO into the inorganic bromine species family (BrO/Br_y). In this study, these two different aspects are treated separately by developing two distinct climatologies. The development of a Br_y profile climatology is the focus of section 6.4.2, while a partitioning profile climatology (BrO/Br_y) is presented in section 6.4.3. The key requirements to derive a suitable stratospheric BrO profile from equation 6.1 is to obtain sufficient information about the dynamical and photochemical state of the sounded atmosphere.

6.4.2 Dynamics of the stratosphere

Since most of the inorganic bromine molecules are located below 35 km, we mainly focus on the lower and middle stratosphere. Hereafter, we will refer to the lower, middle and upper stratosphere to designate the stratospheric layers from the tropopause to 25 km, from 25 km to 35 km and above 35 km, respectively. As already mentioned, the distribution of inorganic bromine in the stratosphere results from the influence of dynamical processes. For typical time scales of the order of months, the transport of air masses in the stratosphere is governed by the mean meridional circulation, which brings inorganic bromine produced in the tropical lower and middle stratosphere to extra-tropical latitudes. In principle, a monthly zonally-averaged Br_y profile climatology is able to reproduce in a satisfactory way the relevant spatial and temporal variations of stratospheric inorganic bromine due to the meridional circulation (e.g. ascending and descending advection in the tropical and polar regions respectively, Holton 1995). However it fails to represent the Br_y variability due to shorter dynamical processes. A more sophisticated climatology is thus needed to reproduce the effects on Br_y due to short-term transport. At the scale of several days, the motion of stratospheric air parcels is driven by zonal winds. As a first approximation, it can be assumed that the air masses are transported adiabatically (motion along quasi-horizontal isentropic surfaces). Zonal winds tend to eliminate the longitudinal gradients of tracers of the stratospheric dynamics (as Br_y). The effect on the distribution of Br_y varies as a function of altitude, latitude and season. Such short-term dynamical effects are well accounted for by the BASCOE 3-D CTM since it uses 6 hourly ECMWF operational analysis of winds and temperatures. This is demonstrated by the fact that short-term changes in measured O_3 columns are consistently captured by the model (see Figure 6.1 in section 6.3.1). The important concept introduced in this work to reproduce the effect on stratospheric Br_y due to short-term transport, is to use stratospheric ozone as a proxy for the dynamical state of the stratosphere. For non-chlorine activated conditions, ozone in the lower and middle stratosphere can be considered as a tracer of the dynamics of the stratosphere (chemical lifetime about one to several months). Since stratospheric inorganic bromine and ozone are both produced mainly in the tropical lower stratosphere and are sensitive to the stratospheric dynamics in a similar way, a correlation between Br_y and O_3 is expected. This is illustrated in Figure 6.10, where the O_3 and Br_y volume mixing ratios, as simulated by the BASCOE model, are plotted for a low stratospheric isentropic level for the 1st March 2004 in the northern hemisphere. The large dynamical patterns, characteristic of this season, are obviously reproduced by both ozone and Br_y VMRs.

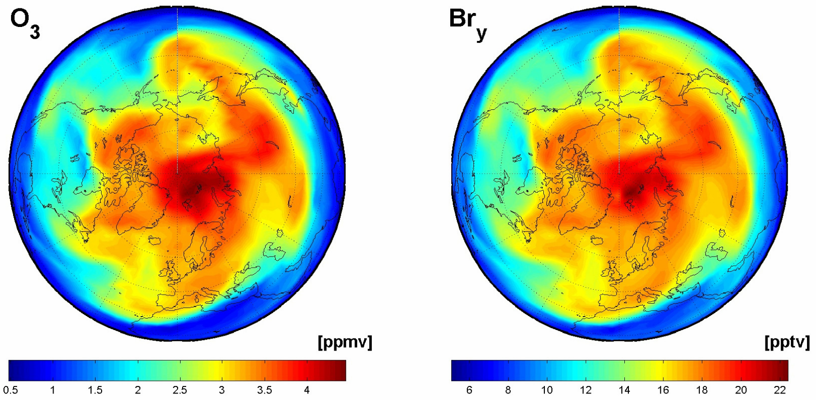

Figure 6.10 Example of BASCOE O_3 and Br_y volume mixing ratios in the northern hemisphere at a potential temperature of 475 K (~60 mb), for the 1st March 2004 at 00:00 UT.

Based on this noticeable property, we propose a stratospheric Br_y concentration profile climatology based on a simple parameterization using several inputs: month, latitude and stratospheric ozone column. The dependency of the Br_y climatology with the month of the year and the latitude allows to reproduce the effect on Br_y due to the seasonal and latitudinal variations of the meridional circulation, and implicitly for the changes in the zonal winds.

The inorganic bromine profile climatology has been generated by considering the set of Br_y profiles, simulated by BASCOE for the period from April 2003 to March 2006. The Br_y profiles have been interpolated on a regular altitude grid (step: 1 km) covering the stratosphere and classified by month, latitude (18 bands defined by the following boundaries: -90°, -80°,…, 80°, 90°) and O_3 column (19 blocks of 25 Dobson unit width centered around 125, 150, …, 550, 575 DU). The inorganic bromine profile climatology is built by calculating the average of the Br_y profiles corresponding to each month, latitude band, and O_3 column bin. Different weights (proportional to the cell areas) have been assigned to the Br_y profiles to account for the fact that the model cells vary in size with latitude and thus must have different contributions to the mean (this effect is particularly important close to the poles).

In order to gain better insight into the consistency of the proposed Br_y parameterization, Figure 6.11 illustrates the correlation between stratospheric O_3 and Br_y vertical columns, as simulated by BASCOE, for two particular cases: (1) northern mid-latitudes (40°N-50°N) in March, (2) southern high-latitudes (70°S-60°S) in September.

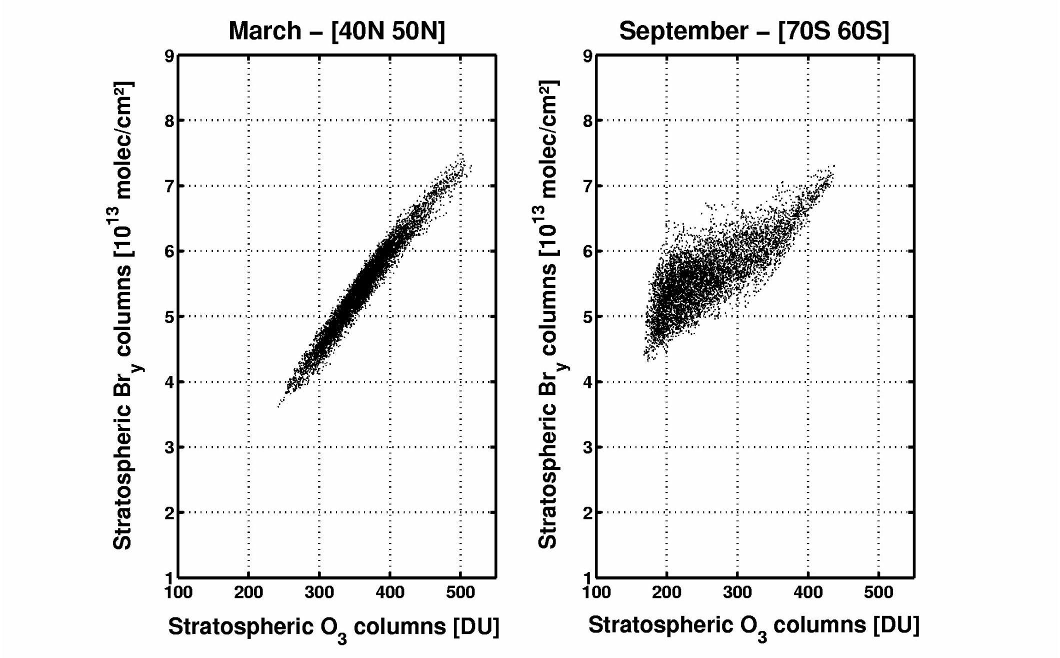

Figure 6.11 Correlation between stratospheric Br_y and O_3 vertical columns from BASCOE, for (left) March [40°N-50°N] and (right) September [70°S-60°S].

For northern mid-latitudes, the correlation between O_3 and Br_y vertical columns is excellent. The correlation coefficient is equal to 0.98. For southern high-latitudes in spring, the correlation deteriorates since stratospheric ozone can no longer be considered as a dynamical tracer (due to its destruction by chlorine species, activated through heterogeneous reactions on the surface of PSCs), and because of the presence of the strong polar dynamical vortex. However, it can be seen that there is only a moderate dispersion of Br_y columns around the mean, for a given O_3 column interval. The relevance of the proposed Br_y climatology will be assessed and consolidated in section 6.4.5, through a comprehensive error analysis.

As already mentioned earlier, the bromine monoxide profile climatology is intended to be used for the retrieval of tropospheric BrO columns from satellite nadir observations. In a first step of the calculation of BrO profiles (see equation 6.1), stratospheric Br_y concentration profiles can be derived by using the Br_y profile parameterization established here, together with the O_3 columns retrieved from the observations. This has several advantages (1) it is simple and requires only limited computation resources, (2) the ozone column is a standard product which is retrieved operationally with an excellent accuracy (error lower than 1 or 2 %), and (3) it guarantees to represent the same air masses and geophysical conditions as the BrO retrieval. However, the retrieved total O_3 column contains a small contribution from tropospheric ozone. This can not be accounted for in the Br_y climatology, since BASCOE does not include any tropospheric processes and is not expected to produce realistic results below the tropopause. In practice, this can be (at least partly) corrected for by subtracting, from the retrieved total O_3 column, a tropospheric contribution estimated from a tropospheric ozone climatology (e.g. Logan, 1999).

6.4.3 Bromine monoxide photochemistry

As mentioned earlier, the bromine monoxide profile is obtained by equation 6.1 through a partitioning factor (BrO/Br_y) calculated as a function of the altitude, and applied to the inorganic bromine profile. In order to evaluate the ratio (BrO/Br_y), it is necessary to identify the dominant photochemical regimes affecting the bromine partitioning during daytime in the lower and middle stratosphere. A detailed description of the gas-phase and heterogeneous stratospheric bromine chemistry can be found in sections 2.2.3 and 2.2.4; see also a list of the most relevant reactions in Table 6.1.

For unperturbed atmospheric conditions, bromine monoxide is in photochemical equilibrium with the bromine reservoirs (mostly $BrONO_2$ and HOBr) formed by the reactions:

$$BrO + NO_2 + M \rightarrow BrONO_2 + M \qquad \text{(RB 1)}$$

$$BrO + HO_2 \rightarrow HOBr + O_2 \qquad \text{(RB 2)}$$

The loss processes of $BrONO_2$ and HOBr are dominated by the photolysis and the reaction with O. Note that bromine nitrate can be converted by heterogeneous reactions on sulphate aerosols into HOBr:

$$BrONO_2 + H_2O \xrightarrow{Het} HOBr + HNO_3 \qquad \text{(RB 3)}$$

This reaction is expected to play an important role on the partitioning factor before sunrise, but a smaller one on daytime bromine photochemistry (for SZA lower than 80°), because of the efficient photolysis of HOBr.

Hence during daytime, bromine nitrate is the major bromine reservoir. As a first approximation, the bromine partitioning factor can be expressed as follows:

$$\frac{BrO}{Br_y} \approx \frac{BrO}{BrO+BrONO_2} = \frac{1}{1+\dfrac{K_{BrONO_2} NO_2}{L_{BrONO_2}}} \qquad (6.2)$$

Where K_{BrONO_2} and L_{BrONO_2} are the formation and loss rates of $BrONO_2$, respectively; NO_2 is the nitrogen dioxide concentration. This relation expresses the balance between the production and the loss of $BrONO_2$, which affects directly the bromine partitioning factor (BrO/Br_y). It has to be emphasized that (1) the reaction rate of formation of $BrONO_2$ varies with altitude through a temperature dependence, and (2) the loss rate of $BrONO_2$ (mostly photolysis) varies strongly with altitude and solar zenith angle. A sensitivity test shows that it depends only slightly on the O_3 column. Consequently, the partitioning ratio BrO/Br_y responds very rapidly to any change in SZA and/or NO_2 concentration.

We propose a partitioning factor BrO/Br_y profile climatology based on a classification according to: month, latitude, stratospheric NO_2 column and solar zenith angle. For this reason, we have calculated the modeled BrO/Br_y profiles for the complete period (04/2003 to 03/2006), on the altitude grid already used for the Br_y climatology. We have selected the BASCOE data corresponding to morning conditions, since the present climatology is designed to be applied for satellite instruments having morning overpasses (GOME, SCIAMACHY, GOME-2). The partitioning factor profile climatology is built by averaging the BrO/Br_y profiles on grids of SZA (5° bins, SZA lower than 80°) and stratospheric NO_2 columns (25 blocks of 0.25×10^{15} molec/cm² width centered around 0.125, 0.375, …, 5.875, 6.125 x 10^{15} molec/cm²).

In order to illustrate the concept of the partitioning (BrO/Br_y) climatology, Figure 6.12 displays the ratio between the stratospheric BrO and Br_y columns as a function of the stratospheric NO_2 columns, simulated by BASCOE for August and December and for two solar zenith angles ranges (SZA≤60° and 60°<SZA≤80°).

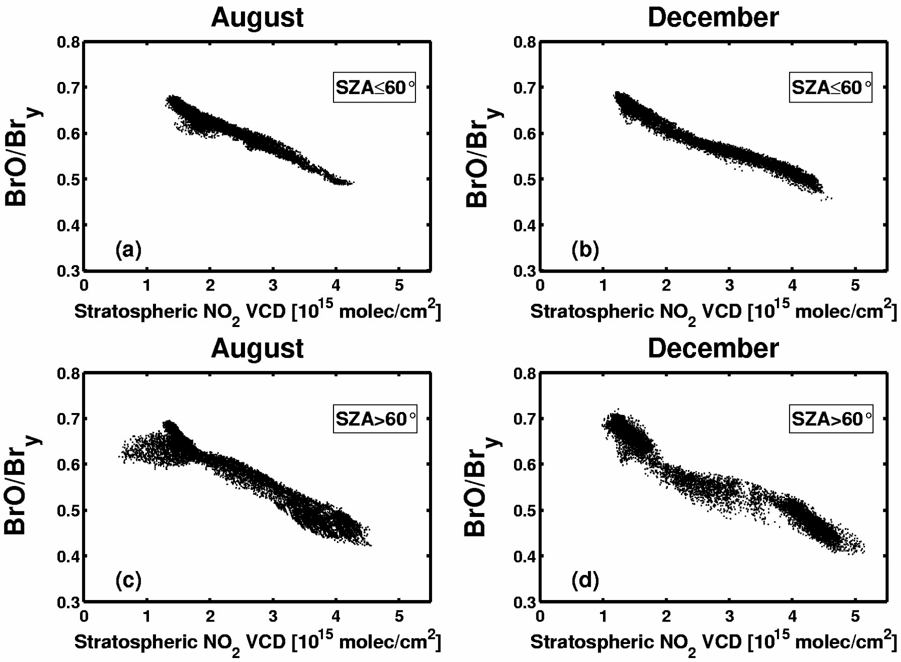

Figure 6.12 Ratio between the stratospheric BrO and Br_y columns, as a function of the stratospheric NO_2 columns (morning conditions; upper plots: SZA≤60°, lower plots: 60°<SZA≤80°), estimated from BASCOE data for August (left plots) and December (right plots).

The inverse dependency of BrO/Br_y with NO_2 is obvious, as well as the diurnal variation of BrO. However a striking feature can be observed in Figure 6.12c, where two photochemical regimes are present in August for low stratospheric NO_2 columns. The lower branch of the scatter plot corresponds to perturbed atmospheric conditions in the Antarctic polar vortex (close to the terminator). Indeed, the polar stratospheric clouds (formed during the winter polar night) provide the surface for a number of heterogeneous reactions leading to the denoxification process and the activation of chlorine species (see e.g. Solomon, 1999). As a consequence, the lower stratospheric inorganic bromine is almost exclusively partitioned between BrO and BrCl (formed by the reaction between bromine and chlorine monoxides), and the bromine photochemistry deviates from the standard regime (essentially controlled by stratospheric NO_2).

It should be noticed that if we restrict ourselves to unperturbed conditions, a parameterization of BrO/Br_y with additional entries as the latitude and month is relatively redundant. In first approximation, the stratospheric NO_2 column is mainly determined by day length (photolysis of the nitrogen reservoirs) and the solar zenith angle (affecting the diurnal equilibrium NO_2/NO). Nevertheless, a general partitioning factor climatology using a classification by latitude and month, is able to reproduce (to some extend) the different photochemical regimes, associated to low NO_2 columns, experienced by the stratospheric inorganic bromine species.

From Figure 6.12, it can be seen that there is a moderate dispersion of the data around the mean curves. It suggests that the error made by using the adopted parameterization of BrO/Br_y is rather small. This will be established in section 6.4.5 through an error assessment.

The advantage of using the stratospheric NO_2 column to parameterize the BrO/Br_y ratio is that, besides the simplicity of the method, this information is easily accessible as an intermediate product in the retrieval of total and tropospheric NO_2 columns from space nadir measurements (e.g., Boersma et al., 2004).

6.4.4 Long-term trend in stratospheric bromine

Due to the evolution of the organic bromine emissions (Montzka et al., 2003), a positive trend in stratospheric bromine of about +2.5% per year has been observed for the 1995-2001 period, while a negative trend of about -1% per year has been identified between 2001 and 2005 (Hendrick et al., 2008). Since model fields used in this study cover three years of data from 04/2003 to 03/2006, the stratospheric BrO climatology is generalized to account for long-term trend, by adding the year as a new entry of the climatology, in the form of a correction factor.

6.4.5 Results and error analysis

In this section, the stratospheric BrO vertical columns estimated from the Br_y and BrO/Br_y climatologies are presented. The suitability of the approach described in the previous sections is addressed through an error analysis. To simplify the discussion, we restrict ourselves to the vertical columns at the time of GOME overpass (similar results are obtained for instruments with late morning or early afternoon overpasses, as SCIAMACHY, GOME-2 and OMI). The instrument, aboard the ESA/ERS-2 satellite, flies in a sun-synchronous orbit, implying that fixed latitudes are always sounded at the same local time. For the period from April 2003 to March 2006, the BASCOE model data at GOME overpass has been selected and the stratospheric BrO, Br_y, O_3 and NO_2 vertical columns have been calculated (tropopause heights estimated from ECMWF pressure and temperature profiles, are used). The climatological stratospheric profiles of Br_y concentration and partitioning ratio (BrO/Br_y) were then evaluated by applying the parameterization, respectively to the calculated O_3 and NO_2 vertical columns. The climatological stratospheric BrO profiles and columns are calculated by equation 6.1. For each month and latitude band, the mean of the BrO columns from the climatology is estimated, together with the root mean square of the difference between the parameterized and the BASCOE modeled stratospheric BrO columns. Results are presented in Figure 6.13. The same approach has been adopted for the Br_y columns. In order to assess the importance of the errors originating from the parameterization of Br_y and BrO/Br_y, both contributions have been considered separately using the following equation (Br_y and BrO/Br_y are independent variables):

$$\sigma^2_{BrO} = (BrO/Br_y)^2\sigma^2_{Br_y} + (Br_y)^2\sigma^2_{BrO/Br_y} \qquad (6.3)$$

Figure 6.13 shows the relative error on the stratospheric BrO columns due to Br_y and BrO/Br_y, respectively. The stratospheric Br_y vertical columns derived from the climatological profiles and the ratio between the BrO and Br_y stratospheric columns, are also presented.

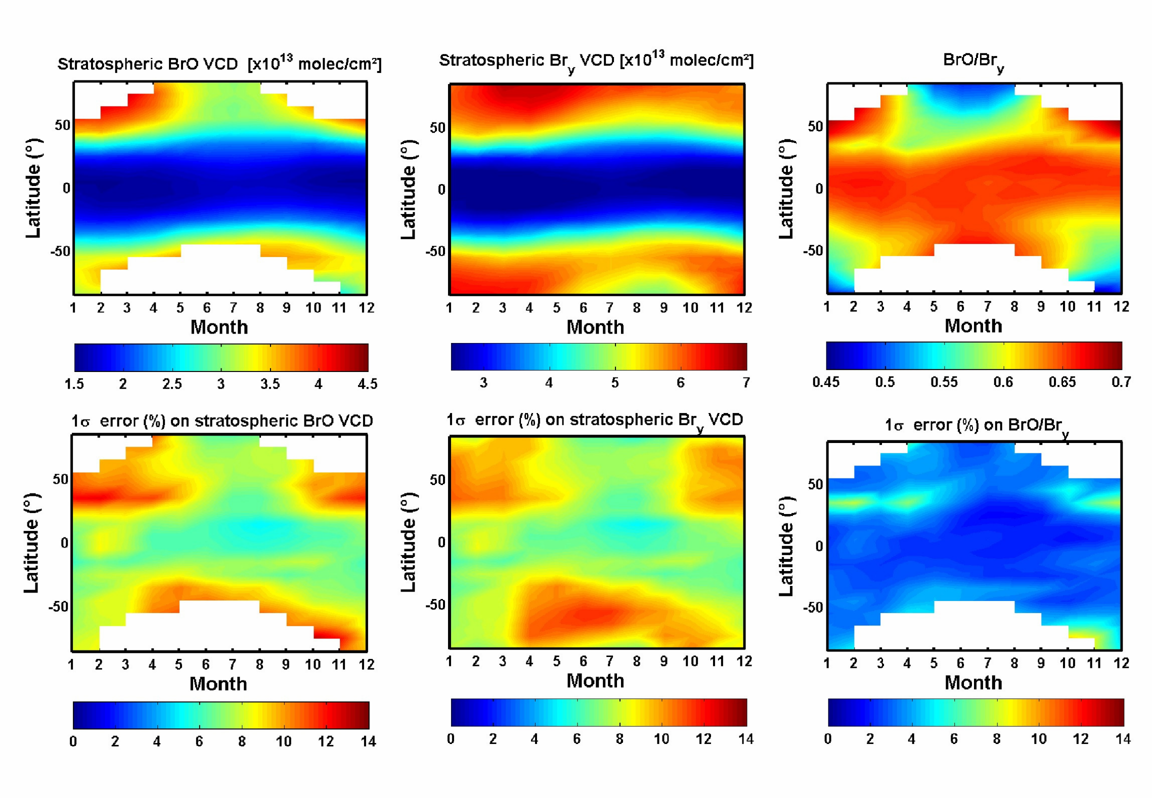

Figure 6.13 Results of the BASCOE climatology at GOME overpass. (Upper plots) Monthly zonal averaged of BrO (left) and Br_y (center) stratospheric vertical columns (expressed in $x10^{13}$ molec/cm²) and the ratio between BrO and Br_y columns (right). (Lower plots) Standard deviation (expressed in %) on BrO columns climatological values and the respective contributions from the Br_y and BrO/Br_y parameterization. The bromine photochemistry for solar zenith angles larger than 80° is not considered here (white regions).

From Figure 6.13, it can be stated that the new stratospheric BrO climatology provides reliable results with a precision better than 14%. It also reveals that:

- the Br_y climatology produces higher Br_y columns at mid- and high-latitudes than for tropical regions, as expected from the dependency of the tropopause height with latitude. One can notice smaller values in the Antarctic polar spring, which are mainly related to the air subsidence in the polar vortex.
- except for perturbed chemistry conditions, the errors on the stratospheric BrO columns are dominated by the errors on Br_y. These errors are maximum at mid- and high-latitudes in winter and early spring during major changes in stratospheric dynamics, leading to a larger scatter in the Br_y/ozone correlations. The moderate errors on Br_y during Antarctic ozone hole conditions indicate that Br_y shows small variations within the vortex since the air over the polar region is well isolated. The use of the O_3 column helps to identify the vortex and discern air masses with Br_y amount substantially different.
- the BrO/Br_y factor exhibits a strong seasonal variation at mid- and high-latitudes, related to the seasonal cycle of stratospheric NO_2.
- the relative error on the stratospheric BrO columns due to errors on the partitioning factor BrO/Br_y is remarkably small for usual photochemical regimes (lower than 8 %). For perturbed chemistry conditions, the standard deviation can reach 12% of the BrO column due to the presence of various photochemical scenarios and dynamical mixing of air with different amount of NO_x.

An important aspect to emphasize is, that the BASCOE stratospheric O_3 and NO_2 columns used to build the stratospheric BrO climatology have been validated through comparisons with measured columns obtained from ground-based observations at mid- and high-latitudes in both hemispheres (see Figures 6.1 and 6.2 in section 6.3.1). The important observed changes in stratospheric O_3 and NO_2 are consistently reproduced by the model, except for polar ozone in the southern hemisphere in ozone-hole conditions, where BASCOE tends to overestimate the stratospheric O_3 columns. In practice, however, this is expected to have a marginal impact on the evaluation of stratospheric BrO profiles from our climatology since Br_y show small variations and correlates only slightly with stratospheric ozone for these conditions (see Figure 6.11 in section 6.4.2).

In summary, the error on the stratospheric BrO column evaluated by the BASCOE climatology, is limited by the accuracy of the modeled BrO. By considering the contribution of the main sources of errors added in quadrature, the overall uncertainty on stratospheric BrO can be kept below 30% under most observational conditions.

6.5 Conclusions

We have presented a new global climatology of stratospheric bromine monoxide, primarily designed for the retrieval of tropospheric BrO columns from satellite nadir instruments (such as GOME, SCIAMACHY and GOME-2), but also of interest for a wider range of applications. The impact of the stratospheric dynamics on the stratospheric BrO distribution is accounted for by a parameterization based on the ozone column, while the effect of photochemistry on stratospheric BrO is determined by considering the stratospheric NO_2 columns and the solar zenith angle. The adopted parameterization is evaluated based on three years of output data from the BASCOE chemical transport model. Model simulations include full gas phase chemistry and relevant heterogeneous reactions, while dynamics is driven by ECMWF wind fields. Regarding the bromine species, the model calculations use up-to-date photochemistry and a realistic total bromine budget (including a contribution from short-lived bromine source gases).

Although primarily based on model simulations, the climatology is also closely linked to an extensive set of stratospheric BrO observations from ground-based, balloon-borne and satellite (SCIAMACHY) platforms. The excellent overall agreement between the model and the observations demonstrates (1) the level of consistency of the currently available BrO observational data set, (2) the ability of our model to reproduce the main mechanisms controlling the distribution of stratospheric bromine monoxide. We estimate that the overall uncertainty of the resulting stratospheric BrO profiles is lower than 30%. However, this error will likely decrease in the future as consolidated kinetic and photochemical data, and improved measurements of inorganic and organic bromine compounds will be available.

Chapter 7

Satellite BrO observations

Abstract

Measurements from the GOME/ERS-2 and GOME-2/MetOp-A satellite nadir UV-visible instruments have been analyzed for tropospheric BrO using a new retrieval technique that combines measured BrO slant columns and estimates of the stratospheric BrO content using the climatology presented in chapter 6. Air mass factors calculated using a radiative transfer model, are applied to account for the impact of observation geometry, clouds, surface albedo and BrO profile shape on the measurements.

It is shown that this method enables to better isolate and quantify the polar BrO surface emissions. Moreover, the separation of stratospheric and tropospheric fractions of the observed total BrO columns allows studying the transport of BrO plumes in both stratosphere and troposphere in more detail.

Supported by correlative ground-based data and a comprehensive error budget, evidences are provided for a global free-tropospheric BrO background with columns of 1-3 x 10^{13} molec/cm². No sign of significant seasonal or latitudinal variation of this tropospheric BrO background could be found.

7.1 Introduction

Satellite UV-visible nadir instruments (such as GOME, SCIAMACHY, GOME-2 and OMI) offer the unique capability to study and monitor BrO at the global scale (Chance, 1998; Richter et al., 2002; Van Roozendael et al., 2002; Wagner and Platt, 1998). However, a quantitative and refined interpretation of the satellite BrO observations requires to resolve the measured total BrO columns into their stratospheric and tropospheric contributions. In past studies (e.g., Wagner and Platt, 1998; Richter et al., Hollwedel, 2005), this troposphere-stratosphere separation has been treated only on limited case studies. Generally, the tropospheric BrO column were derived by subtracting from the measured total column, a stratospheric column estimated from the satellite nadir measurements at the same latitude over a certain geographical sector[1] or at high solar zenith angle (corresponding to high latitude). These procedures make several assumptions, in particular: (1) a weak longitudinal or latitudinal dependence of the stratospheric BrO column, and (2) a negligible impact of the tropospheric BrO content on the stratospheric correction. However, these hypotheses are questionable because of the longitudinal and latitudinal inhomogeneity of stratospheric BrO and the possible overall presence of BrO in the troposphere.

---

[1] This 'reference sector' method was initially developed for the retrieval of tropospheric NO_2 columns (Richter et al., 2002).

One possibility to estimate stratospheric BrO VCDs at the global scale is to use the BrO profiles provided by the SCIAMACHY limb measurements (see e.g. Sinnhüber et al., 2005). Although these profiles are of excellent quality, their use to retrieve tropospheric columns is in fact limited to SCIAMACHY data. Moreover, the retrieval of stratospheric BrO profiles from SCIAMACHY limb observations is only possible in the altitude range from about 15 km to about 30 km.

In this chapter, we have developed a more advanced algorithm to retrieve tropospheric BrO columns from satellite nadir observations. This method uses as stratospheric correction, the stratospheric BrO climatology described in chapter 6 that has been validated and that accounts for the important variation of stratospheric BrO. In addition, the changes in measurement vertical sensitivity in both troposphere and stratosphere for the different atmospheric conditions encountered are explicitly treated. This enables to describe more accurately the spatial and temporal evolution of stratospheric and tropospheric BrO, which might help addressing some of the tropospheric bromine science issues like:

- better understanding the mechanism and different steps leading to the release and sustaining of large amount of bromine in the polar boundary layer.
- characterizing more accurately the free-tropospheric BrO amounts including their latitudinal and seasonal variations at the global scale, with the aim to understand the origin of free-tropospheric bromine and in particular to assess the contribution coming from transport.

In section 7.2, the algorithm developed to retrieve tropospheric BrO vertical columns from satellite observations is presented. This includes also a comprehensive error budget of the retrieval. In sections 7.3 and 7.4, the implementation of the latter retrieval algorithm is treated for a selection of data from the GOME and GOME-2 instruments, respectively. The interpretation of the results is discussed in the light of our current understanding of tropospheric bromine. In section 7.5 the consistency of the satellite-based BrO dataset is evaluated through comparisons with independent ground-based BrO measurements and model calculations. Conclusions are given in section 7.6.

7.2 Retrieval of tropospheric BrO columns from satellite observations – Algorithm description and error analysis

7.2.1 General description

The tropospheric BrO retrieval algorithm is based on a residual technique which consists of three main steps:

1. a slant column density is determined from a calibrated spectrum using a DOAS fit, as further explained in section 7.2.2. This slant column is a "total" SCD in the sense that it includes contribution from absorption by BrO in both the stratosphere and troposphere.
2. the stratospheric contribution to the slant column is estimated using simulated stratospheric BrO profiles. Details are given in section 7.2.4.

3. the residual tropospheric slant column is converted into a vertical column by application of a tropospheric air mass factor. This aspect will be presented in section 7.2.5.

Tropospheric BrO columns are retrieved as follows:

$$VCD_{tropo} = \frac{SCD - SCD_{strato}}{AMF_{tropo}} \tag{7.1}$$

with SCD the slant column density from step 1, SCD_{strato} the stratospheric slant column obtained from step 2, and AMF_{tropo} the tropospheric air mass factor from step 3.
The logical flow of tropospheric BrO retrieval algorithm is illustrated in Figure 7.1.

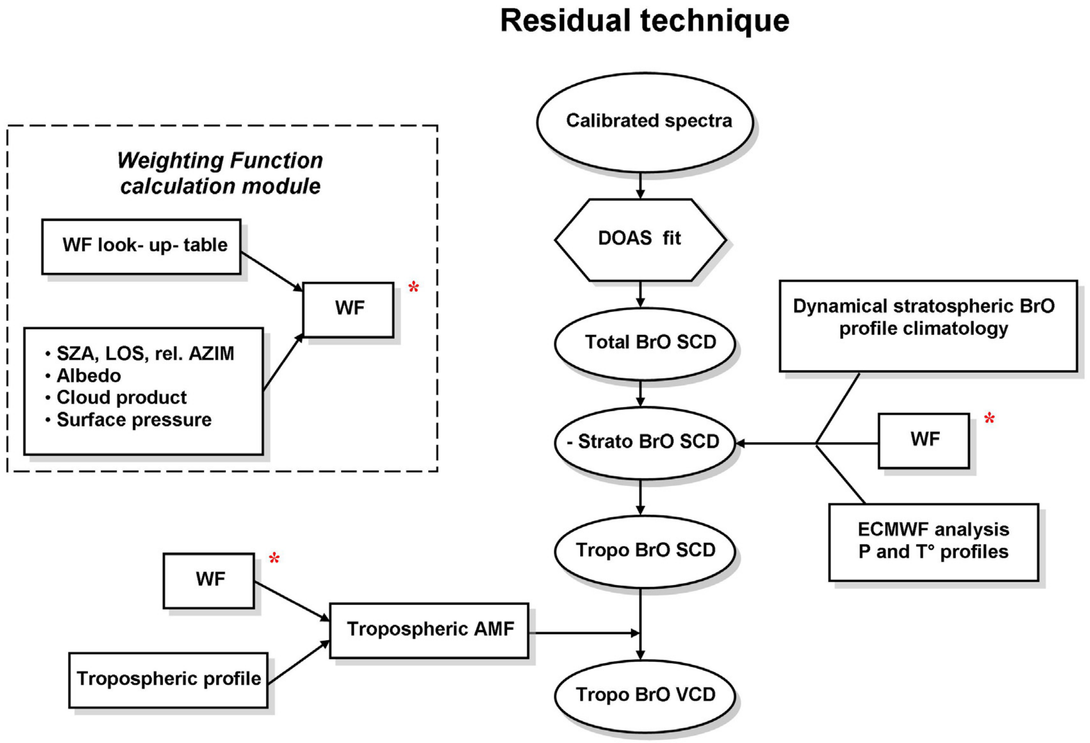

Figure 7.1 Overview of the tropospheric BrO algorithm.

7.2.2 DOAS total slant column retrieval

The measured spectra are analyzed for BrO using the DOAS method (see section 3.3). Briefly, the slant columns of BrO and several atmospheric absorbers (O_3, NO_2, O_4 and eventually HCHO and OClO) are retrieved by adjusting the corresponding absorption cross-sections to the log-ratio of a measured and a reference spectrum. The fitting procedure is achieved in an appropriate wavelength interval and includes, in addition to the atmospheric absorbers cross-sections, a synthetic Ring spectrum, several instrumental corrections and a closure polynomial. Another important aspect of the BrO fitting is related to the wavelength calibration that is achieved based on a non-linear least-squares fitting of the measured spectra to a set of high-resolution solar lines. More details on the DOAS settings used for GOME and GOME-2 BrO slant columns retrieval can be found in sections 7.3.1 and 7.4.1, respectively.

7.2.3 Weighting functions calculation

The stratospheric slant column and the tropospheric air mass factor have in common that they require, prior to their computation, the estimation of the weighting function (WF) representative of the measurement, i.e. the vertical sensitivity of the measurement to BrO (section 3.4.2).

To achieve this goal, we have tabulated a set of pre-calculated weighting functions, sorted according to the following parameters: solar zenith angles (10°, 20°, 30°, 40°, 45°, 50°, 55° , 60°, 65°, 70°, 72°, 74°, 76°, 78°, 80°, 85°), line-of-sight angles (0°, 10°, 20°, 30°, 40°, 50°, 60°), relative azimuth angles (0°, 45°, 90°, 135°, 180°), Lambertian surface albedo (0, 0.03, 0.06, 0.1, 0.25, 0.5, 0.8, 1) and surface pressure (1013, 996, 980, 964, 948, 933, 918, 903, 888, 873, 859, 838, 818, 798, 778, 759, 741, 723, 705, 684, 663, 643, 623, 551, 312, 182, 116 mbar). The WF look-up-table has been generated on a fixed pressure grid using the UVspec/DISORT radiative transfer model. We used 65 atmospheric layers defined by the following layer boundaries pressure (expressed in mbar): 1013, 1009, 1005, 996, 988, 980, 972, 964, 956, 948, 941, 933, 925, 912, 910, 903, 895, 888, 881, 873, 866, 859, 838, 818, 798, 778, 759, 741, 723, 705, 684, 663, 643, 623, 551, 468, 397, 312, 245, 211, 182, 157, 135, 116, 100, 86, 74, 63, 46, 39, 34, 29, 25, 21, 18, 16, 14, 12, 7, 5, 3, 2, 1.5, 1, 0.5. The constructed table contains about 7.8 10^6 entries.

A weighting function for a given measurement is computed by linear interpolation between the values stored in the pre-calculated WF look-up-table[1]. Whereas the viewing geometry angles are easily accessible data, the set of parameters including the albedo, the surface pressure and the cloud data are estimated for each sounded pixel from ancillary data (see details in section 7.2.5). It should be noted that the six parameter grids underlying the WF look-up-table have been chosen to cover all possible measurement conditions and to balance sufficiently accurate interpolation with computational efficiency.

In order to gain better insight into the height dependence of the sensitivity to BrO, Figure 7.2 presents examples of satellite nadir BrO weighting functions when varying the different parameters. The calculations are made for a wavelength of 352 nm (representative of the BrO absorption in the fitting interval) for an aerosol free scene and for a number of representative viewing geometries, surface albedos, surface altitudes and cloud altitudes. For the sake of clarity, the results are presented as a function of the altitude rather than pressure.

---

[1] The advantage of the WF look-up-table approach is that the calculation is fast and simple, and does not require the use of on-the-fly radiative transfer simulations (more complicate to implement in practice).

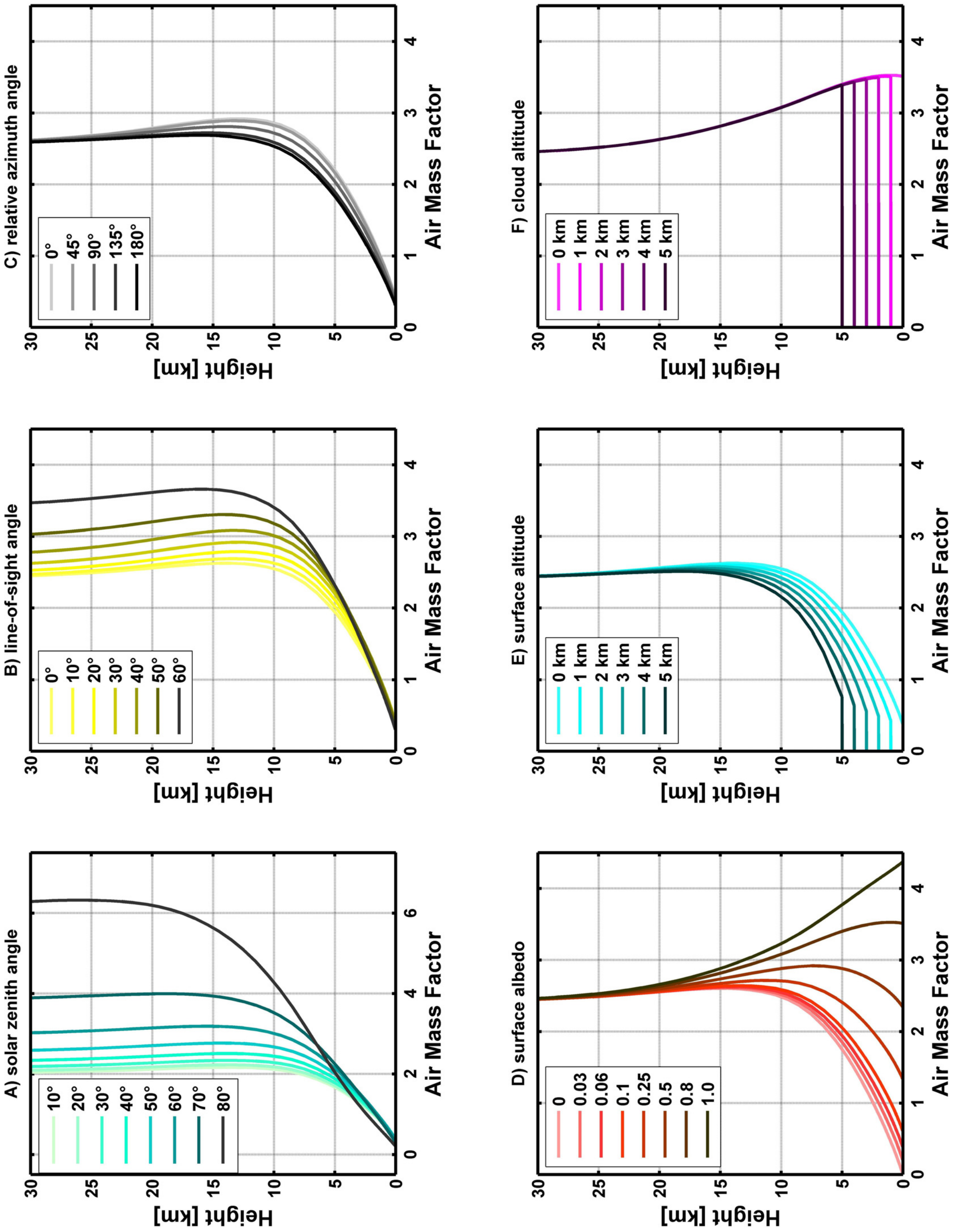

Figure 7.2 Satellite nadir weighting functions (or height-resolved AMFs) at 352 nm for sample measurement conditions (SZA: solar zenith angle, LOS: line-of-sight angle, RAA: relative azimuth angle, A: surface albedo, S: surface altitude). The different curves show the sensitivity of the measurement when varying important parameters for a stratospheric absorber: a) solar zenith angle (LOS: 0°, RAA: 0°, A: 6%, S: 0 km), b) line-of-sight angle (SZA: 45°, RAA: 0°, A: 6%, S: 0 km), c) relative azimuth angle (SZA: 45°, LOS: 30°, A: 6%, S: 0 km), and for a tropospheric absorber: d) surface albedo (SZA: 45°, LOS: 0°, RAA: 0°, S: 0 km), e) surface altitude (SZA: 45°, LOS: 0°, RAA: 0°, A: 6%), f) cloud altitude (SZA: 45°, LOS: 0°, RAA: 0°, A: 6%, S: 0 km).

The upper row of Figure 7.2 shows the dependence of the weightings functions to the viewing geometry:

a) & b) solar zenith angle and line-of-sight angle:
It shows the increase of the WF in the stratosphere with increasing angle (SZA or LOS), expected from the enhancement of the light path. For atmospheric layers above about 20 km, the WF approaches the light path geometrical enhancement factor, while a maximum of the WF is observed between 10 and 15 km (for angles smaller than 60°) due to an increase of the multiple scattering at these altitudes. Below 10 km, the WF curves exhibit a sharp decrease, illustrating the low sensitivity of the satellite nadir measurement in the troposphere for low albedo scenes. This is essentially due to the increase of the Rayleigh scattering in the troposphere that limits the penetration of the light in the lowermost layers of the atmosphere.

c) relative azimuth angle between the sun and the viewing direction (RAA): the dependence of the WF on the relative azimuth angle arises from the shape of the scattering phase functions for the respective scattering processes (only Rayleigh scattering for this example).

One can notice that varying the viewing geometry mainly affects the measurement sensitivity in the stratosphere but only slightly in the troposphere. Therefore the viewing angles are considered important parameters for a stratospheric absorber.
The lower row of Figure 7.2 shows the WFs dependence when varying the following parameters, crucial for a tropospheric absorber:

d) surface albedo: increasing the albedo enhances the WFs from the surface to about 20 km, because longer absorption paths in the lower layers are favored by reflection at the surface and multiple scattering. The case of high surface albedo is optimal for tropospheric observations since the sensitivity is maximum and the weighting functions have a small dependence with the altitude (weak dependence of the AMF to the BrO vertical distribution).

e) surface altitude: we have approximated the surface by a Lambertian reflector, in this case with an albedo of 6%. Besides the obvious insensitivity of the measurement below the surface, one can notice that the WFs increase with decreasing surface altitude. This behavior is specific to low albedo scenes and is due to the increasing importance of Rayleigh scattering on the measurement sensitivity as the surface altitude decreases (surface pressure increases).

f) cloud altitude: the scene is assumed to be completely cloudy and we have approximated the cloud top of an optically thick cloud by a Lambertian reflector with an effective albedo of 80%. The WF curves show that if the cloud lies under a BrO layer, BrO measurements are expected to be enhanced by its reflectivity. On the opposite, if the cloud lies above the BrO layer, it will hide BrO from measurements.
This description of clouds is crude, but it is however consistent with assumptions that are used in the cloud retrieval algorithm FRESCO+ (Koelemeijer et al., 2001; Wang et al., 2008). Here we refer to this cloud model because the output of the FRESCO+

algorithm is used in our tropospheric BrO retrieval algorithm to account for the effect of clouds (see section 7.2.5).

In summary, Figure 7.2 illustrates the large range of sensitivities of satellite nadir BrO measurements, and emphasizes the need to account for all these dependencies when inverting tropospheric columns from BrO slant columns measured by space nadir instruments.

7.2.4 Stratospheric correction

The stratospheric slant column is estimated by:

$$SCD_{strato} = \sum_{i=tropopause}^{TOA} WF_i \cdot \Delta StratBrO_i \tag{7.2}$$

where the summation is made for the layers between the tropopause and the top-of-atmosphere (highest atmospheric layer). The tropopause is determined from ECMWF pressure and temperature profiles using the method of Reichler et al. (2003). WF_i and $\Delta StratBrO_i$ denote the weighting function and the stratospheric BrO partial column of the i^{th} layer, respectively. The latter stratospheric BrO partial column profile is estimated from the stratospheric BrO profile dynamical climatology presented in chapter 6.

For each sounded pixel, a stratospheric BrO profile is calculated using the O_3 and NO_2 (stratospheric) columns retrieved from the same satellite measurement. It should be noted that this approach is particularly convenient, as it requires only limited computational resources. Moreover, the O_3 and NO_2 data products needed are routinely processed and easily accessible, for most of the (past, present and coming) satellite nadir UV-visible instruments.

7.2.5 Tropospheric air mass factor

The tropospheric air mass factor is determined by:

$$AMF_{tropo} = \frac{\sum_{i=surface}^{tropopause} WF_i \cdot \Delta TropBrO_i}{\sum_{i=surface}^{tropopause} \Delta TropBrO_i} \tag{7.3}$$

where the summation is made for the layers between the surface[1] and the tropopause. ΔTropBrO being the profile of tropospheric BrO partial columns corresponding to the layers defined for the WF look-up-table. As already mentioned in section 3.4.2, the AMF depends only on the shape of the profile but not on the normalization of the profile.

Following the discussion on the dependencies of the weighting functions, it is clear that the surface albedo, the clouds and the tropospheric BrO profile may have a dramatic impact on the tropospheric air mass factor. For example, moving from an albedo of

---

[1] The surface pressure is estimated based on the ECMWF analysis.

ocean/land to snow makes the measurement sensitivity at the surface change by one order of magnitude (see Figure 7.2d). Therefore, these parameters must be known with enough accuracy.

Impact of clouds and surface albedo

We consider a satellite pixel as consisting of a clear and a cloudy part, with a fractional area of (1-f) and f, respectively, where f is the cloud fraction. The treatment of partly clouded pixels in the retrieval is based on the hypothesis of the 'independent pixel approximation'. It is assumed that the intensity measured by the instrument is the sum of the intensities of a completely clear and a completely cloudy pixel weighted by (1-f) and f respectively. From the definition of the air mass factor (equation 3.22) it is possible to prove that with the independent pixel approximation, the weighting function for a partly clouded scene is given by (Martin et al., 2002):

$$WF = \Phi \cdot WF_{cloud} + (1-\Phi) \cdot WF_{clear} \tag{7.4}$$

where WF_{cloud} is the weighting function for a completely cloudy scene, and WF_{clear} is the weighting function for a completely cloud-free pixel. The intensity-weighted cloud fraction Φ is defined as:

$$\Phi = \frac{f\ I_{cloud}}{f\ I_{cloud} + (1-f) I_{clear}} \tag{7.5}$$

I_{cloud} and I_{clear} are the backscattered intensities for 100% cloudy and clear scenes respectively. As I_{cloud} and I_{clear} depend mainly on the surface and cloud albedos and on the viewing geometry, we have calculated and stored them in a look-up-table.

To calculate the WF, we use the FRESCO+ cloud product (Wang et al., 2008). FRESCO+ is an algorithm based on the independent pixel approximation which assumes that the cloud and ground surfaces are both Lambertian reflectors. The cloud albedo is fixed at 0.8 and the surface albedo is taken from the monthly averaged database (1° latitude x 1° longitude grid) of Koelemeijer et al. (2003). FRESCO+ makes use of reflectivities as measured by the satellite instrument inside and outside the oxygen A-band (758-778 nm) to simultaneously retrieve an effective cloud fraction and cloud top pressure. FRESCO+ considers thus a Lambertian cloud yielding the same top-of-atmosphere radiance as the real cloud in the scene.

The variables WF_{cloud} and Φ in equation 7.4 are estimated for a Lambertian reflector albedo of 0.8 at the cloud top pressure and with the cloud fraction retrieved by FRESCO+. WF_{clear} is calculated for a surface albedo taken from the climatology of Koelemeijer et al. (2003) at a wavelength of 335 nm.

It is important to notice that the treatment of partly clouded pixels using the equations 7.4 and 7.5 actually corrects for the "ghost column", i.e. the vertical column density below the cloud and thus not seen by the satellite. This is essentially because the AMF calculation, as it is stated in equation 7.3, implies a summation for all the layers from the surface to the tropopause, while in the meantime, for the cloudy part of the pixel, the measurement sensitivity vanishes below the cloud. Consequently, the application of the tropospheric air mass factor implicitly corrects for the ghost column. The latter information is fundamentally coming from the a priori tropospheric profile shape used in equation 7.3. Such a correction can be applied to some extent for small cloud fractions, but fails if a cloud is located above the BrO layer and covers most of the pixel area (shielding effect). In this case, the result of the retrieval is more influenced by the a priori tropospheric profile used than by the measurement itself. To minimize this bias resulting from clouds, the analysis includes only the measurements with a cloud fraction below 0.4 and with a pressure difference between the surface and the top of the cloud below 400 mbar.

Treatment of snow/ice-covered surfaces

Surfaces covered by snow or ice are of particular importance for the retrieval of tropospheric BrO columns since the large emissions of BrO in the polar boundary layer are generally observed over bright surfaces. However, FRESCO+ suffers from an important limitation over scenes covered by snow or ice. Indeed, FRESCO+ can not derive an effective cloud fraction, because the latter is basically determined from the contrast of the cloud with respect to the underlying surface. Therefore, FRESCO+ switches to a snow/ice dedicated mode: if the surface albedo is higher than 0.2 (according to the surface albedo database), the surface is considered as covered by snow or ice and FRESCO+ derives the pressure of an equivalent Lambertian reflector. The albedo of this reflecting surface is equal to the measured reflectivity outside the oxygen A-band.

In our retrieval algorithm, we exploit the snow/ice data by considering the retrieved cloud pressure and albedo as representative of the sounded surface and by using these Lambertian surface properties to calculate WFs. We keep however only the data if the difference between the surface pressure and the retrieved cloud pressure is below 120 mbar (in order to avoid the presence of large and high clouds).

A special case has also been designed for the case of fresh snow scenes: as the snow/ice mode of FRESCO+ is triggered by a monthly-averaged albedo database, the pixels covered by fresh snow are not detected in this mode, but are considered as cloudy pixels in the nominal mode of FRESCO+. Hence, to account for these fresh snow scenes, we include in the analysis the pixels with a cloud fraction larger than 0.7 and with a pressure difference between the surface and the top of the “cloud” smaller than 150 mbar.

Tropospheric BrO profile shape

In order to derive accurate tropospheric BrO AMFs, weighting functions have to be applied to realistic tropospheric BrO profiles. This is clearly the most difficult part of the retrieval algorithm, the vertical distribution of BrO being largely unknown in the troposphere. Nevertheless, our baseline for the retrieval has been to consider two different approaches as a function of the surface albedo value:

1) High albedo (>50%): it is the ideal case, with a high sensitivity for BrO close to the surface. Although the tropospheric AMF presents a relatively weak dependence to the shape of the profile, we have decided however and on a best-efforts basis, to use as vertical BrO profile the output values of a tropospheric model: *p*-TOMCAT.

The *p*-TOMCAT (parallel-Tropospheric Off-Line Model of Chemistry and Transport) model is an off-line three-dimensional tropospheric CTM with a detailed bromine chemistry scheme that contains gas-phase reactions and heterogeneous reactions on cloud particles and aerosols. It includes bromine emissions from sea salt, a parameterization for sea salt aerosol production through blowing snow events and bromocarbon photo-oxidation as well as bromine removal from dry and wet deposition (see Yang et al. (2005) for a detailed description of *p*-TOMCAT). For the present study, the model was run at a horizontal resolution of 5.6° x 5.6° on 31 levels from the surface up to 10 hPa using winds and temperature derived from the ECMWF operational analysis. The output frequency is fixed to 2 hours from 0h UT, but we have kept only the model output at 10h30 local time (typical satellites overpass time).

The strategy we adopted here has been to build a climatology of tropospheric profile shapes from the *p*-TOMCAT output, which could be used easily in our tropospheric BrO retrieval algorithm. On the basis of error–driven considerations, the tropospheric profile climatology has been generated using a classification by month, hemisphere, surface pressure (4 levels) and tropospheric BrO columns (10 blocks of 1×10^{13} molec/cm² width, centered around 0.5,.., 9.5 $\times 10^{13}$ molec/cm²). The key idea of such column-classified profile climatology is that it is able to reproduce most of the variability of BrO in the troposphere. Figure 7.3 illustrates the tropospheric BrO profile climatology for March in the Northern hemisphere for a surface pressure of 1000 mbar.

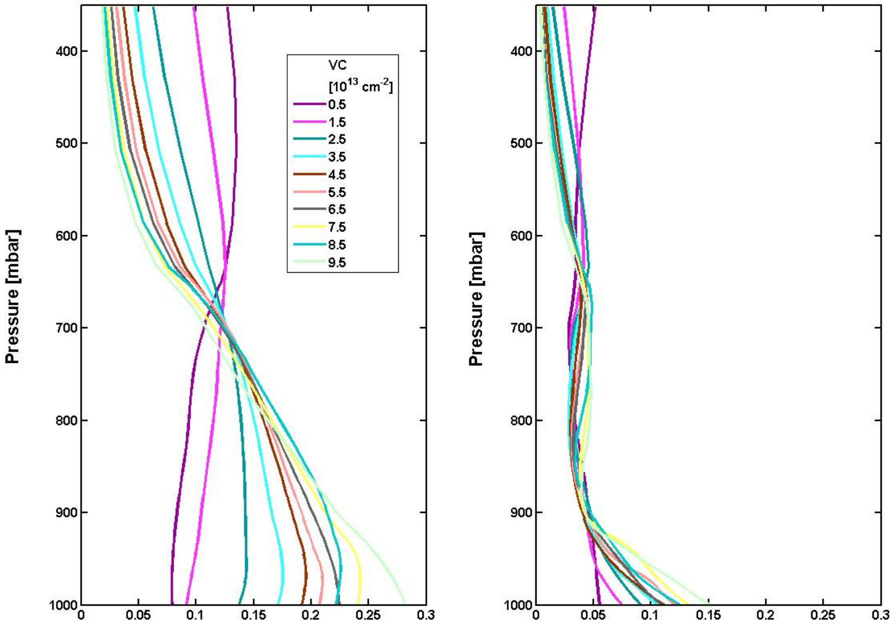

Figure 7.3 Example of results of the tropospheric BrO climatology based on pTOMCAT model data. Profile shapes (left) and standard deviations on climatological values (right) are plotted as a function tropospheric BrO columns (see text), for March in the Northern hemisphere and for a surface pressure of 1000 mbar.

The curves represent the normalized profile shapes and standard deviations for the different tropospheric BrO columns. Two observations can be made that strengthen the adopted climatological approach:

- the profiles are more weighted in the lower part of the troposphere for high tropospheric BrO columns. This behavior is consistent with the increase in BrO column we would expect from the strong bromine emissions occurring in the polar boundary layer.
- the standard deviations on the profiles are relatively small compared to the climatological values.

The advantage of the tropospheric BrO profile climatology is that it is not necessary to have profiles simulated by *p*-TOMCAT on a daily basis and on a regular latitude-longitude grid. The latter profiles might be unrepresentative of some measured situations or lead to severe interpolation issues.

As a consequence of this parameterization, the AMF values are now considered to be function of the vertical column through this profile-column relation. An iterative approach to the AMF calculation is thus needed, where the tropospheric BrO slant column is acting as a constraint on the iteration.

2) Low albedo (<50%): In a first step, we have tested the tropospheric profile climatology presented above, but the results have been found unrealistic. Indeed, a strong artifact appears for these conditions, and is due to a spurious dependence of the tropospheric AMF to the tropospheric slant column noise level. This behavior arises from the strong dependence of the weighting functions with the altitude (see Figure 7.2).

As the measurement sensitivity over dark surfaces (such as oceans) is strongly reduced in the boundary layer, we have assumed the tropospheric BrO profile to have only a contribution in the free-troposphere: a Gaussian profile with a maximum at 6 km high and a full width half maximum of 2 km. With this pragmatic choice, the resulting tropospheric BrO columns must be interpreted as representative of the free-troposphere[1] only (any BrO amount present in the boundary layer will be underestimated).

This is clearly a limitation of our approach. Nevertheless, it is interesting to estimate the detection limit of the satellite measurements with respect to BrO in the boundary layer. Given a slant column detection limit of about 3×10^{13} molec/cm² and assuming a surface albedo of 5% and a BrO profile with constant mixing ratio in the lowest kilometer, a VCD roughly of 6×10^{13} molec/cm² (AMF~0.5) or a mixing ratio of ~20 pptv should be measurable if sustained throughout a single satellite pixel. Unfortunately, the typical tropospheric abundances of BrO measured in the extra-polar boundary layer are either below the BrO detection limit (few pptv compared to 20 pptv) or correspond to localized emissions with a spatial extend smaller than the typical pixel size (dilution effect). One possibility to reduce the detection limit is to average measurements, but it is to the expense of a loss in time and/or spatial resolution. We also need to assume that the source of errors is random and that systematic errors have been accounted for. This last point is very difficult to verify in practice. Note that on the other hand, the same calculation for high surface albedo scenes (~80%; e.g. in polar region) provides a detection limit of ~ 3

---

[1] In contrast, the results for high albedo scenes are sensitive to the entire tropospheric vertical column (free-troposphere+boundary layer).

pptv, owing to the better measurement sensitivity over bright surfaces (AMF ~ 3.5 between 0 and 1 km; see Figure 7.2). This detection limit is well below the BrO amounts frequently observed by ground-based measurements during bromine explosion events (up to 30 pptv). For these cases, the detection of BrO from satellite is feasible, provided that the area of enhanced tropospheric BrO is of the order of a satellite ground-pixel.

7.2.6 Error analysis

The total retrieval uncertainty on the tropospheric BrO vertical columns can be derived by error propagation starting from equation 7.1. Since the different steps of the retrieval algorithm can be considered as independent, they are assumed to be uncorrelated and the total error on the tropospheric vertical column can be expressed as (Boersma et al., 2004; De Smedt et al., 2008):

$$\begin{aligned}\sigma^2_{VCD_{tropo}} &= \left(\frac{\partial VCD_{tropo}}{\partial SCD}\right)^2 .\sigma^2_{SCD} + \left(\frac{\partial VCD_{tropo}}{\partial SCD_{strato}}\right)^2 .\sigma^2_{SCD_{strato}} + \left(\frac{\partial VCD_{tropo}}{\partial AMF_{tropo}}\right)^2 .\sigma^2_{AMF_{tropo}} \\ &= \left(\frac{\sigma_{SCD}}{AMF_{tropo}}\right)^2 + \left(\frac{\sigma_{SCD_{strato}}}{AMF_{tropo}}\right)^2 + \left(\frac{(SCD - SCD_{strato}).\sigma_{AMF_{tropo}}}{AMF^2_{tropo}}\right)^2\end{aligned} \tag{7.6}$$

where σ_{SCD}, $\sigma_{SCD_{strato}}$ and $\sigma_{AMF_{tropo}}$ denote the standard deviation of the errors in the total slant column, the stratospheric slant column and the tropospheric air mass factor, respectively.

We can also write:

$$\sigma^2_{VCD_{tropo}} = \frac{1}{N}.\left(\frac{\sigma_{SCD_{rand}}}{AMF_{tropo}}\right)^2 + \left(\frac{\sigma_{SCD_{syst}}}{AMF_{tropo}}\right)^2 + \left(\frac{\sigma_{SCD_{strato}}}{AMF_{tropo}}\right)^2 + \left(\frac{(SCD - SCD_{strato}).\sigma_{AMF_{tropo}}}{AMF^2_{tropo}}\right)^2 \tag{7.7}$$

$\sigma_{SCD_{rand}}$ and $\sigma_{SCD_{syst}}$ are the random and systematic parts of the error on the slant columns. The random error is reduced when the number of measurements increases. Therefore, in case of averaging, $\sigma_{SCD_{rand}}$ can be divided by the square root of the number of satellite pixels taken into the mean (N). The other sources of uncertainties (SCD_{strato} and AMF_{tropo}) have systematic but also random components that may average out in space or in time. However, these components can hardly be separated in practice and we will consider these uncertainties as systematic. The total error calculated with equation 7.7 is therefore an upper limit of the real error on the tropospheric vertical columns.

Error on total slant columns

The random part of the slant column error is evaluated from the measured slant columns: each satellite orbit is divided into 36 latitude bands of 5° width, the random error on the slant columns is expressed for each latitude bin by the standard deviation of the measured

columns around the mean. Note that it has a tendency to overestimate the true random SCD error as it includes a component coming from the natural variability of BrO that sometimes may be important (e.g., at high latitudes).
The systematic errors on the slant columns are connected to uncertainties on the absorption cross-sections included in the fit and uncertainties related to instrumental effects (wavelength calibration..). The systematic slant column error due to absorption cross-section uncertainties and their correlations have been estimated using the same formalism already used in chapter 5 for the error analysis of the ground-based observations at Reunion Island (details can be found in Appendix B). The impact of the instrumental source of errors has been assessed with sensitivity tests, by varying several parameters of the spectral analysis.
We have performed calculations for a sample of satellite test orbits. It came out of the calculations that the systematic SCD error due to uncertainties on the cross-sections and the instrumental effects can be well approached by a parameterization that has a linear relationship with the retrieved SCD:

$$\sigma_{SCD_{syst}} = 0.12\ SCD + 0.7x10^{13} \quad \text{molec/cm}^2 \tag{7.8}$$

As it is very simple to apply in practice, we have adopted this formulation to calculate the systematic SCD error for each pixel treated in the analysis.
Finally, we have also included for GOME, an error on the equatorial SCD offset that is applied to the measured slant columns (see section 7.3.1.1). We estimate that a reasonable value for this error is of about 1 x 10^{13} molec/cm².

Error on stratospheric slant columns

The error on the stratospheric correction has two contributions, one from the uncertainty on the stratospheric profile used and the other from the uncertainty on the BrO weighting function. As the weighting function in the stratosphere is mainly dependent on the viewing geometry that is known with high accuracy, we consider that only the stratospheric BrO profile error contributes significantly to the stratospheric SCD error. Considering the discussion in chapter 6 on the overall error on the stratospheric BrO profiles from the BASCOE climatology, we estimate the error on the stratospheric slant column to be equal to 20%.

Error on tropospheric air mass factors

The error on the tropospheric AMF depends on input parameters uncertainties and on the sensitivity of the air mass factor to each of them:

$$\sigma^2_{AMF_{tropo}} = \left(\frac{\partial AMF_{tropo}}{\partial A}\right)^2 .\sigma^2_A + \left(\frac{\partial AMF_{tropo}}{\partial f}\right)^2 .\sigma^2_f + \left(\frac{\partial AMF_{tropo}}{\partial CTP}\right)^2 .\sigma^2_{CTP} + \left(\frac{\partial AMF_{tropo}}{\partial TropBrO}\right)^2 .\sigma^2_{TropBrO} \tag{7.9}$$

where σ_A, σ_f, σ_{CTP} and $\sigma_{TropBrO}$ represent respectively the uncertainties on the surface albedo, the cloud fraction, the cloud top pressure and the tropospheric BrO profile shape.

The three first errors are taken from the literature (σ_A:0.02, σ_f: 0.05 and σ_{CTP}: 100 mbar). The error on the profile shape is estimated: (high albedo) from the standard deviations of the profiles simulated by *p*-TOMCAT, (low albedo) by considering a relatively large uncertainty on the altitude of profile maximum (arbitrary fixed at 2 km).

The air mass factor derivatives with respect to the different input parameters are determined for each pixel. For a given parameter, we apply a small perturbation, leaving all other inputs unchanged, and the result of the AMF calculation for this "perturbed state" enables to calculate the Jacobian derivatives.

Note that to estimate the tropospheric AMF and its corresponding error, we need in fact five AMF calculations in total. Therefore we have developed a very efficient routine for fast computation of AMFs in order to face the large amount of satellite data.

7.3 Retrieval of tropospheric BrO columns from GOME observations on ERS-2

7.3.1 GOME slant column retrieval

7.3.1.1 Data analysis

The DOAS settings applied for the retrieval of BrO slant columns from GOME measured spectra are summarized in Table 7.1. The spectral signatures of BrO, O_3, NO_2, O_4, HCHO and OClO are included in the fit together with two cross-sections to correct for the Ring effect. Further, a linear intensity offset correction is applied as well as a polynomial closure term of order 5. As part of the minimization algorithm is also a correction for the spectral instrumental undersampling of GOME in the form of an adjustment to an ad-hoc simulated cross-section. More details on the DOAS procedure applied can be found in Van Roozendael et al. (1999) and Aliwell et al. (2002).

An important difference with respect to these studies (and others e.g. Wagner and Platt, 1998; Richter et al., 1998 and 2002) relies in the choice of the fitting window. GOME BrO slant columns have been previously derived in the wavelength interval from 344.7 to 359 nm, making use of two BrO absorption bands in this region. This fitting window was initially used in order to reduce errors introduced by the strong ozone absorption at shorter wavelengths, according to recommendations published in Aliwell et al. (2002). However, more recent experience with ground-based and satellite BrO retrieval have shown that equally reliable results could be obtained using three (336-351.5 nm; De Smedt et al., 2003; Van Roozendael et al., 2004) or even four (336-359 nm) absorption bands (Van Roozendael, private communication).

Table 7.1 DOAS settings used for GOME BrO slant column analysis

Fitting interval	336-359 nm
Molecular absorption cross-sections[1]	BrO [Fleischmann et al., 2004] O_3 218K [Brion et al., 1993] O_3 243K [Brion et al., 1993] NO_2 221K [Vandaele et al., 1997] + cross-section preshift: 0.017 nm O_4 [Hermans et al.] HCHO [Meller et al., 2000] OClO [Kromminga et al., 2003] 2 Ring cross-sections [Vountas et al., 1998]
Additional terms/corrections	Polynomial (order 5) Offset (constant+slope) Undersampling [Chance, 1998] Wavelength calibration based on Kurucz et al. (1984) solar spectrum.

In this work the extended fitting interval from 336 to 359 nm has been tested on spectra from several satellites and ground-based instruments and the results were found in excellent agreement, reinforcing our confidence in the DOAS analysis. For this reason, we have used this fitting interval for the GOME BrO analysis. Compared to the GOME baseline (344.7-359 nm), the results in the 336-359 nm interval are more stable and less sensitive to interference with HCHO absorption.

Reference spectrum

In principle, the DOAS analysis may use as reference spectrum an extraterrestrial solar spectrum measured by the instrument. However, this approach was found unsuccessful with GOME. The main reason for that is a problem related to the structure of the GOME reflecting diffuser plate used to reduce the intensity during the measurement of the solar spectrum. Small variations in the incident angle of the light on the diffuser plate lead to systematic changes in the spectrum of the reflected light that can interfere with the retrieval of BrO (Richter et al., 2002). To overcome this problem, daily Earthshine spectra are used as reference spectrum. These are selected in a region of the equatorial Pacific Ocean (latitude: [-5° 5°], longitude: [180° 240°]) where the BrO absorption is assumed to be low and stable in time, and where the absorption by species that can interfere with BrO (e.g., formaldehyde) is small. It has to be noted that because a radiance spectrum is used as reference spectrum, the retrieved BrO slant columns are not

---

[1] The cross-sections used are all convolved to the resolution of the instrument.

absolute slant columns. To correct for this, an equatorial slant column offset is applied on the slant columns, which accounts for the absorber column in the reference spectrum. The value of this offset is fixed to 7.5 x 10^{13} molec/cm². The latter has been found to be consistent with test BrO retrievals made around the equator with SCIAMACHY and GOME-2 using daily sun reference spectra, and with the ground-based measurements performed at Reunion-Island (chapter 5).

Geometrical approximation

In order to illustrate the global behavior of BrO as observed by satellite-based instruments and to identify regions having enhanced BrO (see below), it is useful (in a first step) to convert the BrO slant columns into total vertical columns using 'geometrical' air mass factors. The so-called geometrical approximation is based on the assumption of a simple geometrical light path from the sun to the instrument (see Figure 7.4). Here, we consider all scattering processes and albedo effect to have a negligible impact on the light path.

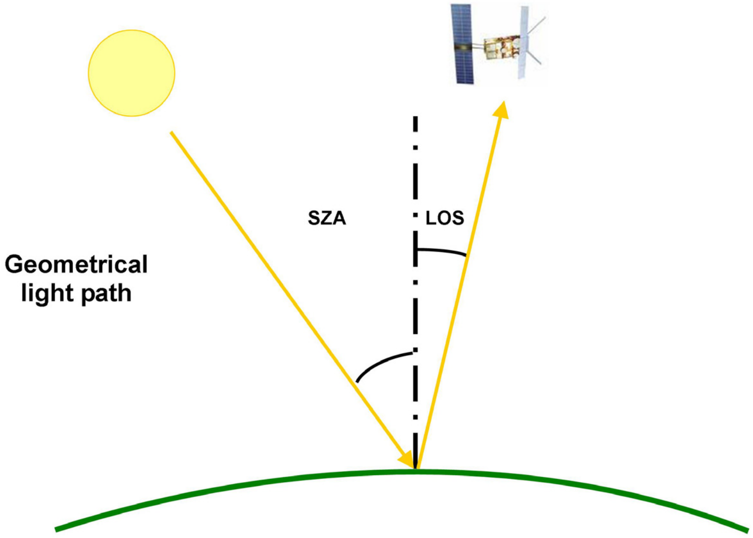

Figure 7.4 Illustration of the geometrical light path approximation.

According to Figure 7.4, the factor of enhancement of the light path with respect to the vertical (AMF) is given by the simple geometrical form:

$$AMF = \frac{1}{\cos(LOS)} + \frac{1}{\cos(SZA)} \tag{7.10}$$

This expression is in fact only valid for SZA lower than 70°. A generalized formulation of equation 7.10 that accounts for the spherical geometry of the Earth and which is valid for SZA up to 85° is provided by:

$$AMF = \frac{1}{\cos(LOS)} + \frac{\sqrt{\cos^2(SZA) + \varepsilon^2 + 2\varepsilon} - \cos(SZA)}{\varepsilon} \tag{7.11}$$

with ε=h/r, h denoting the thickness of the atmosphere (60 km), and r (6370 km) the mean Earth radius.

The geometrical formulation given here is in fact a good approximation of the AMF for a purely stratospheric absorber since only a small fraction of the light is scattered within the stratosphere. Of course, for situations with enhanced tropospheric BrO concentrations, the use of this geometrical air mass factor can lead to substantial errors on the total BrO columns and therefore a realistic air mass factor calculation requires radiative transfer simulations that account for Rayleigh scattering, Mie scattering (clouds and aerosols), surface albedo and atmospheric BrO profile shape (see section 7.2).

7.3.1.2 Results

We have analyzed the complete set of GOME data between 1996 and 2003. The total BrO columns are displayed in Figure 7.5 as a function of the time (daily mean). The results are averaged over five latitudinal bands and the values corresponding to the different types of measured pixels (3 forward scans from east to west followed by a back scan) are presented separately. At first glance, the observed latitudinal and seasonal variations follow qualitatively the expected behavior of stratospheric BrO, with higher values at higher latitudes and a maximum/minimum in winter/summer. A closer look reveals however that the values are higher than the columns predicted by the stratospheric BrO climatology (see Figure 6.13), in particular in polar spring, indicating that significant amounts of BrO must be present in the troposphere. Note also that the peaks and outliers that are found in the BrO time series are due to GOME anomalies such as Peltier cooler switch-offs, instrument or satellite switch-offs, on-board anomalies, or special operations. From Figure 7.5, it is clear that some care must be taken when interpreting the observed year-to-year variations of the total BrO columns. Between 1996 and 2000, systematic variations between the different scans are observed, particularly in the southern hemisphere. After 2000, the strong degradation of the instrument has a dramatic impact on the results for the different types of pixels. We have changed several DOAS settings and tested different approaches for the selection of the reference spectrum but, in spite of all our efforts, the agreement between the results for the different types of pixels could not be improved anymore. Therefore and since the highest quality of data is required to retrieve tropospheric BrO columns, we have decided to treat only the data that exhibit the best consistency between the different scans and that are not too affected by degradation effects, i.e. the years 1999 and 2000.

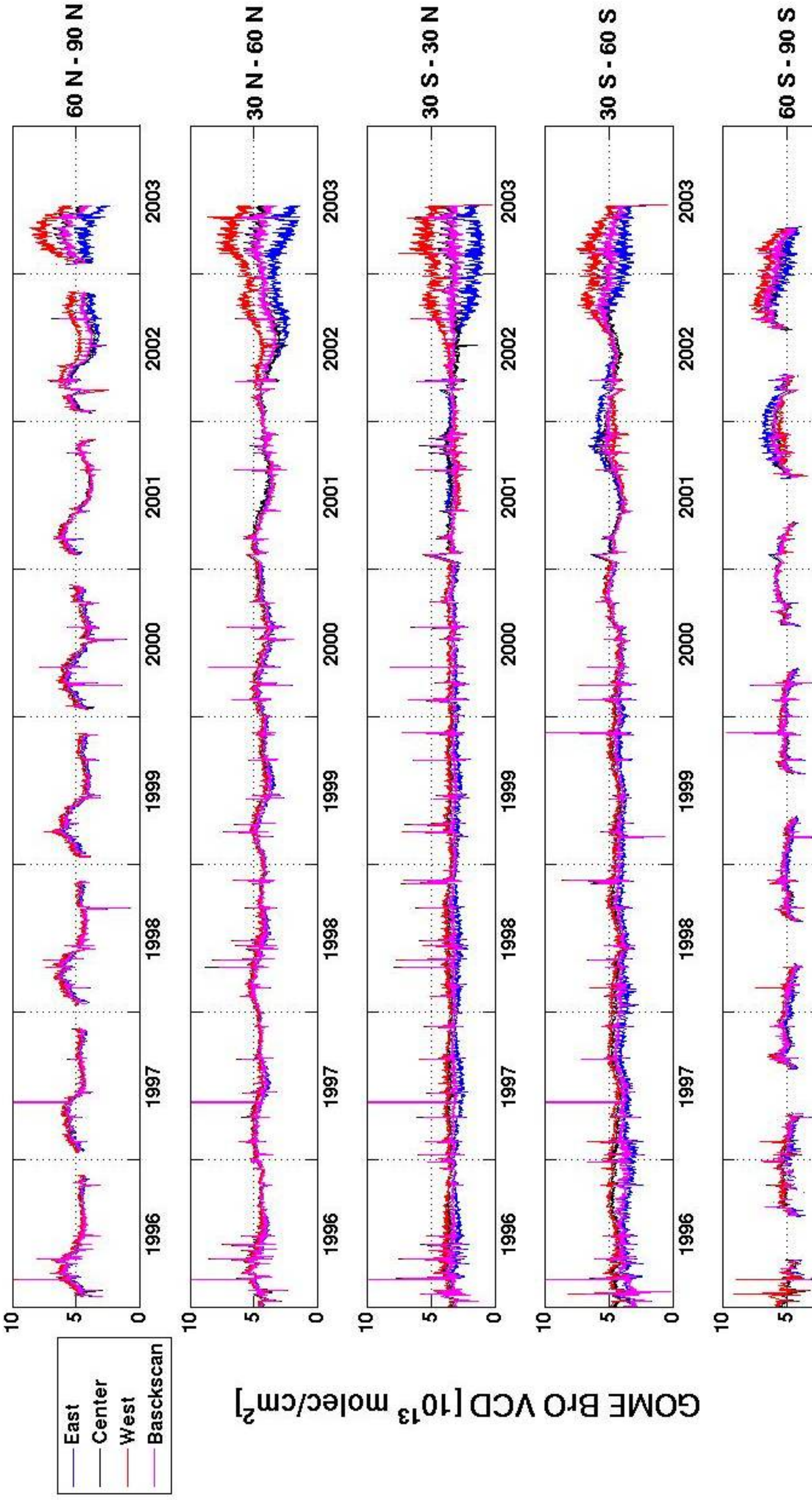

Figure 7.5 Time series of BrO total vertical columns daily averaged for several latitudinal bands. The colored curves correspond to the different types of pixel in a measurement sequence (east, center, west and backscan). The data for solar zenith angles larger than 80° are not considered here.

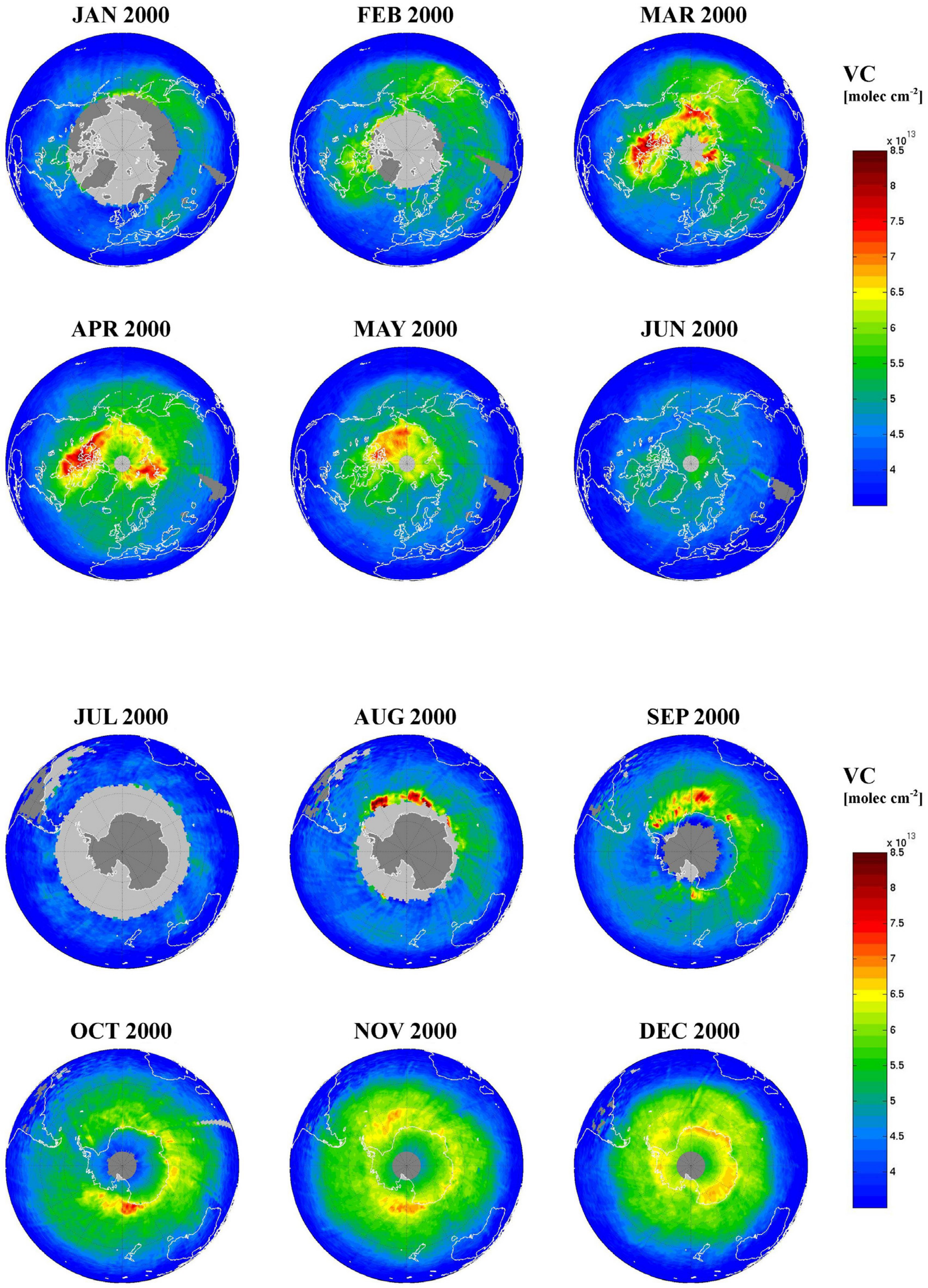

Figure 7.6 Monthly averages of total BrO vertical columns in winter/spring 2000 for the Northern hemisphere (upper plots) and the Southern hemisphere (lower plots). Only data corresponding to solar zenith angles lower than 80° are kept.

As an example, Figure 7.6 displays the spatial distribution of the monthly averaged total BrO columns from GOME for the winter/spring period 2000 in both hemispheres. The areas left in gray correspond to solar zenith angles larger than 80° or regions with no satellite overpass[1]. Very large BrO columns are observed during polar spring in both hemispheres. These events are related to boundary layer BrO emissions and have already been highlighted in previous studies (Wagner and Platt, 1998; Richter et al., 1998, 2002; Chance, 1998). The enhanced BrO columns are observed over sea ice and along the coast lines of the Arctic and Antarctic. The difference in BrO distribution between both hemispheres mainly reflects the differences in sea-ice distribution.

7.3.2 Global tropospheric BrO distribution

In Figure 7.7 monthly averaged tropospheric BrO vertical columns derived from the algorithm described in section 7.2 are displayed in winter/spring season 2000 for both hemispheres.

Several remarks can be made:

- Compared to the total vertical columns presented in Figure 7.6, the polar bromine emissions at the surface are better isolated from the stratospheric BrO background, illustrating the good performance of our stratospheric correction. Moreover, the regions with enhanced tropospheric BrO columns exhibit a better correlation with the area of first year sea ice. This is due to our sophisticated treatment of surface albedo and snow/ice-covered surfaces in the retrieval.
- In the Northern hemisphere, the regions with high tropospheric BrO columns (from March until May) are mainly located near coast lines and over the Arctic Ocean. These regions move towards the North following the sea-ice retreat as the summer is settling. No increased tropospheric BrO can be found after June.
- In the Southern hemisphere, enhanced tropospheric BrO columns are found from August to December and have a more ring like structure following the edge of the Antarctic continent. A striking feature of the Antarctic results is that high tropospheric BrO columns are found even in summer (e.g. December). This has already been pointed out by Richter et al. (2002). The reason for this summer BrO activation is currently unclear.
- Outside the regions with boundary layer BrO emissions, a background tropospheric BrO column of 1-2 x 10^{13} molec/cm² (reaching 3 x 10^{13} molec/cm² in the Southern hemisphere in summer) is observed in all conditions (whatever the latitude or season) in agreement with previous studies using balloon, ground-based and satellite observations (e.g., Fitzenberger et al., 2000; Hendrick et al., 2007; Theys et al., 2007 (chapter 5); Van Roozendael et al., 2002; Richter et al., 2002) that suggest the existence of a global tropospheric BrO content.

---

[1] Over South America, the total BrO columns exhibit a large scatter resulting from the exposure of the satellite instrument to enhanced radiation and high energy particles (this is due to an anomaly of the earth's radiation belts, the so-called South Atlantic Anomaly). Therefore, only the data with reasonable DOAS fitting residuals have been retained.

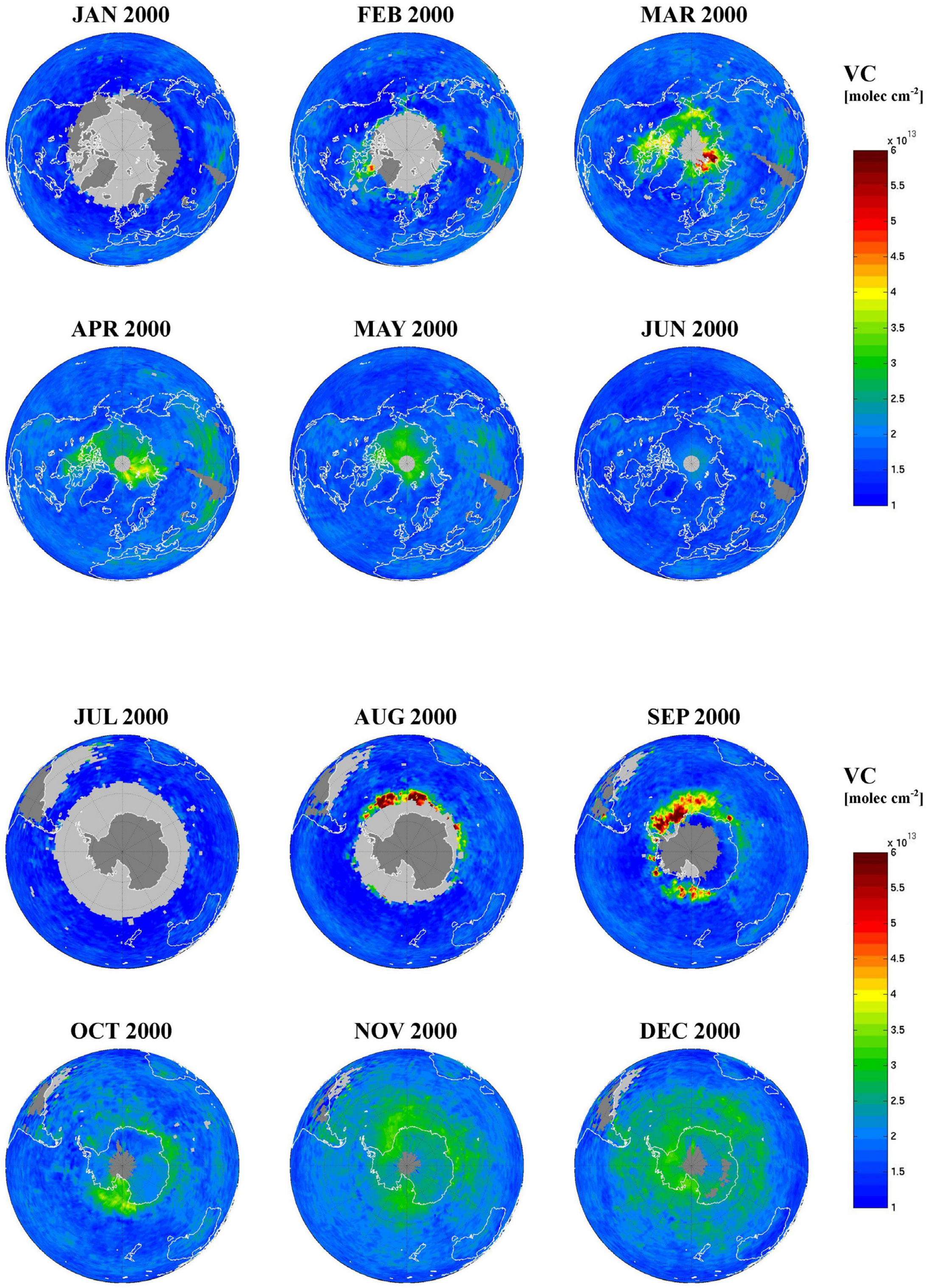

Figure 7.7 Monthly averages of tropospheric BrO vertical columns in winter/spring 2000 for the Northern hemisphere (upper plots) and the Southern hemisphere (lower plots). Only data corresponding to solar zenith angles lower than 80° are kept.

In order to illustrate the separation of the total vertical columns into the stratospheric and tropospheric contributions as achieved by our retrieval technique, Figure 7.8 displays the total[1] vertical columns as a function of the corresponding stratospheric columns for selected months in spring in both hemispheres (North: February-March-April; South: August-September-October).

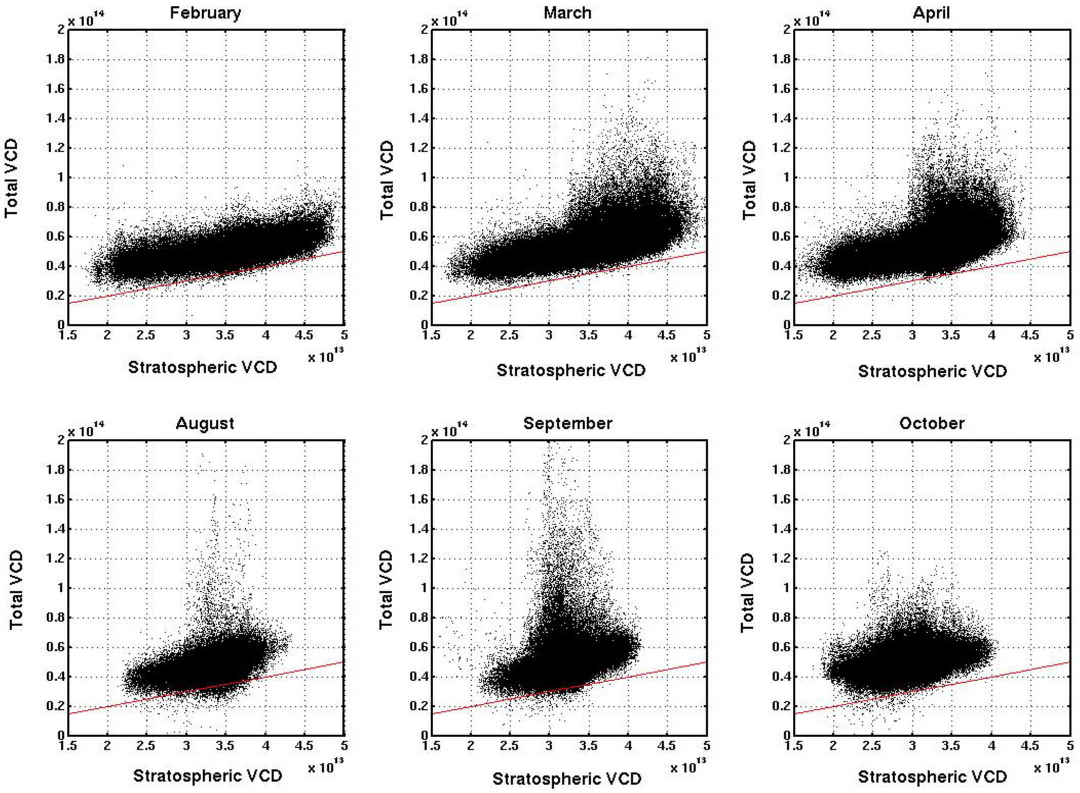

Figure 7.8 Correlation between total and stratospheric BrO columns from 1999 to 2000, for (upper plots) the Northern Hemisphere (February-March-April) and (lower plots) the Southern Hemisphere (August-September-October). Only latitudes poleward of ± 35° and solar zenith angles lower than 80° have been selected. The red lines correspond to the 1:1 lines (Total=Stratospheric BrO vertical columns).

The linear dependence of the total columns with the stratospheric columns is clearly seen, providing an additional evidence of the reliability of the adopted stratospheric correction. However, compared to the purely stratospheric columns, the total vertical columns are offseted by 1 - 2 x 10^{13} molec/cm². As already said, we attribute this non-zero residual column to a global tropospheric BrO background.

In addition to the stratospheric and background tropospheric columns, strong enhancements of the total columns are also visible and reflect the polar boundary layer spring emissions of BrO. According to Figure 7.8, it can be stated that any total column value larger than 8 x 10^{13} molec/cm² has an unambiguous component from the polar

---

[1] No simplified geometrical AMFs are applied here. The total column is the sum of the stratospheric column estimated from the stratospheric BrO climatology and the retrieved tropospheric BrO columns.

boundary layer. The boundary layer BrO presents however a very large variability, (especially in the Southern hemisphere), with vertical columns reaching up to 8 and 13 x 10^{13} molec/cm², respectively in the Northern and Southern hemispheres. Assuming a well mixed boundary layer of 2 km height, it corresponds to upper limits of 20 and 30 pptv of tropospheric BrO respectively; these values agree well with estimates from previous studies (e.g. Wagner and Platt, 1998; Richter et al., 1998, 2002).

Although the results suggest the existence of a tropospheric BrO background in the atmosphere at all latitudes, one can argue that Figures 7.7 and 7.8 provide no firm proof for this assumption. Therefore, Figure 7.9 shows an example of results, with the aim to consolidate our tropospheric BrO column product. Monthly maps of tropospheric BrO slant columns and vertical columns are presented for February 1999 over the Antarctic. This period and location has been selected as it should not be influenced by polar spring boundary layer BrO events.

As can be seen, higher tropospheric BrO slant columns are observed over the Antarctic continent. If a substantial amount of BrO exists in the troposphere, this is qualitatively the behavior we would expect from the tropospheric light path enhancement arising over high reflectivity surfaces. This interpretation is tested on a more quantitative basis in the tropospheric BrO vertical columns map (after applying tropospheric BrO air mass factors). Interestingly, the tropospheric BrO vertical columns are homogeneously distributed throughout the southern hemisphere and exhibit negligible variations when crossing the edge of the Antarctic continent. This supports the existence of a tropospheric BrO background extending over mid- and high latitudes. Besides the fact that our retrieval algorithm seems to be able to correct for surface albedo effects, it also suggests that the hypothesis of a free-tropospheric BrO layer is reasonable. Indeed, assuming a tropospheric BrO profile shape with a maximum close to the surface would reduce the tropospheric air mass factors over low albedo regions by a factor of 2 to 3, while they mainly remain unchanged for high albedo surfaces. Applying these tropospheric air mass factors would therefore lead to a strong and unrealistic albedo dependence of the results.

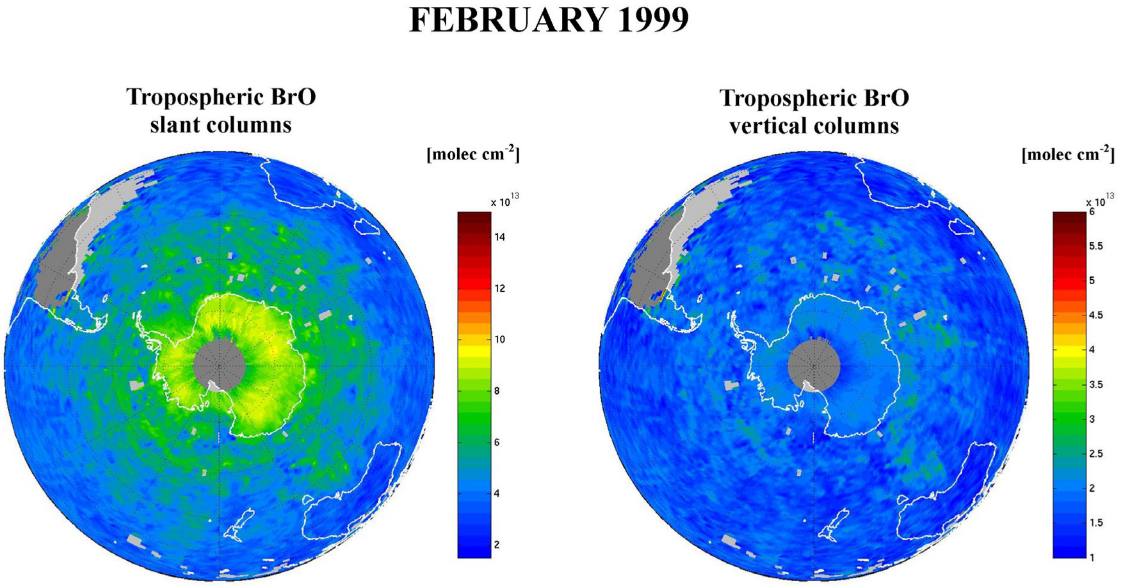

Figure 7.9 Monthly averages of tropospheric BrO slant and vertical columns in February 1999 for the Southern hemisphere. Only data corresponding to solar zenith angles lower than 80° are kept.

7.3.3 Latitudinal and seasonal variations of tropospheric BrO

In this section, we investigate the latitudinal and seasonal variations of the tropospheric BrO vertical column results. For this purpose, we have computed ‘one week moving’ averages of tropospheric BrO columns for different latitudinal bands in both hemispheres. The results are presented in Figure 7.10, together with estimates of the corresponding retrieval errors that include all sources of systematic uncertainties (details are given in section 7.2.6). We have also plotted the monthly averaged tropospheric vertical columns, as well as the variability of the data (1σ) within each latitudinal band and month.

Before entering into the details, it is important to note the huge variability of the resulting tropospheric vertical columns. Although a fraction of this variability originates from the natural variability of tropospheric BrO (e.g. during spring bromine explosion events at high latitudes), an important part of the observed variations results from the propagation of the instrumental noise (and most likely other random sources of uncertainties) through the DOAS analysis. When averaging (as in Figure 7.10), the random error is largely reduced and the total error on the averaged tropospheric BrO vertical columns is dominated by systematic errors. The latter errors (grey-dashed area) are estimated to be in the range from 1 x 10^{13} molec/cm² in summer to 1.5 x 10^{13} molec/cm² in winter.

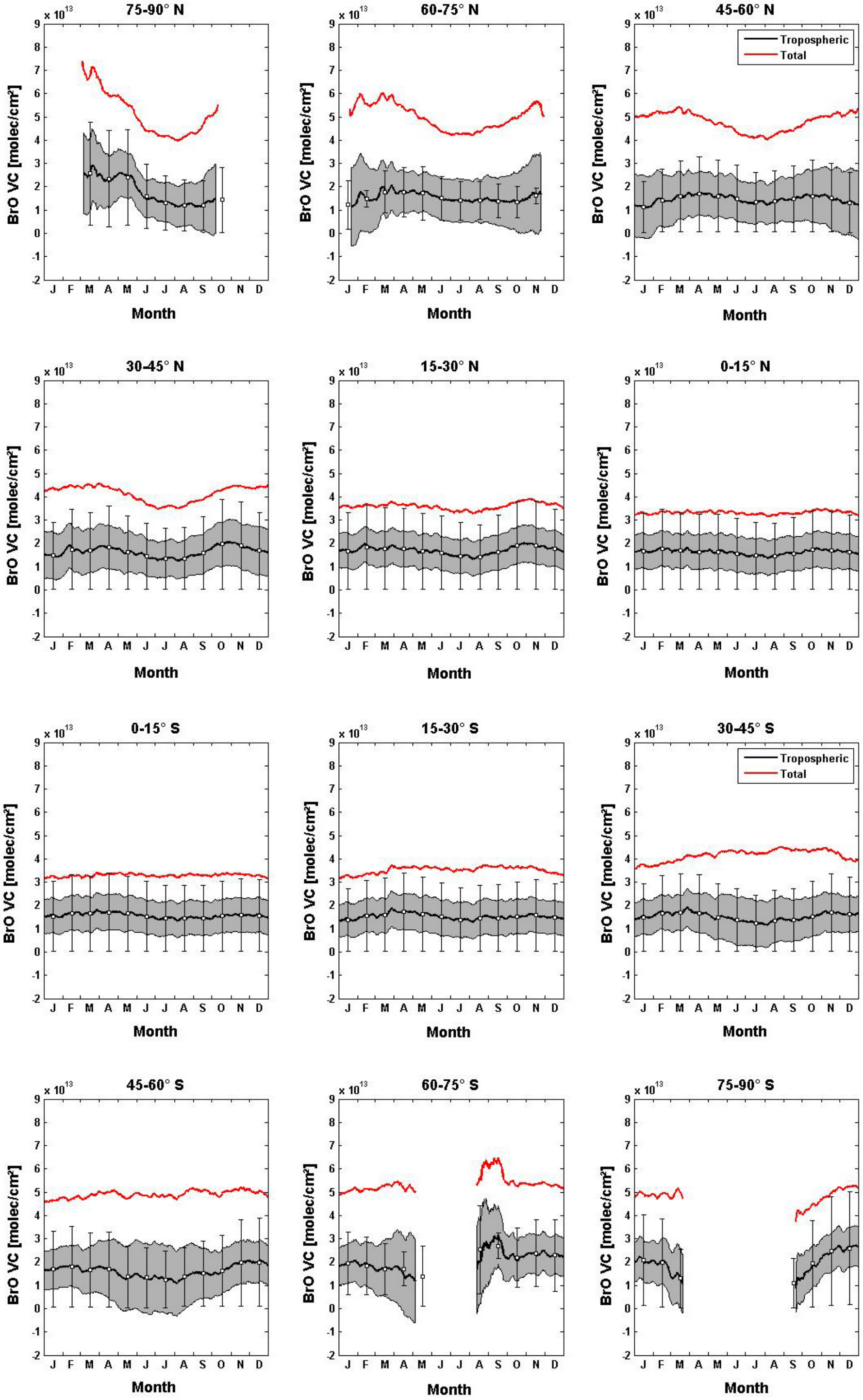

Figure 7.10 Zonal mean of total (red) and tropospheric (black) BrO vertical columns as a function of time of year (7-day moving averages). The grey-dashed area indicates the total error on the tropospheric BrO vertical columns (see text). The white squares are the monthly averaged tropospheric BrO vertical columns, and the error bars correspond to 1-sigma standard deviation of the data around the mean. The data used are from 1999 to 2000, and solar zenith angles lower than 80°.

From Figure 7.10, several observations can be made:

- The polar BrO emissions in spring are located above 60° of latitude in the northern hemisphere, while in the South the spring BrO increase is restricted to the 60°-75° latitude band.
- In the tropics (latitudes between ±30°), the tropospheric BrO columns depend almost exclusively on the assumed value of the BrO slant column over the equator (equatorial offset correction: 7.5 x 10^{13} molec/cm²). Therefore, no real information is coming from the measurements at these latitudes.
- Except the events of BrO emissions at high latitudes, the seasonal and latitudinal variations of the tropospheric BrO columns are generally rather small, with a magnitude lying within the uncertainties of the retrieved tropospheric BrO columns. In comparison, the variations of the total BrO columns (shown with red lines in Figure 7.10) have stronger amplitudes, reflecting the latitudinal and seasonal variations of stratospheric BrO.

To summarize, our analysis tends to confirm the presence of a global tropospheric BrO background with vertical columns of 1-3 x 10^{13} molec/cm², in addition to the polar BrO emissions occurring in spring. Given the relatively large errors on this global tropospheric background (column errors in the range from 1 to 1.5 x 10^{13} molec/cm²), it is however difficult to draw unquestionable conclusions on its latitudinal and seasonal variations.

7.4 Retrieval of tropospheric BrO columns from GOME-2 observations on MetOp-A

7.4.1 GOME-2 slant column retrieval

BrO slant columns have been retrieved from GOME-2 spectra using analysis settings detailed in Table 7.2. The main difference compared to GOME is related to the choice of the reference spectrum: instead of using Earthshine spectra over the equatorial Pacific, the daily solar spectrum measured by GOME-2 is used (no equatorial slant column offset correction is thus applied). Another difference w.r.t. to GOME analysis concerns the fitting interval. Historically, the GOME-2 settings have been established before the final GOME settings were adopted, and at that time we used only three BrO absorption bands (336-351.5 nm). In the future, we intend to use the same fitting interval for GOME-2 and for GOME. Nevertheless, we have performed tests on GOME-2 data and we found small differences between the results analyzed in the different fitting windows (336-351.5 and 336-359 nm).

We have analyzed a total of 14 months of GOME-2 data between June 2007 and August 2008. Examples of results in polar spring are presented in Figure 7.11 (total vertical columns using geometrical air mass factors are displayed). It basically shows that the BrO emission patterns observed by GOME are similarly seen by GOME-2, with an improved spatial resolution.

Table 7.2 DOAS settings used for GOME-2 BrO slant column analysis

Fitting interval	336-351.5 nm
Molecular absorption cross-sections	BrO [Fleischmann et al., 2004] O_3 218K [Brion et al., 1993] O_3 243K [Brion et al., 1993] NO_2 243K [Burrows et al., 1998] O_4 [Hermans et al.] 2 Ring cross-sections [Vountas et al., 1998]
Additional terms/corrections	Polynomial (order 3) Constant offset Wavelength calibration of sun reference by adjustment on convolved Chance and Spurr (1997) solar lines atlas.

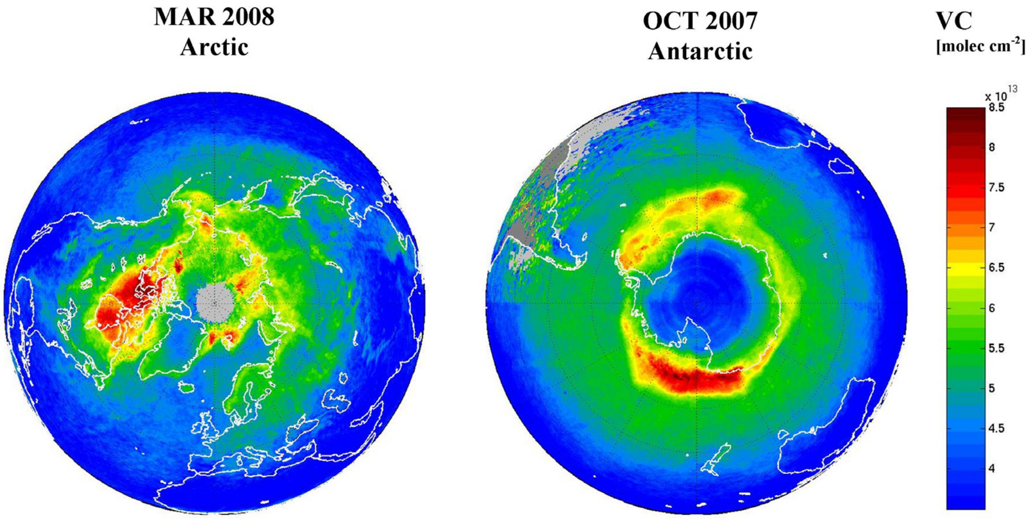

Figure 7.11 Monthly averages of GOME-2 BrO vertical columns for springtime in both hemispheres (NH: March 2008, SH: October 2007). The values have been calculated using geometrical air mass factors.

7.4.2 Transport of tropospheric BrO: case studies

Compared to its predecessors GOME and SCIAMACHY, GOME-2 combines the advantages of a performant spectroscopic design and both good spatial resolution and coverage. Therefore GOME-2 has potentially a better capability to quantify and follow the transport of BrO plumes formed in the polar boundary layer. This aspect is illustrated in the present section with three case studies (two in the Arctic, one in the Antarctic). Here the tropospheric BrO columns have been retrieved from GOME-2 measurements using the same algorithm as for the GOME data.

Case study 1:

Before studying transport events of tropospheric BrO, it is necessary to demonstrate that the stratospheric BrO climatology used is able to reproduce the spatial structures of stratospheric BrO as observed from GOME-2, and eventually to correct them. This is crucial because otherwise one could falsely attribute stratospheric BrO hotspots to the troposphere. For this purpose, Figure 7.12 presents a comparison between the total BrO columns (using geometrical AMFs) measured by GOME-2 and the corresponding stratospheric BrO vertical columns as derived from the BASCOE climatology, for two days in February 2008. The data have been selected in the northern hemisphere in winter, a period found optimal to test our BrO climatology because nice large-scale dynamical structures (of stratospheric origin) are frequently observed in the BrO maps and in the meantime the influence of tropospheric BrO on the measurements is moderate (absence of large and persistent cloud of tropospheric BrO). Figure 7.12 shows that the stratospheric BrO climatology reproduces qualitatively very well the dynamical structures of stratospheric BrO as observed by the satellite. This is further confirmed on a

quantitative basis, when examining the maps of the difference between the total and stratospheric columns that show no strong evidence of remaining structures that would have been not accounted for by the climatology. This is particularly remarkable since both measured and simulated data sets are determined independently from each other.
These results are important especially because it was speculated that the free tropospheric BrO background at mid-latitudes might be at least partly caused by transport of BrO enriched air masses from the polar boundary layer (Hollwedel, 2005). Figure 7.12 shows that this particular aspect can only be studied properly by separating the stratospheric and tropospheric BrO structures in the total BrO column field measured from space.

Case study 2:

A typical event of enhanced tropospheric BrO is presented in Figure 7.13, which shows the total, stratospheric and tropospheric BrO columns in the northern hemisphere over a period of one week in April 2008. It nicely shows the development and the long-range transport of BrO plumes in the Arctic boundary layer.
Two main observations can be made. (1) As for case study 1, total BrO column hotspots seen by GOME-2 exhibit spatial patterns similar to model estimates of stratospheric BrO column. (2) A closer look to the BrO columns results shows also that several BrO hotspots are observed in both stratospheric columns and tropospheric residual columns. This can however not be explained by a mismatch in the stratospheric BrO correction. Even though this behavior must be investigated on a more systematic basis, such a correlation can be explained by the strong dependence between the stratospheric BrO column and the tropopause height. Whereas the latter tropopause is linked to weather systems, it determines temperature and illumination which in turn influence the concentrations of BrO in the troposphere. In any cases, this interesting feature further emphasizes the need for a proper quantitative interpretation of the results, to separate the BrO total columns into their stratospheric and tropospheric contributions.

Total

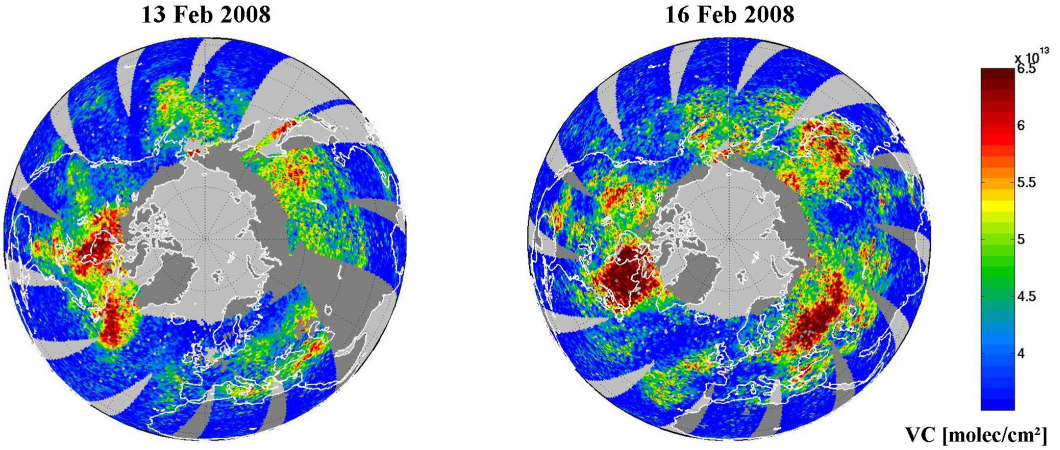

Stratospheric

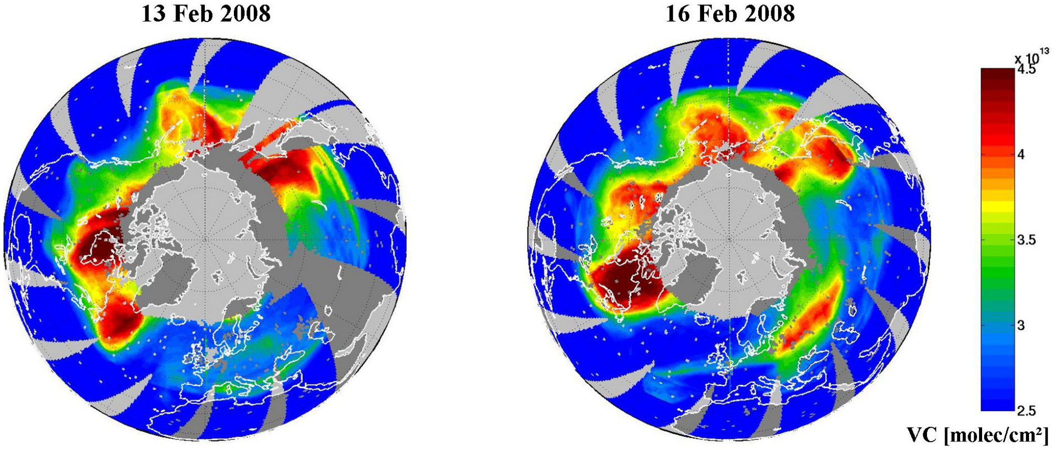

Total minus stratospheric

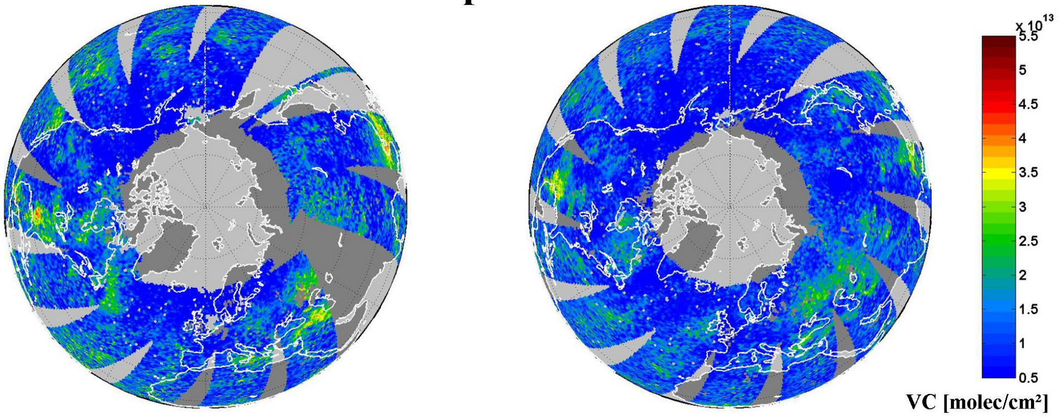

Figure 7.12 GOME-2 total BrO columns (upper plots), stratospheric BrO columns calculated from the BASCOE climatology at GOME-2 overpass (center plots) and the difference between the total and stratospheric BrO columns (lower plots). The results are presented for the (left) 13th and (right) 16th February 2008.

Total BrO

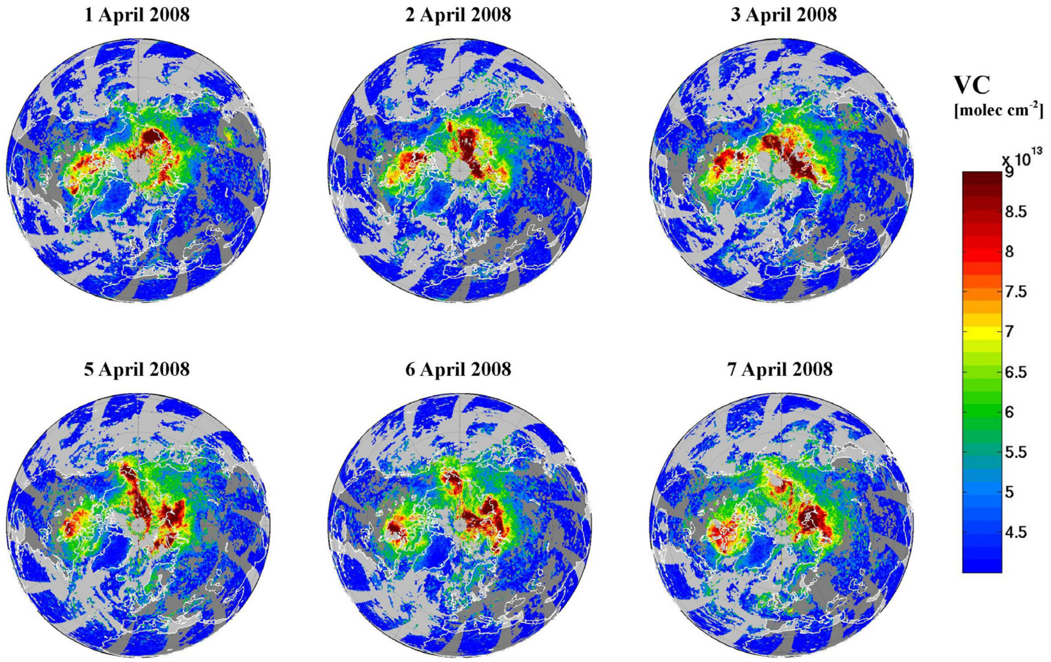

Stratospheric BrO

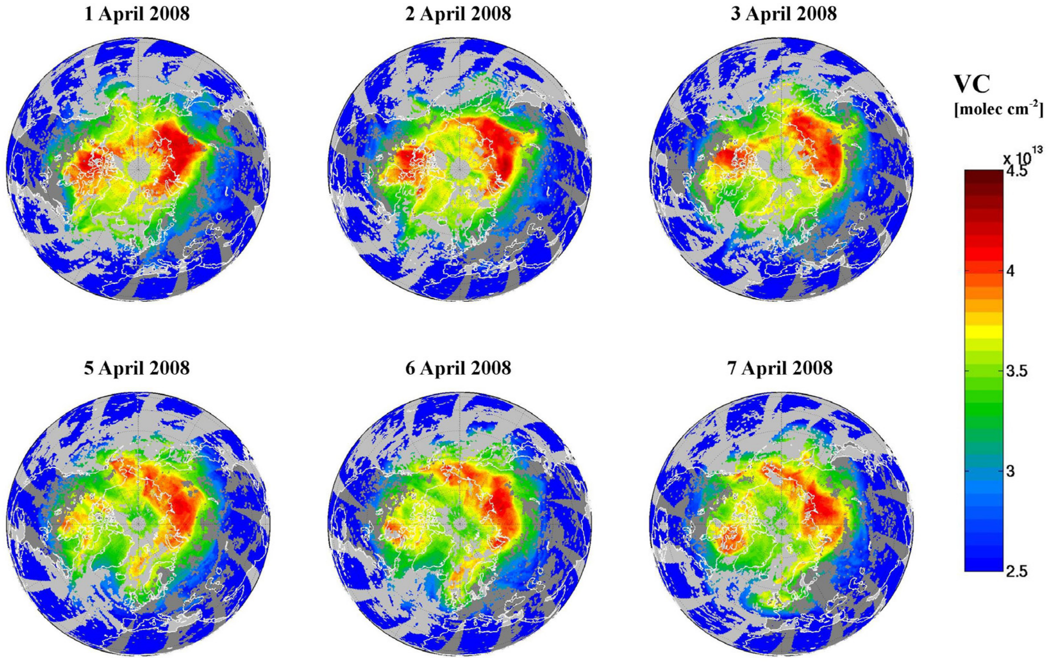

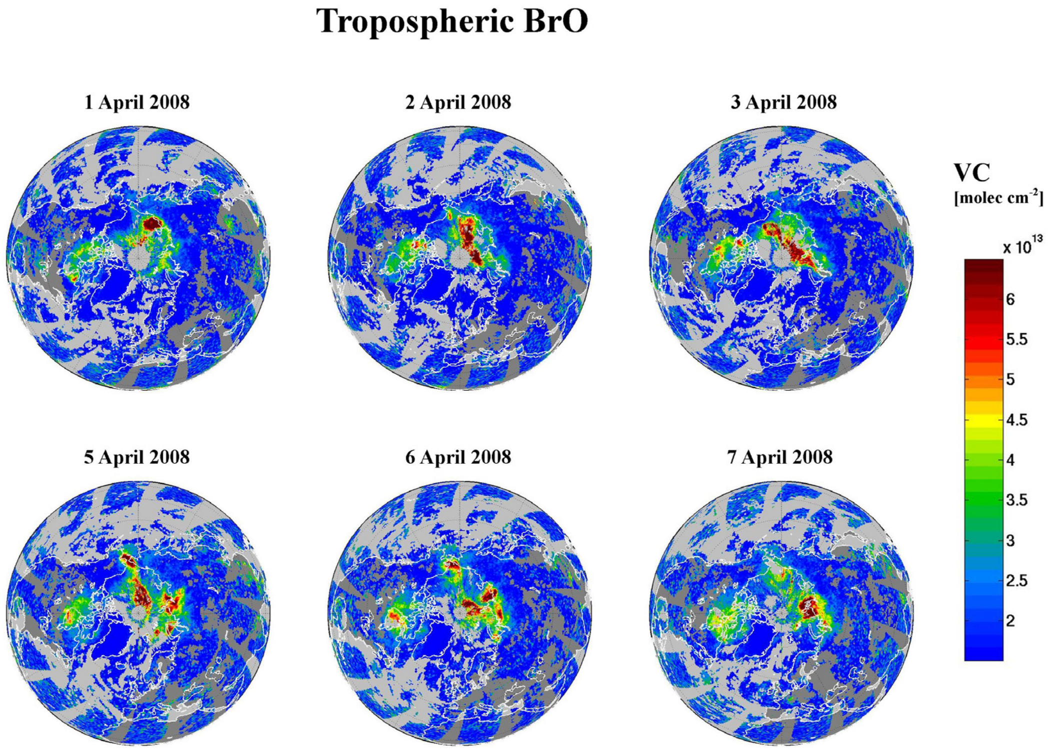

Figure 7.13 Selected days of BrO columns (total, stratospheric and tropospheric) retrieved from GOME-2 measurements. The regions contaminated by clouds have been left gray.

Case study 3:

An example of results over the Antarctic is presented in Figure 7.14, which shows the tropospheric BrO columns for nine days in October 2007. Since the stratospheric BrO column exhibits a weak variability for these days, only the tropospheric contribution of the total BrO column is shown here. One can observe tropospheric BrO plumes that can be followed during several days, demonstrating the life time and transport of these events. Another striking feature in Figure 7.14 is the sudden increase of tropospheric BrO over certain regions, suggesting the fast activation of BrO (within one day) over large areas in the polar boundary layer.

In summary, the three examples presented above illustrate the power of the tropospheric BrO columns retrieval technique when it is applied to the new generation of instruments like GOME-2. These results coupled e.g. with trajectory and tropospheric chemistry models (see e.g., Begoin et al., 2009), could be used to better understand the mechanisms of BrO formation and the chemistry sustaining the activation of bromine in the polar troposphere, but also to assess the importance of transport of polar trosposheric BrO towards mid-latitudes.

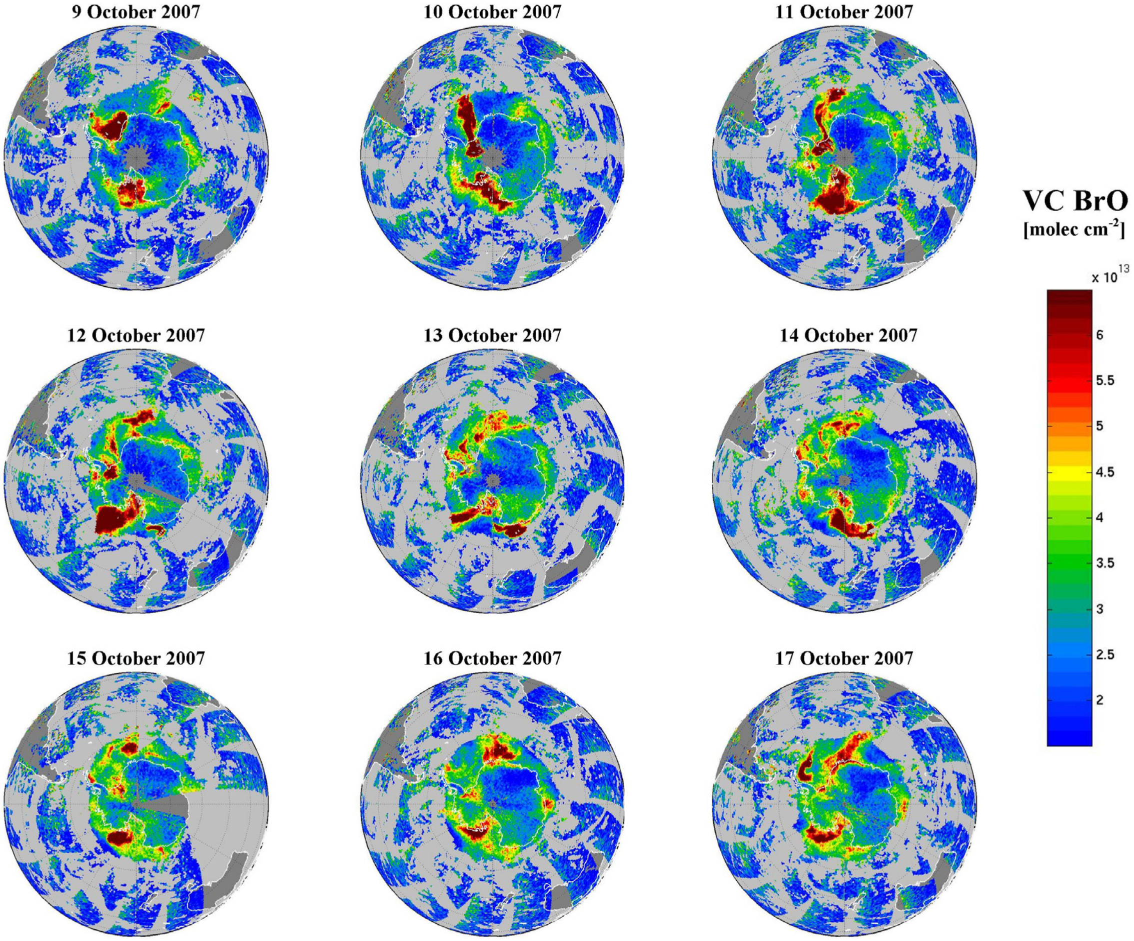

Figure 7.14 Selected days of residual tropospheric BrO columns from GOME-2. The regions contaminated by clouds have been left gray.

7.5 Verification of the retrievals

7.5.1 Comparison to ground-based observations

Total and tropospheric BrO columns retrieved from GOME and GOME-2 have been compared to estimates made from ground-based observations at Harestua (60.22°N, 10.75°E). The retrieval algorithm developed by Hendrick et al. (2007) and already described in section 6.3.2.1 has been applied to ground-based observations in order to retrieve BrO vertical profiles. Total and tropospheric BrO columns are then calculated by integrating the retrieved profiles in the appropriate altitude ranges. As the ground-based BrO profiles are retrieved for a solar zenith angle of 80°, a photochemical correction is applied to the ground-based (total and tropospheric) vertical columns in order to match the solar zenith angle corresponding to the satellites overpass time.

Figures 7.15 and 7.16 show the comparisons between the ground-based and the coincident satellites total and tropospheric BrO columns, respectively for GOME (period: 1999-2000) and GOME-2 (period: July 2007-June 2008). Daily mean GOME and GOME-2 BrO column amounts are calculated using all pixels[1] with a solar zenith angle lower than 80° and falling within a radius of 200 km around Harestua. Here we have not shown the comparisons between the ground-based stratospheric BrO columns and the estimates from the stratospheric BrO climatology, as these results have already been shown in section 6.3.2.1 (Figure 6.3).

In general, GOME and GOME-2 BrO total vertical columns are found to be in good agreement with the BrO total columns inferred from the ground-based observations, in terms of mean level and seasonal variation. Figures 7.15 and 7.16 also indicate that both satellites and ground-based observations are consistent with a tropospheric BrO layer of $1.45 \pm 0.45 \times 10^{13}$ molec/cm² in column. Note that this estimate of the mean tropospheric BrO column amount is roughly consistent with the tropospheric BrO columns of about 1.1×10^{13} molec/cm² inferred from ground-based MAX-DOAS measurements in Reunion Island (chapter 5).

---

[1] Note that an additional selection of the pixels is applied, based on the cloud fractions (as detailed in section 7.2.5).

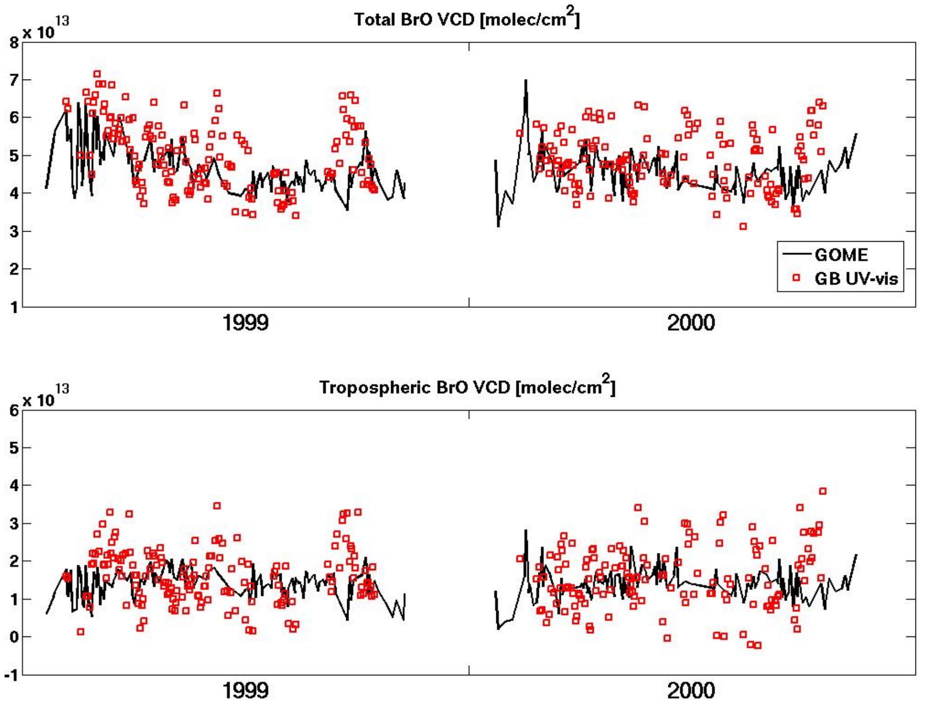

Figure 7.15 Comparison between GOME and ground-based total (upper plot) and tropospheric (lower plot) BrO vertical columns, at Harestua for the period 1999-2000.

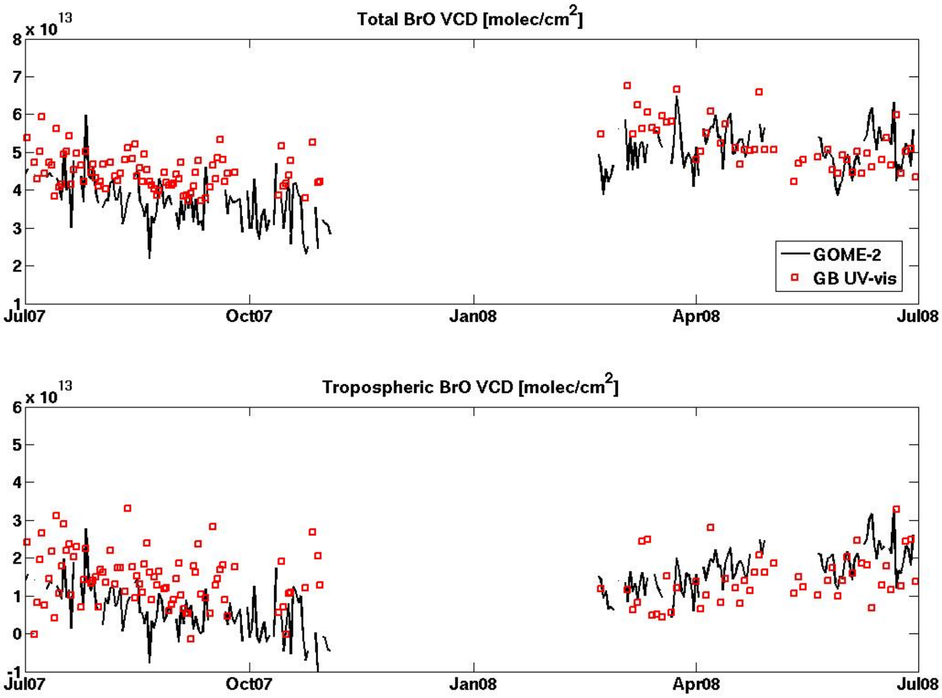

Figure 7.16 Same as Figure 7.15, for GOME-2 observations from July 2007 to June 2008.

7.5.2 Comparison to tropospheric CTM calculations

The tropospheric BrO columns retrieved from GOME data have been compared to the output of the *p*-TOMCAT tropospheric chemical transport model (see section 7.2.5). This comparison exercise has been carried out in a study conducted by Yang et al. (2009)[1] whose aim was to investigate the possible sources of bromine during bromine explosion events. The authors have considered three different sources for the release of bromine. The first two sources, already included in a previous study (Yang et al., 2005), are the emissions from bromocarbons and open ocean sea salt. The last additional source considered is the sea salt aerosols production from snow lying on sea ice during blowing snow events and subsequent bromine release.

In order to assess the importance of the different bromine sources, several model experiments have been conducted: the 'SNOW' run includes a parameterization of the three bromine sources, the 'OCEAN' run omits the blowing snow sea salt source and the 'noHET' run is the same as 'SNOW' but with the heterogeneous reactions switched off in order to isolate the effect of heterogeneous recycling on the BrO fraction.

As an example, Figure 7.17 shows a comparison between simulated and GOME BrO columns (total and tropospheric) in 1998 over Barrow (73°N, 157°W) for comparable solar zenith angles.

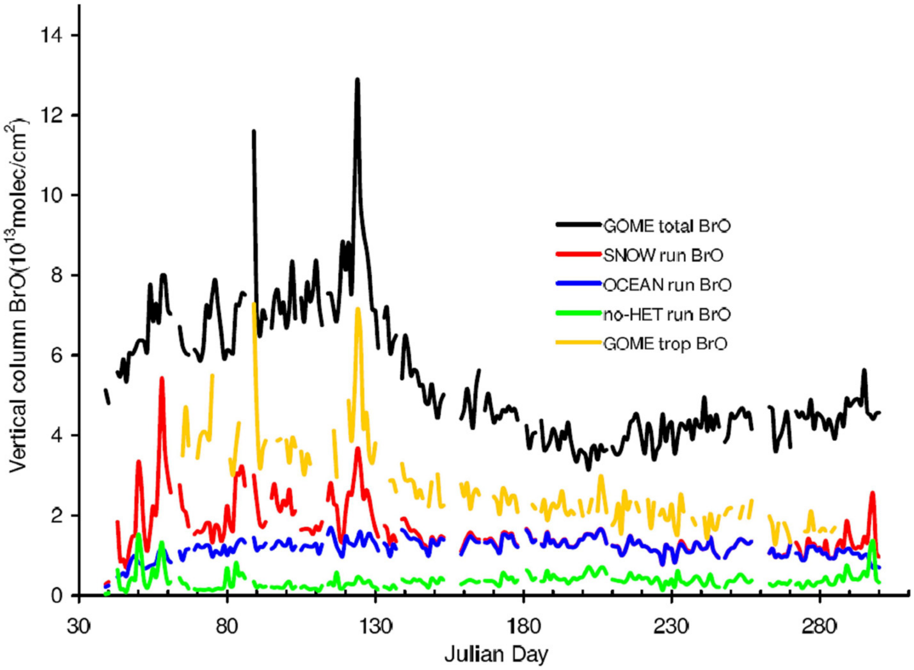

Figure 7.17 Comparisons of modeled tropospheric BrO column (red) with GOME total BrO vertical column (black) and retrieved tropospheric BrO columns (yellow) over Barrow for the year of 1998. The OCEAN and noHET model runs are shown in blue and green lines, respectively. Adapted from Yang et al. (2009).

---

[1] Yang, X., Pyle, J.A., Cox, R.A., Theys, N., Van Roozendael, M., *Snow-sourced bromine and its implications for polar tropospheric ozone*, to be submitted to Atmos. Chem. Phys. Discuss., 2009.

Besides a general tendency of the model to underestimate the tropospheric BrO columns retrieved from GOME, the plot shows that the model successfully reproduce the observed bromine explosion (short duration) events and seasonal variation, only if the snow-sourced bromine is included. Moreover, when the heterogeneous reactions are excluded, BrO is only 30% of the 'SNOW' run indicating the important role of heterogeneous reactivation in sustaining a high fraction of BrO in the gas phase.

More comparisons have been made at different sites in both Arctic and Antarctic regions (not shown). Although the model fails to reproduce all the observed features, the occurrence of bromine explosion events in the satellite record often coincides with an increase of the simulated tropospheric BrO columns ('SNOW' run).

These results shows that the bromine explosion phenomenon is consistent with the release of bromine by blowing snow events, when additional seal salt aerosols are produced in the boundary layer, favoring a reactivation of BrO_x by heterogeneous reactions on their surfaces.

7.6 Conclusions

An algorithm to quantify the global distribution of tropospheric BrO from satellite nadir UV-visible instruments has been developed. The tropospheric BrO columns are retrieved in three steps. First, the BrO absorption is determined from the measured calibrated radiances using the DOAS method. In a second step, the stratospheric component of the signal is removed by subtracting the stratospheric BrO column, calculated using a validated stratospheric BrO climatology (described in chapter 6). In the last step, the tropospheric residual is converted to a tropospheric vertical column by applying an air mass factor that explicitly accounts for changes in measurement vertical sensitivity due to clouds and surface reflectivity (in particular the snow/ice-covered surfaces are properly treated). The algorithm has been successfully applied to a selection of data from GOME and GOME-2 instruments, and it results in a refined interpretation of the nadir BrO observations in particular those related to the following tropospheric BrO issues:

- Polar BrO in the boundary layer: the BrO surface emissions, located over areas of first year sea ice, are well featured and better quantified. In the Northern hemisphere, enhanced boundary layer BrO columns are observed in March and April with values up to 8 x 10^{13} molec/cm². In the Southern hemisphere, large emissions are observed from August to October with boundary layer BrO columns reaching up to 13 x 10^{13} molec/cm². This implies mixing ratios up to several tens of pptv of BrO in the boundary layer. We have also shown that our retrieval method permits to separate the large-scale stratospheric BrO structures from those of tropospheric origin in the total BrO column field measured from space. Therefore the retrieved tropospheric BrO columns allow studying properly and unambiguously the transport of BrO plumes emitted in the polar boundary layer. Furthermore, comparisons between GOME and modeled tropospheric BrO columns using the *p*-TOMCAT CTM revealed that enhanced tropospheric BrO events in the polar region might be at least partly due to high wind speed conditions with blowing snow.
- Global tropospheric BrO background: the measurements are consistent with the presence of a global tropospheric BrO background likely located in the free-

troposphere, with columns of 1-3 x 10^{13} molec/cm². As this interpretation relies strongly on the accuracy of the tropospheric BrO columns, a comprehensive error budget that accounts for all sources of uncertainties in the retrieval has been performed. Moreover, a good agreement between total and tropospheric BrO columns retrieved from satellites and ground-based observations was found, which strengthens the hypothesis of a tropospheric BrO background. The seasonal and latitudinal variations of tropospheric BrO have been investigated. Given the uncertainties on the retrieved tropospheric BrO columns, no noticeable seasonal or latitudinal variation of this tropospheric BrO background could be identified.

Chapter 8

Satellite detection of volcanic BrO emissions[1]

Abstract

Large enhancements of the BrO total column have been detected from analysis of nadir UV-visible observations by the GOME-2 satellite instrument in the vicinity of the Kasatochi volcano (Alaska) during several days after its eruption on the 7 August 2008. The transport of the volcanic plume has been simulated using the FLEXPART dispersion model, and evidence is found that the injection altitude of the BrO plume was located between 8 and 12 km altitude, i.e., in the upper troposphere/lower stratosphere region. Based on these results, the total mass of reactive bromine emitted by the volcano is estimated to be in the range from 50 to 120 tons.

8.1 Introduction

Volcanoes are known to be a major source of particles and gases (e.g., SO_2 and HCl) in the atmosphere. As already mentioned in section 2.3.3, the detection of BrO in a volcanic plume by Bobrowski et al. (2003) using ground-based DOAS measurements, suggested that volcanoes could be also an important source of atmospheric bromine. The importance of such bromine volcanic emissions on the global scale, has been investigated using GOME and SCIAMACHY satellite BrO observations (Afe et al., 2004). Unfortunately, no indication of enhancement of BrO during large volcanic eruptions could be found in any of the sounded eruptions. The reason for this lack of signal in the satellite data remains unclear, but is probably related to (1) the instrumental detection limit, (2) the short lifetime of BrO in a volcanic plume, or (3) a fundamental difference for large eruptions compared to degassing (as observed by Bobrowski et al., 2003).

This chapter reports on GOME-2 satellite measurements of BrO columns performed after the recent massive eruption of the Kasatochi volcano. For the first time, we show clear evidence for the release of a large plume of BrO visible from space during several days while it is transported away from the volcano. The high altitude of the plume not only increased the sensitivity of the satellite measurements but also the chemical lifetime of the BrO plume, explaining why large BrO concentrations could be observed during almost one week after the eruption.

---

[1] This chapter is based on: Theys, N., Van Roozendael, M., Dils, B., Hendrick, F., Hao, N., and De Mazière, M., *First satellite detection of volcanic bromine monoxide emission after the Kasatochi eruption*, Geophys. Res. Lett., 36, L03809, doi:10.1029/2008GL036552, 2009.

8.2 The Kasatochi volcano

The Kasatochi Island (52.17°N, 175.51°W) is part of the Aleutian arc in Alaska (see Figure 8.1). The island has a land area of 5.051 km² and is unpopulated.

Figure 8.1 (left) Location of the Kasatochi Island. (center and right) Pictures showing the Kasatochi volcano before and after its eruption on 7 August 2008. Courtesy to the Alaska Volcano Observatory.

The summit (elevation 314 m a.s.l) is truncated by a large volcanic crater containing a 800 m wide crater lake. The surface of the saltwater lake is less that 60 m a.s.l.
On 7 August 2008, the level of earthquake activity increased in the vicinity of Kasatochi and was also accompanied by volcanic tremor, as reported by the Alaska Volcano Observatory (http://avo.alaska.edu/activity/Kasatochi.php). By 22:30 UTC, Kasatochi began erupting explosively after a period of inactivity of more than 200 years. The eruption sent a huge cloud of ash in the atmosphere (that could be observed from space as illustrated in Figure 8.2) at an altitude of about 10 km[1].

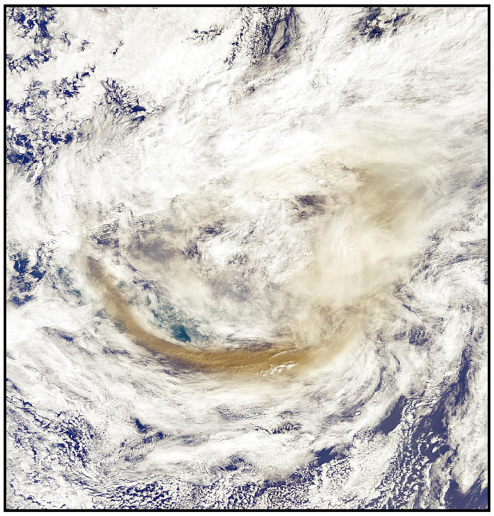

Figure 8.2 Smoke and ash plume from the Kasatochi volcano, visible in brown over a thick layer of clouds. The MERIS instrument on ENVISAT captured this image on 8 August 2008 over Alaska's Aleutian Islands. Courtey to ESA.

---

[1] It should be noted that, because of the hazard to aviation, the eruption has lead to cancellation of 44 flights from Alaska Airlines.

The volcano injected also a very large amount of SO_2 (up to 2 Tg) in the atmosphere, that could be followed during more than 15 days after the eruption by a number of UV-visible (SCIAMACHY, GOME-2 and OMI) and infrared (e.g., IASI) sounders.

8.3 Methods

8.3.1 Data analysis

BrO vertical columns have been retrieved from GOME-2 observations according to the settings presented in chapter 7. In brief, BrO slant columns are derived in the wavelength interval from 336 to 351.5 nm, using the BrO cross-section of Fleischmann et al. (2004). The spectral signatures of NO_2, O_3, O_4, and the Ring effect are also taken into account. Slant columns are converted into vertical columns using geometrical air mass factors adequate for a stratospheric absorber.

8.3.2 Atmospheric transport modeling

The transport of the volcanic BrO plume has been simulated using the Lagrangian particle dispersion model FLEXPART (Stohl et al., 2005). This model has been widely used for long-range atmospheric transport studies, including volcanic plume simulations (e.g., Eckhardt et al., 2008). For the present study it was driven by 3-hourly wind field data from the European Centre for Medium-Range Weather Forecasts with 1°x 1° resolution. Calculations have been performed for a BrO tracer emitted above the volcano at the time of the eruption (22:30-23:00 UTC, on 7 August 2008) within an atmospheric layer of 2 km thickness. An ensemble of forward trajectories has been generated assuming a unit mass source (1 kg of BrO) for atmospheric layer heights varying between 2 and 24 km altitude. The simulations were conducted over six days following the eruption. For each day at the time of GOME-2 overpass (± 0.5 hour), BrO concentrations have been estimated on a latitude-longitude grid of 0.5° x 0.5°. Total vertical columns have been calculated by integrating the concentration profiles using as a weight the averaging kernels of the satellite measurements. The latter were estimated according to Boersma at al. (2004) from the derivative of the retrieved slant column with respect to the true partial column profile, divided by the geometrical air mass factor as used for the GOME-2 retrievals. This approach allows direct comparisons with GOME-2 measured BrO columns. The averaging kernels have been evaluated from radiative transfer calculations performed using a pseudo-spherical version of the DISORT code, accounting for all dependencies on the observation geometry (solar zenith, viewing zenith and relative azimuth angles), the surface albedo (Koelemeijer et al., 2003), the cloud fraction and the cloud top height. Cloud data were obtained from the FRESCO algorithm (Koelemeijer et al., 2001) that is available from the distributed GOME-2 Level 1 data product.

8.4 Results

BrO absorption signatures largely exceeding the detection limit of the GOME-2 instrument have been observed inside the Kasatochi eruption plume. Note that similar BrO absorption was identified in spectra recorded by the SCIAMACHY instrument on ENVISAT.

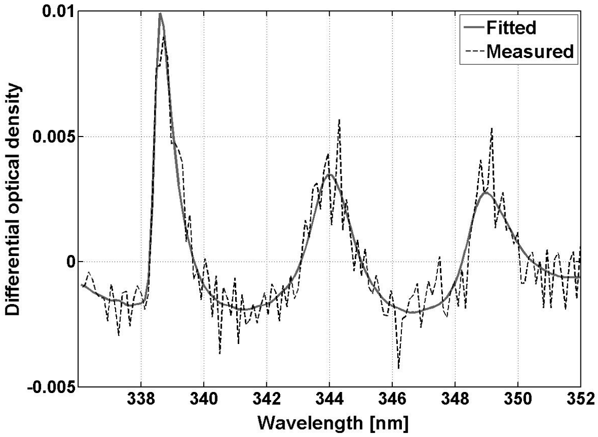

Figure 8.3 Example of a fit to the measured BrO differential absorption as obtained above the volcanic plume on 9 August 2008 (48.2°N, 159.9°W). The slant column, in this case, is 6.34 x 10^{14} molec/cm².

An example of fitting result obtained on 9 August (i.e., two days after the eruption) is shown in Figure 8.3. Different BrO absorption cross-sections have been tested that are highly consistent in terms of the wavelength dependency of their differential structures. An equivalent 10% uncertainty on the retrieved BrO slant columns is attributed from the uncertainty of the BrO absorption cross-sections. The BrO vertical columns measured in the vicinity of the Kasatochi volcano in the period from 8 to 13 August 2008 are presented in Figure 8.4. As can be seen, a large plume of elevated BrO columns extending over an area of about 700 x 500 km² was transported north-east from the Aleutian island. In this period, the BrO column inside the plume reached up to 2.7 (±0.5) x 10^{14} molec/cm². The spatial extent of the plume was found to correlate well with the corresponding SO_2 plume simultaneously measured by GOME-2 (see e.g., http://www.temis.nl/aviation and http://wdc.dlr.de/sensors/gome2).

In order to infer additional information about the altitude of the observed BrO, measurements were compared to a series of FLEXPART simulations, assuming various initial plume heights. A reasonably good correlation between the observed spatial patterns and those calculated by the dispersion model was found when assuming initial injection in layers located at 8-10 km and at 10-12 km. The correlation coefficient between the measured BrO columns and the ones simulated by FLEXPART is larger than 0.6 for atmospheric layer heights between 8 and 12 km, and drops to values lower than 0.45 for heights below 8 km or above 12 km. As an example, Figure 8.4 displays the total BrO columns simulated by FLEXPART using adjusted initial BrO masses in the 8-10 km and 10-12 km layers (see next section). One should notice fine spatial structures in the measurement maps. Most of them can be associated to the presence of clouds, which

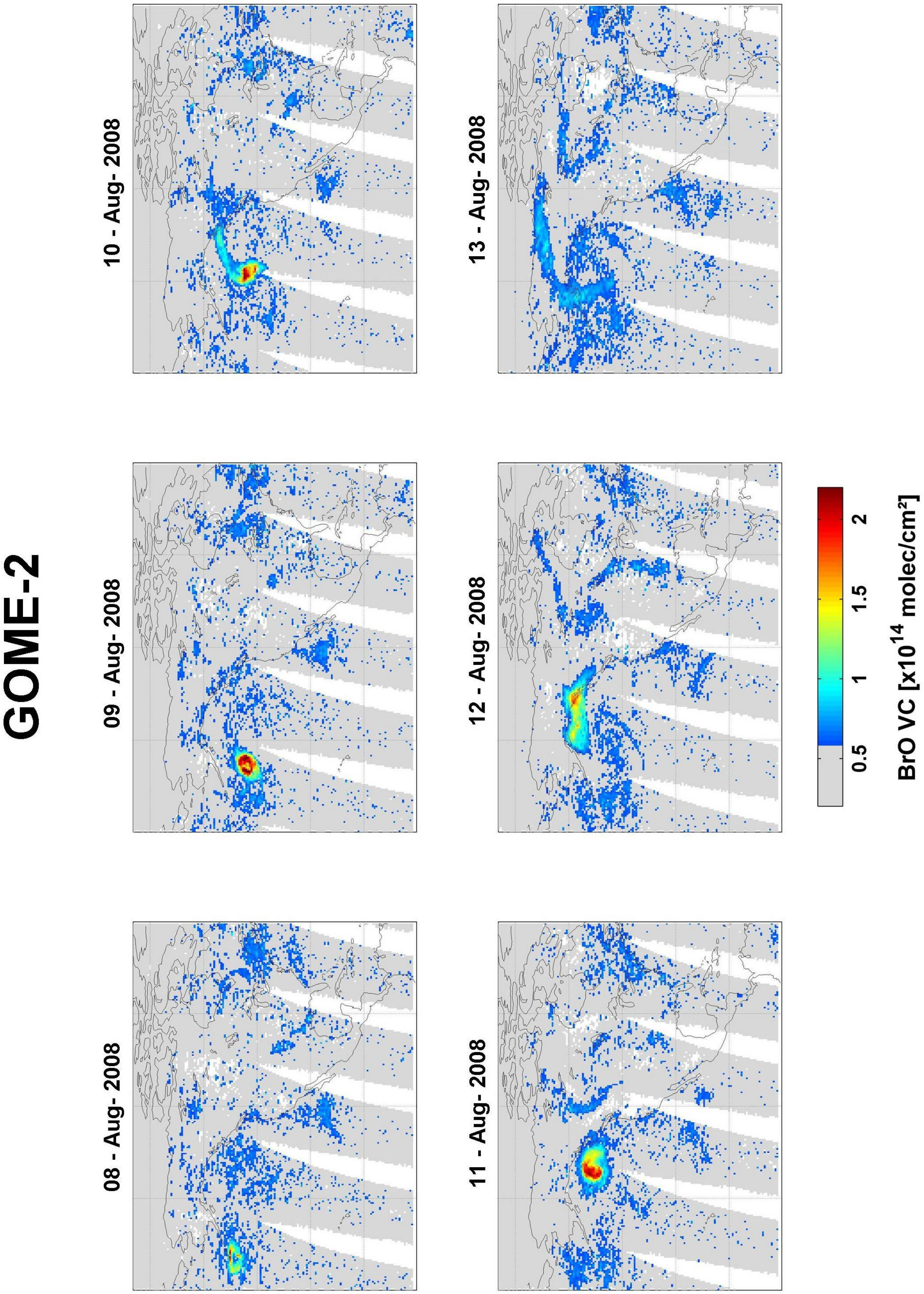

Figure 8.4 GOME-2 measurements of BrO total columns after the eruption of the Kasatochi volcano during the period of 8-13 August 2008.

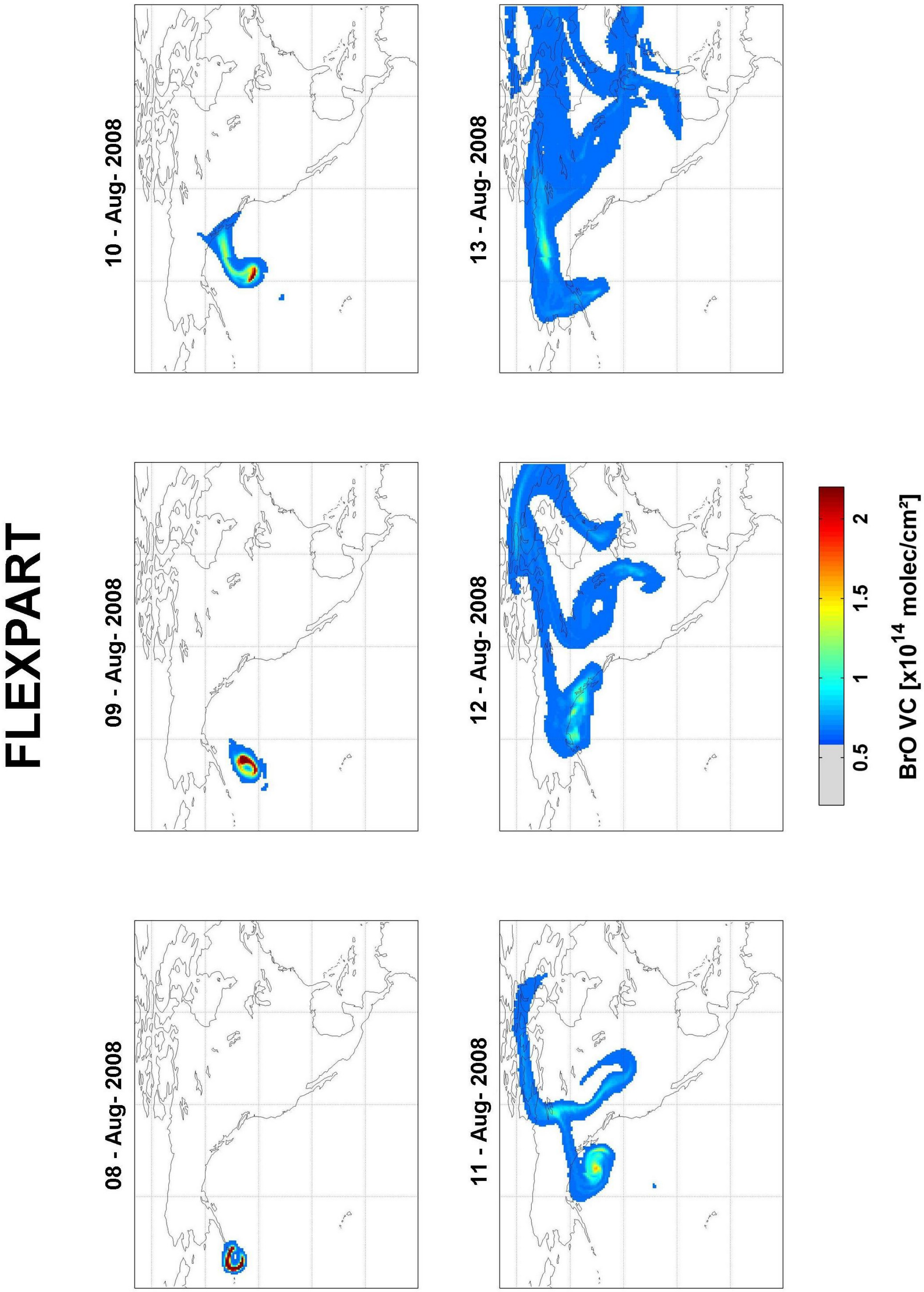

Figure 8.4 (continued) and corresponding FLEXPART column simulations.

either locally enhance the sensitivity to the background tropospheric BrO or possibly cause bias in the retrieved slant columns due to spectral interference effects, e.g., related to imperfect correction for the Ring effect. Besides these cloud-related structures, attention reveals that a number of the observed spatial features actually coincide with the FLEXPART simulations, and therefore can be attributed to remnants from the volcanic BrO plume. Such filamentary structures can be understood as the signature of vertical transport that brings BrO air masses to lower and less dry altitudes where their conversion into HBr or HOBr is favored. The corresponding decrease in BrO concentration is consistently captured by the measured BrO columns, as depicted in Figure 8.4.

8.5 Discussion

Based on the GOME-2 BrO observations presented in this work and the associated FLEXPART simulations one concludes that the Kasatochi volcanic eruption has been accompanied by a massive injection of inorganic bromine species directly into the upper troposphere/lower stratosphere, where efficient near-tropopause transport by jet winds has resulted in fast transport of the plume away from the volcano. The relatively long chemical lifetime of inorganic bromine in this altitude region (typically up to two weeks; von Glasow et al., 2004) explains that significant BrO amounts could be detected as long as six days after the eruption.

Using our BrO column measurements and the FLEXPART simulations, a rough estimate of the total amount of BrO emitted by the volcanic eruption can be derived. Using a least-square fitting routine, the modeled BrO columns have been linearly fitted to the measured BrO columns by adjusting the initial BrO mass emitted in the 8-10 km and 10-12 km layers. In order to isolate the effect of the volcanic emission from the background atmospheric BrO, a normalization was applied to the measurements which consisted of subtracting the BrO columns retrieved outside the region of the volcanic plume in the same latitude zone on the same day. Only the data collected from August 9 to 13 were selected, since the measurement sensitivity on August 8 is likely to have been reduced by volcanic ash emitted near the volcano. It has to be noted that the measured pixels from 9 to 13 August were found to be cloudy most of the time (cloud fraction >50%). Corresponding cloud top heights were in all cases below the estimated BrO plume height, which implies that the sensitivity of the measurement to volcanic BrO was effectively enhanced. Note that this cloud effect has been consistently accounted for in the evaluation approach described in section 8.3.2.

Based on the aforementioned fitting procedure, the total mass of BrO released by the volcano is estimated to lie around 12 tons in the 8-10 km layer and 24 tons in the 10-12 km layer. Taking into account the uncertainty on the measured BrO columns (~20%) and the possible misrepresentation of the simulated atmospheric transport, we finally come to an estimate of 30 to 42 tons for the total mass of BrO released by the volcano.

Owing to the rapid photochemical equilibrium between BrO and its inorganic reservoirs, the total mass of reactive bromine can be inferred from the BrO results. Simulations performed using the stacked box photochemical model PSCBOX (Hendrick et al., 2004) show that in the 8-12 km altitude range BrO represents 30-50% of the total inorganic bromine loading, at the time of the satellite overpass and for different possible loadings of sulfate aerosols present in the atmosphere after a volcanic eruption. Accordingly, the total mass of reactive bromine released into the atmosphere by the Kasatochi eruption is estimated to be in the range of 50 to 120 tons. This estimate is high compared to the source strength of approximately 350 tons yr^{-1} of reactive Br derived by Bobrowski et al. (2003) from the detection of BrO at the Soufrière Hills volcano. However, one must keep in mind that the present observations were obtained after a major eruptive event (probably the largest eruption since Mount Pinatubo), while for degassing volcanoes like the Soufrière Hills significantly smaller emissions are expected to occur.

Further evidences for volcanic BrO emission have been searched for in the existing data base of GOME-2 observations. Since the launch of the satellite in late 2006, five large volcanic eruptions could be monitored based on SO_2 emissions. In addition to the strong signal from Kasatochi, another significant although weaker BrO signature could be detected after the Etna eruption on 13 May 2008. Further work will be needed to assess and quantify these results. However, they seem to suggest that a more regular monitoring of volcanic BrO emissions might be feasible using GOME-2. It is likely that the large spatial coverage of GOME-2 improves the chances to observe volcanic eruption events.

8.6 Conclusions

Using observations from the GOME-2 instrument onboard MetOp-A, a large plume of bromine monoxide has been detected on the first day following the eruption of the Kasatochi volcano on 7 August 2008. The transport of the BrO plume could be followed during six days after the eruption. These results represent the first space-based observation of BrO released by volcanic activity. Lagrangian dispersion modeling results based on the FLEXPART tool show that the volcanic BrO was directly injected in the upper troposphere/lower stratosphere at altitudes ranging from 8 to 12 km, and that the total mass of reactive bromine released in the atmosphere was around 50-120 tons. This corresponds to approximately 25 % of the previously estimated total annual mass of reactive Br emitted by volcanic activity Bobrowski et al. (2003). Our observations further demonstrate the capability of recent atmospheric chemistry sensors to monitor gaseous emissions from volcanoes, which will lead to improved quantification of their impact on the global atmosphere.

These results, of potential importance for the global atmosphere, have been highlighted on the web portal of the European Space Agency – Observing the Earth (http://www.esa.int/esaEO/SEM5P3XX3RF_index_0.html).

Chapter 9

Conclusions and perspectives

This thesis focuses on global measurements of atmospheric BrO using differential optical absorption spectroscopy techniques from the ground and from space, as well as modeling using a stratospheric 3-D chemical transport model. Retrieval techniques were developed to provide quantitative estimations of BrO amounts (vertical columns) in the stratosphere and the troposphere either by combining ground-based observations made under different viewing geometries (multi-axis observations) or through synergistic use of satellite nadir measurements and modeled data.

The main progress and results obtained in this thesis can be summarized as follows:

Stratospheric BrO

- Using an original inversion method for ground-based observations, it has been possible to retrieve stratospheric BrO columns at the tropical site of Reunion Island. The results show a diurnal and seasonal variation coherent with our understanding of stratospheric bromine photochemistry. Based on the latter stratospheric BrO columns, a total stratospheric inorganic bromine content of about 23 pptv is inferred. This represents 6 to 7 pptv more than can be supplied by long-lived organic bromine sources, and thus supports an added contribution from short-lived organic bromine substances as recently suggested in several other studies. Therefore our work participates to the international joint effort to determine the contribution of short-lived species to stratospheric bromine (see e.g., WMO report, 2007).

- The BrO abundances simulated by current stratospheric models are generally based on a simplified approach to account for the bromine short-lived species and are little or not constrained by stratospheric BrO observations. In this thesis, we have implemented in an existing chemical transport model (BASCOE) (1) an up-to-date bromine photochemical scheme and (2) a realistic total bromine budget. The resulting BASCOE modeled BrO profiles have been compared to an extensive set of stratospheric BrO observations from ground-based, balloon-borne and satellite platforms. An excellent overall agreement was found demonstrating our good understanding of stratospheric bromine at the global scale and the good level of consistency of the BrO observations. Elaborating on these BrO simulations, we have built an innovative stratospheric BrO climatology that is able to reproduce the important photochemical and dynamical variations of stratospheric BrO using chemical and dynamical indicators. This climatological approach has been used to estimate the stratospheric contribution to the total BrO columns measured by satellite instruments, with the aim to retrieve tropospheric BrO columns. It has been successfully applied to GOME and GOME-2 satellite observations. In particular, large-scale dynamical structures of stratospheric origin observed in the satellite measured BrO field could be reproduced satisfactorily.

Polar boundary layer BrO

Owing to a new algorithm to retrieve tropospheric BrO columns from satellite measurements that uses the stratospheric BrO climatology and optimally accounts for changes in measurement vertical sensitivity (in particular over snow/ice-covered surfaces), we have made significant progress towards the accurate quantification of polar BrO surface emissions, located over areas of first year sea ice. Our results confirm that enhanced boundary layer BrO columns are observed during spring months with values up to 8 x 10^{13} molec/cm² and 13 x 10^{13} molec/cm², respectively in the Northern and Southern hemispheres. We have also shown that combing satellite BrO observations and estimates of stratospheric BrO using our climatological approach allows studying with less ambiguity the long-range transport of BrO plumes emitted in the polar boundary layer.

BrO in the free troposphere.

- While multi-axis DOAS measurements are regularly used to investigate the abundance of trace gases in the boundary layer, our approach combining zenith-sky twilight and off-axis BrO observations could be used to demonstrate that an important contribution of the tropospheric BrO columns retrieved at Reunion Island, is coming from the free-troposphere (around 6 km altitude). Since quantitative estimations of BrO in the tropical troposphere are very sparse, these results provide valuable support for the hypothesis that tropical biogenic sources of short-lived organic bromine species might be converted into active bromine in the troposphere and affect tropospheric photochemistry (Salawitch, 2006).

- The tropospheric BrO columns retrieved from the satellite measurements using our advanced algorithm are consistent with the presence of a global free-tropospheric BrO background, with columns of 1-3 x 10^{13} molec/cm². This interpretation is supported by correlative ground-based data and a comprehensive error budget on the retrieved tropospheric BrO columns. The seasonal and latitudinal variations of tropospheric BrO have been investigated. Given the uncertainties on the retrieved tropospheric BrO columns, no noticeable seasonal or latitudinal variation could be identified for this tropospheric BrO background of still unknown origin.

Volcanic BrO emissions

For the first time, volcanic BrO emissions were detected by a satellite instrument. Enhanced BrO columns were observed by the GOME-2 instrument in the vicinity of the Kasatochi volcano during six days after its eruption (August 2008). The total mass of reactive bromine released in the atmosphere was around 50-120 tons. In the future, accumulating evidences of volcanic BrO emissions from space might help to better understand the bromine-related chemistry in a volcanic plume and to assess the importance of these bromine emissions on the global atmosphere.

Outlook

In general, future work will focus on the improvement and the validation of the tropospheric BrO columns from space nadir observations, in order to get a better understanding of the role and repartition of bromine monoxide in the troposphere. The following activities could be envisaged:

- Improvement of the DOAS analysis with the aim to create a long-term consistent database of tropospheric BrO measurements from space using GOME, SCIAMACHY and GOME-2 sensors.

- More comparisons are needed between the tropospheric BrO columns retrieved from space and independent tropospheric BrO measurements that will become available from coming ground-based, balloon and aircraft measurement campaigns. In particular, it is interesting to better understand why our tropospheric BrO estimates (and the ones e.g. from Richter et al., 2002; Fitzenberger et., 2000; Van Roozendael et al., Salawitch et al., 2005; Sinnhüber et al., 2005) are still inconsistent with the tropospheric BrO amounts derived in some other studies (Schofield et al., 2004a, 2006; Dorf et al., 2008).

- A promising application of the satellite observations is to investigate the potential of cloudy pixels to provide information on the vertical distribution of BrO in the troposphere. The approach is similar in concept to the one used to derive tropospheric ozone from the TOMS satellite instrument (Ziemke et al., 2001), and is called the “cloud slicing”. This technique takes benefit of the opaque property of clouds to UV radiation and the enhanced measurement sensitivity above the cloud-top. With the cloud-slicing method, the correlation between co-located measurements of above-cloud BrO and cloud-top pressure is exploited to yield tropospheric BrO profile information. One of the major advantages of the cloud-slicing approach is that the results are independent of any constant bias on the retrieved BrO columns. On the other hand, the method provides only BrO profile information in the 300-1000 mbar pressure interval. Within this PhD thesis, we have developed a cloud-slicing technique for BrO, based on the Optimal Estimation Method. First application of this cloud-slicing technique to GOME data reveals that a BrO volume mixing ratio in the range of few tens of pptv to 1 pptv could be present in the global free-troposphere (in reasonable agreement with previous published estimates). However, more work is needed to consolidate these results. In the future, we intend to apply this cloud-slicing technique more particularly to GOME-2 BrO observations over specific regions in the tropics. The objective is to get a better insight into the atmospheric transport, chemical transformation and emission strengths per region of bromine short-lived species and their product gases (e.g., BrO) during their journey from the surface to the tropical lower stratosphere.

This will be achieved in the framework of SHIVA[1], a project in which the UV-visible DOAS group of the Belgian Institute for Space Aeronomy is involved.

- The GOME-2 BrO observations (with improved spatial resolution and coverage) together with estimates of the stratospheric columns from our BrO climatology will certainly enable more in depth analysis of transport BrO events. In particular, a systematic investigation of these events using trajectory models might help us to estimate the supply to the mid-latitude free-troposphere of BrO from the polar boundary layer and the stratosphere.

- More comparisons are needed between the tropospheric BrO columns retrieved from space and modeling results from global tropospheric 3D-CTMs in order to improve both measured and modeling data, and to better understand tropospheric bromine emissions and chemistry.

---

[1] SHIVA - Stratospheric Ozone : Halogen Impacts in a Varying Atmosphere – is an EU funded FP-7 project whose aim is to reduce uncertainties in present and future stratospheric halogen loading and ozone depletion resulting from climate feedbacks between emissions and transport of ozone depleting substances. Details can be found on the SHIVA website: http://shiva.iup.uni-heidelberg.de/

Appendix A

Inverse problem:

The Optimal Estimation Method

This section gives a theoretical introduction on the Optimal Estimation Method (OEM) developed by C. Rodgers to solve inverse problems for atmospheric remote sounding. The objective here is not to give an exhaustive description of the retrieval concepts, but to provide some background on linear inversion problems, the error analysis and characterization of the corresponding retrieval methods. Although there exists a large number of retrieval techniques to solve inverse problems, we restrict ourselves in this work to the widely used Maximum a Posteriori method.

Some quantities important for the understanding of inverse methods will be introduced here without any proof; the reader is referred to the book of Rodgers (2000) for a detailed description of the inverse methods and concepts.

A1. Formal statement of the problem

The inverse problem is the task where the values of some physical parameters must be obtained from observed data. Let us consider the measurements assembled into a vector y (m elements), the measurement vector, and the unknowns into a state vector x (n elements) describing the state of the atmosphere[1]. In contrast to in-situ measurements, remote-sensing observations are often characterized by a complex relationship between what is being measured and what is desired to be known. We can describe the physics of the measurements formally as:

$$y = f(x,b) + \varepsilon \tag{A1}$$

where the function f describes the physics that relate the state to the measured signal, as well as the description of the measuring instrument. The vector of parameters b comprises the quantities which influence the measurement, that are known to some accuracy but are not intended to be retrieved. ε is the experimental error.

In practice, it is necessary to approximate the detailed physics by some forward model F. The equation A1 between the measurement and the state vector becomes:

$$y = F(x,\hat{b}) + \Delta F + \frac{\partial F}{\partial b}(b - \hat{b}) + \varepsilon \tag{A2}$$

---

[1] Often it will represent a profile of some quantity (e.g., the concentration profile of an atmospheric species) given at a finite number of levels.

$\hat{b}$ being the best estimate of the forward model parameters. ΔF is the (often systematic) error in the forward model, and ∂F/∂b(b-$\hat{b}$) describes the errors resulting from uncertainties in the forward model parameters b.

For (weakly) non-linear forward models, equation A2 can be expanded around an a priori state vector x_a:

$$y = F(x_a, \hat{b}) + K(x - x_a) + \Delta F + \frac{\partial F}{\partial b}(b - \hat{b}) + \varepsilon \tag{A3}$$

The term K=∂F/∂x is the forward model matrix or Jacobian matrix, evaluated at $x=x_a$.

The inversion problem consists of computing an estimation $\hat{x}$ of the state vector based on the measurement y and by using a retrieval method R:

$$\hat{x} = R(y, x_a, \hat{b}) \tag{A4}$$

By using equation A3 and by introducing the gain matrix G_y=∂R/∂y (sensitivity of the retrieval to the measurement), we have:

$$\hat{x} = R[F(x_a, \hat{b}), x_a, \hat{b}] + G_y[K(x - x_a) + \Delta F + \frac{\partial F}{\partial b}(b - \hat{b}) + \varepsilon] \tag{A5}$$

Subtract the a priori x_a on both sides:

$$\hat{x} - x_a = A(x - x_a) + G_y[\Delta F + \frac{\partial F}{\partial b}(b - \hat{b}) + \varepsilon] \tag{A6}$$

where

$$A = G_y K = \frac{\partial \hat{x}}{\partial x} \tag{A7}$$

Here, we made the reasonable assumption that the retrieval method is able to reproduce the a priori state (no bias):

$$R[F(x_a, \hat{b}), x_a, \hat{b}] = x_a \tag{A8}$$

A2. Characterization of the retrieval and error analysis

The first term on the right in equation A6 describes the relation between the retrieved state vector and the true state vector through the matrix A (called the averaging kernel matrix), while the other terms stand for the various sources of error (see below). The averaging kernel is key information for the characterization of the retrieval. Indeed, it expresses the sensitivity of the retrieved state vector $\hat{x}$ with respect to the true state vector x. In case of the state vector is a profile, the rows of A can be regarded as smoothing functions. As for the columns of A, they give the response of the retrieval to a

δ-function perturbation in the state vector. Moreover, the full width at half maximum of a given averaging kernel column provides a rough estimate of the vertical resolution of the retrieval at the target altitude. Finally, the trace of the averaging kernel matrix gives the number of degrees of freedom for the signal, which is an estimate of the number of independent pieces of information contained in the measurements.
Regarding the error in the retrieved state vector $\hat{x}$, an expression can be obtained by some rearrangement of equation A6:

$$\hat{x} - x = (A - I)(x - x_a) + G_y K_b (b - \hat{b}) + G_y \Delta F + G_y \varepsilon \qquad \text{(A9)}$$

where $K_b = \partial F / \partial b$ is the sensitivity to the forward model to the forward model parameters.

The error on the retrieved state vector is the sum of four terms (most of them can be expressed in terms of error covariance matrixes):

1) The smoothing error

$$S_s = (A - I) S_e (A - I)^T \qquad \text{(A10)}$$

where S_e is the covariance of the ensemble of states about the mean state. Many remote observing systems cannot see spatial fine structure, the loss of which contributes to the smoothing error. In principle, the actual statistics of the fine structure must be known.

2) The forward model parameter error

$$S_f = G_y K_b S_b K_b^T G_y^T \qquad \text{(A11)}$$

where $S_b = \varepsilon\{(b - \hat{b})(b - \hat{b})^T\}$ is the error covariance matrix of b.

3) The forward model error $G_y \Delta F$

4) The retrieval noise

$$S_m = G_y S_\varepsilon G_y^T \qquad \text{(A12)}$$

A3. The Optimal Estimation Method: maximum a posteriori solution

Generally speaking, the inverse problem is formally ill posed, as there are more elements in the state vector than there are measurements. Hence there is an infinite set of solutions. The solutions include non-physical results as well. The portion of them is exacerbated when the level of measurement noise is increased. Therefore a constraint is usually added in the form of a priori information on the solution, so that it allows a single physical solution to be determined.

The OEM uses a Bayesian statistical approach to solve an inverse problem. Let us assign probability density functions (pdf) to the class of possible measurement and state vectors:

- P(x) is the prior pdf of the state x. It expresses our knowledge of x before the measurement is made.
- P(y) is the prior pdf of the measurement, with a similar meaning.
- P(y|x) is the conditional pdf of y when x has a given value.
- P(x|y) is the conditional pdf of x given y. This is the quantity of interest for solving inverse problems.

The probability density functions are related by the Bayes theorem:

$$P(x \mid y) = \frac{P(y \mid x)P(x)}{P(y)} \tag{A13}$$

The maximum a posteriori method finds the solution $\hat{x}$ that maximizes the posterior pdf of the state vector P(x|y).

In the case of an inverse linear problem (described by a forward model matrix K) in which all the pdf's are Gaussian distributions, i.e.:

$$P(x) = \frac{1}{(2\pi)^{n/2} \left|S_a\right|^{1/2}} \exp\left[-\tfrac{1}{2}(x - x_a)^T S_a^{-1} (x - x_a)\right] \tag{A14}$$

$$P(y \mid x) = \frac{1}{(2\pi)^{m/2} \left|S_\varepsilon\right|^{1/2}} \exp\left[-\tfrac{1}{2}(y - Kx)^T S_\varepsilon^{-1} (y - Kx)\right] \tag{A15}$$

$$P(y) = \frac{1}{(2\pi)^{m/2} \left|S_\varepsilon\right|^{1/2}} \exp\left[-\tfrac{1}{2}(y - \overline{y})^T S_\varepsilon^{-1} (y - \overline{y})\right] \tag{A16}$$

Sa and S_ε being the a priori and measurement error covariance matrixes, respectively.

We can establish using equation A13 that the maximum a posteriori solution is the solution that minimizes the expression:

$$C(x) = (y - Kx)^T S_\varepsilon^{-1} (y - Kx) + (x - x_a)^T S_a^{-1} (x - x_a) \tag{A17}$$

and can be written as:

$$\hat{x} = x_a + (K^T S_\varepsilon^{-1} K + S_a^{-1})^{-1} K^T S_\varepsilon^{-1} (y - Kx_a) \tag{A18}$$

It follows that the averaging kernel matrix is given by:

$$A = (K^T S_\varepsilon^{-1} K + S_a^{-1})^{-1} K^T S_\varepsilon^{-1} K \tag{A19}$$

The error covariance of the solution being:

$$\hat{S} = (K^T S_\varepsilon^{-1} K + S_a^{-1})^{-1} \tag{A20}$$

It is easy to prove that the error covariance of the maximum a posteriori solution is the sum of the smoothing error (equation A10) and the retrieval noise error (equation A12) covariance matrixes, when assuming the smoothing error for an ensemble of states corresponding to the a priori, i.e.: $S_s=(A-I)\ S_a\ (A-I)^T$.

Appendix B

Slant column density DOAS retrieval: Error analysis

In this section, we consider the DOAS inversion as a linear problem that can be treated using the Rodgers formalism presented in Appendix A.

Let us consider:

- an observation vector y with m elements: the differential optical density for all wavelengths considered in the chosen fitting window.
- a state vector x with n elements: the slant column densities of the various absorbers included in the fitting analysis.

The observation vector y and the state vector x are related by the linear expression:

$$y = Kx + \varepsilon \qquad \text{(B1)}$$

K is the forward model matrix (mxn) where the columns are the differential cross-sections of the different absorbers included in the DOAS inversion. ε is the measurement error.

Since the DOAS analysis is fundamentally an over-constrained problem (m>n), no a priori information on the state vector is needed. Therefore the retrieval method looks for a solution that minimizes the following cost function (linear least-squares method):

$$\chi^2 = \frac{1}{m}.\left\| y - Kx \right\|^2 \qquad \text{(B2)}$$

It is easy to prove that the solution $\hat{x}$ (retrieved state vector) is given by:

$$\hat{x} = G_y.y \quad G_y = \frac{\partial \hat{x}}{\partial y} = (K^T K)^{-1} K^T \qquad \text{(B3)}$$

where G_y is the so-called gain matrix and quantifies the interferences between the cross-sections.

The purpose of this section is to evaluate the error on the retrieved state vector. We have seen in Appendix A that the total error is the sum of four error terms that we will now detail in terms of covariance matrix:

1) The smoothing error:

$$S_s = (A-I)S_e(A-I)^T \tag{B4}$$

Since the averaging kernel of the retrieval is:

$$A = G_y K = (K^T K)^{-1}(K^T K) = I \tag{B5}$$

the retrieval method can thus be regarded as an ideal inverse method and the smoothing error is equal to zero.

2) The retrieval noise:

$$S_m = G_y S_\varepsilon G_y{}^T = (K^T S_\varepsilon^{-1} K)^{-1} \tag{B6}$$

where S_ε is the measurement error covariance. This term is easy to calculate and simply expresses the propagation of the noise to the inversion results.

3) The forward model error:

This term includes all possible sources of uncertainties that are not (or can not be) accounted for using the forward model. It comprises e.g. non linear physical processes affecting the measurement. This term can be hard to evaluate and is usually estimated using sensitivity tests.

4) The forward model parameter error:

$$S_f = G_y K_b S_b K_b^T G_y{}^T \tag{B7}$$

where $K_b=\partial y/\partial b$ is the sensitivity of the forward model to the forward model parameters b, and S_b is the error covariance matrix of b. Here, we consider the forward model parameter error as the systematic slant column errors due to absorption cross section uncertainties and their correlations.
The forward model parameters are simply given by the elements of the forward model matrix K (the cross-section matrix), so that the parameter vector $\hat{b}$ is the reshaped matrix K column-by-column:

$$\hat{b}_{i+(j-1)m} = K_{ij} \qquad \begin{matrix} i = 1,-,m \\ j = 1,-,n \end{matrix} \tag{B8}$$

From equation B1 and the definition of the forward parameter vector, we can establish:

$$K_b = \left[x_1.I_m \quad - \quad x_j.I_m \quad - \quad x_n.I_m \right] \tag{B9}$$

Furthermore, since the different cross-sections can be assumed independent from each other, the covariance matrix S_b is (by construction) a block diagonal matrix with the covariance matrixes of the individual cross-section on its diagonal:

$$S_b = \begin{bmatrix} \boxed{S_{b1}} & - & 0 \\ & \backslash & \\ | & \boxed{S_{bj}} & | \\ & \backslash & \\ 0 & - & \boxed{S_{bn}} \end{bmatrix} \tag{B10}$$

The error due to model parameters uncertainties can be evaluated by introducing all the terms calculated above in equation B7:

$$S_f = \sum_{j=1}^{n} x_j^2 \left[G_y S_{bj} G_y^T \right] \tag{B11}$$

where G_y is a function of the forward model matrix K only and x_j are the elements of the state vector (the slant columns of the absorbers). Note that this is evaluated (in principle) at the true state, rather than $\hat{x}$, but the sensitivity to this quantity should not be too large provided the problem is not too nonlinear. This expression is simple and convenient to use. The only difficulty is to apply equation B11 to realistic cross-section error covariance matrixes. They are rather difficult to estimate, since they imply the variances of the cross-sections at any wavelength, but also the correlations between the measured cross-sections for different wavelengths. Usually, the publications dealing with measurements of cross-sections in laboratory only give an estimation of the error in percent valid for the data set on the measurement wavelength range. Here, we have used these values to construct diagonal cross-section error covariance matrixes in order to estimate the forward model parameter error.

Appendix C

List of data sets[1]

Type of data	Location	Period	Origin	Chapter
Ground-based observations Tropospheric and stratospheric (+total) BrO columns	Reunion Island, France (21.06°S, 55.47°E)	07/2004 -07/2005	BIRA-IASB measurement campaign	5
Modelisation Stratospheric BrO profiles and columns	Global	04/2003 – 03/2006	BIRA-IASB stratospheric CTM (BASCOE, version: v4n51)	6
Satellite observations GOME Total and tropospheric BrO columns	Global	1999-2000	ESA level1 off-line data (http://www.esa.int)	7
Satellite observations SCIAMACHY Total BrO columns	21°S +/- 5°	2003-2005	ESA level1 off-line data (http://www.esa.int)	5
Satellite observations GOME-2 Total and tropospheric BrO columns	Global	06/2007-08/2008	EUMETSAT level1 off-line data (http://www.eumestat.int)	7
Volcanic BrO satellite observations GOME-2 Total BrO columns	Vicinity of the Kasatochi volcano (Alaska)	08/08-13/08, 2008	EUMETSAT level1 off-line data (http://www.eumestat.int)	8

Data are available from the author.

---

[1] The present list includes only the data sets generated by the author during the course of his PhD work and presented in this thesis. The other data sets used (e.g., for comparison exercises) are not listed here, but are mentioned in the text (see the References).

Publications

This annex gives a list of the publications, conference proceedings and technical notes published as part of this PhD thesis.

Peer-reviewed papers

Papers as first author:

- Theys, N., Van Roozendael, M., Hendrick, F., Fayt, C., Hermans, C., Baray, J.-L., Goutail, F., Pommereau, J.-P., and De Mazière, M.: Retrieval of stratospheric and tropospheric BrO columns from multi-axis DOAS measurements at Reunion Island (21°S, 56°E), *Atmos. Chem. Phys.*, 7, 4733-4749, 2007.

- Theys, N., Van Roozendael, M., Errera, Q., Hendrick, F., Daerden, F., Chabrillat, S., Dorf, M., Pfeilsticker, K., Rozanov, A., Lotz, W., Burrows, J.P., Lambert, J.-C., Goutail, F., Roscoe, H.K., and De Mazière, M.: A global stratospheric bromine monoxide climatology based on the BASCOE chemical transport model, *Atmos. Chem. Phys.*, 9, 831-848, 2009.

- Theys, N., Van Roozendael, M., Dils, B., Hendrick, F., Hao, N., and De Mazière, M.: First satellite detection of volcanic bromine monoxide emission after the Kasatochi eruption, *Geophys. Res. Lett.*, 36, L03809, doi:10.1029/2008GL036552, 2009.

Contributions have been made to the following papers:

- Dastoor, A., Davignon, D., Theys, N., Van Roozendael, M., Steffen, A., and Ariya, P.: Modeling dynamic exchange of gaseous elemental mercury at polar sunrise, *Environ. Sci. Technol.*, 42, 5183-5188, 2008.

- Fietkau, S., Medeke, T., Richter, A., Sheode, N., Sinnhuber, B.-M., Wittrock, F., Theys, N., Van Roozendael, M., and Burrows, J. P.: Ground-based measurements of tropospheric and stratospheric bromine monoxide above Nairobi (1°S, 36°E), *Atmos. Chem. Phys. Discuss.*, 7, 6527-6555, 2007.

- Hendrick, F., Van Roozendael, M., Chipperfield, M.P., Dorf, M., Goutail, F., Yang, X., Fayt, C., Hermans, C., Pfeilsticker, K., Pommereau, J.-P., Pyle, J.A., Theys, N., and De Mazière, M.: Retrieval of stratospheric and tropospheric BrO profiles and columns using ground-based zenith-sky DOAS observations at Harestua, 60°N, *Atmos. Chem. Phys.*, 7, 4869-4885, 2007.

- Hendrick, F., Johnston, P.V., De Mazière, M., Fayt, C., Hermans, C., Kreher, K., Theys, N., and Van Roozendael, M.: One-decade trend analysis of stratospheric BrO over Harestua (60°N) and Lauder (45°S) reveals a decline, *Geophys. Res. Lett.*, 35, L14801, doi:10.1029/2008GL034154, 2008.

- Hendrick, F., Rozanov, A., Johnston, P.V., Bovensmann, H., De Mazière, M., Fayt, C., Hermans, C., Kreher, K., Lotz, W., Sinnhuber, B.-M., Theys, N., Thomas, A., Burrows, J.P., and Van Roozendael, M.: Multi-year comparison of stratospheric BrO vertical profiles retrieved from SCIAMACHY limb and ground-based UV-visible measurements, *Atmos. Meas. Tech.*, 2, 273-285, 2009.

- Yang, X., Pyle, J.A., Cox, R.A., Theys, N., Van Roozendael, M., Snow-sourced bromine and its implications for polar tropospheric ozone, to be submitted to *Atmos. Chem. Phys. Discuss.*, 2009.

Conference proceedings

- Theys, N., De Smedt, I., Van Roozendael, M., Fayt, C., Chabrillat, S., Chipperfield, M., Post, P., and van der A, R.: Total and tropospheric BrO derived from GOME and SCIAMACHY as part of the TEMIS project, ENVISAT/ERS Symposium, Salzburg, 6-10 September, 2004.

- Theys, N., Hendrick, F., Van Roozendael, M., De Smedt, I., Fayt, C., and van der A, R.: Retrieval of BrO columns from SCIAMACHY and their validation using ground-based DOAS measurements, Atmospheric Science Conference, ESA-ESRIN, Frascati, Italy, 8-12 May 2006.

- Theys, N., Van Roozendael, M., Errera, Q., Chabrillat, S., Daerden, F., Hendrick, F., Loyola, D., and Valks, P.: A stratospheric BrO climatology based on the BASCOE 3D chemical transport model, ENVISAT Symposium, Montreux, 23-27 April, 2007.

Technical notes

- Theys, N., Van Roozendael, M., Errera, Q., Chabrillat, S., Daerden, F., Hendrick, F., Loyola, D., Valks, P., BrO column retrieval algorithms for GOME-2, Ozone SAF visiting scientist project, final report, 2007.

References

Afe O. T., Richter, A., Sierk, B., Wittrock, F., and Burrows, J.P.: BrO emissions from volcanoes: a survey using GOME and SCIAMACHY measurements, *Geophys. Res. Lett.*, 31, L24113, 2004.

Aliwell, S. R., Van Roozendael, M., Johnston, P.V., Richter, A., Wagner, T., et al.: Analysis for BrO in zenith-sky spectra: An intercomparison exercise for analysis improvement, *J. Geophys. Res.*, 107, D140, doi: 10.1029/2001JD000329, 2002.

Anderson, D.E., Jr., The troposphere-stratosphere radiation field at twilight: A spherical model, *Planet. Space Sci.*, 31, 1517-1523, 1983.

Anderson, G.P., Clough, S.A., Kneizys, F.X., Chetwynd, J.H., and Shettle, E.P.: AFGL Atmospheric Constituents Profiles (0-120 km), AFGL-TR-86-0110, AFGL (OPI), Hanscom AFB, MA 01736, 1986.

Anderson, J., Russel, J.M., Solomon, S., and Deaver, L.E., Halogen occultation experiment confirmation of stratospheric chlorine decreases in accordance with the Montreal protocol, *J. Geophys. Res.*, 105 (D4), 4483-4490, 2000.

Arpag, K.H., P.V. Johnston, H.L. Miller, R.W. Sander, and S. Solomon, Observations of stratospheric BrO column over Colorado, 40°N, *J. Geophys. Res.*, 99, 8175-8181, 1994.

Avallone, L.M., Toohey, D.W., Fortin, T.J., McKinney, K.A., and Fuentes, J.D.: In situ measurements of bromine oxide at two high-latitude boundary layer sites: Implications of variability, *J. Geophys. Res.,* 108, 4089, doi:10.1029/2002JD002843, 2003.

Barrie, L.A., Bottenheim, J.W., Schnell, R.C., Crutzen, P.J., and Rasmussen, R.A.: Ozone destruction and photochemical reactions at polar sunrise in the lower Arctic atmosphere, *Nature,* 334, 138-141, 1988.

Bates, D.R., and Nicolet, M., Atmospheric hydrogen, *Pup. Astron. Soc. Pacific*, 62, 1950.

Begoin, M., Richter, A., Kaleschke, L., Tian-Kunze, X., Stohl, A., and Burrows, J.P.: Satellite observations of long range transport of a large BrO cloud in the Arctic, *Atmos. Chem. Phys. Discuss.*, 9, 20407-20428, 2009.

Bingen, C., Fussen, D., and Vanhellemont, F.: A global climatology of stratospheric aerosol size distribution parameters derived from SAGE II data over the period 1984-2000: 1. Methodology and climatological observations, *J. Geophys. Res.*, 109, D06201, doi: 10.1029/2003JD003518, 2004.

Bobrowski, N., Höninger, G., Galle, B., and Platt, U.: Detection of bromine monoxide in a volcanic plume, *Nature*, 423, 273-276, 2003.

Bobrowski, N., von Glasow, R., Aiuppa, A., Inguaggiato, S., Louban, I., Ibrahim, O.W., and Platt. U.: Reactive halogen chemistry in volcanic plumes, *J. Geophys. Res.*, 112,D06311, doi: 10.1029/2006JD007206, 2007.

Boersma, K.F., Eskes, H.J., and Brinksma, E.J.: Error analysis for tropospheric NO_2 retrieval from space, *J. Geophys. Res.*, 109, D04311, doi: 10.1029/2003JD003962, 2004.

Bogumil, K., J. Orphal, T. Homann, S. Voigt, P. Spietz, O.C. Fleischmann, A. Vogel, M. Hartmann, H. Bovensmann, J. Frerik, and J.P. Burrows, Measurements of molecular absorption spectra with the SCIAMACHY Pre-Flight Model: Instrument characterization and reference spectra for atmospheric remote sensing in the 230-2380 nm region, *J. Photochem. Photobiol. A*, 157, 167-184, 2003.

Bovensmann, H., Burrows, J.P., Buchwitz, M., Frerick, J., Noël, S., Rozanov, V.V., Chance, K.V., Goede, A.P.H.: SCIAMACHY: Mission objectives and Measurement Modes, *J. Atm. Sci.*, 56, 127-150, 1999.

Bracher, A., Amekudzi, L., Bramstedt, K., Eichmann, K.-U., Rozanov, A., von Savigny, C., and J.P. Burrows: Global and Validation of SCIAMACHY O3 and NO2 profiles from OL3.0 and IUP/IFE retrieval with collocated measurements from ACE-FTS, GOMOS, HALOE, MIPAS, POAM III and SAGE II. In: Proceedings of the ENVISAT Symposium 2007, 23-27 Apr 2007, Montreux, Switzerland, ESA Publications Division, Nordwijk, The Netherlands, SP-636, 463472br.pdf, 2007.

Brion, J., Chakir, A., Daumont, D., and J. Malicet: High-resolution laboratory absorption cross-sections of O_3. Temperature effect, *Chem. Phys. Lett.,* 213(5-6), 610-612, 1993.

Burrows, J.P., Dehn, A., Deters, B., Himmelmann, S., Richter, A., Voigt, S. and J. Orphal: Atmospheric Remote-Sensing Reference Data from GOME: 1. Temperature-Dependent Absorption Cross Sections of NO_2 in the 231-794 nm Range, *JQSRT,* 60,1025, 1998.

Burrows, J. P., Weber, M., Buchwitz, M., Rozanov, V.V., Ladstädter-Weissenmayer, A., Richter, A., de Beek, R., Hoogen, R., Bramstedt, K., Eichmann, K.-U., Eisinger, M., and Perner, D.: The Global Ozone Monitoring Experiment (GOME): Mission Concept and First Scientific Results, *J. Atm. Sci.*, 56, 151-175, 1999.

Butler, J.H., King, D.B., Lobert, J.M., Montzka, S.A., Yvon-Lewis, S.A., Hall, B.D., Warwick, N.J., Mondeel, D.J., Aydin, M., and Elkins, J.W.: Oceanic distributions and emissions of short-lived halocarbons, *Global Biogeochemical Cycles*, Vol. 21, GB1023, doi:10.1029/2006GB002732, 2007.

Butz, A, Bösch, H., Camy-Peyret, C., Chipperfield, M., Dorf, M., Dufour, G., Grunow, K., Jeseck, P., Kühl, S., Payan, S., Pepin, I., Pukite, J., Rozanov, A., von Savigny, C., Sioris, C., Wagner, T., Weidner, F., and Pfeilsticker, K.: Inter-comparison of stratospheric O3 and NO2 abundances retrieved from balloon borne direct sun observations and Envisat/SCIAMACHY limb measurements, *Atmos. Chem. Phys.*, 6, 1293-1314, 2006.

Carpenter, L.J., and Liss, P.S.: On temperature sources of bromoform and other reactive organic bromine gases, *J. Geophys. Res.*, 105 (D16), 20539-20547, 2000.

Chance, K. and R. Spurr: Ring effect studies: Rayleigh scattering including molecular parameters for rotational Raman scattering, and the Fraunhofer spectrum, Appl. Optics, 36, 5224-5230, 1997.

Chance, K., Analysis of BrO measurements from the Global Ozone Monitoring Experiment, *Geophys. Res. Lett.*, 25, 3335-3338, 1998.

Chandrasekhar, S: Radiative transfer, Dover Publications, Inc., New York, 1960. originally published in 1950.

Chapman, S.: On ozone and atomic oxygen in the upper atmosphere, *Phil. Mag.*, 10, 1930.

Chipperfield, M. P.: Multiannual simulations with a three-dimensional chemical transport model, *J. Geophys. Res.*, 104 (D1), 1781-1805, 1999.

Chipperfield, M.P.: New Version of the TOMCAT/SLIMCAT Off-Line Chemical Transport Model: Intercomparison of Stratospheric Tracer Experiments, *Q. J. R. Meteorol. Soc.*, 132, 1179-1203, doi:10.1256/qj.05.51, 2006.

Coulson, K.L.: Ultraviolet radiation from the sun and sky. In: Solar and terrestrial radiation, New York, Academic Press:142-61, 1975.

Crutzen, P.J., The influence of nitrogen oxides on the atmospheric ozone content, *Quart. J. Met. Soc.*, 96, 1970.

Daerden, F., Larsen, N., Chabrillat, S., Errera, Q., Bonjean, S., Fonteyn, D., Hoppel, K., and Fromm, M. : A 3D-CTM with detailed online PSC-microphysics : analysis of the Antarctic winter 2003 by comparison with satellite observations, *Atmos. Chem. Phys.*, 7, 1755-1772, 2007.

Dahlback, A., and Stamnes, K.: A new spherical model for computing the radiation field available for photolysis and heating at twilight, *Planet Space Sci.*, 39(5), 671-683, 1991.

De Smedt, I., Van Roozendael, M., Jacobs,T.: Optimization of DOAS settings for BrO fitting from SCIAMACHY nadir spectra - Comparison with GOME BrO retrievals, technical note available from http://www.oma.be/ BIRA-IASB/Molecules/BrO, 2003.

De Smedt, I., Müller, J.-F., Stavrakou, T., van der A, R., Eskes, H., and Van Roozendael, M.: Twelves years of global observations of formaldehyde in the troposphere using GOME and SCIAMACHY sensors, *Atmos. Chem. Phys.*, 8, 4947-4963, 2008.

Dorf, M., Bösch, H., Butz, A., Camy-Peyret, C., Chipperfield, M., Engel, A., Goutail,F., Grunow, K., Hendrick, F., Hrechanyy, S., Naujokat, B., Pommereau, J.-P., Van Roozendael, M., Sioris, C., Stroh, F., Weidner, F., and Pfeilsticker, K.: Balloon-borne stratospheric BrO measurements: Intercomparisons with ENVISAT/SCIAMACHY BrO limb profiles, *Atmos. Chem. Phys.*, 6, 2483-2501, 2006a.

Dorf, M., Butler, J.H., Butz, A., Camy-Peyret, C., Chipperfield, M.P., Kritten, L., Montzka, S.A., Simmes, B., Weidner, F., and Pfeilsticker, K.: Long-term observations of stratospheric bromine reveal slow down in growth, *Geophys. Res. Lett.*, 33, L24803, doi: 10.1029/2006GL027714, 2006b.

Dorf, M., Butz, A., Camy-Peyret, C., Chipperfield, M.P., Kritten, L., and Pfeilsticker, K.: Bromine in the tropical troposphere and stratosphere as derived from balloon-borne BrO observations, *Atmos. Chem. Phys.*, 8, 7265-7271, 2008.

Eckhardt. S., Prata, A.J., Seibert, P., Stebel, K. and Stohl, A.: Estimation of the vertical profile of the sulfur dioxide injection into the atmosphere by a volcanic eruption using satellite column measurements and inverse transport modeling, *Atmos. Chem. Phys.*, 8, 3881-3897, 2008.

Errera, Q. and Fonteyn, D.: Four-dimensional variational chemical assimilation of CRISTA stratospheric measurements, *J. Geophys. Res.*, 106 (D11), 12253-12265, 2001.

Errera, Q., Daerden, F., Chabrillat, S., Lambert, J.C., Lahoz, W.A., Viscardy, S., Bonjean, S., and Fonteyn, D.: 4D-Var Assimilation of MIPAS Chemical Observations: Ozone and Nitrogen Dioxide Analysis, *Atmos. Chem. Phys.*, 8, 6169-6187, 2008.

Farman, J.C., Gardiner, B.G., and Shanklin, J.D.: Large losses of total ozone in Antarctica reveal seasonal ClO_x/NO_x interaction, *Nature*, 315, 207-210, 1985.

Feng, W., Chipperfield, M.P., Dorf, M., Pfeilsticker, K., and Ricaud, P.: Mid-latitude ozone changes: studies with a 3-D CTM forced by ERA-40 analyses, *Atmos. Chem. Phys.*, 7, 2357-2369, 2007.

Fietkau, S., Medeke, T., Richter, A., Sheode, N., Sinnhuber, B.-M., Wittrock, F., Theys, N., Van Roozendael, M., and Burrows, J. P.: Ground-based measurements of tropospheric and stratospheric bromine monoxide above Nairobi (1°S, 36°E), *Atmos. Chem. Phys. Discuss.*, 7, 6527-6555, 2007.

Fish, D. J., R. L. Jones, and E. K. Strong, Mid-latitude observations of the diurnal variation of stratospheric BrO, *J. Geophys. Res.*, 100, 18,863-18,871, 1995.

Fitzenberger, R., Bösch, H., Camy-Peyret, C., Chipperfield, M.P., Harder, H., Platt, U., Sinnhuber, B.-M., Wagner, T., and Pfeilsticker, K.: First profile measurements of tropospheric BrO, *Geophys. Res. Lett.*, 27, 2921-2924, 2000.

Fleischmann, O. C., Hartmann, M., Burrows J. P., and Orphal, J.: New ultraviolet absorption cross-sections of BrO at atmospheric temperatures measured by time-windowing Fourier transform spectroscopy, *J. Photochem. Photobiol. A*, 168, 117–132, 2004.

Frieß, U., Hollwedel, J., König-Langlo, G., Wagner, T., and Platt, U., Dynamics and chemistry of tropospheric bromine explosion events in the Antarctic coastal region, *J. Geophys. Res.*, 109, D06305, doi:10.1029/2003JD004133, 2004.

Frieβ, U., Monks, P.S., Remedios, J.J., Rozanov, A., Sinreich, R., Wagner, T., and Platt, U.: MAX-DOAS O_4 measurements: A new technique to derive information on atmospheric aerosols: 2. Modeling studies, *J. Geophys. Res.*, 111, D14203, doi:10.1029/2005JD006618, 2006.

Froidevaux, L., Livesey, N.J., Read, W.G., Salawitch, R.J.: Temporal decrease in upper atmospheric chlorine, *Geophys. Res. Lett.*, 33, L23812, doi: 10.1029/2006GL027600, 2006.

Fromm, M., Alfred, J., and Pitts, M.: A unified, long-term, highlatitude stratospheric aerosol and cloud database using SAM II, SAGE II, and POAM II/III data: Algorithm description, database definition, and climatology, *J. Geophys. Res.*, 108(D12), 4366, doi:10.1029/2002JD002772, 2003.

Geer, A.J., Lahoz, W.A., Bekki, S., Bormann, N., Errera, Q., Eskes, H.J., Fonteyn, D., Jackson, D.R., Juckes, M.N., Massart, S., Peuch, V.-H., Rharmili, S., and Segers, A.: The ASSET intercomparison of ozone analysis: method and first results, *Atmos. Chem. Phys.*, 6, 5445-5474, 2006.

Grainger, J.F. and Ring, J.: Anomalous Fraunhofer lines profiles, *Nature*, 193, 762, 1962.

Greenblatt, G.D., J.J. Orlando, J.B. Burkholder, and A.R. Ravishankara, Absorption measurements of oxygen between 330 and 1140 nm, *J. Geophys. Res.*, 95, 18577-18582, 1990.

Harder, H., Camy-Peyret, C., Ferlemann, F., Fitzenberger, R., Hawat, T., Osterkamp, H., Perner, D., Platt, U., Schneider, M., Vradelis, P., and Pfeilsticker, K.: Stratospheric BrO Profiles Measured at Different Latitudes and Seasons: Atmospheric Observations, *Geophys. Res. Lett.*, 25, 3843-3846, 1998.

Harder, H., Bösch, H., Camy-Peyret, C., Chipperfield, M., Fitzenberger, R., Payan, S., Perner, D., Platt, U., Sinnhuber,B., and Pfeilsticker, K.: Comparison of measured and modeled stratospheric BrO: Implications for the total amount of stratospheric bromine, *Geophys. Res. Lett.*, 27 , 3695 - 3698, 2000.

Hausmann, M., and Platt, U.: Spectroscopic measurement of bromine oxide and ozone in the high Arctic during Polar Sunrise Experiment 1992, *J. Geophys. Res.*, 99, 25399-25414, 1994.

Hebestreit, K., Stutz, J., Rosen, D., Matveiv, V., Peleg, M., Luria, M., and Platt, U.: DOAS measurements of tropospheric bromine oxide in mid-latitudes, *Science*, 283, 55-57, 1999.

Heckel, A., Richter, A., Tarsu, T., Wittrock, F., Hak, C., Pundt, I., Junkermann, and Burrows, J.P.: MAX-DOAS measurements of formaldehyde in the Po-Valley, *Atmos. Chem. Phys.*, 5, 909-918, 2005.

Hendrick, F., Barret, B., Van Roozendael, M., Boesch, H., Butz, A., De Mazière, M., Goutail, F., Hermans, C., Lambert, J.-C., Pfeilsticker, K., and Pommereau, J.-P.: Retrieval of nitrogen dioxide stratospheric profiles from ground-based zenith-sky UV-visible observations: Validation of the technique through correlative comparisons, *Atmos. Chem. Phys.*, 4, 2091-2106, 2004.

Hendrick, F., Van Roozendael, M., Kylling, A., Petritoli, A., Rozanov, A., Sanghavi, S., Schofield, R., von Friedeburg, C., Wagner, T., Wittrock, F., Fonteyn. D., and De Mazière, M.: Intercomparison exercise between different radiative transfer models used for the interpretation of ground-based zenith-sky and multi-axis DOAS observations, *Atmos. Chem. Phys.*, 6, 93-108, 2006.

Hendrick, F., Van Roozendael, M., Chipperfield, M.P., Dorf, M., Goutail, F., Yang, X., Fayt, C., Hermans, C., Pfeilsticker, K., Pommereau, J.-P., Pyle, J.A., Theys, N., and De Mazière, M.: Retrieval of stratospheric and tropospheric BrO profiles and columns using ground-based zenith-sky DOAS observations at Harestua, 60°N, *Atmos. Chem. Phys.*, 7, 4869-4885, 2007.

Hendrick, F., Johnston, P.V., De Mazière, M., Fayt, C., Hermans, C., Kreher, K., Theys, N., and Van Roozendael, M.: One-decade trend analysis of stratospheric BrO over Harestua (60°N) and Lauder (45°S) reveals a decline, *Geophys. Res. Lett.*, 35, L14801, doi:10.1029/2008GL034154, 2008.

Hendrick, F., Rozanov, A., Johnston, P.V., Bovensmann, H., De Mazière, M., Fayt, C., Hermans, C., Kreher, K., Lotz, W., Sinnhuber, B.-M., Theys, N., Thomas, A., Burrows, J.P., and Van Roozendael, M.: Multi-year comparison of stratospheric BrO vertical profiles retrieved from SCIAMACHY limb and ground-based UV-visible measurements, *Atmos. Meas. Tech.*, 2, 273-285, 2009.

Hermans et al., O_4 absorption cross-sections:http://www.aeronomie.be/spectrolab/o2.htm.

Hollwedel, J., Wenig, M., Beirle, S., Kraus, S., et al.: Year-to-year variability of polar tropospheric BrO as seen by GOME, *Adv. Space Res.*, 34, 804-808, 2004.

Hollwedel, J.: Observations of Tropospheric and Stratospheric Bromine Monoxide from Satellite, PhD. Thesis, University of Heidelberg, 2005.

Holton, J.R., Haynes, P.H., McIntyre, M.E., Douglass, A.R., Rood, R.B., and Pfister, L.: Stratosphere-Troposphere Exchange, *Rev. Geophys.*, 33(4), 403-439, 1995.

Hönninger, G., Leser, H., Sebastian, O., and Platt, U.: Ground-based measurements of halogen oxides at the Hudson Bay by longpath DOAS and passive MAX-DOAS, *Geophys. Res. Lett.*, 31, L04111, doi: 10.1029/2003GL 018982, 2004a.

Hönninger, G., von Friedeburg, C., and Platt, U.: Multi-axis differential absorption spectroscopy (MAX-DOAS), *Atmos. Chem. Phys.*, 4, 231-254, 2004b.

Höpfner, M., Orphal, J., von Clarmann, T., Stiller, G., and Fischer, H.: Stratospheric $BrONO_2$ observed by MIPAS, *Atmos. Chem. Phys.*, 9, 1735-1746, 2009.

Johnston, H.S.: Reduction of stratospheric ozone by nitrogen oxide catalysts from supersonic transport exhaust, *Science*, 173, 1971.

Kaleschke, L., Richter, A., Burrows, J., Afe, O., et al.: Frost flowers on sea ice as a source of sea salt and their influence on tropospheric halogen chemistry, *Geophys. Res. Lett.*, 31, L16114, doi: 10.1029/2004GL020655, 2004.

Koelemeijer, R.B. A., Stammes, P., Hovenier, J.W., and de Haan, J.F. (2001), A fast method for retrieval of cloud parameters using oxygen A-band measurements from the Global Ozone Monitoring Experiment, *J. Geophys. Res.*, 106, 3475-3490, 2001.

Koelemeijer, R. B. A., J. F. de Haan and P. Stammes, A database of spectral surface reflectivity in the range 335-772 nm derived from 5.5 years of GOME observations, *J. Geophys. Res.-Atm.*, 108(D2), 4070, doi: 10.1029/2002JD002429, 2003.

Koike, M., Kondo, Y., Matthews, W.A., Johnston, P.V., et al.: Assessment of the uncertainties in the NO_2 and O_3 measurements by visible spectrometers, *J. Atm. Chem.*, 32, 121-145, 1999.

Kovalenko, L.J., Livesey, N.L., Salawitch, R.J., Camy-Peyret, C., Chipperlfield, M.P., Cofield, R.E., Dorf, M., Drouin, B.J., Froidevaux, L., Fuller, R.A., Goutail, F., Jarnot, R.F., Jucks, K., Knosp, B.W., Lambert, A., MacKenzie, I.A., Pfeilsticker, K., Pommereau, J.-P., Read, W.G., Santee, M.L., Schwartz, M.J., Snyder, W.V., Stachnik, R., Stek, P.C., Wagner, P.A., and Waters, J.W.: Validation of Aura Microwave Limb Sounder BrO observations in the stratosphere, *J. Geophys. Res.*, 112, D24S41, doi:10.1029/2007JD008817, 2007.

Kreher, K., Johnston, P.V., Wood, S.W., Nardi, B., and Platt, U.: Ground-based measurements of tropospheric and stratospheric BrO at Arrival Heights, Antarctica, *Geophys. Res. Lett.,* 24, 3021-3024, 1997.

Kromminga, H., Orphal, J., Spietz, P., Voigt, S., and J.P. Burrows: New measurements of OClO absorption cross-sections in the 325-435 nm and their temperature dependence between 213-293K, *J. Photochem. Photobio. A.,* 157, 149-160, 2003.

Kurucz, R.L., Furenlid, I., Brault, J., and Testerman, L.: Solar flux atlas from 296 to 1300 nm, National Solar Observatory, Sunspot, New Mexico, U.S.A., 1984.

Lambert, J.-C., Van Roozendael, M., De Mazière, M., Simon, P.C., Pommereau, J.-P., Goutail, F., Sarkissian, A., and Gleason , J.F. : Investigation of pole-to-pole performances of spaceborne atmospheric chemistry sensors with the NDSC, *J. Atmos. Science*, Vol. 56, 176-193, 1999.

Lary, D.J.: Gas phase atmospheric bromine photochemistry, *J. Geophys. Res.,* 101, 1505-1516, 1996.

Lary, D.J., Chipperfield, M.P., Toumi, R., and Lenton, T.: Heterogeneous atmospheric bromine photochemistry, *J. Geophys. Res.*, 101, 1489-1504, 1996.

Lary, D.J., Halogens and the chemistry of the free troposphere, *Atmos. Chem. Phys.*, 5, 227-237, 2005.

Leser, H., Höninger, G., and Platt, U.: Max-DOAS measurements of BrO and NO_2 in the marine boundary layer, *Geophys. Res. Lett.,* 30, 1537, doi:10.1029/2002GL015811, 2003.

Levenberg, K.: A Method for the Solution of Certain Problems in Least Squares, *Quart. Appl. Math.* 2, 164-168, 1944.

Logan, J.A.: An analysis of ozonesonde data for the troposphere: Recommendation for testing 3-D models and development of a gridded climatology for tropospheric ozone, *J. Geophys. Res.*, 104, 16115-16149, 1999.

Mahajan, A.S., Oetjen, H., Lee, J.D., Saiz-Lopez, A., McFiggans, G.B., and Plane, J.M.C., High bromine oxide concentrations in the semi-polluted boundary layer, *Atmos. Envir.,* 43, 3811-3818, 2009.

Marquardt, D.: An algorithm for Least-Squares Estimation of Nonlinear Parameters, *SIAM J. Appl. Math.* 11, 43-441, 1963.

Martin, R.V., Chance, K., Jacob, D.J., Kurosu, T.P., Spurr, R.J.D., et al.: An improved retrieval of tropospheric nitrogen dioxide from GOME, *J. Geophys. Res.*, 107(D20), 4437, doi:10.1029/2001JD001027, 2002.

Martinez, M., Arnold, T., and Perner, D.: The role of bromine and chlorine chemistry for arctic ozone depletion events in Ny-Ålesund and comparison with model calculations, *Ann. Geoph.,* 17, 941-956, 1999.

Matveev, V., Peleg, M., Rosen, D., Tov-Alper, D., et al., Bromine oxide-ozone interaction over the Dead Sea, *J. Geophys. Res.,* 106, 10375-10387, 2001.

Mayer, B. and A. Kylling: Technical note: The libRadtran software package for radiative transfer calculations – description and examples of use, *Atmos. Chem. Phys.,* 5, 1855-1877, 2005.

McElroy, M.B., Salawitch, R.J., Wofsy, S.C., and Logan, J.A.: Reductions of Antarctic ozone due to synergetic interactions of chlorine and bromine, *Nature*, 321, 759-762, 1986.

McElroy, C.T., McLinden, C.A., and McConnell, J.C.: Evidence for bromine monoxide in the free troposphere during the Arctic polar sunrise, *Nature,* 397, 338-341, 1999.

Meller, R., and G. K. Moortgat, Temperature dependence of the absorption cross-sections of formaldehyde between 223 and 323 K in the wavelength range 225– 375 nm, *J. Geophys. Res.*, 105, 7089–7101, 2000.

Middleton, W. E. K., Vision through the Atmosphere, Univ. of Toronto Press, Toronto, 1952.

Molina, M.J. and Rowland, F.S.: Stratospheric sink for chlorofluoromethanes: chlorine atome-catalysed destruction of ozone, *Nature*, 249, 810-812, 1974.

Molina, L.T. and Molina, M.J.: Production of Cl_2O_2 from the self-reaction of the ClO radical, *J. Phys. Chem.*, 91, 433-436, 1987.

Montzka, S., Butler, J.H., Myers, R.C., Thompson, T.M., et al.: Decline in the tropospheric abundance of halogen from halocarbons: Implications for stratospheric ozone depletion, *Science*, 272, 1318-1322, 1996.

Montzka, S.A., Butler, J.H., Hall, B.D., Mondeel, D.J., and Elkins, J.W.: A decline in tropospheric organic bromine, *Geophys. Res. Lett.*, 30(15), 1826, doi:10.1029/2003GL017745, 2003.

Munro, R., Eisinger, M., Anderson, C., Callies, J., Corpaccioli, E., Lang, R., Lefebvre, A., Livschitz, Y., and Albinana, A. P.: GOME-2 on MetOp, in: Proc. of The 2006 EUMETSAT Meteorological Satellite Conference, Helsinki, Finland, 12–16 June 2006, EUMETSAT P.48, 2006.

Noxon, J.F.: Nitrogen dioxide in the stratosphere and troposphere measured by ground-based absorption spectroscopy, *Science*, 189, 547-549, 1975.

Oppenheimer, C., Tsanev, V.I., Braban, C.F, Cox, R.A., Adams, J.W., Aiuppa, A., Bobrowski, N., Delmelle, P., Barclay, J., and McGonigle, A.J.: BrO formation in volcanic plumes, *Geochim. Cosmochim. Acta*, 70, 2935-2941, 2006.

Palmer, P.I., Jacob, D.J., Chance, K., Martin, R.V., et al.: Air-mass factor formulation for spectroscopic measurements from satellites : application to formaldehyde retrievals from GOME, *J. Geophys. Res.*, 106(D13), 14539-14550, doi:10.1029/2000JD900772, 2001.

Pfeilsticker, K., Sturges, W.T., Bösch, H., Camy-Peyret, C., Chipperfield, M. P., Engel, A., Fitzenberger, R., Müller, M., Payan, S., and Sinnhuber, B.-M.: Lower stratospheric organic and inorganic bromine budget for the arctic winter 1998/99, *Geophys. Res. Lett.*, 27, 3305-3308, 2000.

Platt, U., and Stutz, J.: Differential Optical Absorption Spectroscopy (DOAS), Principle and Applications, ISBN 3-340-21193-4, Springer Verlag, Heidelberg, 2006.

Preston, K. E., R. L. Jones, and H. K. Roscoe, Retrieval of NO_2 profiles from ground-based UV-visible measurements – method and validation, *J. Geophys. Res.*, 102, 19,089-19,097, 1997.

Pundt, I., Pommereau, J.-P., Chipperfield, M.P., Van Roozendael, M., and Goutail, F.: Climatology of the stratospheric BrO vertical distribution by balloon-borne UV-visible spectrometry, *J. Geophys. Res.*, 107(D24), 4806, doi:10.1029/2002JD002230, 2002.

Rayleigh, L.: On the transmission of light through an atmosphere containing many small particles in suspension, and on the origin of the blue of the sky, *Phil. Mag.*, 41, 447-454. Also: in the scientific papers of Lord Rayleigh, Vol. 4, Dover, New York, 1964 (1899).

Read, K.A., Mahajan, A.S., Carpenter, L.J., Evans, M.J., et al.: Extensive halogen-mediated ozone destruction over the tropical Atlantic Ocean, *Nature*, 453, 1232-1235, 2008.

Reichler, T., Dameris, M., and Sausen, R.: Determining the tropopause height from gridded data, *Geophys. Res. Lett.*, 30(20), 2042, doi: 10.1029/2003GL018240, 2003.

Richter, A., Wittrock, F., Eisinger, M., and Burrows, J.P.: GOME Observations of Tropospheric BrO in Northern Hemispheric Spring and Summer 1997, *Geophys. Res. Lett.*, 25, 2683-2686, 1998.

Richter, A., Eisinger, M., Ladstätter-Weissenmayer, A., and Burrows, J.P.: DOAS zenith-sky observations, 2, seasonal variation of BrO over Bremen (53°N) 1994-1995, *J. Atmos. Chem.*, 32, 83-99, 1999.

Richter, A., Wittrock, F., Ladstätter-Weissenmayer, A., and Burrows, J. P.: GOME measurements of stratospheric and tropospheric BrO, *Adv. Space Res.*, 29, 1667-1672, 2002.

Rodgers, C. D.: Inverse Methods for Atmospheric Sounding, Theory and Practice, World Scientific Publishing, Singapore-New-Jersey-London-Hong Kong, 2000.

Roscoe, H.K., Johnston, P.V., Van Roozendael, M., Richter, A., et al.: Slant column measurements of O_3 and NO_2 during the NDSC intercomparison of zenith-sky UV-visible spectrometers in June 1996, *J. Atmos. Chem.*, Vol. 32, 281-314, 1999.

Roscoe, H.K., Hill, J.G.T., Jones, A.E., Sarkissian, A.: Improvements of the accuracy of zenith-sky measurements of total ozone by visible spectrometers II: use of daily air-mass factors, *J. Quant. Spectrosc. Radiat. Trans.* 68, 327-336, 2001.

Rozanov, A., Rozanov, V., Buchwitz, M., Kokhanovsky, A., and Burrows, J.P.: SCIATRAN 2.0. A new radiative transfer model for geophysical applications in the 175-2400 nm spectral region, *Adv. Space Res.*, 36(5), 1015-1019, 2005a.

Rozanov, A., Bovensmann, H., Bracher, A., Hrechanyy, S., Rozanov, V., Sinnhuber, M., Stroh, F., and Burrows, J.P.: NO2 and BrO vertical profile retrieval from SCIAMACHY limb measurements: Sensitivity studies, *Adv. Space Res.*, Vol. 36(5), 846-854, doi:10.1016/j.asr.2005.03.013, 2005b.

Saiz-Lopez, A., Plane, J.M.C., and Shilito, J.A.: Bromine oxide in the mid-latitude marine boundary layer, *Geophys. Res. Lett.*, 31, L03111, 2004.

Saiz-Lopez, A., Mahajan, A.S., Salmon, R.A., Bauguitte, S.J.-B., Jones, A.E., Roscoe, H.K., and Plane, J.M.C.: Boundary layer halogens in coastal Antarctica, *Science*, 317, 348, doi:10.1126/science.1141408, 2007.

Salawitch, R.J., Weisenstein, D.K., Kovalenko, L.J., Sioris, C.E., Wennberg, P.O., Chance, K., Ko, M.K.W., and McLinden, C.A.: Sensitivity of ozone to bromine in the lower stratosphere, *Geophys. Res. Lett.*,32, L05811, doi: 10.1029/2004GL021504, 2005.

Salawitch R.J., Atmospheric chemistry: biogenic bromine, *Nature*, 439, 275-277, 2006.

Salby, M., Pielke, R., Dmowska, R.: Fundamentals of Atmospheric Physics, *International Geophysics Series*, Academic Press, 628 pp, 1996.

Sander, S.P., Friedl, R. R., Golden, D. M., Kurylo, M.J., Huie, R.E., Orkin, V.L., Moortgaat, G.K., Ravishankara, A.R., Kolb, C.E., and Molina, M.J.: Chemical Kinetics and Photochemical Data for Use in Atmospheric Studies. Evaluation Number 14: update of key reactions, Tech. rep., Jet Propulsion Laboratory, California Institute of Technology, Pasadena, California, 2003.

Sander, S.P., Friedl, R.R., Ravishankara, A.R., et al.: Chemical Kinetics and Photochemical Data for Use in Atmospheric Studies, Evaluation Number 15: update of key reactions, Tech. rep., Jet Propulsion Laboratory, California Institute of Technology, Pasadena, California, 2006.

Schofield, R., Kreher, K., Connor, B.J., Johnston, P.V., Thomas, A., Shooter, D., Chipperfield, M.P., Rodgers, C.D., and Mount, G.H.: Retrieved tropospheric and stratospheric BrO columns over Lauder, New Zealand., *J. Geophys. Res.*, 109, D14304, doi:10.1029/2003JD004463, 2004a.

Schofield, R., Connor, B.J., R., Kreher, K., Johnston, P.V., Rodgers,C.D.: The retrieval of profile and chemical information from ground-based UV-visible spectroscopic measurements, *J. Quant. Spectrosc. Radiat. Transfer*, 86, 115-131, 2004b.

Schofield, R., Johnston, P.V., Thomas, A., Kreher, K., Connor, B. J., Wood, S., Shooter, D., Chipperfield, M. P., Richter, A., von Glasow, R., and Rodgers, C. D.: Tropospheric and stratospheric BrO columns over Arrival Heights, Antartica, 2002, *J. Geophys. Res.*, 111, D22310, doi:10.1029/2005JD007022, 2006.

Schroeder, W.H., Anlauf, K.G., Barrie, L.A., Lu, J.Y., et al.: Arctic springtime depletion of mercury, *Nature*, 394, 331-332, 1998.

Sheode, N., Sinnhuber, B.-M., Rozanov, A., and Burrows, J. P.: Towards a climatology of stratospheric bromine monoxide from SCIAMACHY limb observations, *Atmos. Chem. Phys. Discuss.*, 6, 6431-6466, 2006.

Simpson, W. R., von Glasow, R., Riedel, K., Anderson, P., Ariya, P., Bottenheim, J., Burrows, J., Carpenter, L., Frieβ, U., Goodsite, M.E., Heard, D., Hutterli, M., Jacobi, H.-W., Kaleschke, L., Neff, B., Plane, J., Platt, U., Richter, A., Roscoe, H., Sander, R., Shepson, P., Sodeau, J., Steffen, A., Wagner, T., and Wolff, E.: Halogens and their role in polar boundary-layer ozone depletion, *Atmos. Chem. Phys.*, 7, 4375-4418, 2007.

Sinnhuber, B.-M., Arlander, D. W., Bovensmann, H., et al.: Comparison of measurements and model calculations of stratospheric bromine monoxide, *J. Geophys. Res.*, 107 (D19), 4398, doi:10.1029//2001JD000940, 2002.

Sinnhuber, B.-M., Rozanov, A., Sheode, N., Afe, O.T., Richter, A., Sinnhuber, M., Wittrock, F., Stiller, G.P., von Clarmann, T., Linden, A., and Burrows, J.P.: Global observations of stratospheric bromine monoxide from SCIAMACHY, *Geophys. Res. Lett.*, 32, L20810, doi: 10.1029/2005GL023839, 2005.

Sinnhuber, B.-M., and Folkins, I.: Estimating the contribution of bromoform to stratospheric bromine and its relation to dehydration in the tropical tropopause layer, *Atmos. Chem. Phys.*, 6, 4755-4761, 2006.

Sioris, C. E., Kovalenko, L.J., McLinden, C.A., Salawitch, R.J., Van Roozendael, M., Goutail, F., Dorf, M., Pfeilsticker, K., Chance, K., von Savigny, C., Liu, X., Kurosu, T.P., Pommereau, J.-P., Bösch, H., and Frerick, J.: Latitudinal and vertical distribution of bromine monoxide in the lower stratosphere from Scanning Imaging Absorption Spectrometer for Atomspheric Chartography limb scattering measurements, *J. Geophys. Res.*, 111, D14301, doi:10.1029/2005JD006479, 2006.

Soller, R., Nicovich, J.M., and Wine, P.H.: Temperature-dependent rate coefficients for the reactions of Br($^2P_{3/2}$), Cl($^2P_{3/2}$), and O(^{3}PJ) with $BrONO_2$, *J. Phys. Chem. A*, 105, 1416-1422, 2001.

Solomon, S., Garcia, R., Rowland, F., and Wuebbles, D.: On the depletion of Antarctic ozone, *Nature*, 321, 755-758, 1986.

Solomon, S.: Stratospheric ozone depletion: a review of concepts and history, *Rev. Geophys.*, 37, 275-316, 1999.

Stamnes, K., Tsay, S.-C., Wiscombe, W., and Jayaweera, K.: Numerically stable algorithm for discrete-ordinate-method radiative transfer in multiple scattering and emitting layered media, *Appl. Opt.*, 27, 2505-2509, 1988.

Stohl, A., Forster, C., Frank, A., Seibert, P., and Wotawa, G.: Technical note: The Lagrangian particle dispersion model FLEXPART version 6.2., *Atmos. Chem. Phys.*, 5, 2461-2474, 2005.

Stutz, J., Ackermann, R., Fast, J.D., and Barrie, L., Atmospheric reactive chlorine and bromine at the Great Salt Lake, Utah, *Geophys. Res. Lett.,* 29, 1380, doi:10.1029/2002GL014812, 2002.

Theys, N., Van Roozendael, M., Hendrick, F., Fayt, C., Hermans, C., Baray, J.-L., Goutail, F., Pommereau, J.-P., and De Mazière, M.: Retrieval of stratospheric and tropospheric BrO columns from multi-axis DOAS measurements at Reunion Island (21°S, 56°E), *Atmos. Chem. Phys.*, 7, 4733-4749, 2007.

Theys, N., Van Roozendael, M., Errera, Q., Hendrick, F., Daerden, F., Chabrillat, S., Dorf, M., Pfeilsticker, K., Rozanov, A., Lotz, W., Burrows, J.P., Lambert, J.-C., Goutail, F., Roscoe, H.K., and De Mazière, M.: A global stratospheric bromine monoxide climatology based on the BASCOE chemical transport model, *Atmos. Chem. Phys.*, 9, 831-848, 2009.

Theys, N., Van Roozendael, M., Dils, B., Hendrick, F., Hao, N., and De Mazière, M.: First satellite detection of volcanic bromine monoxide emission after the Kasatochi eruption, *Geophys. Res. Lett.*, 36, L03809, doi:10.1029/2008GL036552, 2009.

Tuckerman, M., Ackermann, R., Golz, C., Lorenzen-Schmidt, H., et al.: DOAS-observation of halogen radical-catalysed Arctic boundary layer ozone destruction during the ARCTOC-campaigns 1995 and 1996 in Ny- Ålesund, Spitsbergen, *Tellus,* 49B, 533-555, 1997.

Vandaele, A.-C., C. Hermans, P.C. Simon, M. Carleer, R. Colin, S. Fally, M.-F. Mérienne, A. Jenouvrier, and B. Coquart, Measurements of the NO2 absorption cross-section from 42000 cm-1 to 10000 cm-1 (238-1000 nm) at 220 K and 294 K, *J. Quant. Spectrosc. Radiat. Transfer*, 59, 171-184, 1997.

Vandaele, A.-C., Fayt, C., Hendrick, F., Hermans, C., Humbled, F., et al.: An intercomparison campaign of ground-based UV-visible measurements of NO_2, BrO and OClO slant columns: Methods of analysis and results for NO_2, *J. Geophys. Res.*, 110, D08305, doi: 10.1029/2004JD005423, 2005.

Van Roozendael, M., Fayt, C., Lambert, J.-C., Pundt, I., Wagner, T., Richter, A., Chance, K.: Development of a bromine oxide product from GOME, European Symposium on Atmosph. Measurements from Space, ESA WPP-161, 543-547, 1999.

Van Roozendael, M., Wagner, T., Richter, A., Pundt, I., Arlander, D., Burrows, J. P., Chipperfield, M., Fayt, C., Johnston, P. V., Lambert, J.-C., Kreher, K., Pfeilsticker, K., Platt, U., Pommereau, J.-P., Sinnhuber, B.-M., Tornkvist, K. K., and Wittrock, F.: Intercomparison of BrO measurements from ERS-2 GOME, ground-based and balloon platforms , *Adv. Space Res*., 29, 1661-1666, 2002.

Van Roozendael, M, I. De Smedt, C. Fayt, F. Wittrock, A. Richter, O. Afe: First validation of SCIAMACHY BrO columns, in Proc. Second Workshop on the Atmospheric Chemistry Validation of ENVISAT (ACVE-2), Frascati, Italy, 3-7 May, 2004.

Vigouroux, C., De Mazière, M., Errera, Q., Chabrillat, S., Mahieu, E., Duchatelet, P., Wood, S., Smale, D., Mikuteit, S., Blumenstock, T., Hase, F., and Jones, N.: Comparisons between ground-based FTIR and MIPAS N_2O and HNO_3 profiles before and after assimilation in BASCOE, *Atmos. Chem. Phys.*, 7, 377-396, 2007.

von Friedeburg, C.: Derivation of Trace Gas Information combining Differential Optical Absorption Spectroscopy with Radiative Transfer Modelling, PhD thesis, University of Heidelberg, 2003.

von Glasow, R., Sander, R., Bott, A., and Crutzen, P.J., Modeling halogen chemistry in the marine boundary layer. 1: Cloud-free MBL, *J. Geophys. Res.,* 107, 4341, 2002a.

von Glasow, R., Sander, R., Bott, A., and Crutzen, P.J., Modeling halogen chemistry in the marine boundary layer. 1: Interactions with sulfur and cloud-covered MBL, *J. Geophys. Res.,* 107, 4323, 2002b.

von Glasow, R., von Kuhlmann, R., Lawrence, M. G., Platt, U., and Crutzen, P. J.: Impact of reactive bromine chemistry in the troposphere, *Atmos. Chem. Phys.*, 4, 2481-2497, 2004.

von Glasow, R. and Crutzen, P.J.: Tropospheric halogen chemistry in the atmosphere, edited by: Keeling, R.F., vol.4., Treatise on Geochemistry, edited by: Holland, H.D. and Turekian, K.K., 1-67, Elsevier-Pergamon, Oxford, 2007.

Vountas, M., Rozanov, V.V., and Burrows, J.P.: Ring effect: Impact of rotational raman scattering on radiative transfer in earth's atmosphere, *J. Quant. Spectrosc. Radiat. Transfer.*, 60, 943-961, 1998.

Wagner, T., and Platt, U.: Satellite mapping of enhanced BrO concentrations in the troposphere, *Nature*, 395, 486-490, 1998.

Wagner, T., Dix, D., von Friedeburg, C., Friess, U., Sanghavi, S., Sinreich, R., and Platt, U.: MAX-DOAS O_4 measurements: A new technique to derive information an atmospheric aerosols-Principles and information content, *J. Geophys. Res.*, 109, D22205, doi:10.1029/2004JD004904, 2004.

Wamsley, P.R., Elkins, J.W., Fahey, D.W., Dutton, G.S., et al.: Distribution of halon-1211 in the upper troposphere and lower stratosphere and the 1994 total bromine budget, *J. Geophys. Res.*, 103, D1, 1513-1526, 1998.

Wang, P., Stammes, P., van der A, R., Pinardi, G., and van Roozendael, M.: FRESCO+: an improved O_2 A-band cloud retrieval algorithm for tropospheric trace gas retrieval, *Atmos. Chem. Phys.*, 8, 6565-6576, 2008.

Wilmouth, D.M., T.F. Hanisco, N.M. Donahue, J.G. Anderson, Fourier transform ultraviolet spectroscopy of the $A^{2\Pi}{}_{3/2} \leftarrow X^{2\Pi}{}_{3/2}$ transition of BrO, *J. Phys. Chem. A.*, 103, 8935-8945, 1999.

Wittrock, F., Oetjen, H., Richter, A., Fietkau, S., Medeke, T., Rozanov, A., and Burrows, J.P.: Max-DOAS measurements of atmospheric trace gases in Ny-Ålesund – Radiative transfer studies and their application, *Atmos. Chem. Phys.*, 4, 955-966, 2004.

Wofsy, S.C., McElroy, M.B., and Yung, Y.L.: The chemistry of atmospheric bromine, *Geophys. Res. Lett.*, 2, 215-218, 1975.

World Meteorological Organization (WMO), Global ozone research and monitoring project, in Scientific Assessment of Ozone Depletion: 1998, Rep. 44, Geneva, 1998.

World Meteorological Organization (WMO), Global ozone research and monitoring project, in Scientific Assessment of Ozone Depletion: 2002, Rep. 47, Geneva, 2003.

World Meteorological Organization (WMO), Scientific Assessment of Ozone Depletion: 2006, Global ozone research and monitoring project, Geneva, Switzerland, 2007.

Yang, X., Cox, R. A., Warwick, N. J., Pyle, J. A., Carver, G. D., O'Connor, F. M., and Savage, N. H.: Tropospheric bromine chemistry and its impacts on ozone: A model study, *J. Geophys. Res.*, 110, D23311, doi:10.1029/2005JD006244, 2005.

Yang, X., Pyle, J.A., Cox, R.A., Theys, N., Van Roozendael, M., Snow-sourced bromine and its implications for polar tropospheric ozone, to be submitted to *Atmos. Chem. Phys. Discuss.*, 2009.

Ziemke, J.R., Chandra, S., and Bhartia, P.K.: "Cloud slicing": A new technique to derive upper tropospheric ozone from satellite measurements, *J. Geophys. Res.*, 106(D9), 9853-9867, 2001.

List of Acronyms

AMF	Air Mass Factor
AK	Averaging Kernel
ASM	Azimuth Scanner Module
BIRA-IASB	Belgian Institute for Space Aeronomy
BrO	Bromine monoxide
Br_y	Inorganic bromine species (Br_y=Br+BrO+$BONO_2$+HOBr+HBr+BrCl)
CCD	Charge-Couple Device
CFC	ChloroFluoroCarbon
CTM	Chemical Transport Model
DOAS	Differential Optical Absorption Spectroscopy
DSCD	Differential Slant Column Density
DU	Dobson Unit
ECMWF	European Centre for Medium-Range Weather Forecasts
ENVISAT	ENVIronmental SATellite
ERS-2	Second European Remote Sensing satellite
ESA	European Space Agency
ESM	Elevation Scanner Module
EUMETSAT	EUropean organization for the exploitation of METeorological SATellites
FWHM	Full With at Half Maximum
GOME	Global Ozone Monitoring Experiment
LOS	Line-Of-Sight
MAXDOAS	Multi-Axis DOAS
MBL	Marine Boundary Layer
MetOp	Meteorological Operational satellite
NDACC	Network for the Detection of Atmospheric Composition Change
ODE	Ozone Depletion Event
ODP	Ozone Depletion Potential
OEM	Optimal Estimation Method
OHP	Observatoire de Haute-Provence
OMI	Ozone Monitoring Instrument
O_3	Ozone
PBL	Polar Boundary Layer
PMD	Polarization Measurement Device
pptv	Parts Per Trillion Volume
PSC	Polar Stratospheric Cloud
RTE	Radiative Transfer Equation
RTM	Radiative Transfer Model
SCD	Slant Column Density

SCIAMACHY	SCanning Imaging Absorption spectroMeter for Atmospheric CartograpHY
SZA	Solar Zenith Angle
UV	Ultra Violet
VCD	Vertical Column Density
VSLS	Very Short-Lived Substances
WF	Weighting Function
WMO	World Meteorological Organization

Notes